ROLE OF ENERGY LOCALIZATION ON CHEMICAL REACTIONS AT EXTREME CONDITIONS

by

Brenden W. Hamilton

A Dissertation

Submitted to the Faculty of Purdue University

In Partial Fulfillment of the Requirements for the degree of

Doctor of Philosophy

School of Materials Engineering

West Lafayette, Indiana

May 2022

THE PURDUE UNIVERSITY GRADUATE SCHOOL
STATEMENT OF COMMITTEE APPROVAL

Dr. Alejandro Strachan, Chair

School of Materials Engineering

Dr. Steven Son

School of Mechanical Engineering

Dr. Eric Kvam

School of Materials Engineering

Dr. Davin Piercey

School of Materials Engineering

Approved by:

Dr. David F. Bahr

Dedicated to the Spanish Inquisition, whom no one expects [1].

ACKNOWLEDGMENTS

TABLE OF CONTENTS

LIST OF TABLES

LIST OF FIGURES

11

ABSTRACT

High explosives represent a class of materials known as energetic materials, in which providing an external stimulus of impact, heat, and electric shock can result in rapid exothermic reactions. Hence, there has always been a considerable research focus into the development, production, optimization, and control of these materials, aiming to increase explosive capabilities while also decreasing overall sensitivity to ignition.

The study of impact induced chemical initiation of explosives is an inherent multiscale problem that requires time and length scales not accessible by a single experiment or calculation. The works presented here provide a theoretical effort to contribute to bottom-up modeling of the physics and chemistry phenomena in reacting high explosives using molecular dynamics simulations. Focus will be placed how energy localizes in the molecular crystal TATB, an insensitive high explosive.

The first energy localization topic covered is an intra-molecular localization and distribution of the kinetic energy. Molecular dynamics is inherently classical, which partition energy equally between all modes. However, most molecular explosives should follow a quantum description, where energy is partitioned between modes following the Bose-Einstein distributions. A semi-classical approximation called the 'quantum thermal bath' is applied here to study classical vs. quantum effects for both shock and thermal initiation of chemistry. These results show, not only the importance of the changes to specific heat, which is expected, but the influence of the zero-point energy on reactivity.

The idea of energy localization is then expanded to the microstructural level, focusing on hotspots, which are areas of extreme temperature following interactions between a shockwave and the microstructure. To date, hotspots have been characterized and described by the localization of their temperature fields only. This work develops a description of the potential energy field in the hotspot, which is markedly different from the temperature field and cannot be predicted from it, as has been previously assumed. This latent potential energy, that is non-thermal, manifests from intra-molecular strain in which individual molecules in the hotspot become highly distorted. This strain energy is shown to be driven by plastic flow during the formation of the hotspot.

Lastly, the influence of the latent PE in hotspots on chemical reactivity is assessed. Reactive molecular dynamics calculations of shock induced pore collapse creates a hotspot in which

deformed molecules can be separately assessed from undeformed ones. Deformed molecules are shown to react faster, follow different ensemble statistics, and undergo different first step reaction pathways. To better study these deformation under equilibrium, the Many-Bodied Steered MD method is developed in which multiple deformation modes are explored. It is shown that different deformation paths in the same molecule leads to different mechanochemical accelerations of kinetics and a different alteration of first step reaction pathways.

1. INTRODUCTION

This initial introduction chapter will serve as a brief review of general, scientific works and principles related to shock compression and energy localization in energetic materials, specifically, high explosives, which shall be the focus of this work. The topics covered in this chapter will be highly relevant to each of the major results chapters (3-5) and are presented here to minimize repetition of information. Each of the following chapters will present significantly more in-depth introduction and methods sections that will be highly relevant to that chapter. In general, the collection of works presented in this dissertation is focused on understanding the way in which energy localizes in molecular solids, and how that energy localization can affect chemical reactions.

Energetic materials (EMs) have relevant operating conditions of 1000s of kelvin and 10s of gigapascals, which typically results in ultrafast chemical reactions on the order of nanoseconds [2]. These extreme conditions, typically generated via ultra-high strain rate compaction, or shockwave compression, often prove difficult to study due to the diminutive time and length scales of the relevant physics and chemistry to the initiation of reaction and lead up to detonation. Hence, here I will utilize the predictive all-atom modeling technique of molecular dynamics (MD) to study shock energy localization and shock induced reaction phenomena. In the subsequent subsections, I will provide a general review on the initiation of reactions and detonations in EMs and how the material's microstructural features are known to play a substantial role in these processes. The remaining sections will be as follows: Chapter 2 will discuss all relevant methodologies and procedures used in the majority of studies, Chapter 3 will focus on contrasting the classical and quantum descriptions of thermal and mechanical insults, Chapter 4 will discuss thermo-mechanical energy localization of potential energy in an HEs microstructure, Chapter 5 will discuss mechanochemistry in hotspots and how to mimic it, and Chapter 6 will consist of a general summary, conclusions, and outlook.

1.1   Shock Compression of Condensed Matter

Most of the work discussed here will assess the response of energy localization in energetic materials under shock loading. Hence, it is crucial to undergo a basic review of shockwaves in matter as the theory will prove quintessential to explaining the results hereafter. It should be first

noted that shock compression is a dynamic compression. In static compression, the entire material can be thought of as in equilibrium, with respect to the timescales of compression. In dynamic compression, which is typically faster than stress equilibrations, the high strain rates lead to a non-equilibrium state in which material that has interacted with the shockwave is in a shocked state (which can be considered locally in equilibrium), and some material will have yet to undergo compression. The shockwave will propagate across the material, compressing as it goes. Since subsonic acoustic waves are often the primary contributors in equilibrating compressive stresses in a material, the supersonic shockwave will always propagate faster than equilibration events. In this work, I will mainly focus on the transient state, in the regime of nanometers behind the shock front, in which the material is still far from total equilibrium, however local equilibrium is often achieved for temperature and pressure fields.

A shockwave can be simply defined as a compression wave in which the wave velocity, U_s, is greater than the local material sound speed. This leads to a nearly discontinuous rise in temperature and pressure (and therefore energy) behind the shock front, with all shocked atoms increasing their velocity in the direction of the wave propagation by a net particle velocity, U_p, as shown in Figure 1.1. Shockwaves are typically induced (in the lab setting) via an impact into the free surface of a sample. Experimentally this can be done by impact with a flyer plate from a gas gun [3] or laser induced shockwaves [4]. In the case of a piston impact with perfect conservation of momentum, the piston velocity (velocity of the flyer plate) will be exactly equal to the U_p. In the case of disparity of density in the flyer and sample, or when shockwaves transverse over a material interface, a special technique known as impedance matching is used to assess the shock state of each component of the system [5].

Simple 1-D conservation laws, known as the Rankine-Hugoniot Jump Conditions, relate the shock variables U_p, U_s, pressure (P), specific volume (v), and energy (E) in a set of three equations in which knowing two of the variables results in being able to solve for the other three. The jump conditions only apply directly for the case of a single, planar, steady-state wave, and are as follows:

$$\frac{v}{v_o} = \frac{U_s - U_p}{U_s}$$

$$P - P_o = \rho_o U_s U_p$$

$$E - E_o = \frac{1}{2}P(v_o - v)$$

derived from the mass, momentum, and energy conservation laws, respectively. In this case, energy (E) is in units of energy per mass.

The shock response of a material is displayed in plots known as Hugoniot curves (see Figure 1.2) and are typically plotted in P-v or U_s-U_p space. These curves are the locus of shock states available to a material, from a given initial thermodynamic state, where each individual point represents a single shock. However, Hugoniot curves do not represent the path of compression for the shock rise. The path of compression is P-v space is the Rayleigh line, a straight line from the initial state to the shocked state with equation

$$P - P_o = \frac{U_s^2}{v_o^2}(v_o - v)$$

In the case of re-shocking samples or two-wave features, a Rayleigh line cannot cross a P-v Hugoniot curve, and multiple-wave features are needed to access areas in P-v space such as elastic-plastic Hugoniot curves.

When a shock reaches an open surface, the shocked material can freely expand outwards. This causes a pressure release at the surface, generating a backward moving relief wave know as a rarefaction wave. The speed of the rarefaction wave is dependent on the initial shock and the material's Hugoniot and can be solved from impedance matching [5], and multiple waves often form a rarefaction fan. When a planar, 1-D shock reaches a planar, free surface, the velocity of the expanding material, due to conservation of momentum, will be $2U_p$. In the case of curved surfaces, such as porosity in a sample or surface roughness, shock focusing can cause the expanding velocity to be much higher [6–9].

Once a shockwave has begun to propagate across a material, it has two criteria for the shock to be sustained and stable:

$$\frac{U_s}{c_o} > 1$$

$$\frac{(U_s - U_p)^2}{c_1^2} < 1$$

where c_o is the sound speed of the unshocked material and c_1 is the sound speed of the shocked material. Since sound speed is affected by the material's pressure, lateral relaxations and plasticity behind the shockwave can lower the shocked sound speed, causing instability based on the second criteria, which can dampen or weaken the shockwave. While the extreme conditions of shocks can

lead to a variety of materials processes such as plasticity and phase transformations [10–13], the majority of this work will focus on how shock energy is localized in molecules and the microstructure, and how that corresponds to chemical reactivity in high explosives.
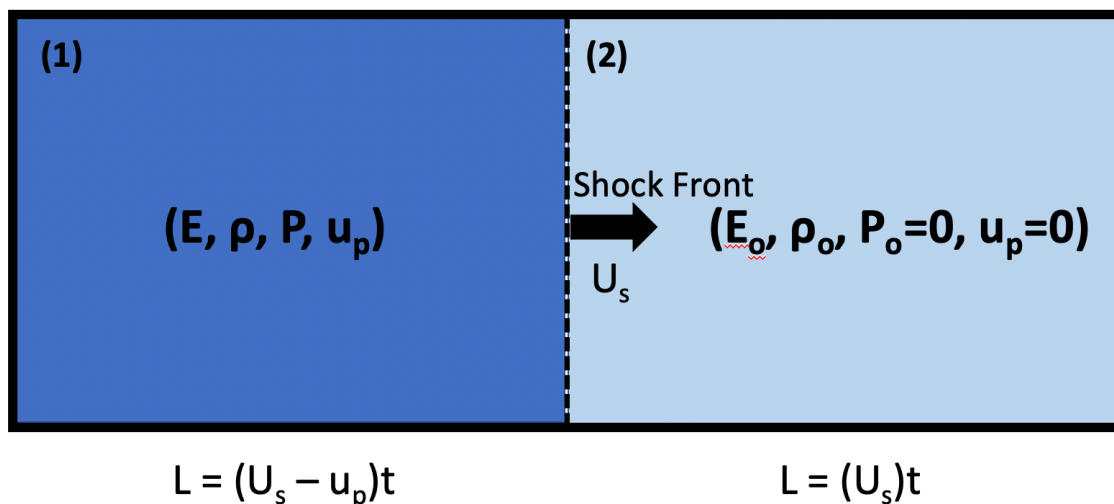
Figure 1.1: Diagram of a 1-D planar shockwave in a homogenous medium. The dashed line represents the shockwave, traveling at velocity Us. The dark blue is the shocked material, traveling at velocity Up with thermodynamic state (E, ρ, P, T) and the light blue material is unshocked, at rest, with thermodynamic state (E_o, ρ_o, P_o, T_o).

1.2   Shock Initiation of Energetic Materials

As the totality of this work fill be focused on a class of materials known as high explosives (HEs), which fall under the umbrella of energetic materials (EMs), it is necessary to define these terms. EMs are a unique class of material that often exist in a metastable state, in which leaving this state for a lower energy state results in a sizeable exothermic release. Specifically, HEs are EMs that exist as organic, molecular crystals such as RDX, PETN, and TATB. The key to HEs is that they contain both the necessary fuel and oxidizer for combustion within a single molecule. In contrast, low explosives are typically fuel-oxidizer mixtures that cannot detonate, only deflagrate. When HE systems receive an influx of energy that is enough to incite chemical reaction, they will decompose into simple gaseous products such as H_2O, CO_2, N_2, and NH_3, releasing massive levels of energy that often results in an explosion, or even a detonation, depending on the system and its environment [14].

One of the most commonly studied methods of initiating these reactions in HEs is shock compression. As discussed in Section 1.1, the shock compression of a condensed matter system results in a rise in local temperature, pressure, and internal energy [15,16], and results in non-hydrostatic, transient states directly behind the shockwave than can induce events like defect nucleation [17,18], plasticity [10,19], phase transformations [20–22], and melting [11]. Shock loading in inherently non-equilibrium in that the compression wave transverses the material at supersonic velocities with picosecond pressure rise times, resulting in a spatially dependent material description during the loading event. In the case of shock loading of HE materials, the increase in temperature and deviatoric stresses can rapidly induce chemical reactions. The initiation of chemical reactions in HEs is generally assumed to follow a few key steps in which, firstly, excess energy is generated in concerted regions know as 'hotspots' due to interactions between the shockwaves and the material's microstructure/defects [23–25], then, the increase in energy, both in hotspots and in the bulk material, preferentially couples with low frequency molecular modes, known as 'doorway modes', which leads to their over-excitement on rapid timescales. Thusly, this excess energy then moves into high-frequency modes via a process called vibrational up-pumping [26,27], which leads to the excitation of bond vibrations that can result in prompt chemistry. Under the up-pumping description of shock initiation, chemical decomposition occurs under extreme, yet equilibrium, conditions.

Over the past few decades, work has been done to assess shock induced reaction kinetics [26,28–30], decomposition pathways [31–34], and the products equation of state [35,36], as well as safety metrics like time to explosion [37–39] and sensitivity [24,31,40,41]. However, experimentally probing decomposition pathways is exceptionally difficult at these time and length scales. Hence, the bulk of the early research on shock induced chemistry in condensed systems involved MD simulations with density functional theory (DFT) or density functional tight binding (DFTB). The development of the classical reactive force field ReaxFF [42] enabled significantly larger simulations of shock decomposition for longer timescales than capable with DFT/DTFB. Yet, at the time, it was impossible to experimentally validate these chemistry predictions, until the development of ultrafast spectroscopy coupled with laser-driven shocks, resulting in spectroscopic images in reacting liquid/polymer HEs such as PVN [43] and nitromethane [35]. Since then, experimental advances [4,44,45] and the development of coarse grained and multiscale models [8,46,47] have allowed for much more direct comparisons with

experiments. While bulk, shock induced chemistry studies can lead to numerous insights into the nature of EMs, the grand challenge for these materials is related to heterogenous initiation (hotspots) and shock to detonation transition. Additionally, recent advances have begun to suggest the importance of non-equilibrium states [48,49] and mechanochemistry [50–54] for shock induced chemical reactions.

1.3   Hotspot Formation and Criticality

In the case of HEs, a typical shock compression event (1-10s GPa) usually does not heat the bulk crystal to a hot enough temperature to induce the rapid chemistry necessary to lead to detonation. Often, the shock initiation of chemistry that does lead to explosion or detonation relies on the interaction of the shock with the materials microstructure/defects that localizes excess energy into 'hotspots' [2,55]. Hotspots result in small regions of high temperature and, therefore, prompt chemistry. If the energy release from the hotspot chemistry is significant enough, the hotspots can grow via self-propagation and coalesce into a deflagration or detonation [25]. Hotspots were first shown to be of importance through shock desensitization experiments in which weak compaction waves would remove large microstructural defects, like porosity, from an HE sample without causing ignition, which then rendered the sample non-detonable when re-shocked [56]. Additionally, experiments in gelled nitromethane, which included defects from silica nanobeads and air bubbles, showed the superiority of the latter in decreasing the run to detonation distance [57]. It was also shown that more numerous small bubbles were superior to a few larger ones. While the collapse of bubbles (or more generally, porosity) is known to be the most important hotspot formation mechanism, hotspots can also form via plasticity, shear bands, friction, shock interaction with grain boundaries, viscous heating, and jetting [58].

Hotspot reactions are a type of Frank-Kamenetskii problem in which exothermic chemistry directly competes with thermal transport [59]. If the reaction's energy release is enough to overcome conduction losses, the hotspot can expand as a steady-state deflagration [60]. This has led many to define the state of a hotspot by its temperature and size, where a given size and shape will have a minimum 'critical' temperature for which it transitions to a steady deflagration [39]. Since the initial conditions of the hotspot control events such as run to detonation, time to

explosion, and detonation failure, studies of shock formation of hotspots have been of interest for decades in both experimental and theoretical work [27,45,51,61–63].

One key aspect of hotspot chemistry is the marked difference in reactivity within hotspots formed dynamically (pore collapse, shear bands) compared to those formed thermally under equilibrium conditions. Wood and Cherukara showed, through all-atom simulations of hotspots in RDX, the onset of steady deflagration was much quicker in hotspots formed under dynamical loading (shock induced pore collapse) than hotspots of identical size, shape, temperature, and pressure formed via thermal loading under equilibrium conditions [61]. Kroonblawd and Fried inspected local chemistry in shocked TATB, showing that the reactions in shear bands had kinetics more than an order of magnitude faster than for the bulk shock region without defects [51]. In both cases, these effects were hypothesized to be from, and attributed to, covalent mechanochemistry, i.e. a deformation of intra-molecular bonds accelerating reaction rates [64]. A significant portion of this work (Chapters 4 and 5) will be spent on the formation of, and local reactions in, hotspots, attempting the elucidate the underlying physics that govern hotspot phenomena and mechanochemistry at extreme conditions.

1.4   Steady Detonation

Detonation is a steady state propagation of a supersonic reaction front, or when the propagation of the chemical reaction zone becomes a shockwave [23]. Hence, not all explosions or reactions in HEs are detonations. As the shock front raises the temperature and pressure to induce prompt chemistry, the rapid, exothermic nature of the reaction supports the shock, leading to a steady state solution at a constant velocity (detonation velocity). Detonations can be induced from shock initiation (shock to detonation transition) or thermal initiation (deflagration to detonation transition). In both cases, the initial reactions (often from hotspots) are far behind the shock front. The reaction is only considered a detonation when the reaction wave has overtaken the leading shockwave, accelerating it to the detonation velocity. This time delay is known as the run to detonation, and is a function of the material, its microstructure, and the local environment (temperature, pressure, confinement, etc.). Predicting run to detonation from first principles information and the material's microstructure remains a grand challenge, with predictions of run to detonation usually requiring phenomenological models fit to other experiments [38,65].

The simplest theoretical model for detonation is described by the Zeldovich–von Neumann–Doering (ZND) theory [5]. ZND theory assumes a steady state, 1D detonation wave in a continuous, homogenous material and that the shock front is a discontinuity, with a reaction rate of zero ahead of the shock and a finite rate behind the shock. The shock front takes the material to a high pressure point on the unreacted Hugoniot (shock equation of state) known as a von Neumann spike (Figure 1.2, point B). From point B, reaction begins to occur, and the material expands across a finite reaction zone, which ends at the Chapman–Jouguet (CJ) point (Figure 1.2, point C). Figure 1.2, which shows a Rayleigh line that starts at the initial condition (point A) and is tangent to the products' Hugoniot (point C), represents a steady detonation wave. The detonation velocity can be obtained from the Rayleigh line slope. The intersection of this Rayleigh line with the Hugoniot of the reactants marks the von Neumann spike. The point of tangency to the product Hugoniot is the CJ state. Because these are steady state conditions, knowing the HE and product's Hugoniot curves allow for prediction of detonation velocity and CJ pressure without simulating an actual detonation [66]. Using methods described in Section 2.4, inexpensive and accurate predictions of detonation velocity can be made from molecular dynamics simulations on the order of a few cubic nanometers [66].
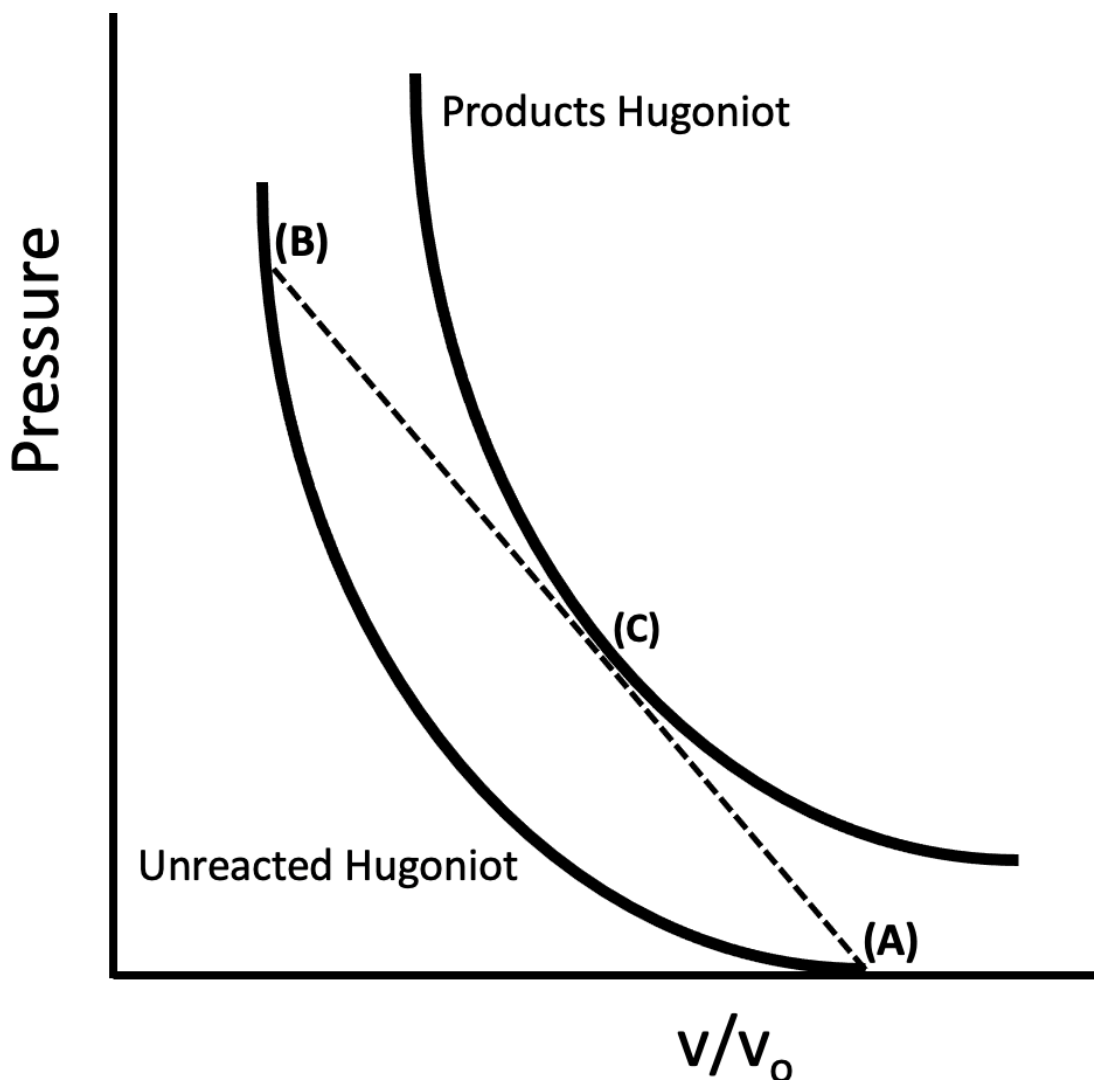
Figure 1.2: Example P-V Hugoniot curve in which the Rayleigh line represents the wave for a steady state detonation. Point A is the unshocked state, Point B is the von Neumann spike, Point C is the CJ state.

1.5   1,3,5-triamino-2,4,6-trinitrobenzene (TATB)

Almost all results discussed in the following chapters will deal with the insensitive high explosive (IHE) 1,3,5-triamino-2,4,6-trinitrobenzene, known commonly as TATB. Since TATB is highly complex in both its mechanical and chemical response, relative to other HEs, it is necessary to thoroughly review its structure and properties here.

Structurally, TATB is a triclinic unit cell with a $P\bar{1}$ crystal structure [67]. The planar TATB molecules sit in graphitic-like sheets, known as basal planes, that have a hexagonal-like packing

in the plane. Figure 1.3 shows a top-down view of a single basal plane (lattice vector $\mathbf{c}$ into the page) and a view of the basal planes in the coordinate frame of lattice vector $\mathbf{a}$ and $N_{(001)} = a \times b$, top and bottom images, respectively. These renderings are from replications of the unit cell that form a nearly orthorhombic supercell. Intra-planar interactions are governed by the strong inter-molecular hydrogen bonding, whereas the inter-planar interactions are dominated by weak van der Waals forces. In the top panel of Figure 1.3 (top-down view of a basal plane) the carbon atoms are rendered at 5x the size of all other atoms to help showcase the molecular symmetry of the planes.
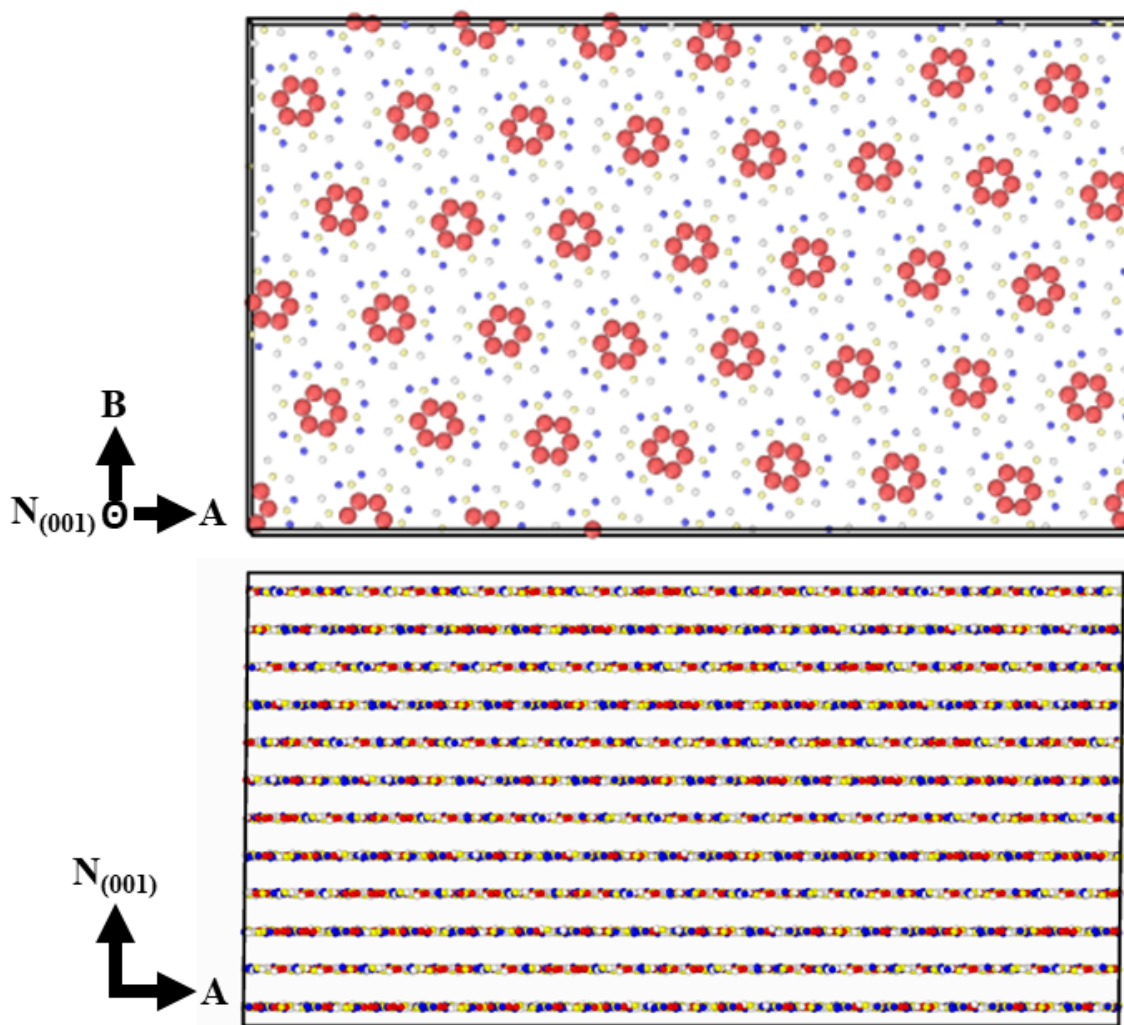
Figure 1.3: TATB crystal structure. Top image is of a single basal plane in the direction where lattice vector $\mathbf{c}$ is into the page. The bottom image is of the plane formed from $\mathbf{a}$ and $N_{(001)} = a \times b$, which shows the basal plane stacking. Red atoms, which represent the inner carbon ring, have been enlarged to show the 6-fold symmetry of the molecules within the planes.

Owing to the non-symmetric crystal structure, TATB has highly anisotropic mechanical and thermal properties. The strong bonding withing the planes relative to the inter-plane interactions leads to elastic constants such that $C_{11} \cong C_{22} \cong 3.4C_{33}$ [68]. The role of TATB's anisotropy in its shock loading response has been well characterized for shock strengths near 10 GPa [69]. Zhao et. al. utilized all-atom MD simulations to assess TATB's shock response in a variety of crystallographic orientations spanning the bounding cases of along and perpendicular to the basal planes. The rise in shock temperature and compression level increased in cases in which the shock direction was more closely aligned with the lattice vector **a** (nearly perpendicular to basal planes). Additionally, this work showed significant orientation effects on the wave structure (single vs 2-wave response) and deformation mechanisms, which ranged from a variety of crystal level defects, such as buckling and twinning, to plasticity and intense shear localization, dependent on the orientation of the crystal. MD and isotropic continuum simulations [9] explored the mechanics of TATB pore collapse for a subset of the previously studied orientations, but for shock speeds ranging from 500 to 2000 m/s, enacting a range of viscoplastic and hydrodynamic responses. Significant disparity between MD results and an isotropic, elastic-plastic continuum model's results for weak shocks highlighted the significance of anisotropic effects in shock loading of TATB.

Work from Laforcaude et. al. directly studied defect formation in TATB using equilibrium compression simulations in an all-atom MD framework utilizing rigid molecules [70]. For stresses in the [100] and [010] directions, a buckling mechanism deforms the basal planes into a chevron like pattern, which retains the hydrogen bonding between molecules at the apexes of the chevrons. Stresses of pure shear along (011) type planes lead to a defect referred to as non-basal gliding, which manifests similar to a screw dislocation between planes. Figure 1.4 shows examples of both buckling and non-basal glide type defects. Stresses in the [001], which is the softest direction, can induce transverse glide in the planes and volume conserving phase transformations [71]. These crystalline defects, as well as shear band formation [51], become the main mechanisms for relieving deviatoric stresses under shock loading, both in single crystals [51,69] and porous [9] and polycrystalline TATB [72].
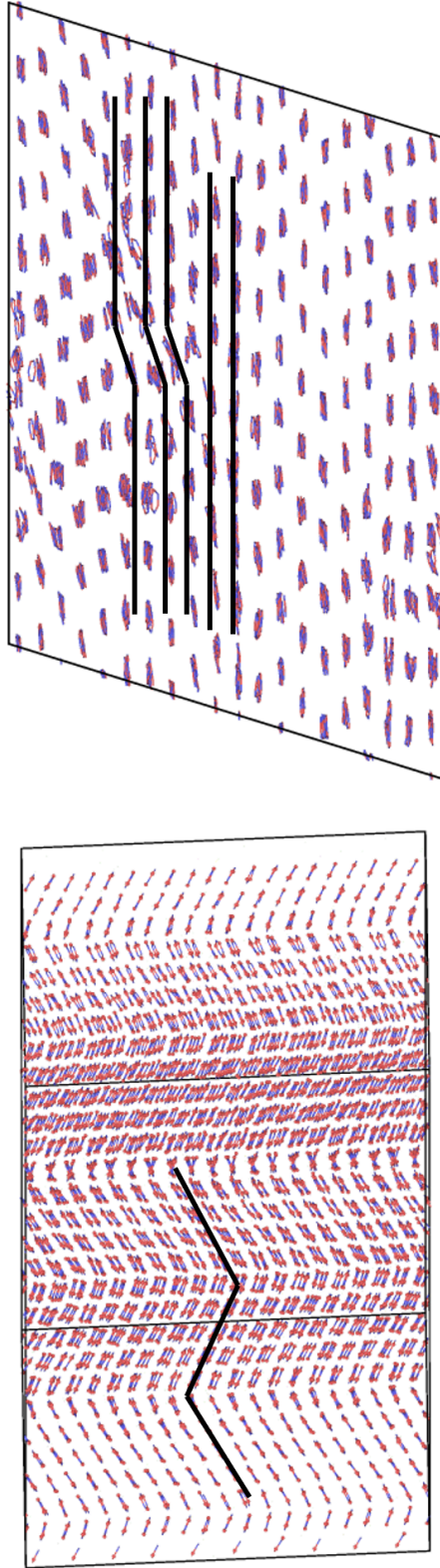
Figure 1.4: a) Non-basal glide defect from shear stresses along the (011) and b) plane buckling defect (chevron formation) from [100] stresses.

In addition to highly anisotropic mechanical properties, TATB exemplifies an extreme bounding case for thermal conductivity in a molecular material [73]. Defect free TATB has an in plane (along [100] and [010], or the **a** and **b** lattice vectors) thermal conductivity value of 1.07 W/mK and an out of plane (along [001] or lattice vector **c**) of 0.52 W/mK. This factor of two difference can lead to highly anisotropic hotspot relaxations in hotspots where the material remains crystalline [74,75].

1.6   Scope and Motivation

In this work, I aim to assess how localizations of energy in TATB (or more general, in molecular crystals) results and influences chemical reactions. A majority of this work will focus on the rise of internal energy from molecular deformations and its role in mechanochemistry (Chapters 4 & 5). Firstly, energy localization will be assessed in the role of how energy is distributed among modes within the molecule (Chapter 3), inspecting the effects of treating kinetic energy distributions under classical and quantum statistics in regard to chemical reactivity and shock initiation. Thereinafter, shock simulations of the collapse of porosity will be utilized to assess how energy is heterogeneously deposited into the microstructure (Chapter 4), specifically the rises in both kinetic energy and potential energy using a nonreactive simulation. This is followed by reactive simulations of the same pore collapse set up to reveal how the molecular potential energy increases within hotspots (through intra-molecular deformations) leads to mechanochemical acceleration of reactions. Additionally, an advanced methodology is developed to recreate the molecular deformations of hotspots under equilibrium conditions to better develop models for the altered kinetics and reaction pathways as a function of the level and style of deformation (Chapter 5).

Throughout the majority of work utilizing atomistic simulation to focus on mechanochemistry in high explosives [51,61,76] and dynamic compression induced mechanochemistry, in general [50,52], the emphasis has been on reporting the ensembled effect. That is to say, the underlying distributions have been mostly neglected. In previous works, the reacting system undergoes an overall deformation, typically a shock or shearing, that enacts deformations within the molecules. Overall, this can lead to acceleration of reactions and alteration of reaction pathways,

which has been often noted. However, the molecular deformations are diverse in nature, with previous works failing to assess the varying contributions of each of these deformations to the net mechanochemical effect on the system. The work discussed here attempts to begin to rectify this.

Our ability to accurately predict initiation of chemical reactions, the timescales in which they propagate, and the resulting thermodynamics of the reaction is vital to understanding and predicting sensitivity of EMs to accidental ignition and explosion, as well as phenomena such as the run to detonation and detonation failure. Additionally, understanding the underlying physics and chemistry framework that governs explosive hotspots, their formation and coalescence into a deflagration/detonation, is vital to the engineering community to design and tailor microstructures of EMs for specific properties and uses. Inherent control of an EM's sensitivity, ignition delay times, and detonation capability from just the microstructure remains a significant grand challenge in the community [2].

In general, this work aims to help develop the fundamental sciences framework of how shock induced chemistry, especially in hotspots and with mechanochemistry, occurs at the atomic scale, in a way that allows for upscaling of models influence the design and utilization of energetic materials. As an inherent multiscale problem, the initiation and reactivity of EMs at the macroscale can be heavily influenced by both the material descriptors at the microstructural level and the molecular level, with the thermo-mechanical states of individual molecules influencing the chemical response of the system [51,77].

2. METHODOLOGIES

2.1 Classical Molecular Dynamics

Many macroscopic properties of materials such as the elastic constants, phonon thermal conductivity, coefficient of thermal expansion, and the melting temperature can be determined via the spatial and temporal averages of atomic interactions through the branch of physics known as statistical mechanics. Hence, over the last 65 years [78], substantial advances have been made to develop computational capabilities that predict the dynamics of atoms through time propagating simulations under controlled thermodynamic states. Great care has been taken to define algorithms that reproduce the proper ensemble statistics and thermodynamic conditions as used experimentally. However, often, and in the case of much of this work, atomic dynamics are treated in a purely classical mechanics sense, i.e., their dynamics follow Newton's second law. The error associated with using classical dynamics to approximate a quantum mechanical system will be discussed in Chapter 3. These molecular dynamics (MD) simulations solve $F = ma$, continuously evolving atomic positions and velocities for a chosen timestep. Advances in high performance computing have allowed positions and velocities of different atoms to be calculated in parallel, greatly increasing the efficiency of molecular dynamics.

In classical MD, forces are typically calculated from a user defined potential energy surface:

$$-\nabla U = m\ddot{x}(t)$$

This potential energy surface, also known as the interatomic potential or forcefield, has a variety of functional forms such as dreiding [79], ReaxFF [42], and EAM [80], each of which having their pros and cons. The positions and velocities of atoms are integrated in time by taking small time steps, alternating when the positions or velocities are updated by half steps. The most common approach to this is the Verlet algorithm [81,82], where:

$$x_i(t + \Delta t) = 2x_i(t) - x_i(t - \Delta t) + \ddot{x}_i\Delta t^2$$

To accurately integrate these equations of motion, small timesteps must be taken, which are on the order of femtoseconds, which typically limits the total simulation time to the order of nanoseconds. However, recent advances in accelerated simulation techniques [83] and using graphical processing units [84] has allowed for simulations of moderate size (number of atoms) to reach well into the microsecond regime. For all of the work shown here, MD simulations will be

implemented using the LAMMPS [85] code developed at Sandia National Laboratory. For isothermal-isochoric and isothermal-isobaric simulations the Nose-Hoover thermostat [86] is used with Parrinello-Rahman boundary conditions [87], unless specified differently. Specific numerical parameters for each thermodynamic ensemble will be specificized on a study-by-study basis in the subsequent chapters. The remaining subsections of this chapter will be dedicated to describing the specific forcefields used here (2.2 and 2.3) and the complex integration methods utilized for shock compression (2.4).

2.2   Classical, Nonreactive TATB Forcefield

The simulations utilized throughout this work can be classified in a binary style: reactive and non-reactive. While using a reactive forcefield can allow for close examination of chemical reactions, which is vital to the understanding of energetic materials, they are typically more than an order of magnitude more computationally costly than their non-reactive counterparts and require significantly smaller timesteps. Hence, when applicable (Chapter 4), I will describe inter-atomic forces with a non-reactive potential in which bonding topology is explicitly defined.

The state-of-the-art, non-reactive potential for TATB is that from Bedrov et. al. [68], which has since been improved on by Kroonblawd [88] and Mathew [89]. The bond vibration, angle bend, and improper dihedral degrees of freedom are modeled harmonically such that

$$E_{bond} = K(r - r_o)^2$$
$$E_{angle} = K(\theta - \theta_o)^2$$
$$E_{imp} = K(\chi - \chi_o)^2$$

where χ is the improper dihedral angle, the angle between the planes of atoms ijk and jkl where the dihedral is made of atoms ijkl. Proper dihedrals are modeled with a cosine series,

$$E_{dih} = K[1 + dcos(\phi)]$$

where ϕ is the proper dihedral angle, which is mathematically defined the same way as the improper dihedral angle, where the atoms ijkl are spatially defined differently. Van der Waals interactions are calculated with the commonly used Buckingham potential,

$$E_{vdW} = Ae^{-\frac{r}{\rho}} - \frac{C}{r^6}$$

combined with short-ranged r^{-12} potentials that corrects for divergence issues at small interatomic distances, which comes into play under the shock loading conditions studied here.

A RATTLE constraint is applied to restrict all N-H bonds to their equilibrium length, which allows for use of a larger timestep [90], which will typically be 0.2 fs for all non-reactive simulations in this work. An intramolecular O-H repulsion is included and defined as a bonded interaction, which is treated harmonically, and helps to stabilizes the molecular shape [89]. All non-bonded terms (van der Waals) are assessed in real space using a cutoff of 11 Å, and all electrostatic interactions (Coulomb) are calculated between constant partial charges, which are placed at each nuclei, evaluated with the Wolf potential using a damping parameter of 0.2 Å^{-1} and an 11 Å cutoff [91]. The advantage of the cutoff based Wolf potential compared to particle-particle particle-mesh (PPPM) [92] is greater versatility in performing simulations with non-periodic boundaries and offers little difference in computational cost. Lastly, by design, all intra-molecular, non-bonded interactions are ignored, which allows for a complete separation of inter- and intra-molecular potential energy, on a molecule-by-molecule basis. This will be used advantageously in Chapter 4.

2.3   The ReaxFF Reactive Forcefield

In contrast to the non-reactive TATB forcefield from Bedrov et. al. [68], the ReaxFF reactive potential [42], which has valid parametrizations for most CHNO based energetic materials, does not require explicit bonding information to be pre-defined. These many-bodied, reactive potentials dynamically assess which atoms should be bonded to one another while the simulation occurs. While user defined pairwise distance cutoffs or any other method of drawing chemical bonds could achieve dynamic bonding rather easily, a prerequisite condition for any forcefield is that any and all energy-position functions (be it 2-body or many-bodied) be smooth and continuous such that the force, its first derivative, is also continuous for all atomic arrangements. Force discontinuities provide considerable computational instability and therefore untrustworthy simulation results. Hence, it is crucial for any reactive potential to properly describe the interactions of all initial and final states of a reaction using a single, continuous functional form. The breaking of bonds should not cause energy and force discontinuity.

The computational cost to calculate simple order parameters from a predetermined neighbor list, $\mathcal{O}(N)$, is significantly lower than that of calculating the total electronic state with quantum mechanical or *ab initio* methods such as DFT or Hartree Fock, which scale as, at least, $\mathcal{O}(N^3)$. Therefore, order parameter based forcefields allow for simulations with orders of magnitude more particles to be run over significantly longer timescales [93,94]. Hence, a local order parameter is used to denote the covalent bonding in ReaxFF, referred to as bond orders (BO). Energies and forces are constructed as a function of BOs, allowing for smooth and continuous descriptions of both, with the BOs evolving with the atomic positions. This allows for continuous energies and forces while the system transitions from reactants to products. By modelling all interactions, the covalent and electrostatic, in one potential, ReaxFF can be parametrized for a spectrum of materials from high explosives to proteins and amino acids to metal oxides [95]. A summary version of the ReaxFF energy contributions is [96]:

$$E_{total} = E_{bond} + E_{over} + E_{angle} + E_{tors} + E_{vdW} + E_{Coul} + E_{specific}$$

E_{bond} is the energy contribution of all two bodied interactions, for atoms currently bonded, as a function of their interatomic distance. E_{over} applies a sharp energy penalty any time an atom has too many bonds and experiences over-coordination based on standard atomic valences. This does not prevent over-coordination entirely, but greatly mitigates it. Three and four body energy contributions are given, respectively, by E_{angle} and E_{tors}. These are determined from angle changes in bond angles and torsional angles. Like E_{bond}, these are only applied to bond connected three and four atom systems. E_{Coul} is the pairwise electrostatic contributions for all atom pairs, independent of bonding. E_{vdW} is the dispersive energies of all atom pairs, independent of bonding. Lastly, the system specific energy contributions, $E_{Specific}$, acts as a catch all term for a variety of unique energy descriptors and is not always included in specific parametrizations. These terms are often required to capture distinct properties of complex systems [97]. All the ReaxFF parametrizations used in this work will feature a low gradient attractive term. This 'LG' term accounts for the long-range London dispersion which leads to significantly better predictions of densities and equations of state for HEs [98].

The terms labelled bond, angle, tors, and over are directly dependent on the atom's BOs, whereas as Coul and vdW are charge dependent. The BO between any two atoms i and j can be expressed as:

$$BO_{ij} = \exp\left(p_{bo1}\left(\frac{r_{ij}}{r_o^\sigma}\right)^{p_{bo2}}\right) + \exp\left(p_{bo3}\left(\frac{r_{ij}}{r_o^\pi}\right)^{p_{bo4}}\right) + \exp\left(p_{bo5}\left(\frac{r_{ij}}{r_o^{\pi\pi}}\right)^{p_{bo6}}\right)$$

where the p_{bo} terms are empirical parameters. For the Coul and vdW terms, a charge equilibration scheme is applied at each step to calculate partial atomic charges based on the current atomic environment [99].

Numerous parameterizations of ReaxFF exists for a variety of materials, however, they are not completely interchangeable for materials made from identical sets of elements [97]. I.e., the same elemental parametrization usually cannot correctly model all materials one could create, such as high explosives and amino acids, which require different parametrizations [95]. It should be noted that, while ReaxFF has been the cutting edge for reactive all-atom potentials over the last 2 decades, recent development in machine learning based potentials have made great strides in short amounts of time [100–103].

2.4   Simulations of Shock Loading

The shock compression of materials can invoke numerous material responses such as plasticity [10,17,51], phase transitions [20–22], and chemical reactions [76,104,105]. MD simulations are a reliable tool in studying the shock response of materials, as they operate on the same timescales as the shock rise time [106] and many of the material responses at shock temperature and pressure [61,107]. Therefore, it is critical to develop and utilize computational methodologies that accurately induce or mimic shock compression. The simplest of these, but also typically the most computationally costly, is to create an explicit shockwave, often referred to as Non-Equilibrium Shock Loading or a Direct Shock technique. Additionally, numerical methods exist to mimic shock compression, under equilibrium, using a combination of barostats and thermostats, namely the multiscale shock technique (MSST) [108] and the Hugoniostat [109]. The next three subsections will explain each of these methodologies, which will all be used throughout the subsequent chapters.

2.4.1 Non-Equilibrium Loading (Direct Shock)

The direct shock simulation method, the only one of the three methods discussed here that invokes an actual shockwave, is by far the most exact method for studying shock compression. However, by its nature, it necessitates large computational cells with at least one non-periodic boundary and is limited in time by the size of the cell and the strength of the shock.

To run a direct shock simulation, the system requires a free surface for which to impact the sample. From there, an explicit piston (a perfectly rigid slab of material or fully reflective momentum mirror) is defined at one of the free surfaces and acts as the flyer plate. The piston can then be given velocity $V = U_p$, in the direction of the shock, or the shock can be conducted in a reverse ballistic approach where the piston is fixed in space and the sample is given velocity $V = -U_p$ [16]. Under Galilean invariance, the ballistic and reverse ballistic set ups are identical. All direct shock simulations performed in this work will be done in the reverse ballistic style for computational convenience.

Once the shockwave begins to propagate across the material, as shown in Figure 2.1, the simulation has a predetermined end of life. Since a free surface is created for impacting the sample, an equal and opposite free surface exists at the far end of the sample. Since MD simulations are typically limited to be on the order of a few million atoms to 10s of millions, the distance between surfaces is typically only a few hundred nanometers. The typically U_s is on the order of 10 nm/ps, causing the wave to reach the free surface and cause a rarefaction wave on the order of 100s of picoseconds. In a study of a material under a specific shock state (temperature and pressure), that shock state, and therefore the simulation, is only in existence and valid until the rarefaction wave reaches the area of interest and changes the pressure and temperature conditions. Hence, slower materials responses (>=nanoseconds) are prohibited by the size limitations of MD. Even if the simulation could computationally be simulated long enough, the desired shock conditions will not survive long enough. Previous works in shock absorbing boundary conditions (SABCs) have allowed for these effects to be prevented [17,107], but the more typical approach is to utilize equilibrium shock approximation techniques such as MSST and the Hugoniostat [108,109].
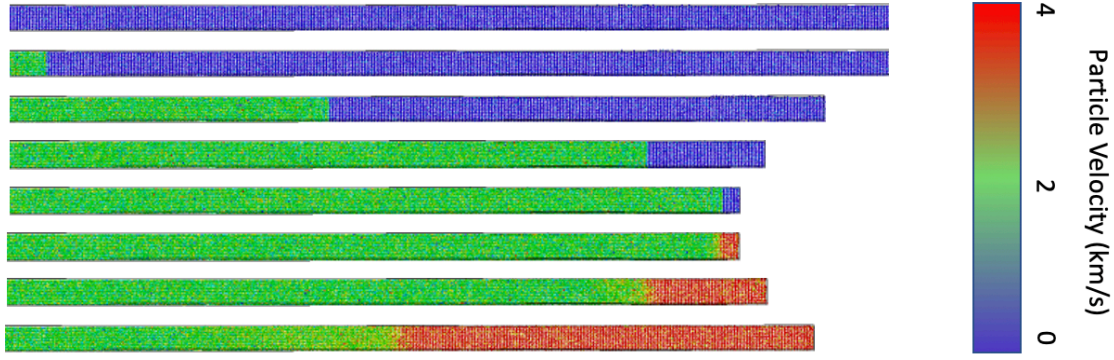
Figure 2.1: Propagation of a shockwave in an aluminum sample from a direct shock simulation using a reverse ballistic set up. Atom color is U_p, which is shifted to the setting of ballistic impact using Galilean invariance, where the initial shock wave is the gree-blue interface (green atoms are shocked) and resultant rarefaction wave is the red-green interface (red atoms have been relieved of pressure).

2.4.2 MSST

The first of the two equilibrium shock approximation techniques used in this work is the multiscale shock technique (MSST) developed by Reed et. al. [108], which has been used to study numerous shock responses of materials such as chemical reactions [30,110], phase transformations [111], and metallization of organic molecules [105]. MSST enacts a uniaxial compression that follows the P-v path of a user defined Rayleigh line and compresses continually until the energy jump condition is satisfied. The MSST equation of motion (for the system volume) stabilizes at a constant volume when the system is such that the P-v state is both on the Rayleigh line and on the Hugoniot of the material. By using a barostat that homogeneously compresses the system and prevents any explicit shockwave from developing, MSST can be applied to a small periodic system, which solves the issues with direct shocks regarding reflections and computational cost, and still results in the system reaching a shocked state.

The pressure-dependent rate type barostat of MSST is an extension of the Andersen barostat [112], but the set pressure is derived from the Rankine Hugoniot jump conditions, not a single provided value, and therefore evolves with the system:

$$\ddot{v} = \frac{P_{set} - P(t)}{Q}$$

35

$$\dot{r} = \frac{\dot{p}}{m} + \frac{1}{3}\frac{\dot{v}}{v}r$$

where Q is a fictitious piston mass and P_{set} is determined by

$$P_{set} - P_o = U_s^2 \rho_o \left(1 - \frac{\rho_o}{\rho}\right)$$

a combination of the mass and momentum jump conditions where U_s is chosen by the user, and the density values are calculated on the fly via the MD code. Formally, the MSST equation of motion for the volume of the system is written as

$$Q\ddot{v} = \frac{\partial T}{\partial v} - \frac{\partial V}{\partial v} - P_o - \frac{U_s^2}{v_o^2}(v_o - v)$$

which is equivalent to the Andersen barostat equation above by way of the jump conditions [113]. This forms metastable states for any point on the Rayleigh line, where $\ddot{v} = 0$ and $\dot{v} \neq 0$ in the equation of motion, and this forms stable nodes (stationary state) where the pressures are equal, and the energy satisfies the jump conditions, $\ddot{v} = 0$ and $\dot{v} = 0$. Hence, MSST compresses the system along the Rayleigh line searching for points that correspond with the system's Hugoniot equation of state. MSST also inherently satisfies the two shock stability conditions described in Section 1.1 by forcing the initial path on the Rayleigh line to be one of compression. For implementation in MD simulations, an additional artificial viscosity term is added to the equation of motion to help to prevent unphysical oscillations during compression. This functions by coupling the piston's kinetic energy to the atomic dynamics, where the piston has mass Q.

2.4.3 Hugoniostat

The alternative option to MSST is the Hugoniostat, which was first developed in a constant strain formalism [114], and later expanded into a constant stress version [109], which will be used in this work. Similar to MSST, the Hugoniostat compresses a small periodic system to a shocked state without needing an explicit shockwave or a free surface. This is done via integral feedback loops for the pressure and the energy of the system, which takes each to values that correspond to the shock Hugoniot state for the user specified pressure. A barostat dynamically compresses the system to the desired stress level along a specific axis, and an ergostat, similar to a thermostat but works in terms of energy/heat, is utilized to keep the system energy equal to the Hugoniot energy defined by the jump conditions for the current pressure and volume of the system. These dynamics

36

allow the system to be compressed while energy in taken in and out of the system to acquire the correct thermodynamic state. The Hugoniostat equations of motion are as follows:

$$\dot{r}_i = \frac{p_i}{m_i} + \mu_P \eta r_i$$

$$\dot{p}_i = F_i - (\mu_P \eta + \mu_H \zeta)p_i$$

$$\dot{\zeta} = \frac{\mu_H}{v_o B_o}[E - E_H(t)] - \beta_H \zeta$$

$$\dot{\eta} = \frac{\mu_P}{B_o}(P_{zz}(t) - P_{zz}) - \beta_P \eta$$

where η is strain rate and ζ is heat flow, μ is a coupling rate, and β is the damping parameter. Subscript P represents parameters for the barostat and subscript H for the ergostat. B_o is the bulk modulus at zero pressure. Since the ergostat works by using the Hugoniot energy for the instantaneous state, not the final pressure, as the final volume is not known *a priori*, the Hugoniostat compresses the system along the material's Hugoniot instead of the proper Rayleigh line, as the energy jump condition relates to initial and final states only, which collectively make up the Hugoniot. Additionally, by not allowing the pressure to change during reaction, the Hugoniostat does not correctly adhere to ZND theory for a single shock that initiates chemistry. However, the overall reacted Hugoniot curves will still make accurate predictions of CJ states and detonation velocity [32].

3. CLASSICAL VS. QUANTUM NUCLEAR EFFECTS IN CHEMICAL INITIATION

3.1   Introduction

The extreme majority of molecular dynamics simulations are conducted using classical dynamics to propagate the positions and velocities of atoms, as described in Section 2.1. However, not all atomic dynamics are well described by this approximation. The two main fundamental inconsistencies with using classical dynamics to describe a material in which $k_b T < \hbar\omega$ (materials placed firmly in the quantum mechanical regime) are a lack of a zero-point energy and a temperature independent specific heat, whose value is a constant at the high temperature limit [117].

Isothermal (isochoric) molecular dynamics simulations are intended to follow the statistics of the canonical ensemble of statistical mechanics (NVT statistics) [86]. The classical partition function for the canonical ensemble is

$$Z(N, V, T) = \sum e^{-\beta E}$$

where $\beta = \frac{1}{k_b T}$ and the summation is over all available microstates. The probability of being in any one microstate is described by the Maxwell-Boltzmann distribution:

$$P_i(R_i, p_i) = \frac{e^{-\beta H_i}}{Z}$$

Therefore, the thermodynamic free energy for the canonical ensemble, Helmholtz Free Energy, is

$$F = E - TS = -k_b T * log Z$$

which results in the expectation value of any squared term in the Hamiltonian providing $\frac{1}{2} k_b T$ of energy, a principle known as the equipartition of energy [118–120]. Each mode receives this equivalent amount of energy, independent of its vibrational frequency. Therefore, treating classical, atomic dynamics under the harmonic approximation, the internal (vibrational) system energy is described as

$$E_{CM}(T) = (3N - 6) k_b T$$

where the 6 subtracted degrees of freedom (DoFs) are from the three translational and three rotational DoFs.

However, solving the equations of motion for the harmonic oscillator in terms of quantum mechanics, instead of classical mechanics, leads to energy eigenvalues of $E_n = \left(n + \frac{1}{2} \right) \hbar \omega$. Therefore, the partition function of the quantum mechanical system in the canonical ensemble is

$$Z(N, V, T) = \sum e^{-\beta \hbar \omega \left(n + \frac{1}{2} \right)} = \frac{e^{-\frac{\beta \hbar \omega}{2}}}{1 - e^{-\beta \hbar \omega}}$$

where the second equivalence is from solving a power series for the infinite summation. In contrast to the Maxwell-Boltzmann statistics of the classical canonical ensemble, the quantum mechanical description leads to Bose-Einstein statistics [121,122]:

$$\langle n \rangle = \frac{1}{e^{\beta \hbar \omega} - 1} \ and \ \langle E \rangle = \hbar \omega \left(\frac{1}{2} + \frac{1}{e^{\beta \hbar \omega} - 1} \right)$$

Deriving the same canonical Helmholtz free energy for Bose-Einstein statistics is

$$F = -k_b T log(Z) = k_b T log\left(1 - e^{-\beta \hbar \omega} \right) + \frac{\hbar \omega}{2}$$

which results in the quantum mechanical zero-point energy of $\frac{1}{2} \hbar \omega$ per vibrational mode, which is the residual kinetic energy for a system with a temperature of 0 K. Under the classical energy description, kinetic energy goes to zero at zero temperature. Under the harmonic approximation, the quantum mechanical vibrational energy is

$$E_{QM}(T) = \sum k_b \left[\frac{\theta_i}{2} + \frac{\theta_i}{\exp\left(\frac{\theta_i}{T} \right) - 1} \right]$$

where $\theta_i = \hbar \omega_i / k_b$.

In general, the harmonic approximation is acceptable in the quantum mechanical description because anharmonicities commonly only influence low frequency modes (which are highly classical) and because high frequency modes (can be heavily quantum if $k_b T < \hbar\omega$) are practically harmonic [117]. The classical harmonic approximation is highly accurate for many materials simulations such as metals [123], which have Debye temperatures near room temperature, and polymers [106], whose mechanics are dominated by low frequency phonon modes. However, there are numerous cases in which the classical approximation is not valid for predicting materials properties and phenomena.

Importantly, these energy descriptions lead to highly different definitions of the specific heat, $C_v = \frac{\partial E}{\partial T}_v$, in which the classical specific heat is not temperature dependent and is equal to the high temperature limit ($3Nk_b$) of the quantum mechanical description. Between the classical and quantum dynamics descriptions, energy distributions differ significantly, in HE molecules, between vibrational DoFs. For shock compression of organic matter such as HEs, classical molecular dynamics leads to an underprediction of shock temperatures by 20-30% [124].

For HEs such as TATB, using a classical approximation leads to an overprediction of the specific heat at room temperature by roughly a factor of 3 [125]. At detonation levels of shock pressures, this can lead to an underprediction of temperature by several hundred kelvin, which will heavily influence predictions of reactivity, kinetics, and sensitivity, if made by classical molecular dynamics. While classical MD with reactive forcefields or *ab initio* based forces have predicted a menagerie of properties and processes such as reaction kinetics [46,51,126], first step reaction pathways [31,34,127,128], detonation products [29,30,104,129,130], shock influenced IR spectra [32,33,36], detonation and CJ states [66,105,113,130], and hotspot criticality [25,46,131,132], these have all been made with a classical propagation of atoms, calling into question how this classical assumption influences these results. In this chapter, I will assess the role of specific heat and zero-point energy on TATB reactivity by utilizing classical molecular dynamics simulations and a semi-classical approximation of quantum dynamics with a colored noise thermostat based on non-Markovian Langevin dynamics [133–135].

In the most rigorous methods, short of solving the Schrodinger Equations for each phonon at each timestep, quantum dynamics of phonons can be solved by the path integral (PI) method, first extended to quantum mechanics by Paul Dirac in 1933 [136] and extended to completion by Richard Feynman from 1948-1965 [137]. The PI method replaces the concept of a unique, single

trajectory of each classical particle for a system of particles with a functional integral over an infinite set of possible quantum mechanical trajectories in order to compute a quantum expectation value. However, the PI formulation of molecular dynamics leads to immense computational cost due to the need to simulate multiple replica copies of the system that are interconnected by harmonic potentials [138]. The cost of PI methods and unified classical phonon – quantum electron methods such as Car-Parrinello MD [139] have resulted in a majority of all-atom approaches relying on the Born-Oppenheimer approximation using either *ab initio* or classical forces.

Recent advances have allowed for 'semi-classical' approaches in which a stochastic or colored-noise heat source can mimic quantum effects such as the presence of a zero-point energy and a temperature dependent specific heat [133,134]. These 'quantum thermal bath' (QTB) simulations result in no noticeable increase in computational cost compared to fully classical, isothermal dynamics, since the QTB functions as a weighted thermostat using on the fly filtered white noise [140]. The QTB has been applied to various topics such as low temperature dislocation motion [123], phase transitions in ice [141], phenolic polymer pyrolysis [142], and shock induced reactions in methane [143]. Additionally, the QTB method has been extended from isothermal dynamics to work in conjuncture with the MSST method (see Section 2.4.2), which has shown to properly predict shock temperatures by including temperature dependent specific heat effects and a zero point energy [143]. In this chapter, I will apply the QTB and QB-MSST methods to thermal decomposition and shock initiation of TATB to establish the role of quantum nuclear effects on HE initiation and assess the level of prediction error by comparing to results from strictly classical methods.

3.2   Methods

3.2.1   Classical Molecular Dynamics Simulations

All-atom simulations is this chapter are conducted with the LAMMPS code [85] with atomic forces calculated using the ReaxFF [42] forcefield, as described in Section 2.3. Two different ReaxFF parametrizations will be used here, designated ReaxFF-2018 [7] and ReaxFF-LG [98]. Dynamics are propagated with a timestep of 0.1 fs. Partial atomic charges are calculated with the charge equilibration method (qEQ) [99] with a threshold of 1×10^{-6}. All isothermal

simulations are conducted using a Langevin style thermostat [135] with a damping of 200 fs, unless specified otherwise. The TATB supercell used in these simulations is an orthorhombic transformation of the original crystal in the setting of Cady and Larson [67], generated with the generalized crystal cutting method (GCCM) [144]. The supercell lattice vectors are

$$\mathbf{A} = -5\mathbf{a} - 3\mathbf{b} + 0\mathbf{c}$$
$$\mathbf{B} = \mathbf{a} - 7\mathbf{b} + 0\mathbf{c}$$
$$\mathbf{C} = \mathbf{a} + 2\mathbf{b} + 6\mathbf{c}$$

Comparative data will be shown for HMX and LLM-105 in which 3x3x3 and 5x5x3 replications of the standard unit cells are used [145,146].

To establish a baseline of the predictive power of the ReaxFF forcefield, Section 3.3 will compare ReaxFF decomposition results to that from density functional theory (DFT) and density functional tight binding (DFTB). DFT simulations with the Perdew−Burke−Ernzerhof (PBE) [147] generalized gradient approximation functional are conducted under the Born-Oppenheimer approximation where all electronic structure calculations are treated independently of phonon motion. A D2 empirical correction (PBE+D2) [148] is applied and PAW pseudopotentials are utilized here [149,150]. These are implemented and utilized via the widely used VASP code [151,152]. A 2x1x1 unit cell is used. A 400 eV cutoff without spin polarization, calculated at the Γ-point only, is utilized with a self-consistent field accuracy threshold of 1×10^{-4} eV. Partial occupancies are calculated above the fermi level with a Gaussian thermal smearing at a width of 0.05 eV.

DFTB simulations are conducted using the DFTB+ code at the self-consistent charge level (DFTB-2) [94]. The integration of the equations of motion are performed using a LAMMPS code coupled with DFTB+ [85]. Utilizing four SCF cycles per timestep, the electronic band structure is calculated at the Γ-point without spin polarization. At all times, the electronic temperature is instantaneously set to be equal to that of the phonon temperature [153].

Isothermal decomposition kinetics are determined using two methods. For results in Section 3.3, the critical time of decomposition is equal to the time in which all initial HE molecules have undergone some initial reaction. For Section 3.5, the critical time is determined as the time it takes for half of the exothermicity of the reaction to occur. The former leads to kinetics of a 1st reaction step, while the latter is more of a single step global kinetics.

To best determine reaction pathways. a local bonding environment scheme is applied instead of traditional species counts [46]. Each individual atomic bonding environment is described in the form $X[B_1B_2B_3B_4]$, in which X is the element of some central atom and B_i are the element of each and every atom bonded to X. Each atom in the system is treated as X exactly once. For example, the total descriptors for CO_2 would be two O[C] and one C[OO]. Additionally, summing over these bond descriptors can result in explicit counts of molecular species to compare intermediate and final product amounts and rates from experiments or previous calculations.

3.2.2 Quantum Corrections to Classical Simulations

To assess the expected results from a quantum mechanical description and to validate the results of the quantum thermal bath simulations (described in Section 3.2.3), quantum post corrections can be applied to classical all-atom simulations to predict the quantum mechanical zero-point energy, specific heat, and shock temperature. The first two can be determined from weighted integrations over the classical vibrational density of states (vibDoS), which is defined as [117]

$$D(\omega) = \frac{\beta\tau}{2Nk_bT} \sum_{j=0}^{3N} m_j \sum_{n=0}^{N-1} v_j(n\Delta t) e^{-\frac{i2\pi\omega n\Delta t}{2}}$$

where one can define the quantum zero-point energy and specific heat, respectively, as

$$ZPE = k_bT \int_0^\infty \partial\omega\, D(\omega) \left(\frac{\beta\hbar\omega}{2} + \frac{\beta\hbar\omega}{e^{\beta\hbar\omega}-1} \right)$$

$$C_v(T) = k_b \int_0^\infty \partial\omega\, D(\omega) \left(\frac{(\beta\hbar\omega)^2 e^{\beta\hbar\omega}}{(1-e^{\beta\hbar\omega})^2} \right)$$

where the vibDoS spectra is calculated from a fully classical propagation of dynamics. The terms multiplied into the vibDoS are known as quantum weighting functions.

Knowing the energy input into the classical shock simulations, either from running a classical MD shock simulations or by solving the Hugoniot jump conditions, solving for the upper bound of integration in the below equality will result in an accurate prediction of the expected shock temperature, were the simulations a fully quantum mechanical description. $C_v(T)$ is the temperature dependent specific heat from the quantum mechanical system.

$$\Delta E = \int_{300}^T C_v(T) \partial T$$

3.2.3 Quantum Thermal Bath (QTB) and QB-MSST

In Section 3.4 and 3.5, a semi-classical approximation of dynamics will be employed through a colored noise thermostat known as the Quantum Thermal Bath (QTB). The QTB operates via a Langevin style thermostat in which the (traditionally) random noise component is filtered in an attempt to force the system to follow the Bose-Einstein distribution, as well as add in a zero-point energy. The typical, classical Langevin thermostat follows the dynamics of

$$m_i \ddot{r}_i = f_i + R_i - m_i \gamma \dot{r}_i$$

where R is a random noise force and γ is a friction factor such that $-m\gamma\dot{r}$ is a dissipative force. In the classical Langevin thermostat, the random force R is entirely white noise. For the QTB thermostat, the stochastic force R is a colored noise chosen to follow the Bose-Einstein distribution. The resultant power spectral density of the colored, stochastic force can be defined as

$$I_{R_{i\kappa}R_{j\zeta}}(\omega) = \int_{-\infty}^{\infty} \langle R_{i\kappa}(t)R_{j\zeta}(t+\tau)\rangle e^{i\omega\tau} d\tau$$

and its relation to gamma is given by the fluctuation-dissipation theorem [154],

$$I_{R_{i\kappa}R_{j\zeta}}(\omega) = 2m_i\gamma\delta_{ij}\delta_{\kappa\zeta}\Theta(\omega, \text{T}) \;\; where \;\; \Theta(\omega, \text{T}) = \hbar\omega\left(\frac{1}{2} + \frac{1}{e^{\beta\hbar\omega} - 1}\right)$$

which results in the same quantum harmonic approximation energy defined in Section 3.1. The second term in $\Theta(\omega, T)$ is the Bose-Einstein contribution, and the first term, the $\frac{\hbar\omega}{2}$, is the zero-point energy contribution. This definition of the power spectral density can be shown to satisfy the Wiener−Khinchin theorem [155]. In the classical Langevin system, $\Theta(\omega, T) = k_b T$. In this sense, the modes are taken to have the vibrational density of states of a classical or quantum harmonic oscillator for each of the respective classical and quantum Langevin heat baths.

The choice of the friction factor, γ, is a key component for implementing the QTB. A weak coupling (small γ) will cause the system to deviate from the Bose-Einstein distribution, drifting towards a classical equipartition of energy, since that is what is prescribed by the typical equations of motion. For too strong a coupling, like any Langevin thermostat, the system will tend towards Brownian motion, or fully random dynamics. Additionally, zero-point energy leakage can occur in highly anharmonic systems, in which the necessary coupling to prevent this ZPE leakage is too strong [156].

The implementation of the QTB in LAMMPS is that of Barrat and Rodney [140]. The initial description of the QTB requires the calculation of all random forces prior to initiating the

simulation. Conversely, the Barrat and Rodney implementation employs a style of noise synthesis in which the memory requirement is significantly lower and is totally independent of the simulation length. This frequency-dependent filter discretizes the contributions of the colored noise force, R, into a predetermined number of bins, N_f, resulting in a method much more employable in molecular dynamics without greatly increasing computational cost.

Qi and Reed extended the QTB method to work in tandem with the MSST method, described in Section 2.4.2 [108,143]. The thermostat couples to the velocity equation of motion with MSST, which is normally just controlled with a barostat. This attempts to continually evolve the kinetic energy of the shocked system to track with the power spectrum of the quantum harmonic oscillator for all temperatures. However, the thermostat described above is derived only as an isothermal one. Hence, QB-MSST must actively update the QTB set temperature to correspond with the state of the shock, based on the current energy of the system. The set temperature is updated every β timesteps, based on the average energy over the previous β timesteps. The set temperature is updated via the following equation of motion

$$\dot{T}_{QM} = \gamma\eta\frac{M(e(t) - e_o)}{3Nk_b}$$

where M defines the energy quantity change within the chosen constraints.

In the below sections, to quantify the influence of nuclear quantum effects on HE reactions, TATB shock loading is explored for U_p of 0.5 – 3.0 km/s, using MSST and QB-MSST to generate results for a classical baseline and the semi-classical, quantum bath, respectively. Additionally, classical Langevin and QTB thermostats are employed for isothermal decomposition simulations to eliminate effects of different P-V-T responses for classical and quantum shock loading.

Prior to shock loading or thermal heating, the system is thermalized for 50 ps using at 300 K using isothermal-isochoric simulations with the respective classical or quantum thermostat. The damping parameter for all thermostats was set to 200 fs and the frequency cutoff for QTB/QB-MSST simulations is 0.5 1/fs. This cutoff was parametrized to match the QTB simulation's ZPE with the predicted ZPE from integrating over the vibDoS of a classical simulation [117] (see Section 3.2.2), as shown in Figure 3.1. Both ReaxFF parametrizations accurately predict the total ZPE per molecule for TATB and correctly predict the curvature of E(T) for both the classical and quantum distributions. The linear response of the classical prediction leads to the equipartition of energy and the temperature independent specific heat of $3Nk_b$. The low temperature curvature of

the quantum prediction provides the temperature dependent specific heat, the first derivative of this curve. The difference in absolute energy values for the two parametrizations is related to the different training sets for ReaxFF-2018 and ReaxFF-LG.
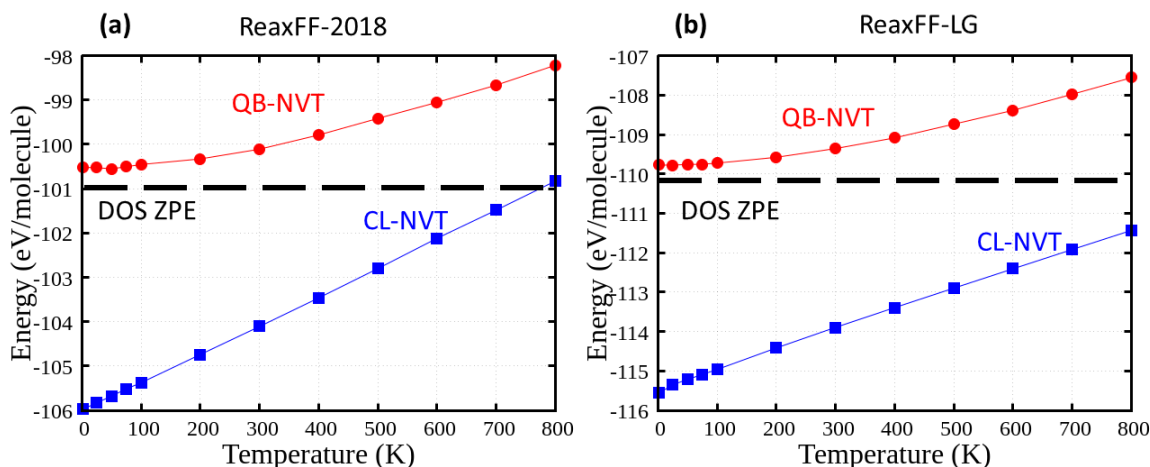
Figure 3.1: Energy-Temperature response for TATB with classical and quantum thermostats for two different ReaxFF parametrizations. Dashed line represents predicted ZPE from integrating over the vibDoS of the classical simulations.

The temperature dependent specific heat (quantum) can be predicted by weighted integration over the vibDoS or by a numerical derivative of the QTB E(T) curves in Figure 3.1. Figure 3.2 shows these C_v curves, as well as that from Ref. [125], and the classical limit. The QTB thermostat, similar to the ZPE predictions, well predicts the temperature dependent specific heat, both its absolute value and the desired curvature. Differences from the QTB and ZPE curves compared to the quasi-harmonic approximation results stems from slightly inaccurate vibrational frequencies in ReaxFF.
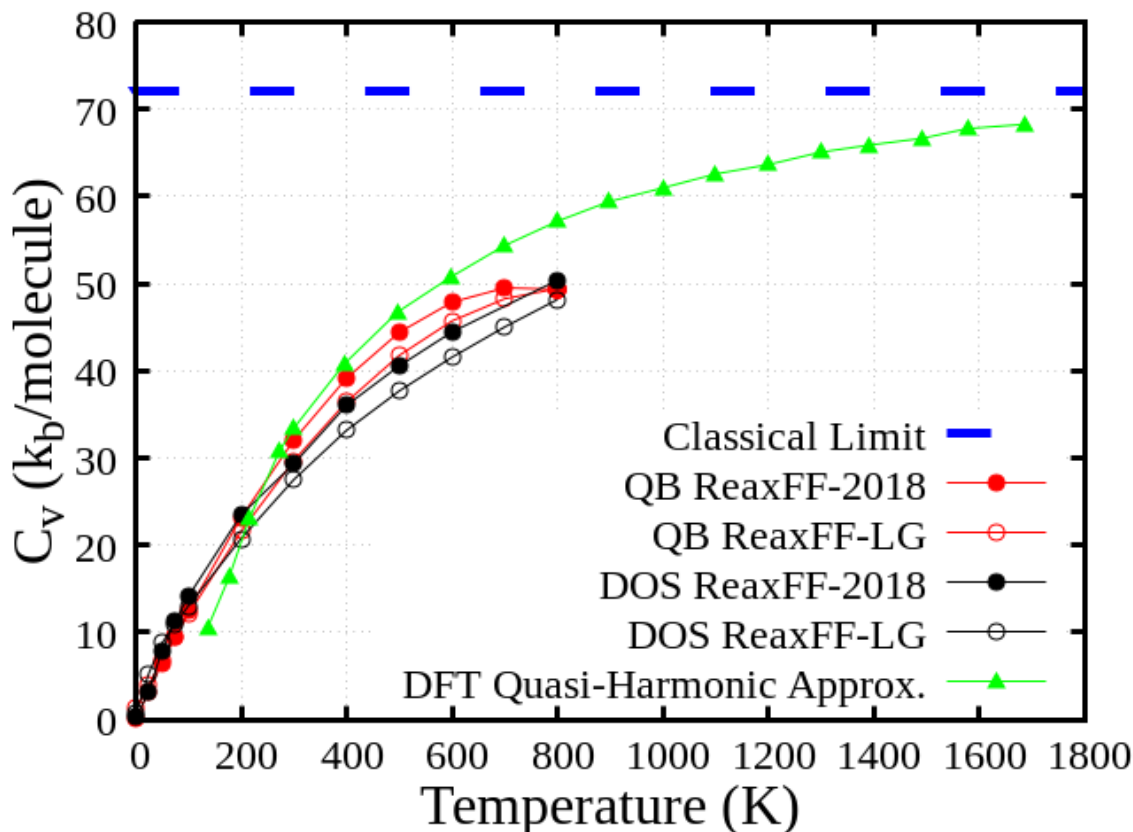
Figure 3.2: TATB temperature dependence of specific heat using the vibDoS and QTB approaches. DFT Quasi-harmonic approximation results are from Ref. [125]

3.3 Thermal Decomposition of Insensitive HE Materials: Validation to DFT and DFTB

Before directly comparing quantum and classical predictions of HE initiation, I aim to establish a baseline for the predictive power of reactive molecular dynamics overall, making predictions for first step reaction pathways of multiple HE materials and comparing predictions of reaction paths and kinetics for ReaxFF, DFTB, and DFT. This will place the relative accuracy of ReaxFF for the remainder of this work, whilst also providing a baseline response for HE materials, especially the predicted reaction pathways of TATB and LLM-105.

Figure 3.3 below shows predicted bonding environments from DFT, DFTB, and ReaxFF for isothermal decomposition of LLM-105 at 2250 K and ambient density. DFTB data is an average of 10 independent calculations due to the required small system size (8 molecules). Due to large computational costs, DFT results are just a single simulation of the 8 molecule system, and are,

therefore, significantly more noisy. These results show that all four methods predict a hydrogen transfer from the amino group to the nitro group as a primary pathway (same pathway as TATB [34]), which can be intra- or inter-molecular. An alternate reaction pathway of NO_2 scission also appears in lower amounts. Figure 3.4 shows example schematics of each of the available reactions. The time histories of the hydrogen transfer reactions are shown by the increase in O[NH] and O[H] bonding environments while N[CHH] decreases. As shown in Figure 3.4, the hydrogen transfer occurs from the H atom moving groups, causing N[CHH] to become N[CH] and elevating O[N] to O[NH]. The formation of O[H] develops from a breaking of the O-N bond, a path that is known to lead to the formation of water. Increase in the amount of N[OO] environments shows the NO_2 scission reaction. In some cases, the NO_2 can form HONO molecules or NO radicals as next step, intermediate reaction. While the different methods show different relative amounts of each pathway, such as high NO_2 scission in ReaxFF-LG, these results validate ReaxFF in predicting the extreme conditions reaction qualities of insensitive HEs.
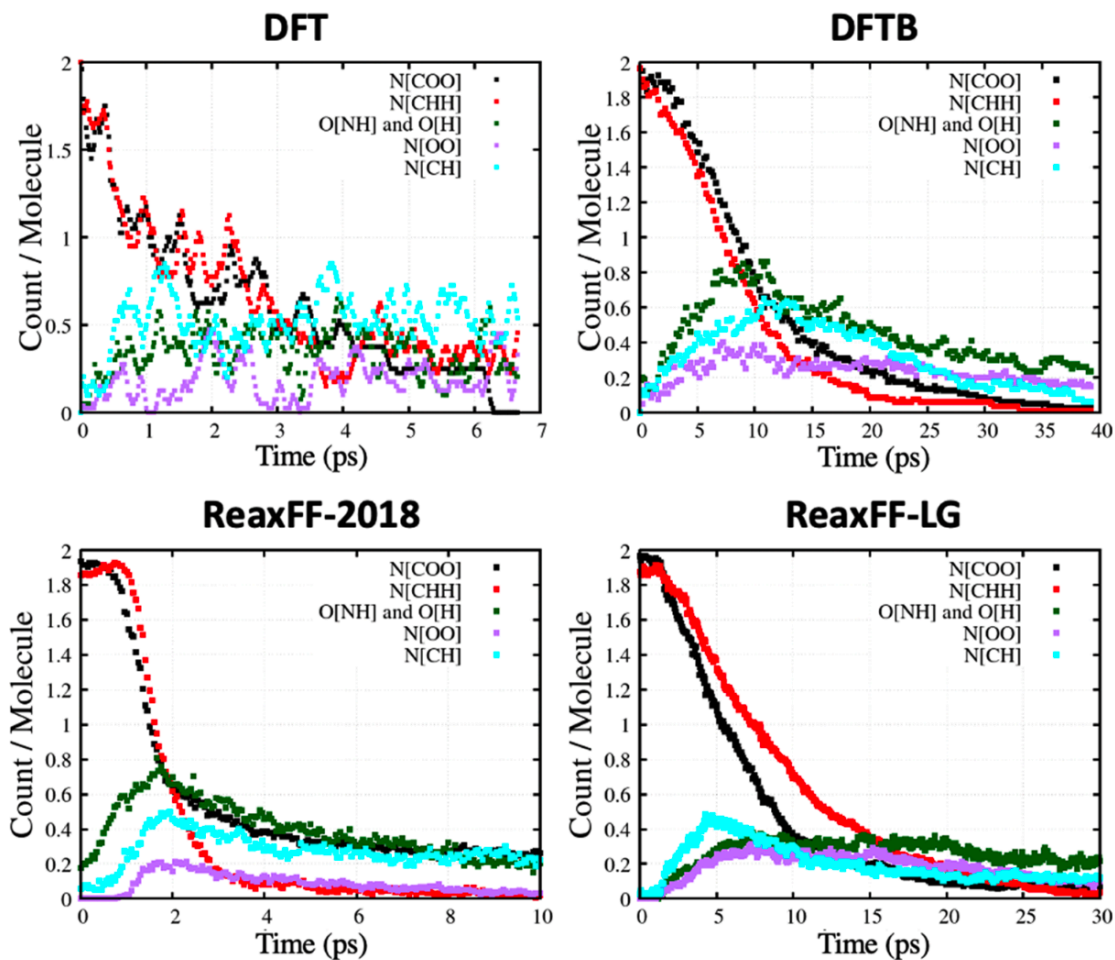
Figure 3.3: DFT, DFTB, and ReaxFF bonding environment predictions for isothermal decomposition of LLM-105 at 2250 K and ambient density. DFTB data is an average of 10 independent calculations due to the required small system size (8 molecules). Due to computational costs, DFT results are just a single 8 molecule system.
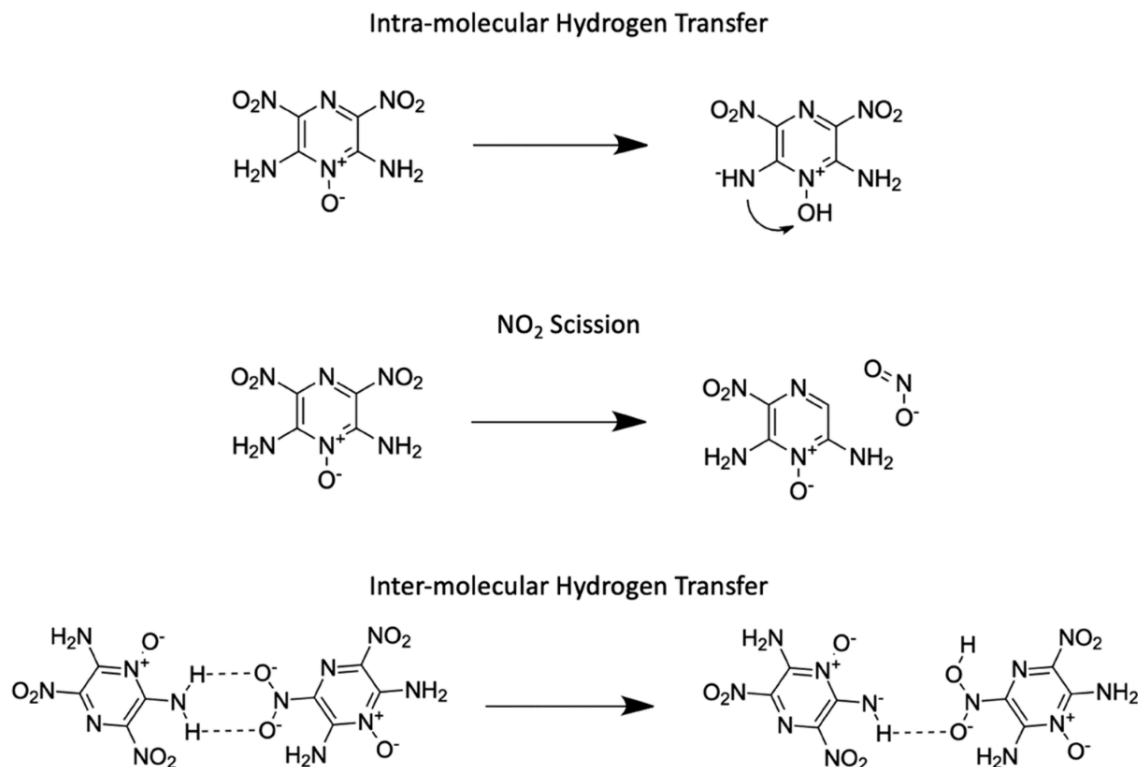
Figure 3.4: 1st step reaction pathway schematics for LLM-105. Top row shows the unimolecular hydrogen transfer pathway, the center row is the unimolecular nitro scission reaction, and the bottom row displays a bimolecular hydrogen transfer reaction.

Using the ReaxFF potential, the bonding environment method can be utilized to predict 1st step reaction pathways for effectively any HE. In Figure 3.5, I show the environment populations for the environments corresponding to various 1st step reaction possibilities in HMX, LLM-105, and TATB. HMX reactions are almost entirely NO_2 scission and HONO elimination paths, as is previously confirmed [37,157]. TATB simulations predict hydrogen transfer, with the vast majority being the intra-molecular path (uni-molecular decomposition) as was previously predicted from quantum chemistry [34]. The validation of these predictions is critical for the remainder of this work, in which a majority of the predictions rely on the assumption that ReaxFF accurately models these events.
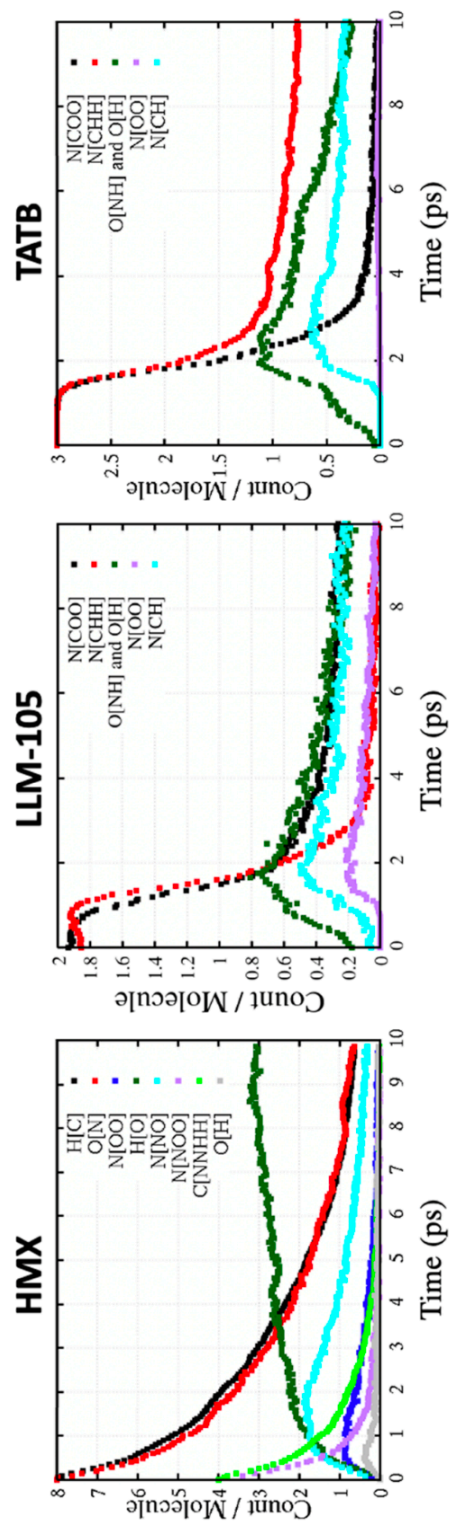
Figure 3.5: Predictions of bonding environments for 1st step reaction pathways for HMX, LLM-105, and TATB, using ReaxFF-2018.

Moving from reaction pathways to reaction kinetics, Figure 3.6 shows isothermal decomposition kinetics predictions for ReaxFF, DFTB, and DFT in which the critical timescale is set to be the time at which all initial LLM-105 molecules have undergone any reaction. For high temperatures, near detonation conditions, ReaxFF-2018 has similar kinetics to DFT and DFTB, however it is much too fast at low temperatures. Overall, ReaxFF-LG greatly underpredicts reaction timescales as compared to DFT and DFTB, but gives a more accurate slope, which is the activation barrier. The majority of hotspot work in following chapters will have temperatures 2500K and up, however, most of the isothermal decomposition work (Chapter 3 and 5) will span temperatures in which these ReaxFF kinetics begin to deviate from DFT heavily.
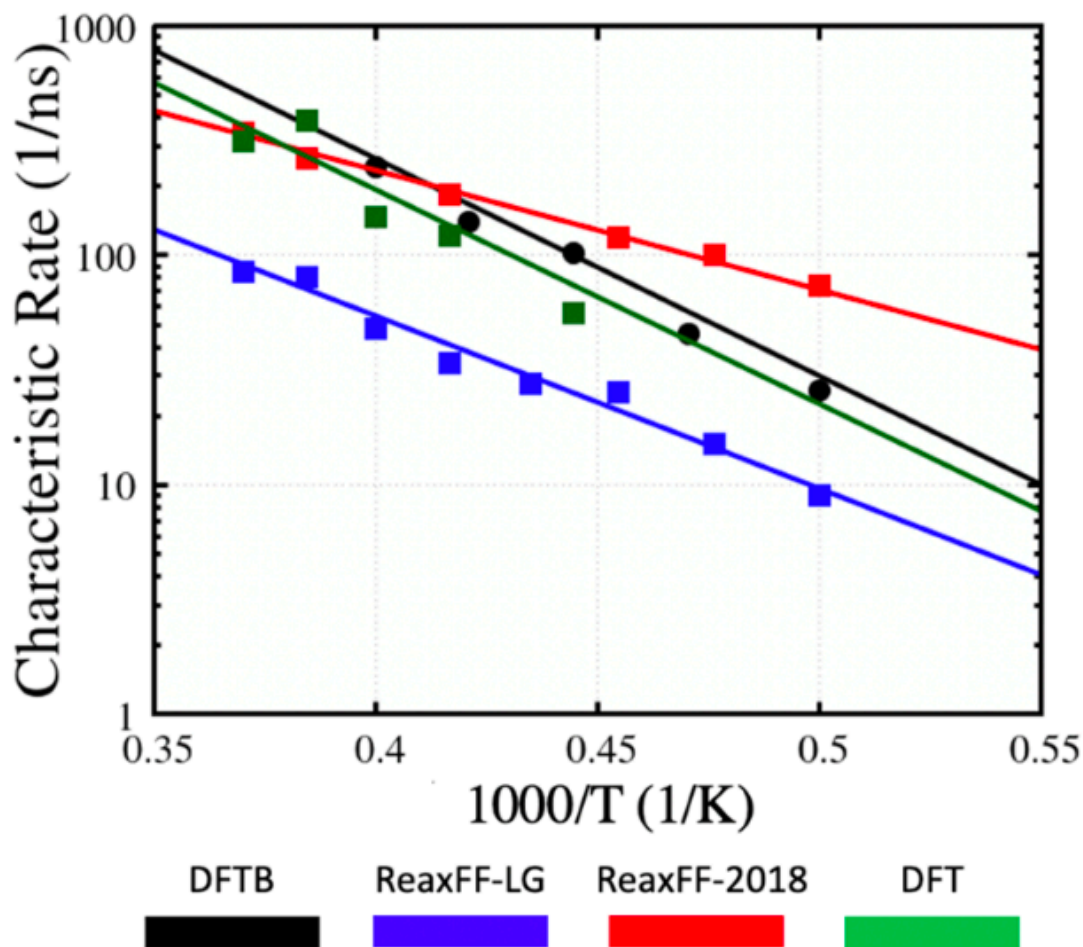
Figure 3.6: LLM-105 isothermal decomposition kinetics predictions for ReaxFF, DFTB, and DFT. Critical timescale is set to be the time at which all initial LLM-105 molecules have undergone reactions, where the characteristic rate is the inverse of this.

3.4 Classical vs Quantum Shock Initiation

3.4.1 Shock Response of TATB: MSST and QB-MSST

Now that the use of the ReaxFF potential has been well justified for TATB and similar insensitive HEs, the remainder of this chapter will focus on assessing the role of quantum nuclear effects on the initiation of chemical reactions in TATB, starting with shock initiation. Figure 3.7 shows the unreacted Hugoniot curves for TATB using both MSST and QB-MSST, as well as

experimental results from Ref. [158]. Open and closed symbols designate which ReaxFF parametrization was used.

Comparing classical to quantum (blue to red), the quantum, QB-MSST, shows slightly higher pressures for all levels of compression. Because the shock temperature for a given compression is higher in the quantum description, the virial component of the pressure is slightly higher. In the P-V Hugoniot (left panel of Figure 3.7), the 'Pressure' is taken as the volumetric pressure, or the trace of the stress tensor. In the U_s-U_p curve (right panel), the jump conditions are solved using the stress tensor component in the shock direction, which is significantly higher than the hydrostatic pressure, on MD timescales, in which the shock state is non-hydrostatic. In the experiments, the pressure measurements are most likely taken after the system reaches a hydrostatic state, whereas the MD simulations still maintain significant levels of deviatoric stress, leading to the simulation-experiment disparity in the U_s-U_p curve. Another origin of this discrepancy is that the experiments had lower initial densities, whereas the simulations were conducted at theoretical max density of the perfect crystal (experiments: 1.876 g/cm^3, ReaxFF: 1.935 g/cm^3) [158].
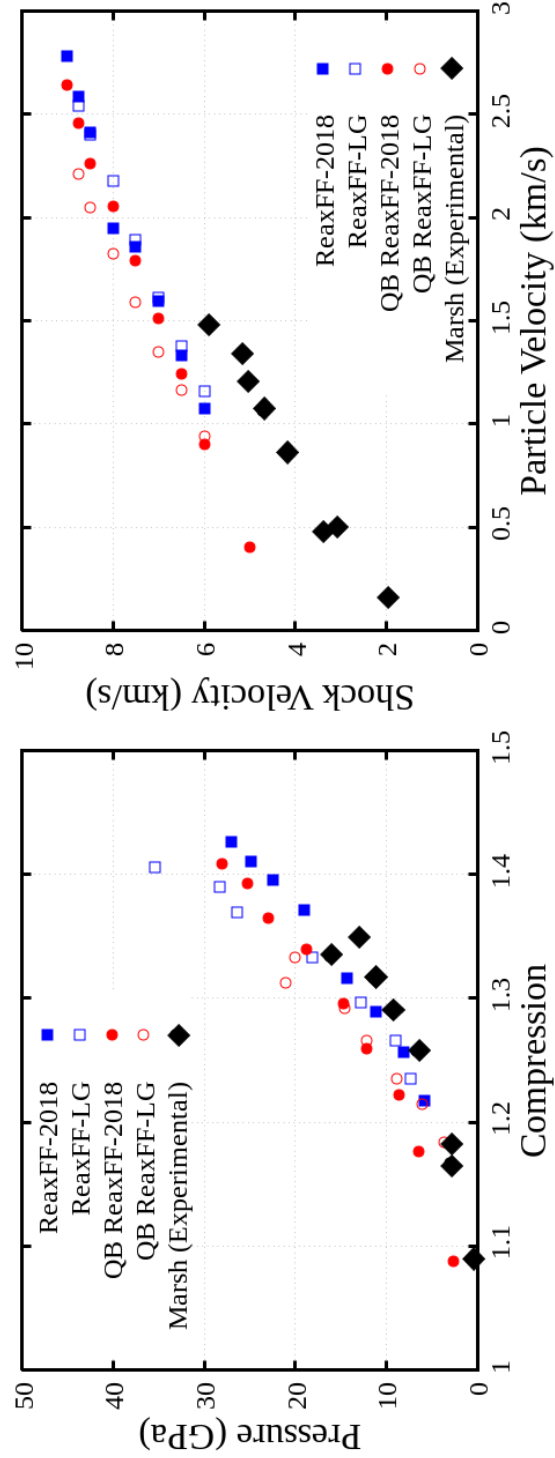
Figure 3.7: Shock Hugoniot curves for TATB using both classical dynamics and a quantum heat bath. Experimental results are from Ref. [158]. Left panel is the P-V Hugoniot where pressure is the trace of the pressure tensor. Right panel is the Us-Up curve, where Us is derived from the jump conditions using the shock direction component of the stress tensor, not the trace.

In addition to the standard shock Hugoniot curves, Figure 3.8 shows the kinetic energy (KE) of the system for each chosen shock velocity (MSST's independent variable). Both the increase in KE from the unshocked state and the absolute KE are shown, in the left and right panels respectively. Since the energy imparted to the system from a shock is controlled by the jump conditions, only the difference in U_s-U_p curves between the classical to quantum should lead to discrepancy in the rise in energy, as $\Delta E = \frac{1}{2} U_p^2$ [5]. It should also be noted that the absolute KE is much higher in the quantum description due to the ZPE contribution. This magnitude of increase due to ZPE is significantly higher than the shock increases, with the strongest classical MSST shocks barely reaching the unshocked total KE of the QTB TATB system. Hence, for any given shock, the rise in KE is roughly the same for both systems, but the absolute KE is much higher for the quantum description of energy.
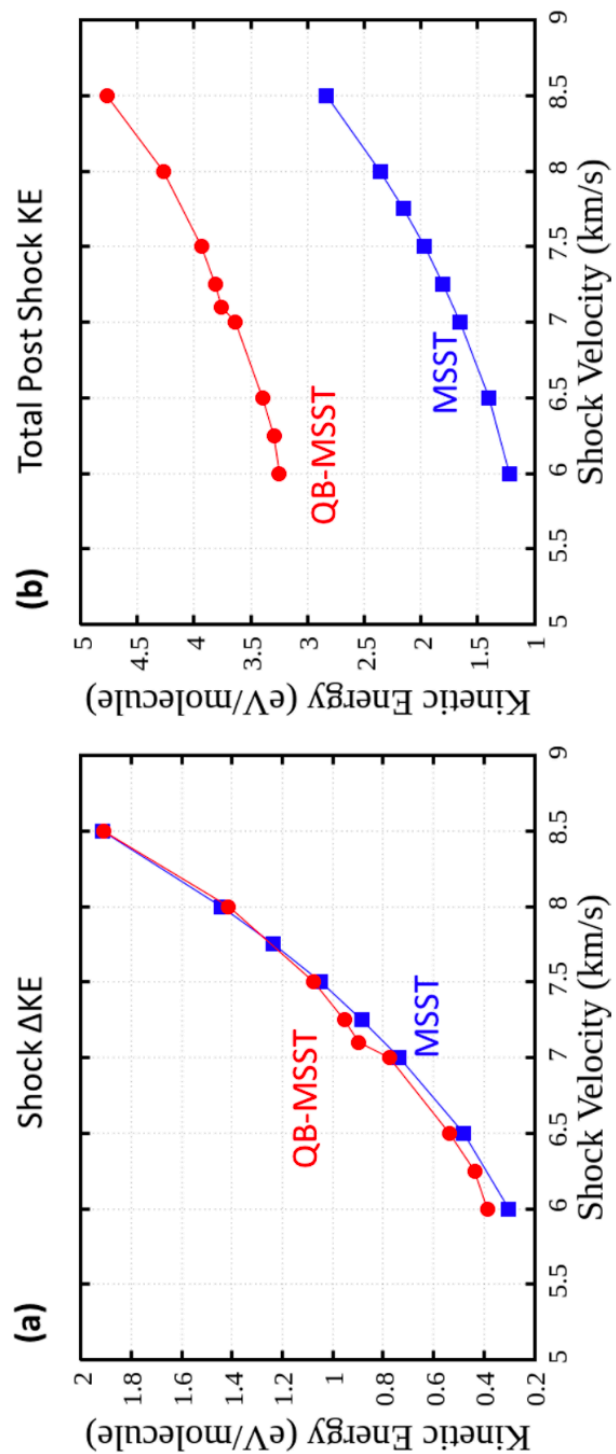
Figure 3.8: Kinetic energy responses of MSST and QB-MSST shocks for ReaxFF-2018 showing the change in kinetic energy and absolute kinetic as a function of shock velocity. Total KE in the right panel includes contributions from the zero-point energy of the quantum mechanical system.

57

The kinetic energies of Figure 3.8 can be displayed in terms of temperature, where the classical MSST simulations have a specific heat of $3Nk_b$, and the quantum bath simulations have that of the quantum harmonic oscillator. Figure 3.9 shows the post-shock, but pre-reaction, temperatures for MSST and QB-MSST shocks using both ReaxFF-2018 and ReaxFF-LG. For both potentials, the quantum correction for temperature from Section 3.2.2 is applied to the MSST results and is shown in the green points, which overlay the QB-MSST results almost perfectly. As with the E(T) and specific heat plots in Section 3.2.3, this well validates that QB-MSST is returning the expected results and our choice of QTB parameters are well converged across the large range of pressures and temperatures experienced here. Interestingly, the difference in classical and quantum shock temperatures increases with increasing shock strength. This results in the idea that the classical approximation may be worse near detonation conditions, which should be more classical in nature, if the initial state is highly quantum (room temperature).
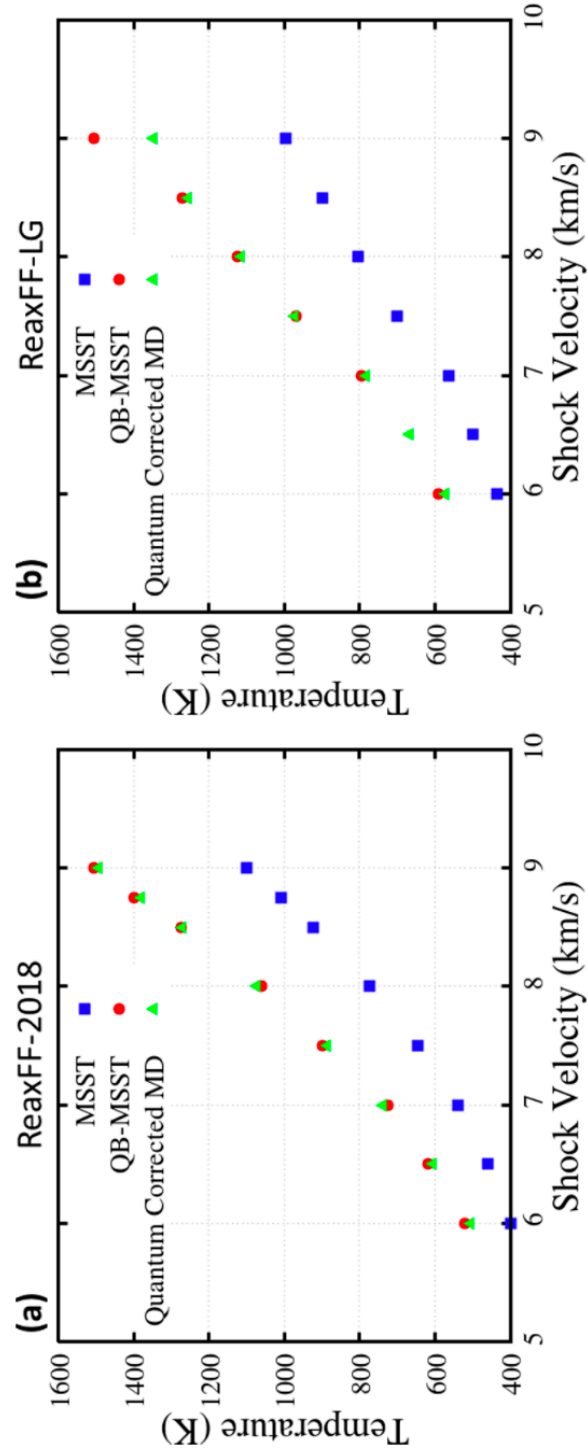
Figure 3.9: Comparison of post-shock temperatures for MSST and QB-MSST, as well as a post-processed quantum correction to MSST simulations using a quantum specific heat calculation shown in Section 3.2.2 Panel (a) is ReaxFF-2018 and (b) is ReaxFF-LG.

3.4.2 Thresholds for Chemical Initiation

It should be expected that, since the MSST and QB-MSST descriptions of shock compression led to different P-V-T responses in TATB, especially in temperature, the shock initiation of TATB will occur (on MD timescales) at different shock strengths for classical vs quantum simulations. It is not clear, however, if these thresholds will occur at the same temperature, same KE, or some other quantity. Figure 3.10 shows, for ReaxFF-2018, the same shock temperature curve as in Figure 3.9 and a curve of total KE in the units of temperature assuming a classical specific heat. The latter will be denoted as 'classical temperature' henceforth.

The primary ambition in this section is to determine the influence of using a QTB versus a classical heat bath on the minimum shock velocity needed to initiate significant chemical decomposition. The threshold is defined as the lowest shock velocity (U_s) needed to produce a temperature increase to at least 2000 K in the first 500 ps from the completion of shock compression (the highest shock temperature before chemistry is ~1300 K). Blue and red horizontal lines in Figure 3.10 show the shock temperatures corresponding to the predicted threshold shock velocity from MSST and QB-MSST simulations, respectively. Despite the increase KE being roughly the same for classical and quantum shocks, the large difference between the two thresholds in both temperature and U_s is immediately apparent. The threshold for QB-MSST simulations is a shock velocity of 6.25 km/s (U_p = 1.2 km/s and P = 14 GPa) while classically, it is U_s = 8 km/s, (U_p = 2.1 km/s and P = 34 GPa). The lower U_s threshold is anticipated, as the quantum system shocks will reach much higher temperatures, for a given shock strength, compared to classical shocks. The unexpected trend is the difference in threshold temperature, 600 K for quantum and 750 K for classical.

Additionally, a single, shared threshold in (total) KE is a possibility. Due to the ZPE contributions, the quantum system will reach some absolute value of KE for a lower U_s than a classical shock. Figure 3.10(b) compares the absolute kinetic energy for both cases. Despite the quantum mechanical system reacting for much lower shock temperatures, a much higher absolute KE is needed, compared to the classical shocks, with the classical KE threshold being much lower than the quantum threshold. However, the total kinetic energy of the quantum system at room temperature is roughly 930 K. This leads to the increase in KE, not absolute KE, needed to initiate chemistry, much lower for the quantum system, which tracks with the temperature threshold results and the specific heat differences.

It was shown in Section 3.4.1 that a classical simulation and a quantum post-processing is all that is needed to accurately describe the shock temperature for a system with a quantum description. However, this post-processing would only consider contributions from the temperature dependent specific heat, not the ZPE contributions. The simplest assumption, that chemistry will initiate at the same temperature, would lead to the post-processed classical simulations predicting a threshold of $U_s = 7.26$ km/s, almost exactly halfway in between the simulated classical threshold and simulated quantum threshold. This threshold is determined by the intersection of the blue threshold line with the red temperature Hugoniot in Figure 3.10(a). Table 3.1 lists the threshold values for classical and quantum descriptions, as well as this misguided post-correction method.

Overall, the decrease in the threshold shock strength in the quantum description is only partially caused by the increase in shock temperature from the specific heat. By also decreasing the temperature threshold for chemistry, the quantum description threshold is considerably lower than what could be ascertained from simulation post-processing only. Since the only other quantum effect used here is the inclusion of a frequency dependent ZPE, it can be shown that roughly half of the decrease in threshold is due to the specific heat effects, and half due to ZPE effects, with the former lowering the threshold by roughly 60%, and the latter around 40%. I.e., the significance of the specific heat and the ZPE effects can be thought of as roughly equivalent for predictions of threshold shock strengths.
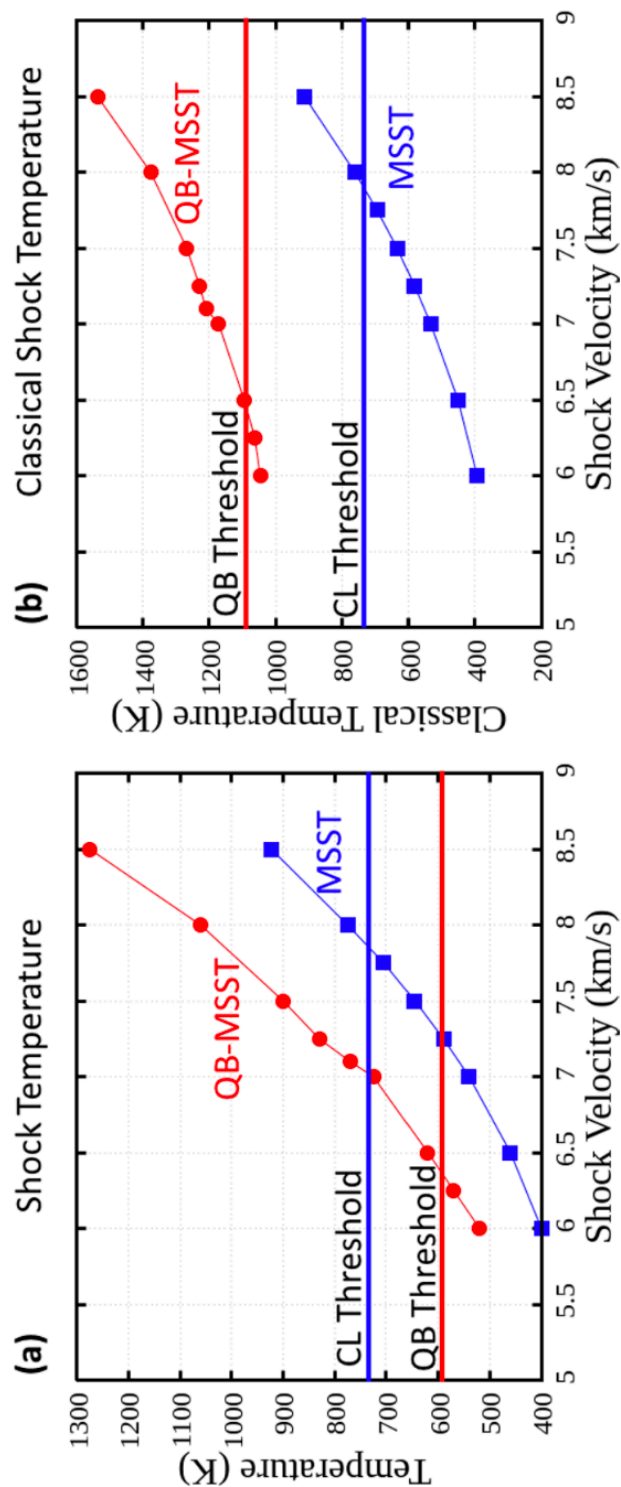
Figure 3.10: Comparison of post-shock temperatures for ReaxFF-2018 via (a) the temperature and (b) the classical temperature ($KE/3Nk_b$). Solid lines represent thresholds for initiation of chemistry. Note: The classical temperature QTB 300 K equivalent is 930 K.

Table 3.1: Reaction thresholds for MSST, QB-MSST, and quantum post-corrections to MSST simulations as outlined in Section 3.2.2

Descriptor	MSST	Post-Correction	QB-MSST
Pressure (GPa)	34	26	14
Us (km/s)	8.0	7.25	6.25
Up (km/s)	2.1	1.6	1.2
Temperature (K)	725	725	600
Classical T (K)	725	725	1085
ΔClassical T (K)	425	425	155

The shocks in Figures 3.7 – 3.10 are all compared at the same shock state, or, more generally, the same energy input. In Figure 3.11 shocks are compared at different energy inputs, but at states at which the temperature is equal for the classical and quantum descriptions. At a shock temperature increase of 770 K, the classical and quantum shock speeds are 8.0 and 7.1 km/s, respectively, and for 1025 K, they are 8.85 and 8.0 km/s. For the lower temperature set, Figure 3.11(a), the quantum system, which is at a lower pressure and the same temperature, reacts on a timescale much faster than the classical system. At the higher temperature, the deviation between quantum and classical is much lower and the classical reacts slightly faster, albeit within the margin of error for stochastic fluctuation between simulations with different initial configurations. However, the main takeaway from these results is that in the shock compression regime, the different P-V-T responses make a one-to-one comparison impossible for the classical and quantum systems. Hence, in the subsequent section, isothermal decomposition simulations will be used to more closely assess the effect on kinetics from quantum nuclear dynamics.
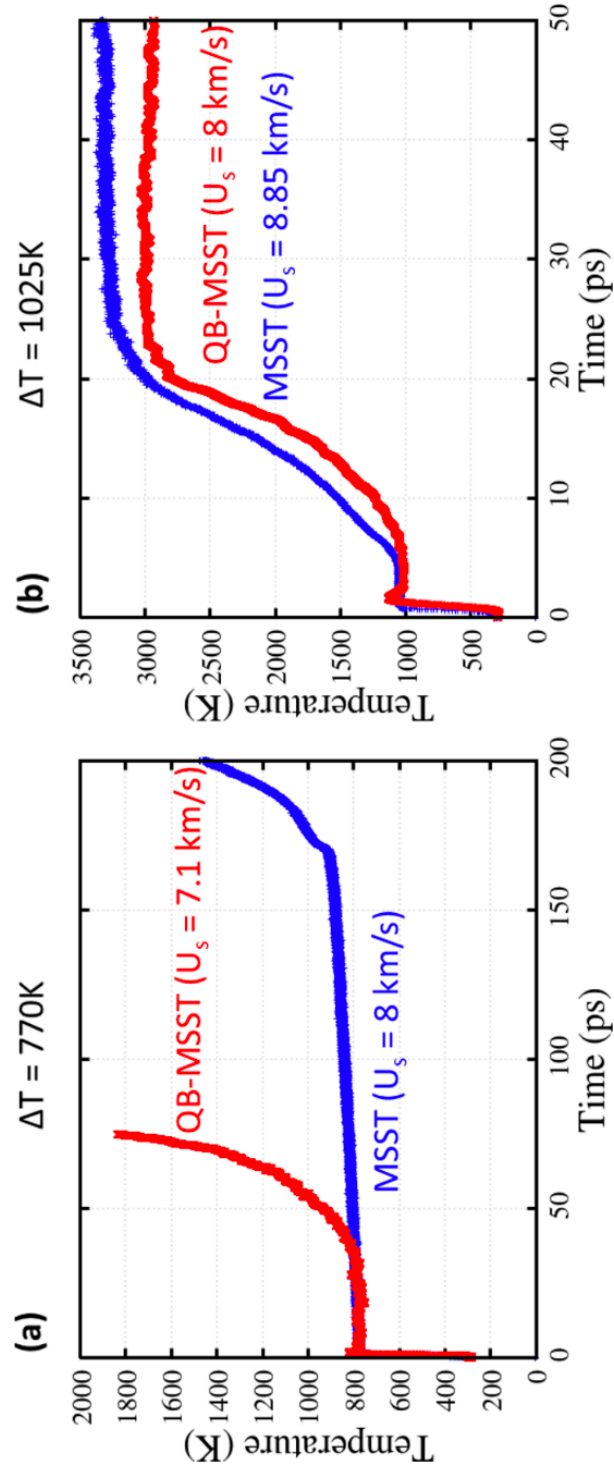
Figure 3.11: Temperature time evolution for MSST and QB-MSST shocks with identical temperature rises but different shock strengths: (a) 800 K and (b) 1025 K. The necessary shock velocities to reach these temperatures are listed in the figure inset text.

3.5   Classical vs Quantum Thermal Decomposition

Using isothermal-isochoric simulations for thermal decomposition removes the compressive work factor from consideration, as well as the specific heat leading to different temperature rises. Retaining constant temperature allows for a simple kinetics analysis that essentially isolates the effects due to ZPE. Simulations are run at the experimental density (TMD ~ 1.93 g/cm^3) for a temperature range of 1500 K to 3000 K. Figure 3.12 shows the Arrhenius style kinetics for thermal decomposition using ReaxFF-2018 with classical NVT and QTB simulations. The right panel shows the kinetics adjusted where total KE (including ZPE) is used in units of temperature, the classical temperature of the system.

For the classical simulations, the activation energy is found to be 21.8 ± 0.9 kcal/mol with a prefactor of 10.9 ± 1.2 ps^{-1} and the quantum system results in lower values for both, 16.6 ± 0.4 kcal/mol and 4.6 ± 1.1 ps^{-1}, where

$$k(T) = A e^{-\frac{E_a}{k_b T}}$$

The QTB kinetics were reassessed in terms of total KE (panel b in Figure 3.12), in which the Arrhenius data still appears linear. By using the classical temperature definition to calculate Arrhenius kinetics, a considerably higher activation barrier of 22.8 ± 0.5 kcal/mol and a prefactor of 10.4 ± 1.1 ps^{-1} is found, which are both much closer to the classical simulation predictions. Compared to the classical simulations, the activation barrier for TATB thermal decomposition with a quantum bath is 21% lower. The differences in activation energy are qualitatively consistent with the lower threshold for shock-induced chemistry, shown in Section 3.4.2, and the accelerated reaction timescales in Figure 3.11.

For the case with the same kinetic energy, Figure 3.12(b), the only difference is the distribution of energy. The classical simulations will follow equipartition and distribute energy equally between all DoFs. The quantum system will have a frequency dependent energy distribution following the Bose-Einstein distribution, as discussed in Section 3.1. Hence, specific modes, typically high frequency modes with high Debye temperatures compared to $k_b T$, will have more energy in the quantum system and lower energy in the classical due to the frequency dependence of the ZPE contributions. That is, for quantum and classical systems at the same total kinetic energy, the frequency dependence in the quantum system will lead to greater energy in high frequency modes and lower energy in low frequency modes, with respect to the classical

system. For TATB, this leads to a slightly higher activation barrier for the quantum system, 1 kcal/mol difference.
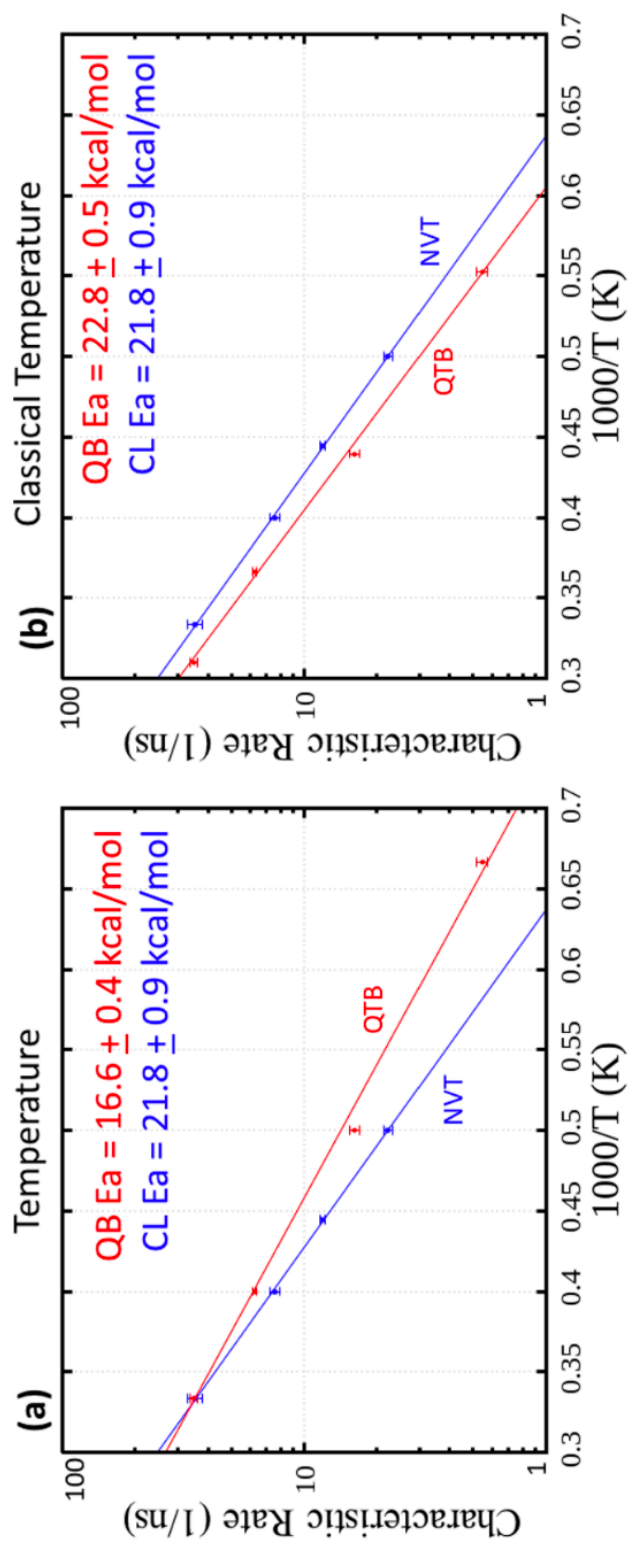
Figure 3.12: Arrhenius kinetics where the x-axis is in terms of (a) temperature and (b) KE in units of T. Errors bars are a 95% confidence interval for N=5 independent simulations.

These differences in the classical and quantum decompositions at the same total KE are shown in Figure 3.13 where panel a shows the PE decay over the thermal decomposition, in which the classical description system releases energy from the reaction slightly faster than the quantum system. Panel b) displays the vibrational power spectrum for both systems at 1800 K worth of total KE, which describes the energy levels of individual frequencies. As expected from the Bose-Einstein distribution, the classical system energy is higher for low frequency (0-1000 1/cm) and the quantum system is at a higher energy level for high frequency (1700+ 1/cm).

The primary reaction pathways for TATB, described in Section 3.3 (Figure 3.5) are intra- and inter-molecular hydrogen transfers [34]. Both of these mechanisms are controlled by the proximity of, and collisions between, amino and nitro groups. Especially for the bi-molecular process, the motion of these groups will be dominated by slow phonon modes of motion, not high frequency both vibrations like and $N-NO_2$ bond break would. In the case of the same total kinetic energy, the quantum description would have lower energy in these modes, therefore reducing their reactivity and increasing the energy barrier with respect to the classical system.
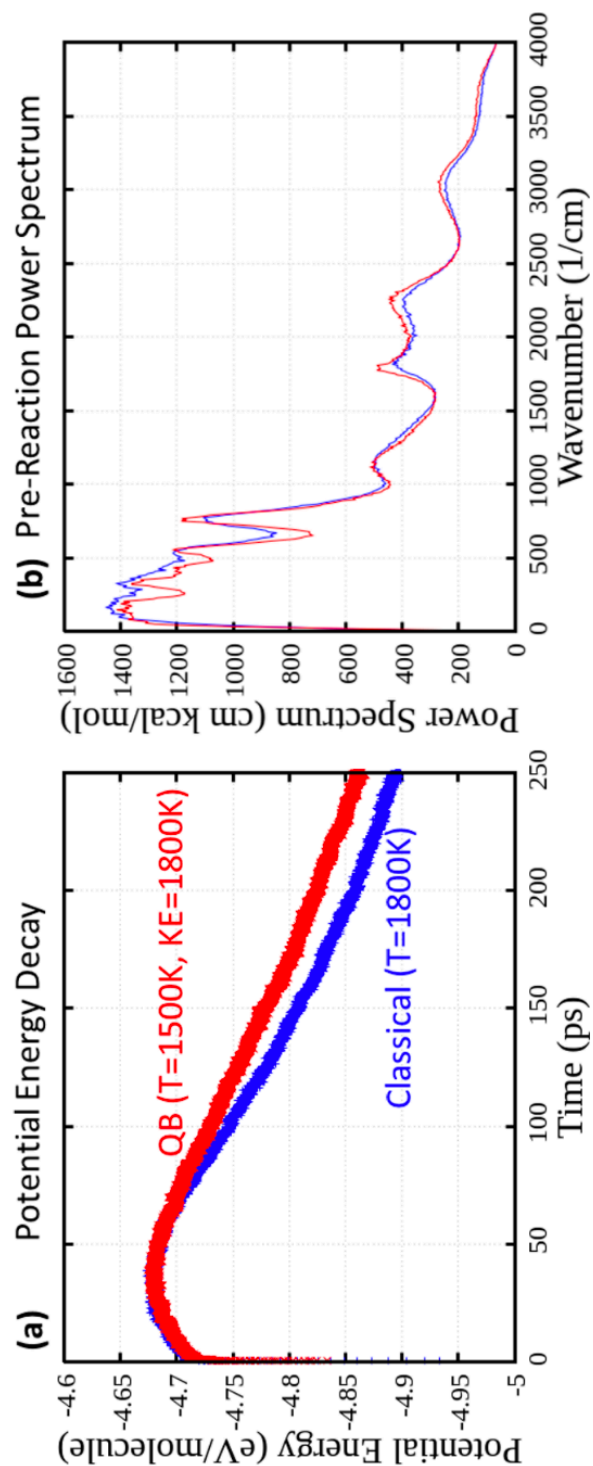
Figure 3.13: (a) Potential energy time history for thermal decomposition at the same total KE and (b) vibrational power spectra for classical and quantum systems at KE=1800K prior to any chemical reaction.

Lastly, the classical and quantum systems will be compared for product formation amounts, comparing H_2O, CO_2, N_2, and NH_3. Comparisons are made at two different temperatures, 2500 K and 2700 K, where the classical 2700 K and the quantum 2500 K have nearly identical levels of total KE. Figure 3.14 shows the time evolution of these chemical species for ReaxFF-LG. In both cases the product levels are slightly higher for the higher temperature and are slightly higher for the quantum mechanical description.
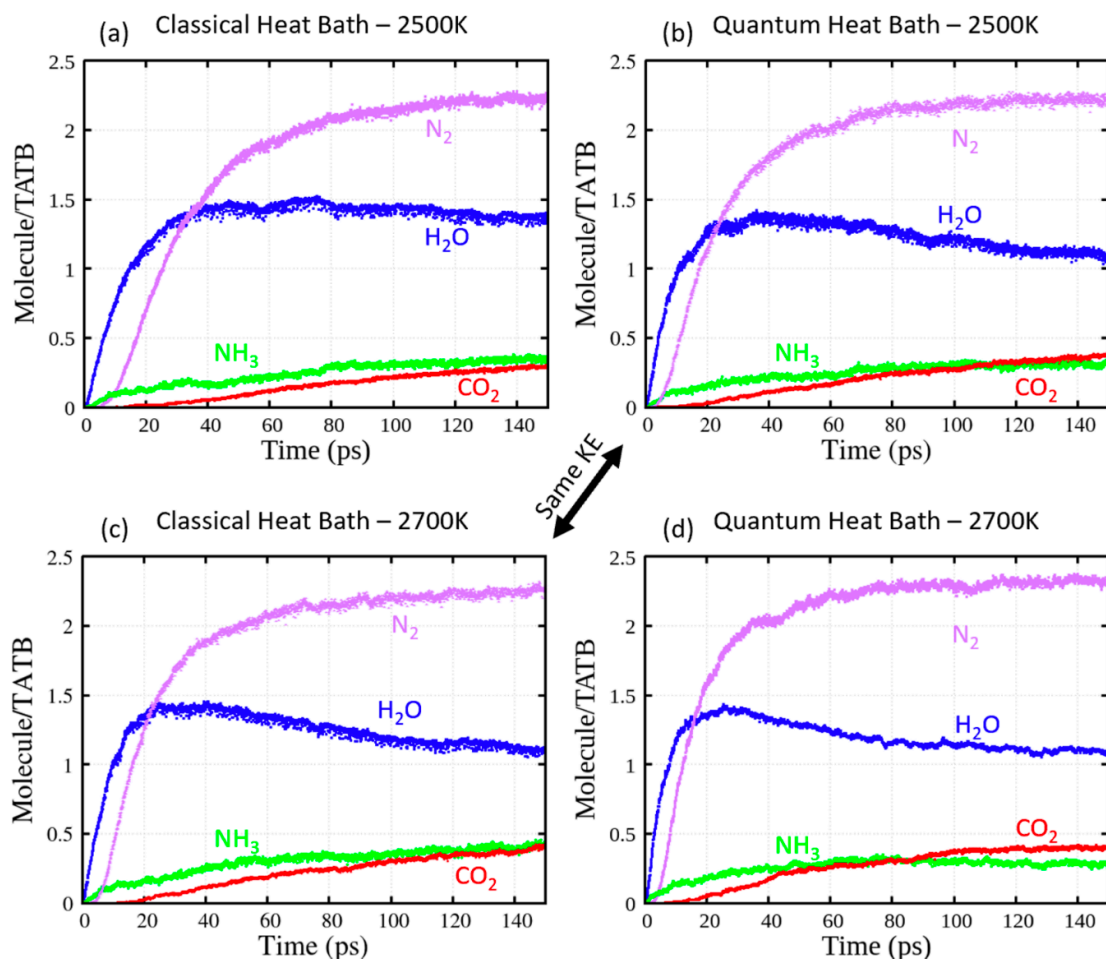
Figure 3.14: TATB thermal decomposition products for ReaxFF-LG using classical and quantum statistics at 2500 K and 2700 K. Panels b and c both have a total kinetic energy of 2700 K.

3.6   Conclusions

In this chapter, ReaxFF results were directly compared to DFTB and DFT results for thermal decomposition for multiple HE materials, HMX, TATB, and LLM-105, to validate the use of ReaxFF to describe these materials. Using a semi-classical heat bath that pushes all-atom systems to follow the quantum mechanical Bose-Einstein distribution, comparisons were made for shock initiation and thermal decomposition of both statistical descriptions. Using classical mechanics to describe the dynamics of atoms in which $k_b T < \hbar\omega$ leads to two major inconsistencies with quantum mechanics: a lack of a zero-point energy at zero temperature and a temperature independent specific heat that is always at the high temperature limit of $3Nk_b$. The quantum thermal bath (QTB) allows for a correction of these inconsistencies via a colored-noise thermostat whose power spectral density matches that of the quantum mechanical harmonic oscillator. Quantum mechanical post-corrections to classical simulations was also utilized to make predictions of temperature rise.

Both MSST simulations with the quantum thermal bath (QB-MSST) and MSST simulations with a quantum mechanical post-correction temperature predict nearly identical shock temperatures a wide range of shock strengths, demonstrating that both methods can correct for the lack of a temperature dependent specific heat in classical shock simulations. Both an increases in the shock rise in temperature and a lowering of the necessary shock temperature to initiate chemical reaction are induced via the inclusion of quantum statistics. For MSST, post-corrected MSST, and QB-MSST approaches, the threshold pressures to induce prompt chemistry were found to be 34, 26, and 14 GPa, respectively. The two quantum mechanical adjustments made here, a temperature dependent specific heat and an inclusion of a zero-point energy, are culprit to these initiation trends. Decreases in the initiation threshold can are attributed equally to increases in shock temperature from specific heat and lower of the temperature threshold from the ZPE.

The effects of the zero-point energy can be further assessed via thermal decomposition simulations under isothermal-isochoric conditions using both classical and quantum descriptions of the system. As expected, the quantum description lowers the activation barrier by approximately 21%. Conversely, when the kinetics are plotted in the setting of kinetic energy, instead of temperature, the new quantum description activation barrier is 1.0 kcal/mol higher than the barrier for the classical description. The results from the fact that the classical description at equivalent

kinetic energy has higher energy in low frequency modes, which govern the 1st step reaction mechanisms for TATB.

Overall, by assuming classical dynamics approximations for initiation and reactions in HEs, considerable increases to reactivity are missed. The expected decrease from increased temperature is compiled with additional effects from zero-point energy that have been neglected by the community to this point. While quantum based, colored noise thermostats have numerous drawbacks such as an isothermal nature and coupling effects such as ZPE leakage [156], including these effects into modeling initiation and detonation are critical, especially with the considerable, recent rise in multiscale modeling efforts that are grounded in classical molecular dynamics, producing models for chemistry and mechanics alike [7,9,46,159].

4.   INTERNAL STRAIN ENERGY IN SHOCK INDUCED HOTSPOTS

4.1   Introduction

The initial introduction on the formation and criticality of hotspots given in Section 1.3 will be extended here. Hotspots, which can be defined at localizations of excess energy as compared to the surrounding material, are typically formed by the interaction of a shockwave and the local material's microstructure. Common mechanisms of hotspot formation include the collapse of porosity, shear band formation, jetting, shock interaction with grain boundaries, viscous heating, and friction [58]. While all these mechanisms contribute to the overall reactive response of the material, none do more so than the collapse of porosity. Shock desensitization experiments first showed the impact of porosity on run to detonation [56]. Initial weak shocks can/will compact porosity in plastically bonded explosive samples without initiating critical chemistry that leads to a detonation. Upon recovery, these weakly shocked samples, which no longer possess porosity, were found to be highly non-detonable to stronger, follow-up shocks.

The chemical prowess of hotspots formed from the collapse of porosity can be attributed the large amounts of P-V undergone due to the recompression of the material expanded into the pore. Work from Holian et. al. developed simple scaling laws for hotspot temperatures in which the scaling is derived directly from the work done on the system [162]:

$$\frac{3}{2} k_b \Delta T = \frac{1}{2} P (V_{00} - V_0)$$

where the V_{00} term is the specific volume the material reaches during expansion into the void, with V_0 being the initial, unshocked specific volume. Hence, the greater the material expands into the void prior to recompression to V_f, the greater the increase in temperature, with a theoretical max temperature rise as V_{00} goes to the volume of the initial void. Using the Hugoniot jump conditions, the theoretical max temperature scaling can be reproposed as

$$3k_b \Delta T_{max} = mU_s U_p$$

Holian et. al. goes on to show that it is necessary to induce molecular jetting to reach the necessary expansion to maximize temperature. The onset of jetting for a simple crystal is related to the cohesive energy, in which the minimum particle velocity needed, U_p^*, is

$$E_{coh} = \frac{1}{2} m U_p^{*2}$$

The importance of porosity on ignition and run to detonation was further exemplified through shock induced run to detonation experiments in gelled nitromethane [57]. The experiments, which included defects from silica nanobeads (inclusions) and air bubbles (pores), showed the superiority of the latter in decreasing the run to detonation distance. It was also shown that more numerous, smaller bubbles were superior to a few larger ones.

The shock induced collapse of porosity is controlled by different mechanical collapse mechanisms in which their manifestation is dominated by the shock strength, among other things like pore size and shape [163–165]. For low speeds, the viscoplastic mechanism dominates, in which collapse occurs after the passage of the shockwave, driven to alleviate pressure, especially the high deviatoric states. Often, for cylindrical pores, the viscoplastic mechanism is characterized by lateral collapse of the material, via plastic flow, in which little of the upstream face of the pore expands into the void space. This mechanism is relatively slow and results in significant plasticity of the surrounding material of the pore, in all directions. At higher speeds, the hydrodynamic collapse mechanism begins to emerge. This is characterized in cylindrical pores by the upstream face of the pore flowing outward in a jet stream of fluid-like material to fill the void. This collapse mechanism is driven by the shockwave, typically occurring on timescales of the wave transversing the pore. The hydrodynamic collapse results in significant plasticity near the upstream face of the pore, as well as on the downstream face upon impact. Typically, the collapsing material accelerates to velocities on the order of $2U_p$. [5]

In cases in which the particle velocity is extremely high or the geometry of the pore significantly focuses the shock energy at the upstream face (such as high aspect ratio voids), jetting occurs [166–168]. Jetting, or molecular ejecta, can expand material to gas level densities and result in significantly higher hotspot temperatures upon recompression from a (most likely) hydrodynamic collapse behind the ejecta. The ability of jetting to localize kinetic energy is inherently tied to the area/volume of the void that the jetting molecules can expand into. If the pore is too small to allow for expansion, the temperature increase will be limited.

Continuum simulations of pore collapse in HMX showed that the viscoplastic collapse (2–10 GPa) features significant local shear band formation and the hydrodynamic collapse (20–40 GPa) is dominated by local melting/plasticity [63]. When the hotspot temperatures are normalized by the bulk shock temperature, the viscoplastic collapses creates relatively higher temperatures than the hydrodynamic collapse, showing the importance of plastic flow in localizing energy.

The study of mechanical hotspot formation at larger scales has been rapidly advanced as of recent due to the development of numerous multiscale models based on atomistic calculations. Direct comparisons for the collapse of porosity for HNS and HMX using continuum models and all-atom molecular dynamics have led to better validated models to extend the time and length scales of high resolution simulations [7,169].

Specifically, tandem MD and continuum simulations in TATB assessed shock induced pore collapse of cylindrical pores for different orientations and a range of particle velocities [9]. Weak shock simulations were conducted using both the all-atom model and the isotropic elastic-plastic continuum model, which showed significant deviation during pore collapse. This is most likely a result of the orientation dependent defect mechanisms explored by Lafourcade et. al., discussed in Section 1.5 [70,72] and shows the importance of anisotropic effects in TATB.

The reactivity of hotspots can be assessed as a Frank-Kamenetskii problem in which exothermic chemistry directly competes with thermal transport [59]. In the original F-K works, the critical conditions were set to be temperatures above the point in which heat gain is equal to heat loss. For the spatially varying temperature F-K problem and the uniform temperature Semenov problem [60], the goal is to study homogenous, adiabatic ignition to assess conditions of accidental ignition and explosion. Craig Tarver expanded this analysis to the criticality of hotspots in which modern multi-step kinetics models and complex heat transport solutions were used to assess the critical temperature of hotspots in HEs for varying size, shape, and dimension [37,39]. In the case

of hotspots, a critical hotspot is defined as when exothermic chemistry heat release outstrips thermal transport away from the hotspot, can form a steady state deflagration wave.

With the recent advancements in high-performance computing, shock induced hotspot initiation can be studied from the atomistic point of view with explicit descriptions of chemistry and thermal transport. The 'AB' toy model HE system was used to explore void size, number density, and location effects on the transition to deflagration and detonation [25]. Wood and Cherukara performed the first all-atom shock to deflagration simulation in a solid HE material [61]. Via a cylindrical pore collapse in RDX, the dynamically formed hotspot was shown to react significantly faster than a statically formed hotspot at the same shape, size, temperature, and pressure. This was attributed to (most likely) mechanochemistry and non-statistical reactions, however, to explicit proof of that was found. Shocks in TATB at near-detonation conditions formed significant levels of shear bands [51]. Isolated kinetics studies of the material in the shear bands and the surrounding crystal showed the shear bands to have reaction rates an order of magnitude faster or greater. These mechanochemically active shear bands have been actively included as contributors to the run to detonation in recent ignition and growth type models [170]. Shock simulations with 1-D pores (planar gaps) showed that increasing shear during impact by providing a lateral velocity to one side of the pore decreases the necessary impact velocity to form a critical hotspot [132]. This is attributed as the first direct proof of mechanochemical acceleration in hotspot reactions from the collapse of porosity, but the molecular mechanisms responsible were not explored.

The field of mechanochemistry is highly broad, ranging from the alteration of covalent bonds altering the available transition states to ball milling of reactive metals to alter the microstructure and increase reactivity [53,171,172]. The former can be referred to as covalent mechanochemistry (CMC). The subsequent chapter (5) will deal intimately with CMC. The only necessary information on the topic here is the ideology that deforming covalent bonds can both accelerate reaction kinetics and alter reaction paths [173–175].

4.2   Methods

4.2.1   Pore Collapse Simulations and Analysis

All simulations in this chapter were conducted with the nonreactive Bedrov potential [68], described in Section 2.2, using a timestep of 0.2 fs unless specified otherwise. Two orientations were generated, with the first denoted as (001), and the second as (100). For (100), the x axis of the cell is aligned with the [100], the [120] is approximately parallel to the cell y axis, and $N_{(001)} = a \times b$, which is normal to the basal planes, is oriented along the shock direction, the z axis. For (100), the z axis is the $N_{(100)} = b \times c$, which is parallel to the basal planes, and the x axis is aligned along [001]. Both simulation cells are replicated from these nearly orthorhombic supercells, which were created using the generalized crystal-cutting method (GCCM) [144]. Both GCCM solutions are derived from the triclinic $P\bar{1}$ crystal in the setting of Cady and Larson [67] with relaxed lattice parameters according to the Bedrov potential at ambient density.

Two types of pore shapes were utilized, cylinders and diamonds. The center of each void is placed in the geometric center of a cell. For cylindrical pores, a circular cross-section is used. The circle has a diameter of 40 nm and the pore extends the length of the x axis, which is short compared to the y and z axis in the pseudo-2D architecture of these simulations. The diamond cross section pores are placed in the same orientation and location as the cylindrical ones. Each diamond pore is oriented such that the primary (elongated) axis is aligned with the shock direction, which is the z cartesian axis. The length along the shock direction is 40 nm, with an aspect ratio of 5:1 with the perpendicular axis. Figure 4.1 displays renderings of both cylindrical and diamond pore set ups. Inset figures shown a zoom of the two crystallographic orientations used here.
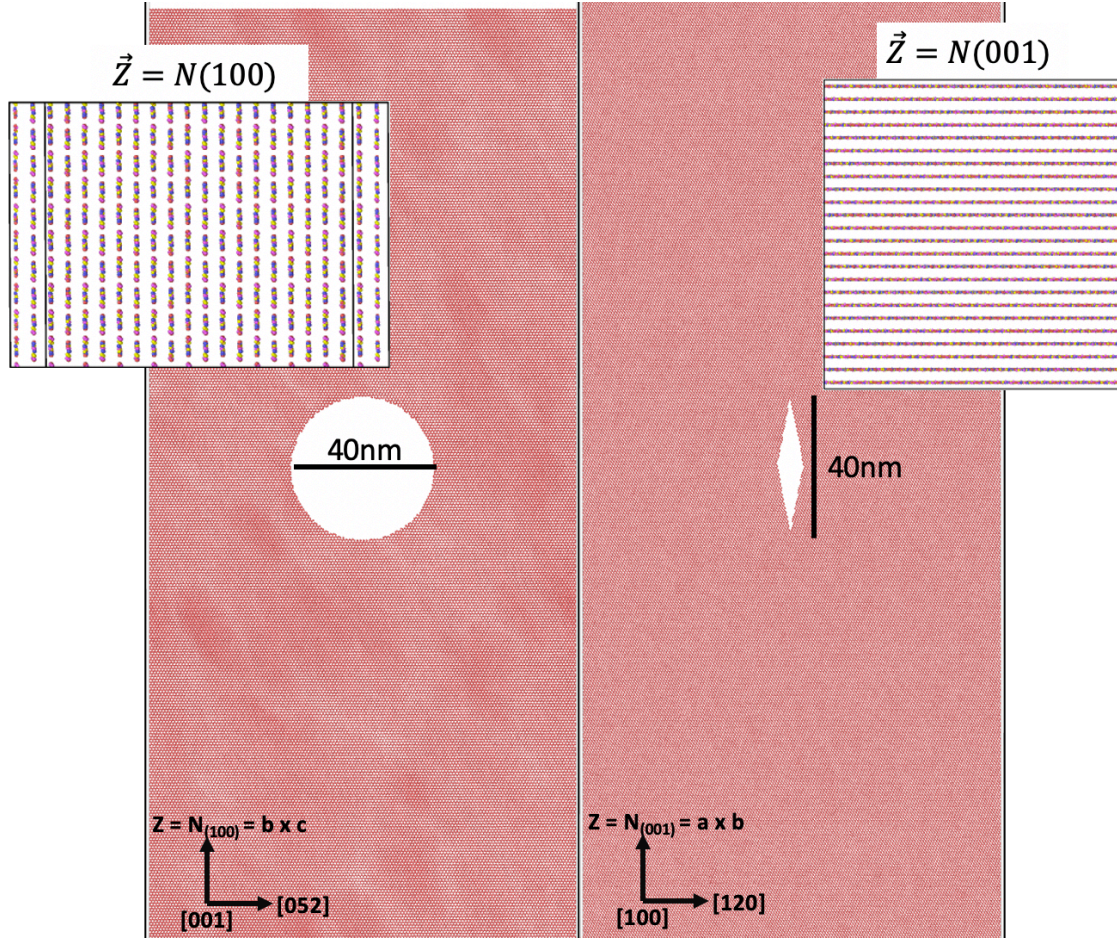
Figure 4.1: Renderings of the cylinder and diamond defects. Inset figures display the two crystallographic orientations used here.

To generate free surfaces, which are created on both ends of the system along the shock direction (z), a 5 nm long region in the shock direction (infinite in the other directions) is deleted from both boundaries outwards. This results in a system that is non-periodic in the shock direction, which prevents self-interactions across the boundary during shock loading. Both non-shock directions are fully periodic.

To initialize the samples, systems are thermalized over a 25 ps run under the canonical ensemble (isothermal-isochoric or NVT ensemble) at 300 K. A timestep of 0.5 fs was used and a Nose-Hoover-style thermostat with a 100 fs dampening [86]. Newly created free surfaces tend to generate acoustic waves that transverse the system to relax pressure, and these take significant time to self-dampen, with a perfect crystal oscillating like a spring. If order to help dampen these waves, the velocity vector of each atom is stochastically chosen from the Maxwell-Boltzmann

distribution, at 300 K, every 0.5 ps, during the first 2.5 ps of the thermalization. This disturbs the collective motion of the acoustic waves and helps to attenuate the breathing modes developed by the relaxation of surface relaxations that typically require long timescales to naturally dampen in a perfect crystal in which the free surfaces are in close proximity to each other (sub-micrometer length).

The thermalized configurations are input as the initial condition for reverse ballistic shock simulations, described in Section 2.4.1, which are conducted under the microcanonical ensemble (adiabatic or NVE conditions). A timestep of 0.2 fs is used. To generate a rigid and infinitely massive piston, all TATB molecules whose center of mass (COM) lies within the bottom 1.5 nm of the cell, in the shock direction, are fixed in space throughout the simulation, set with no net velocity and are grouped as a rigid body. The shock is generated from by impacting the rest of the material on the piston. Reverse ballistic impact simulations are run at U_p = 0.5, 1.0, 1.5, and 2.0 km/s for both diamonds and cylinders, in both the (100) and (001) orientation.

Simulation trajectories of the all-atom simulations, for a smoother and more discrete analysis of local hotspot fields, are coarse grained to a molecular basis. The positions and velocities of each molecule are taken to be the COM values, which are defined as a weighted average across the subset of atoms within the molecule. The molecular stress tensor is the sum of the stress tensors for the subset of atoms within the molecule. Three kinetic energy (KE) values are computed: the molecular kinetic energy, KE_{tot}, the molecular translational KE, KE_{trans}, and the roto-librational and vibrational KE, KE_{ro-vib}. These are computed, respectively, as

$$K_{tot} = \sum \frac{1}{2} m_i \mathbf{v}_i \cdot \mathbf{v}_i$$

$$K_{trans} = \frac{1}{2} M \mathbf{V} \cdot \mathbf{V}$$

$$K_{ro-vib} = K_{tot} - K_{trans}$$

where variables denoted with lowercase letters represent atomic scale quantities indexed over an entire molecule, and variables denoted with capital letters represent molecular center of mass values. An intra-molecular vibrational temperature is defined as the roto-librational kinetic energies in units of temperature (Kevin) through assuming a classical specific heat

$$K_{ro-vib} = \frac{63}{2} k_B T$$

The factor of 63 is taken from the 3 rotational and 60 unconstrained vibrational DoFs in the TATB molecule, as TATB has 72 total DoFs, 3 translational, 3 rotational, and 66 vibrational, where all 6 N-H bond vibrations are held fixed in this work.

MD computed atomic stress tensor components are in units of energy (stress*volume) and need to be normalized by a meaningful volume to describe the true, local stress field of the material. Smoothed molecular stresses for a given molecule are obtained by summing the molecular stresses (component by component) within a local sphere with a radius of 1.5 nm centered at the given molecule and normalizing the summed stress by the sphere volume. Local temperature and energy fields are also smoothed in this manner.

The intra-molecular potential energy (PE) is defined as

$$PE_{intra} = \sum PE_{bond} + \sum PE_{ang} + \sum PE_{dih} + \sum PE_{imp}$$

where each of the PE terms is summed over the total number of bonds/angles/dihedrals in the molecule and are described by the harmonic, cosine series, and tabulated terms of the forcefield [68] described at the beginning of Section 2. All intramolecular non-bonded interactions are excluded by design, which allows for rigorous separation of inter- and intra-molecular potential energy terms.

Intra-molecular strains are quantified through each individual molecule's principal inertia tensor. Using the molecule's atomic coordinates, referenced by the molecule COM, the inertia tensor, I, for each molecule is computed. The eigenvalues, that are the principal moments of inertia, and eigenvectors, that are the axes for the principal rotational frame, are calculated via diagonalizing the molecular inertia tensor. A TATB molecule is approximately a disk at its minimum energy configuration, with minimal out of plane thermal fluctuation at ambient pressure and temperature. Hence, I_1 and I_2, which have axes within the plane of the 'disk' and are the smaller two of the three principal moments, are nearly equivalent for undeformed TATB. The ratio I_2/I_1 is therefore a reliable metric for measuring general out of plane deformations within the molecule, which mainly manifests as out of plane bending and rotations of the amino and nitro groups.

4.2.2 Shock Trapping Internal Boundary Conditions

In direct shock simulations, free surfaces must be created to allow for an impact to generate the shockwave. Whenever a shock wave reaches a free surface, it expands material out into the empty space and creates a backwards propagating relief wave, known as a rarefaction wave. In experimental samples, individual grains are on the scale of micrometers and samples are on the scale of millimeters to centimeters, if not larger. Hence, the timescales of any rarefaction wave are on the order of nanoseconds to microseconds. In MD simulations, where the space between the impact surface and the downstream free surface are tens to hundreds of nanometers, rarefaction waves can release the pressure of the shocked state in tens of picoseconds, which highly limits the timeframe in which a shocked state can be analyzed. While rarefaction waves are physical, their rapid timescales in all-atom simulations can limit the ability to study phenomena that occur after shock loading, as the release wave can alter or even mitigate these events prior and/or during their activation and propagation.

Previous works have developed methods know as shock absorbing boundary conditions (SABCs) which absorb/annihilate the initial shock wave at the free surface, preventing the formation of a rarefaction wave [17,107]. The absorbing boundaries from Cawkwell and Sewell, Ref [17], place another rigid piston at the far end of the sample when the shockwave reaches the free surface. The formation of the rarefaction wave occurs when the surface material can expand forward. By placing a rigid piston, formed at shock density, at the end of the system before the material can expand, the shockwave cannot reflect or form a rarefaction wave. In a reverse ballistic system, the new piston has zero velocity and in a ballistic set up the new piston has a velocity of U_p. This effectively absorbs the shockwave at the downstream boundary. The two pistons then trap the shocked material at shock density with velocity of U_p, forcing the system to stay in the shocked state indefinitely.

In the method implemented by Zhao, Germann, and Strachan [107], two converging, planar shockwaves which are identical except in their velocity vector, which is equal and opposite, annihilate when they converge. Two equal samples are impacted off each other to form the two shock waves. The boundary in the shock direction is kept periodic and is driven inward at the rate of compression of the shock so that the proper volume is kept and the distance between unshocked atoms through the periodic boundary is constant. Once the two shockwaves converge and annihilate, the periodic boundaries stop compressing and the system is kept at constant volume at

the shock state which no active shock waves. This is a nearly identical solution for both styles of SABCs, but requires different initial designs.

Both SABC methods require that the wave front to be nearly planar and the simulations must have premeditated boundary conditions that allow the SABCs to be utilized. Multiple, non-planar rarefaction waves can be created in simulations of pore collapse or systems with complex microstructures such as plastically bonded explosives. In these cases, a separate SABC would be needed to individually attenuate each wave, or the SABCs would fail and allow some waves to continually transverse the system and reflect at the boundaries. Three rarefaction waves, or more, develop, in addition to the initial shock, from a shock induced pore collapse with a single, cylindrical pore, as shown in Figure 4.2(b). While using traditional SABCs to deal with all three waves (or more), which all propagate at different velocities and have different shapes, would prove computationally challenging, the methodology developed here aims to only trap all waves behind rigid barriers. This would prevent interaction between any rarefaction waves and the area of interest, such as a hotspot. Shock Trapping Internal Boundaries (STIBs) are a generalization of SABCs that decrease the aforementioned SABC requirements, allowing for problems involving multiple, non-planar waves.

For the pore collapse simulations conducted in this work, STIBs are applied at the point in time in which all shockwaves are, on average, furthest from the hotspot. Unlike SABCs, which encompass the shock fronts, STIBs are imposed between all shockwaves and the area of interest, as shown in Figure 4.2. STIB regions are required be at least as wide as the cutoff distance for all particle-particle force interactions and should have a density that is roughly that of the bulk shocked material, where the STIB is preferably made from bulk shocked material. The LAMMPS implementation for STIBs is shown in Appendix A.

The molecules contained between STIBs are fully dynamic, treated as the same flexible molecules as before STIBs are applied. Therefore, material between STIBs evolve in a uniform field that is equivalent to the shock conditions. Any material that is exterior to the STIBs is unable to interact with material between the STIBs and can therefore be removed. This can meaningfully increase the computational efficiency for massive all-atom shock simulations, which scale $\mathcal{O}(N)$, if the area of interest is small compared to the original simulation cell. As shown in Figure 4.2(a), for the collapse of a 40nm diameter cylindrical pore, the two STIB regions are defined as 3 nm

thick slabs with molecularly rough boundaries at approximately 10 nm from the top and bottom of the hotspot.

The primary advantage of STIBs over SABCs is that STIB regions can be any shape. The only true requirement is that the region of interest be encapsulated by traps/boundaries such that it cannot interact with external regions. For the circular hotspot case, a single STIB, that is defined as a cylindrical shell that encompasses the hotspot and its surroundings, could also be used. This would make the distance from hotspot to boundary more constant for all directions. Parallelepiped-shaped STIB systems would be a useful route to trap individual shear bands or other large structures such as grain boundaries.
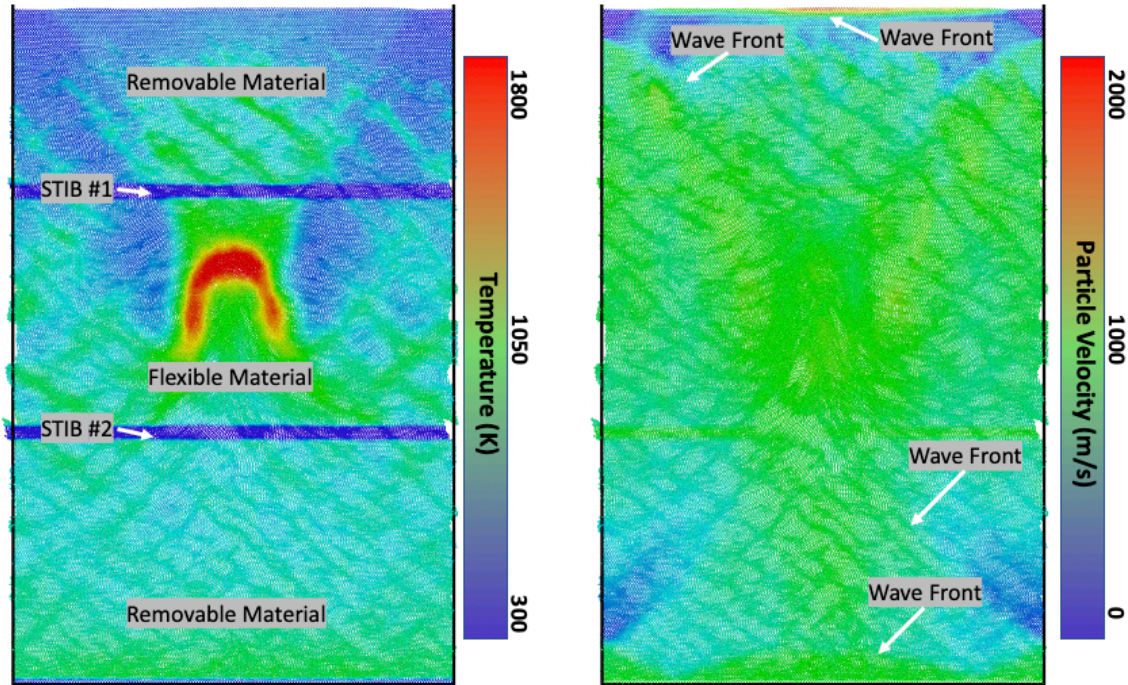
Figure 4.2: STIB example in which the left panel shows the temperature map from a 40 nm pore collapse in TATB following a 2 km/s particle velocity shock. The two frozen regions are the STIB regions and prevent interactions between the internal and external regions. The right panel shows the same frame colored as particle velocity to show the 4 wave fronts, which are the original shock, the re-shock from pore collapse, the reverse wave from re-shock, and the relief wave from the expanding collapse of the pore. All 4 wave fronts are well beyond the STIB regions.

4.3   The Potential Energy Hotspot

4.3.1   Energy Localization

For this first results section, analysis will be focused purely on the pore collapse simulation using a cylindrical pore in the (001) orientation shocked at 2.0 km/s, which results in a hydrodynamic collapse and a large, single hotspot, which is corroborated by previous simulations of similar pore collapses [7,61,62,176]. As discussed in Section 4.1, shock induced, hydrodynamic pore collapse results in the upstream surface expanding into the pore at high velocity followed by a subsequent impact along the downstream surface. In this specific case, the collapse incurs additional shear deformation around the hotspot, leading to an amorphous structure with temperatures of ~2000 K. STIBs are applied at 27.5 ps after total volumetric collapse of the pore.

The hotspot temperature field, where temperature is the molecular vibrational temperature that has been locally smoothed (see Section 3.1), exhibits a crescent shape distribution immediately after collapse, shown in Figure 4.3. The increase in local KE also increases local PE, which is expected from the equipartition theory [153]. Additionally, PE increases due to local plastic deformation and disorder. While the crescent shape of the KE hotspot is eventually the shape of the PE hotspot, the PE hotspot is 'hotter', larger, and exhibits a variety of other shapes directly following the collapse. The rise is PE is manifested in intra-molecular PE, which signifies the root cause of this energy rise, in addition to equipartition, is intra-molecular strain. This strain can occur by strain of covalent bonds or many-bodied deformations that alter the molecular shape.

The inter-molecular PE field, which is controlled by pressure and molecular disorder, is mostly homogenous, with texture at early times due to acoustic waves generated by the pore collapse. Hence, most of the excess PE, with respect to equipartition, is intra-molecular, not inter-molecular. Hence, this PE is mainly stored in vibrational DoFs and is therefore readily available for influencing chemical decomposition. This excess PE is a plausible explanation for why hotspot kinetics in dynamical hotspots are considerably faster than pure thermal kinetics. Additionally, this is a nearly instantaneous rise in intra-molecular energy, especially compared up-pumping [26,27], which is described in Section 1.2, and is a well-defined but lengthy process, on the order of 10s of picoseconds.

The crescent shape of the KE hotspot seen here is a manifestation of the mechanisms of collapse. The hydrodynamic collapse, which expands and recompresses material on the

downstream face, leads to the hotspot 'core', which is the circular region at the top-center of the hotspot. Shock focusing [166,167] leads to significant shear deformation along the sides of the pore, which forms the two 'legs' of the hotspot. The KE field relaxes to this steady-state crescent shape within the first picosecond of collapse. Over long timescales, the crescent shape become more circular and fades in magnitude due to thermal transport [75,177] and a lack of reactions in the nonreactive potential used here. The PE hotspot starts as a more robust localization of energy, which a circular shape and localizations behind the hotspot core where plastic flow occurs. This PE hotspot evolves dramatically over the first 5 ps (post-collapse) before forming a more crescent like shape. This decoupling between the two hotspots, KE and PE descriptions, displays a lack of local equilibrium in the hotspot which may form path-dependent thermomechanical states that incur mechanochemistry or non-equilibrium reactions.

The initial chemical reactions within the shock induced hotspot from Ref. [61], which is of similar size and temperature to the hotspot formed here, occur almost immediately, and exothermic reactions occur within ~40 ps of the collapse, causing a steady state deflagration to occur. The highly strained molecular configurations and the excess PE persist for timescales past 100ps post collapse. Hence, the deformed molecules will not have relaxed prior to the initiation of chemical reaction and will heavily influence it. Hotspot mechanochemistry will be fully explored in Chapter 5 by applying the results seen here to reactive MD simulations.
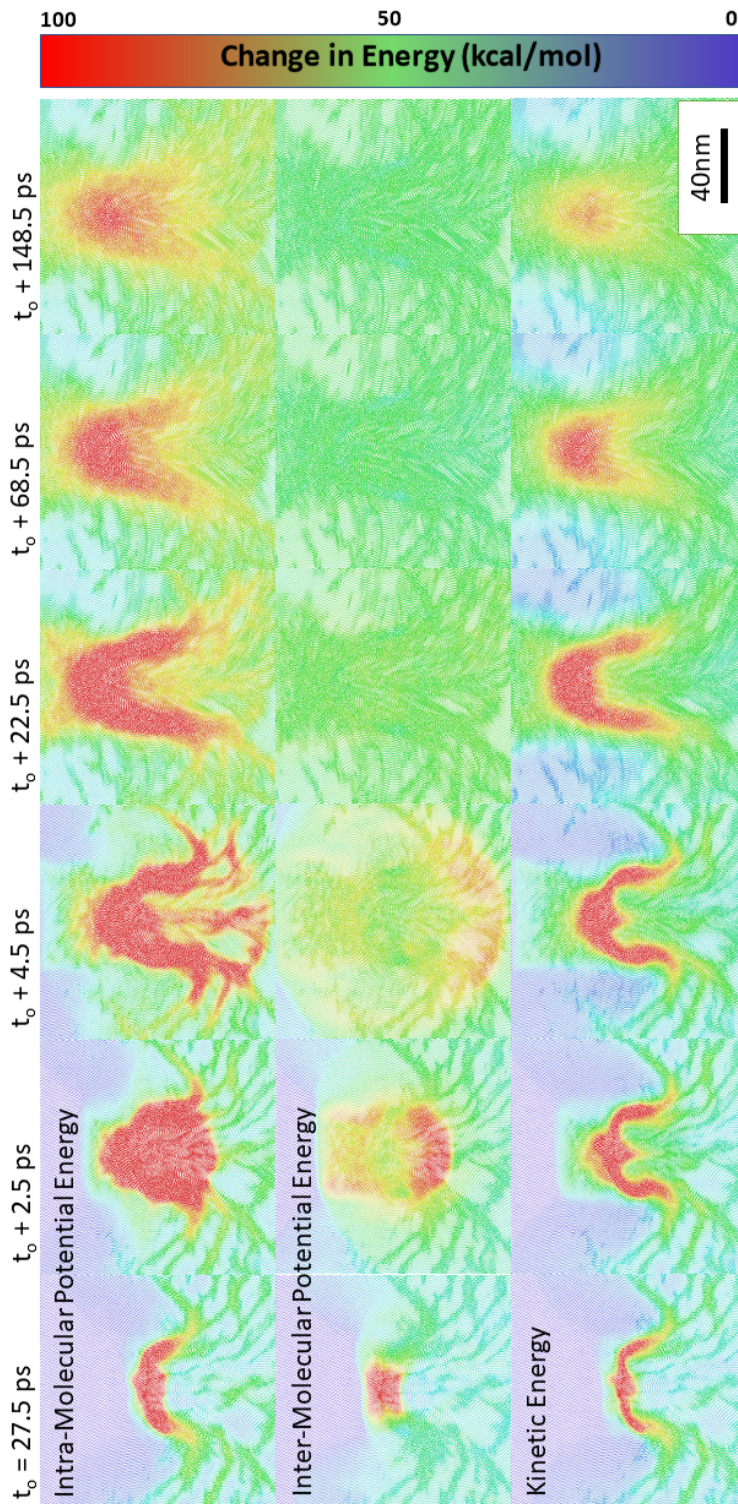
Figure 4.3: Trajectory snapshots rendered with the OVITO software package46 showing the temporal evolution of the hotspot in terms of KE (temperature) and PE (separated into intra- and intermolecular terms). Time t0 represents complete volumetric collapse of the pore. Change in energy is measured with respect to perfect crystal at 300 K and 0 GPa. The black circle in the top left frame represents the initial pore size and location.

4.3.2 Hotspot Relaxation

While the heat maps of Figure 4.3 provide excellent insight into how the hotspot forms and evolves in time, a numerical representation will allow for better comparison between the KE and PE descriptions and to explore their temporal evolution more explicitly. Hence, the function A(E), which is a cumulative distribution of the total area that possesses an energy that exceeds a cutoff value of E, is defined for each hotspot at various times. By calculating this A(E) for a continuum of energy levels from unshocked levels to the hotspot peak, an overall Energy vs Area cumulative distribution is generated. The functions are calculated from fields by discretizing them with a Eulerian binning with square bins of area equal to 6.25 nm^2 and are shown in Figure 4.4. The PE hotspot is numerically shown to possess more total area, for any given cutoff energy level (note the x intercept values), and it has a higher peak energy level than the KE description. The evolution of the distributions over time also reveals that the PE hotspot persists for longer times, such that the peak value of the KE distribution decreases a factor of approximately 1.5 times more than the peak value of the PE distribution over the 120 ps analyzed here.

The processes that govern the transition to deflagration are typically chemical kinetics and heat transport. Therefore, it is critical in determining the overall shock response of heterogenous HEs to understand and be able to model the temporal evolution of hotspots. A hotspot's KE fields are well described via the heat equation with well parametrized material constants such as thermal conductivity [75]. However, the base physics and materials science mechanisms that govern the temporal evolution of the hotspot's PE fields are not inherently obvious. These changes in local PE are most likely controlled by fundamental processes such as molecular conformational changes, plastic flow, and pressure fluctuations.
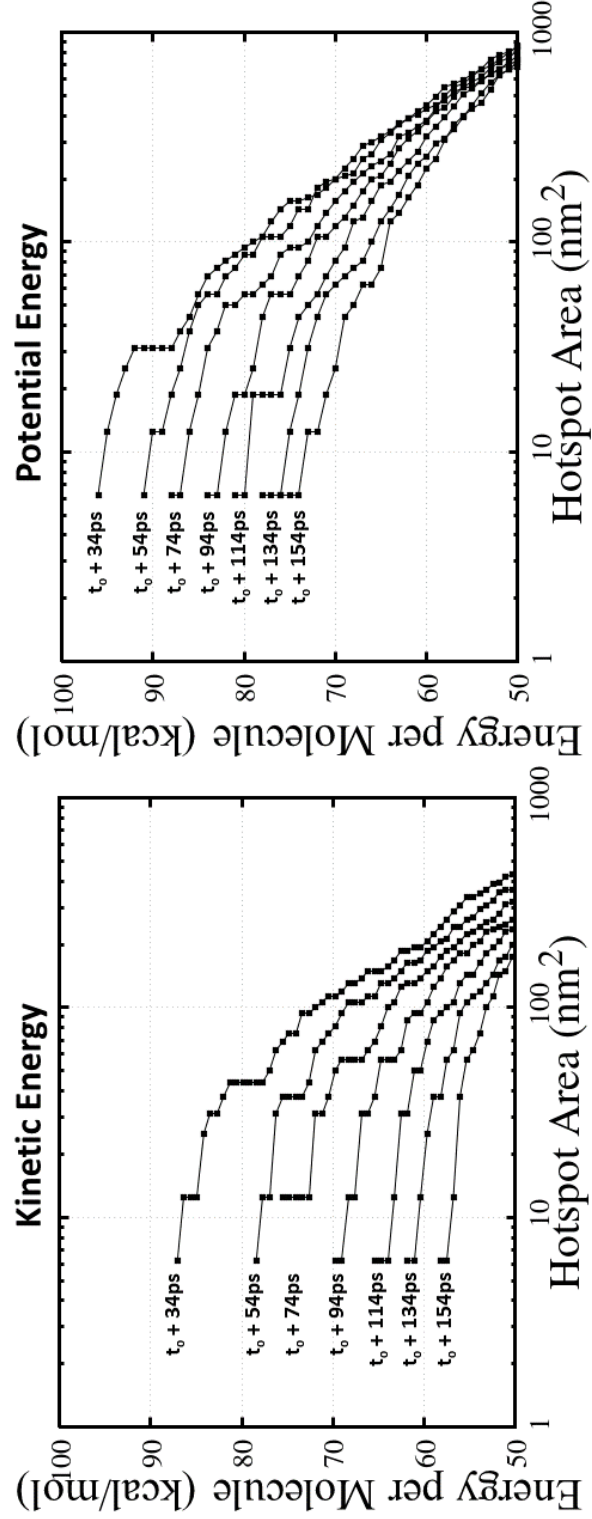
Figure 4.4: Energy-size distributions within the hotspot for KE and PE rises, with respect to the bulk shocked material. Areas are first discretized with an Eulerian binning process in the plane of the hotspot.

The time evolution of the difference in the PE and KE increase, i.e., the PE in excess to equipartition, was tracked for the length of the simulation in each molecule to assess the level relaxation that occurs within the intra-molecular strain, which directly relates to the amount excess PE. Only molecules within a defined hotspot region are assessed, and they are additionally grouped into 4 bins based on their degree of internal strain at 5 ps after total collapse (t_o +5 ps), see Figure 4.5. The degree of internal strain of the planar TATB molecule will be described with the I_2/I_1 metric, which is described in Section 4.2.1. I_2/I_1 has a minimum value of 1.0 and an equilibrium value, due to thermal fluctuations, of ~1.07. Molecules above 1.5 experience deformations that would most likely incur prompt bond breakage if the forcefield allowed for such events. Molecules are binned in groups with I_2/I_1 ranges of 0.25, from 1.25 to 2.00 and up.

If equipartition holds, the average PE decrease should be equal to the average KE decrease during thermal conduction, if no intra-molecular strain relaxation occurs. Figure 4.5 shows that for each group of I_2/I_1, the time history of $\Delta PE - \Delta KE$ decay is mostly flat, with minor decrease at early times (>10 kcal/mol) most likely related to acoustic relaxations around/near the hotspot. This indicates that, beyond the equipartition effect, there is negligible relaxation of molecules with large, intra-molecular distortions. The excess PE here is a latent component of the energy, and this latent energy, mostly derived from molecular strain, experiences negligeable relaxation on time scales of KE relaxation within and around the hotspot. The molecules with the highest latent PE are those corresponding to the brown and blue curves of Figure 4.5. Large latent PE relaxations would manifest in significant negative slopes for these curves, causing them to approach the values of the red and black curves.

The temporal extend of this latent PE is crucial for understanding hotspot criticality, as it survives as an excess energy well beyond the timescales of chemical initiation for typically high explosives at hotspot temperatures, those above 2000 K [29,178–181]. Hence, this latent PE, which has magnitudes on the level of the activation energy of condensed phase EMs. Figure 4.6 shows the individual contributions of PE and KE to the time histories in Figure 4.5. The wide span of the PE curves, with respect to the KE curves, and the increased spacing of the PE curves with increased deformation, shows the general relationship of the latent PE and the molecular deformation, corroborating the hypothesis of the root cause of the latent PE. Additionally, the nearly identical slopes of the PE decay in all four I_2/I_1 bins adds additional validation to the idea that nearly all of the energetic relaxations in the hotspot are thermal. While the two analysis

performed in this subsection have shown significant power at understanding the evolution of the latent PE over time, they lack a spatial understanding of the localization, which can greatly influence the energy balance needed for a critical hotspot [39].
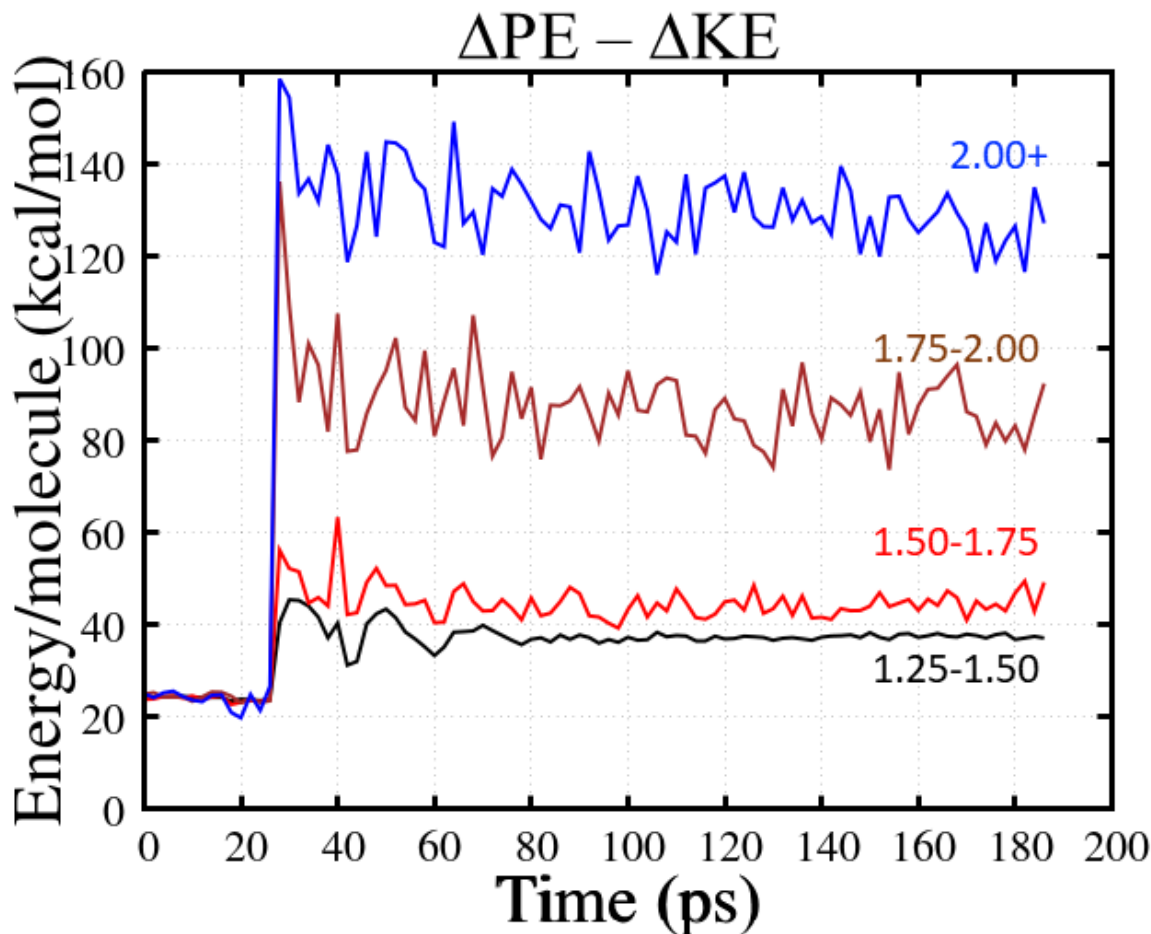
Figure 4.5: Time history of $\Delta PE - \Delta KE$ within the hotspot and its surrounding area where the increment is with respect to the bulk shock. The hotspot area is a 25 nm radius cylinder, centered at the hotspot center. Molecules in each curve are binned by the ratio of their first and second principal moments of inertia I_2/I_1. N decreases with increasing I2/I1, leading to larger fluctuations at high strain level groups.
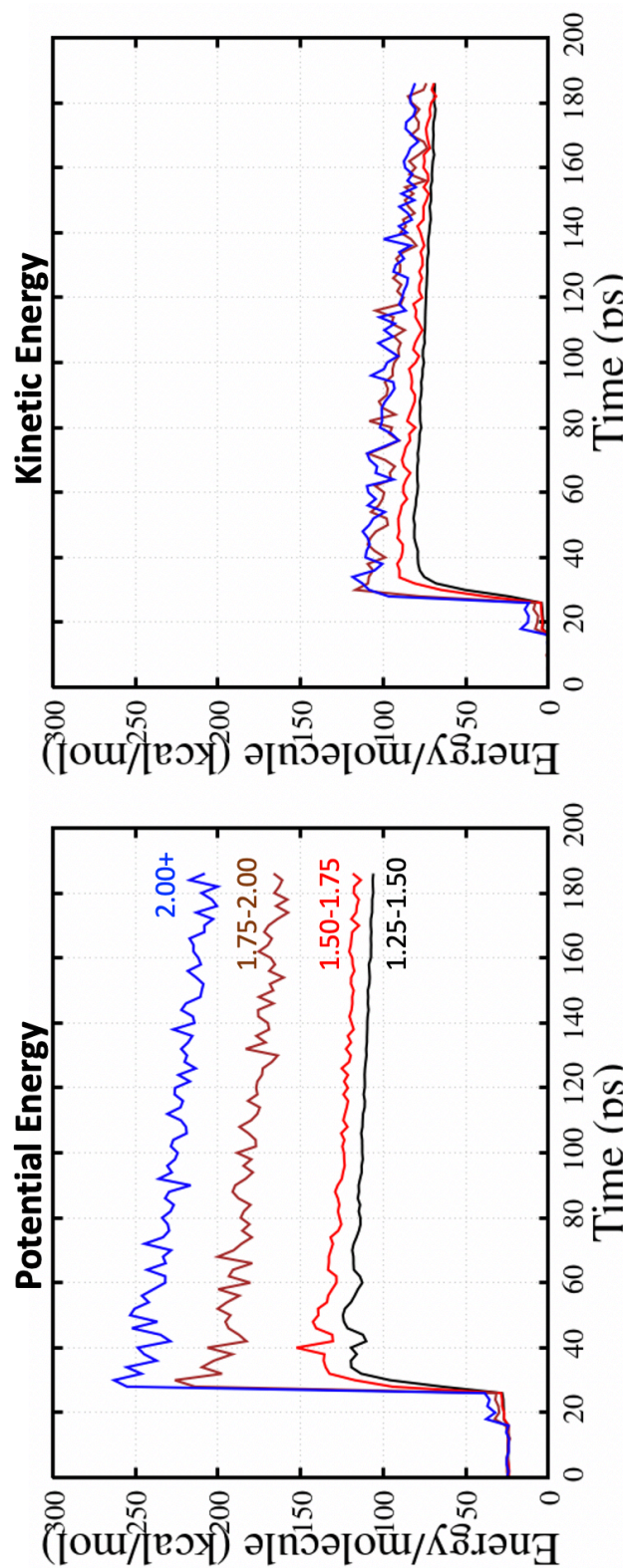
Figure 4.6: Time history of pure PE and KE (total PE and KE rise above 300 K) for all molecules within a 25 nm cylindrical radius of the hotspot center. I2/I1 bins equivalent to those in Figure 4.5.

4.3.3 Spatial Localization

The spatial localization of temperature in hotspot formation has been well studied. However, the previous subsections well establish that the PE hotspot localization is not thermodynamically inference-able from the KE hotspot. This subsection will explore the PE spatial localization with respect to the latent PE and PE distributions. The entire system, at $t_o + 2.5$ ps is binned in a 2D Eulerian binning with a bin area of 6.25 nm^2. Figure 4.7(a) shows each bin's average, absolute PE as a function of its average vibrational temperature. PE(T) curves from a compressed, single crystal sample and a compressed, amorphous sample made via the melt and quench method, both at 22 GPa, are included as bounding cases, shown as blue and red curves, respectively. The scatter of the bins PE-T relation reveals a broad distribution of PE states for a given temperature, when at high temperature values which most likely corresponds to the hotspot. These points follow a trend that is decidedly unlike either of the static samples: crystal and amorphous. The absence of a direct, one-to-one PE temperature relationship provides further proof that the hotspot state cannot be uniquely defined by its kinetic energy alone, as has been done for a majority of the existing literature. Interestingly, the distribution appears such that even a two-phase model that utilizes a mixture of crystal and amorphous could not fully capture the underlying local complexity of the hotspot.

The bins are arbitrarily grouped based on PE(T) locations (see Figure 4.7(a) color scheme) and mapped into cartesian space, which is displayed in Figure 4.7(b). Spatially, these clusters group into physically definable regions, with the black points being the unshocked material, the purple points becoming the region shocked by only the elastic precursor wave, and the orange region which is areas shocked by the plastic wave, which is the last wave generated from the initial impact. The last two zones, which are the high and low temperature sections of the highly disparate PE-T section, correspond to the hotspot and map spatially as a hotspot core (lime) with a surrounding hotspot halo (dark green). It should be noted that the maximum temperature for any of the bins is lower than the melting temperature for the potential used here, predicted to be 3400 K at 22 GPa [182] indicating that the hotspot molecules are solids that have undergone extreme plastic deformation, but are not a liquid. This most likely explains the mechanism that locks in the high intramolecular strain for times longer than thermal transport away from the hotspot: by limiting flow that would allow for the molecules to conformationally relax. Figure 4.8 shows the equivalent to Figure 4.7(a) at later times. These show that as time evolves, the disparity between

the PE and KE, locally as these are binned, lessens considerably. However, Figure 4.9 shows the all-molecule representation of these plots at $t_o + 10$ ps, which shows the continuation of the non-one-to-one trend between the PE-T relationship. Interestingly, Figure 4.9 shows two distinct tails, high PE and high KE. However, no molecules have both a high PE and high KE value. The persistence of the long PE tail, which would be unaccounted for in most chemical kinetics models, will have the ability to heavily influence the reactivity and criticality of a hotspot.

Common and state-of-the-art models used within the framework of continuum and coarse grained simulations describe chemical kinetics in hotspots exclusively in terms of their temperature and pressure, the same as they would pure thermal chemistry [38,46,47,183,184]. These chemistry models may potentially differentiate kinetics models for various phases such as melts but overlook the effects from plastically worked solids that will include a latent PE. The latent PE of the hotspot further complicates the hotspot criticality problem, which is often defined as the race between heat generation via exothermic reactions and thermal transport that can quench the hotspot [59,60]. As the intra-molecular strain will most likely alter the local kinetics within hotspot, and latent PE decay is not apparently governed by the physics of heat transport, this increases the overall complexity of how to define multi-physics phenomena at extreme conditions. As this section focused solely on the pore collapse of a cylindrical pore, at 2.0 km/s, with the (001) orientation, the next section will directly contrast the results for each of these control variables.
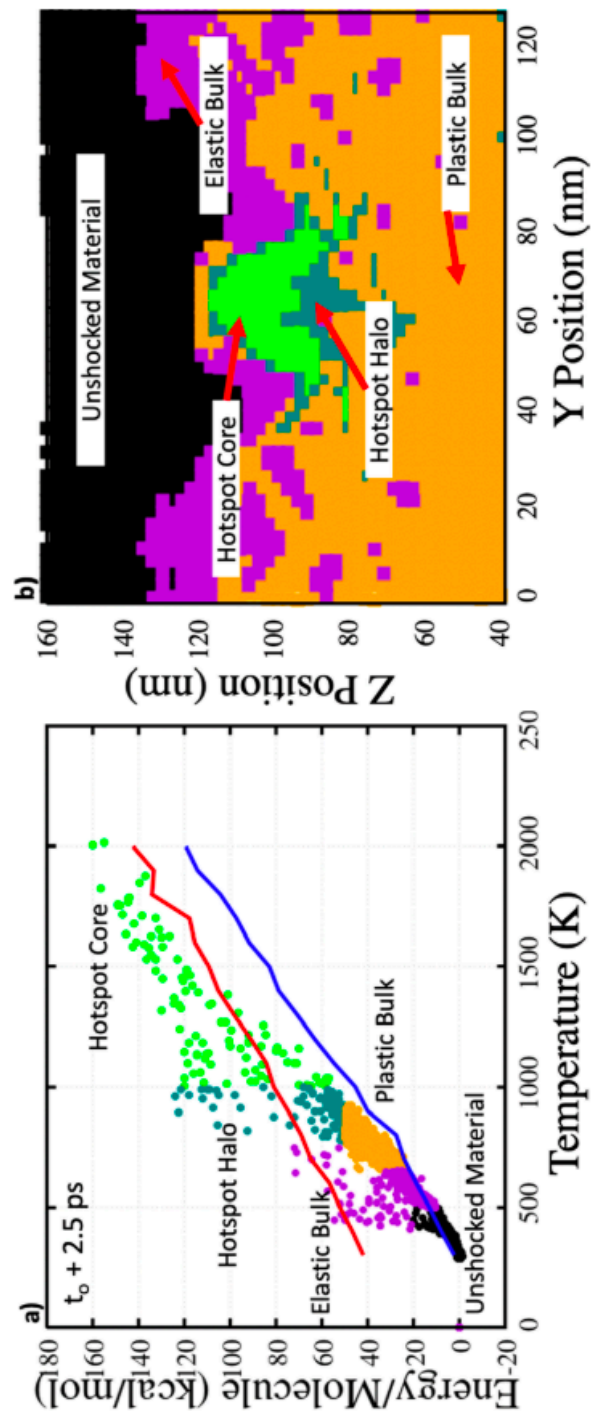
Figure 4.7: (a) PE-temperature distribution (points) compared to isobaric curves for perfect crystal (blue line) and a melt-formed amorphous (red line) system. (b) Cartesian mapping of each bin, clustered arbitrarily from PE-T as shown by color scheme of panel a.
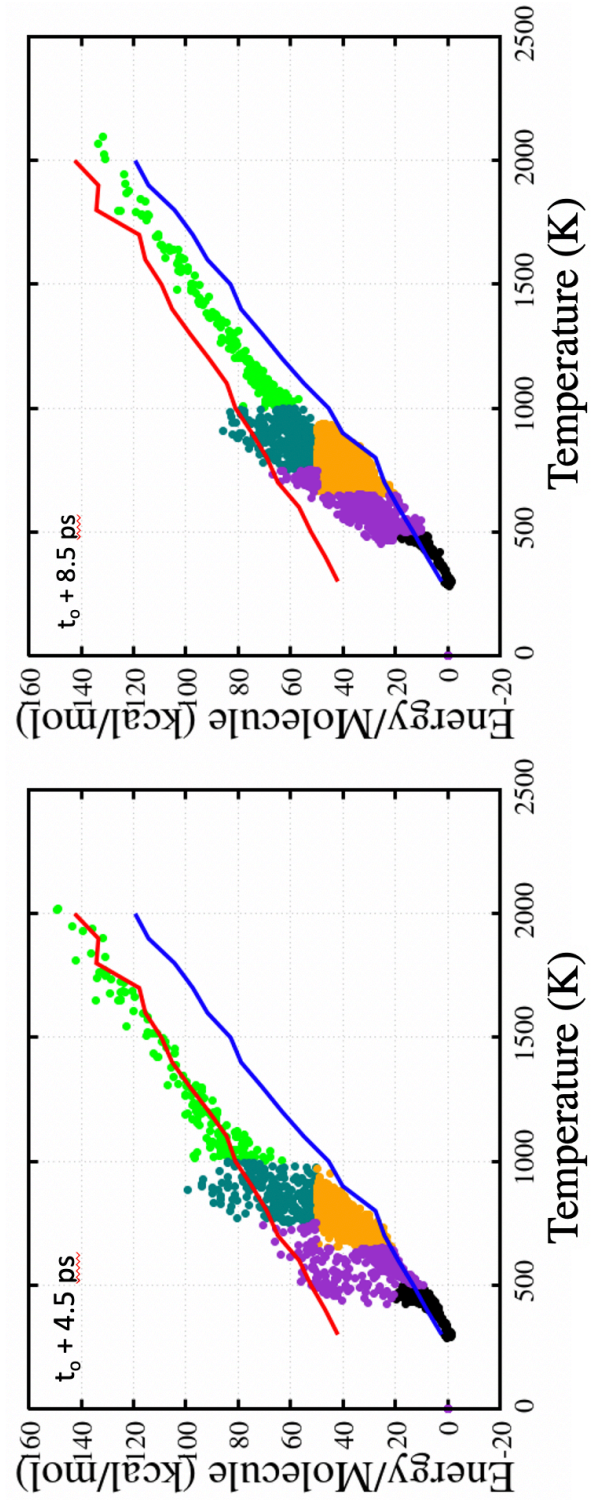
Figure 4.8: PE-T distributions of Eulerian bins, colored and binned identical as Figure 4.7(a), but at later times in the simulation.
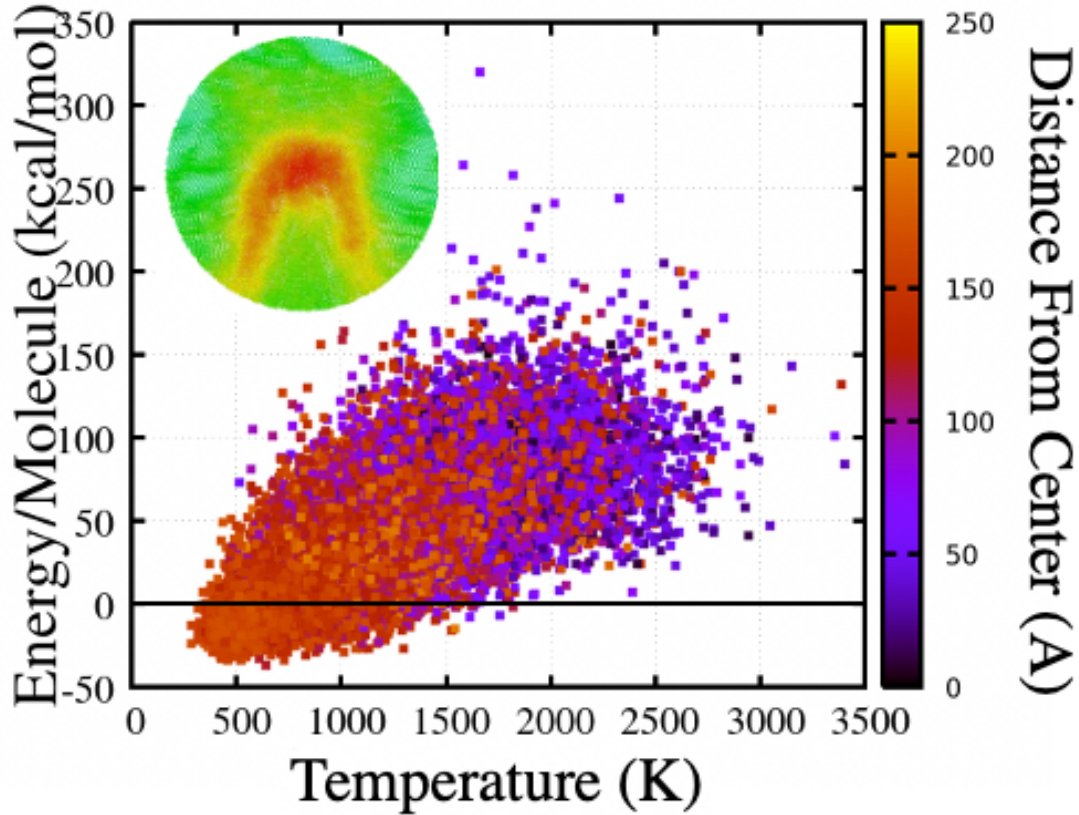
Figure 4.9: All molecule PE-T distribution for $t_o + 10$ ps, showing the high PE and T tails persist in time. Color is distance of molecule from the geometric center of the hotspot core.

4.4 Effects of Orientation, Pore Shape, and Shock Strength

4.4.1 Crystal Level Processes in Collapse

To better understand the potential role of crystal orientation, shock strength, and pore shape on the amount of latent PE in the hotspot, one must first assess the collapse mechanisms in play at the molecular and crystal scales, especially focusing on material structure and deformation during collapse, which will profoundly alter the general size and shape of the hotspot [6,7]. Beginning with assessing only the pores with cylindrical cross sections, see Figure 4.10, crystal orientation has very little effect on the active material deformation processes that occur during collapse (comparing rows 1 and 2 in Figure 4.10). While the shapes of the collapse may be slightly different, the trends of viscoplastic or hydrodynamic collapse are the same. Across each row, comparing for

different shock speeds, the expected results occur, as discussed in Section 4.1, where increasing shock strength drives from a viscoplastic to hydrodynamic response.

In the viscoplastic regime, which is dominant for the weak shocks such as U_p=0.5 km/s, the pores with cylindrical cross sections undergo a mostly lateral collapse process that is dominated by plastic flow. Typically, static, compressive stresses on/near the pore surface, that endure after the passage of the shock, drive the viscoplastic collapse [165]. The hydrodynamic regime, which becomes dominant for stronger shocks, is driven by the shock and occurs on time scales similar to the passage of the shock, where the shockwave drives the upstream face of the pore into the void, rapidly expanding it. Often, for this collapse process to occur, the material strength is dwarfed by the considerably larger shock induced stresses. It is this lack of strength assumption that allows hydrocodes, which treat all material as a fluid, to accurately model shock compression of solids [7,185].

As visible in Figure 4.10, the material accelerated off of the upstream face of the pore in the (100) shock at 2.0 km/s appears highly disordered, with no defined, periodic structure. Most likely, this occurred due to the significant plastic flow that is mediated by shock focusing during the hydrodynamic collapse [166,167]. Interestingly, for the collapse of the (001) oriented system, the collapsing material retains structure of the basal planes, albeit highly deformed, despite being in what should be a hydrodynamic regime. The (001) orientation of the crystal is highly compressible compared to the (100) case, with $C_{11} \cong 3.4 C_{33}$. [68,186]. In the collapse along (001), the graphitic sheets (commonly referred to as basal planes) undergo significant deformation in which intra-layer sliding and non-basal gliding defect mechanisms, discussed in Section 1.4, are activated. Additionally, significant plane buckling occurs, but the individual planes remain intact via the inter-molecular hydrogen bonding. The (001) orientation has a unique mechanical response in which a very limited amount of slip systems can be activated in order to nucleate plastic deformation [70]. At high pressure conditions, this lack of plastic slip aggregates with considerable instabilities that prevent significant amounts of dislocation motion [187]. This often forces the dominant plastic deformation mechanism to be shear banding [51,69,188]. Nanoscale shear bands can form within the bulk shocked region without prior defects in order to alleviate the considerable deviatoric stresses formed [189,190] and can act as hotspots on their own, raising the temperature of material surrounding a hotspot and accelerating local chemistry at detonation conditions [51].
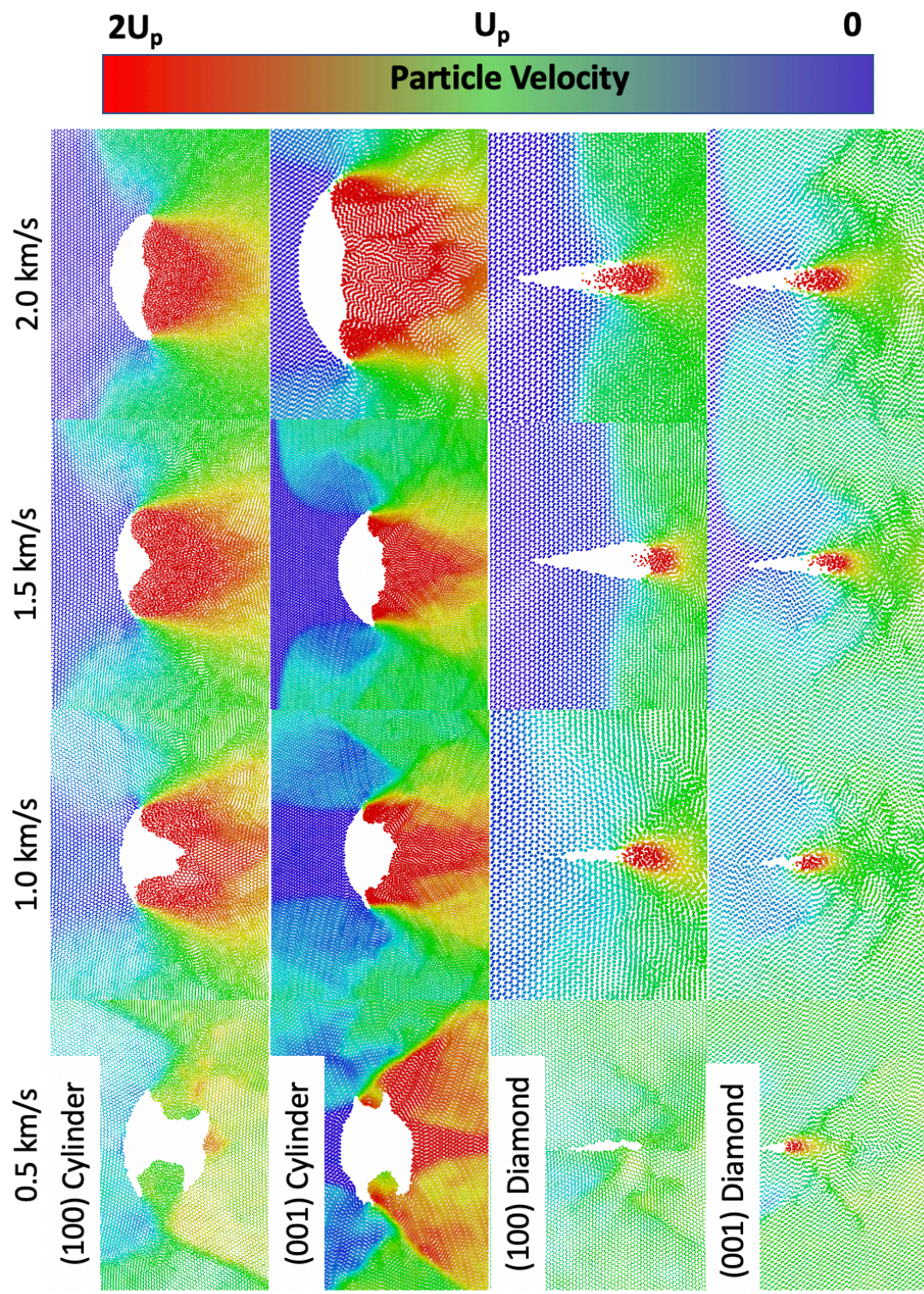
Figure 4.10: Heat map of particle velocity (velocity vector component in the shock direction) during the collapse, shown with molecular resolution. Each row corresponds to a defect shape and TATB orientation. Each column corresponds to a shock speed.

Figure 4.11 displays the molecular center of mass radial distribution function (RDF) for material that enters the void space during collapse, both the (100) and (001) orientation. This is done both pre- and post-total volumetric collapse to analytically assess the local structuring of material for the 2.0 km/s shocks. The pre-collapse panel, Figure 4.11(a) also displays the RDF for a shocked TATB crystal at the same shock strength as the pore collapse, but in an initially defect free area. This shocked crystal, however, does include numerous crystalline defects, which overall broadens the peaks with respect to the perfect crystal.

The distinct peaks in the pre-collapse (001) RDF and the amorphous structure for the (100) RDF analytically confirms the previously discussed structural differences in the collapsing material: the (100) collapse results in amorphous material expanding into the void, as is shown in the rendering in Figure 4.10, while the (001) expands material that retains an overall structure that is similar to the perfect crystal, but highly deformed. However, post-collapse, both hotspots are in an amorphous state with little to no overall structure (Fig. 4.11(b)), indifferent of the during-collapse structure. Overall, the varying paths of deformation for collapse and the disparate plastic flow between the (100) and (001) hydrodynamic collapse will most likely lead to different shapes and sizes of hotspots and potentially significantly different latent PE.
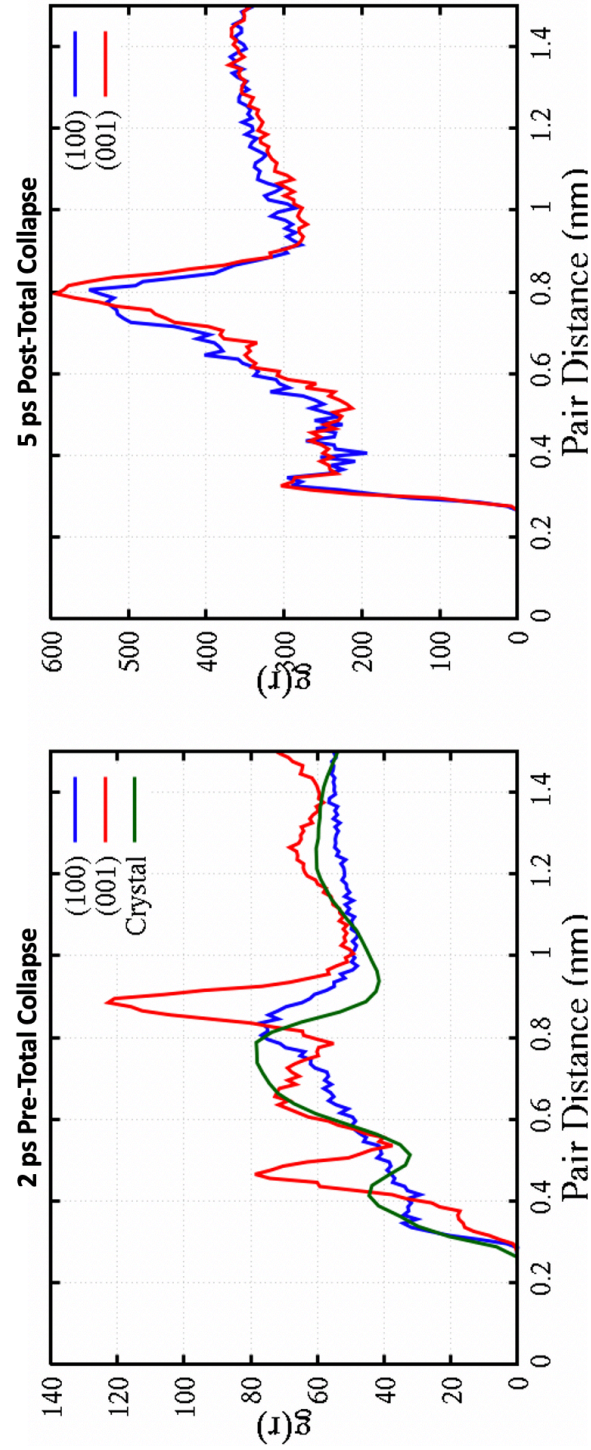
Figure 4.11: Molecular center of mass radial distribution functions for material in the hotspot for 2.0 km/s shocks of cylindrical pores in both orientations. Panel a shows the RDFs before total collapse of porosity, i.e. the RDF of the collapsing material mid-collapse. Panel b is post collapse. The green line in the pre-collapse panel is from the shock crystal in the (001) case, far from the pore, prior to collapse.

As discussed above, the viscoplastic mechanism for the cylindrical cross section, which is activated by weak shocks, experiences a collapse driven by deformations that are mediated by plastic flow to remove high deviatoric stresses in the surrounding material. In the case of pores with diamond shaped cross sections, weak shocks are also dominated by viscoplastic collapse that is manifested in a lateral collapse of the pore. However, these diamond pores, which feature a high aspect ratio, have a much smaller volume than the cylinders and simply close without significant plasticity, as the necessary change in volume in much lower and significantly less strain is needed in the collapse direction. Hence, the resulting hotspot in these cases is almost indistinguishable from the surrounding shocked crystal, as there is almost no additional energy rise, either thermal or latent. Where the hydrodynamic collapse would be the dominant mechanism in cylinders, the diamond pores undergo a collapse process that is driven through gaseous ejection of molecules into the void, or 'jetting', from the upstream tip of the diamond.

To alleviate the shock pressure, shocks at free surfaces will cause material to expand into the surrounding vacuum. From conservation of momentum, this expanding material travels at a velocity of $2U_p$ if the surface is flat [5]. When the surface is not flat, as is often the case with 2D and 3D microstructural defects, the phenomena of shock focusing can localize significantly more energy locally in the material near high curvature areas and results in ejecta velocities at or above the shock velocity [6,166,167]. In TATB, which has significantly anisotropic elastic and plastic responses of the crystal with respect to the orientation of the basal planes [69], the shock focusing effects could easily create noteworthy differences in the mechanism for jetting and amount of ejecta for the (001) and (100) cases. However, as can be shown from inspection of Figure 4.10, nearly equal levels of ejecta are created in the (100) and (001) pores with diamond cross sections.

In the 2.0 km/s shocks of the two orientations with diamond pores, the location of the shock front, relative the lead molecules in the jetted plume, is highly disparate. For the shock in (100), the ejecta expands quickly and outpaces the shockwave moving along the side of the pore, which can be viewed as the sharp interface between blue and green regions in Figure 4.10. The response is the opposite for (001) in which the front of the ejecta plume is always behind the plastic shock front, both at early times and near total volumetric collapse. In both orientations, the ejecta molecules have a range of velocities greater than $2U_p$. These are roughly from 4 to 6 km/s and from 5 to 7 km/s for the (001) and (100), respectively. However, the relative increase of ejecta

velocities with respect to the shock velocities is not the primary reason for the difference in shockwave to ejecta locations in the different orientations.

Figure 4.12 displays the velocity wave profiles (particle velocities) for all shock speeds and orientations used in this chapter, where molecular COM V_z is exactly equal to U_p in this case. Both orientations can be seen to have an elastic-plastic wave structure in Figure 4.12. The (100) has an elastic wave that initiates a particle velocity of approximately 0.2 km/s for all impact speeds. This also leads to no discernable shock pressure rise in the bulk material. Conversely, the elastic wave for (001) shock with impact velocity of 2.0 km/s initiates a particle velocity of 1.4 km/s, which creates considerable stress in the crystal. Both cases, the second, plastic wave has particle velocity of 2.0 km/s and pressures of 23.5 GPa and 26.5 GPa, for (001) and (100) respectively, which is well characterized in Ref. [9].

For (100), the plastic wave initiates all collapse mechanisms, including jetting and any lateral relaxations. This allows for the ejecta, which moves on the order of the shock velocity, to rush out in front of the wave and fully expand into the volume of the pore. However, in the case of the (001) orientation, the elastic wave generates enough pressure in the surrounding crystal to initiate a lateral relaxation, analogous to a viscoplastic type collapse, but does not initiate any jetting mechanisms prior to the plastic wave reaching the pore. Once the plastic wave reaches the upstream tip of the diamond pore, jetting begins to occur, and material expands into the void space. In this course of events, the lateral collapse mechanism is initiated well before any ejecta can form. This allows for the viscoplastic closure of the pore to "choke off" the ejecta, limiting its volumetric expansion and creating total volumetric collapse of the pore prior to the upstream expansion of the pore being able to recompresses the ejecta on the downstream face of the pore. It is this gaseous recompression that is known to lead to extreme thermal energy localization in hotspots [6,45,162,191]. This gaseous expansion and recompression mechanism is in full effect for the (100) case, but the lateral collapse of the (001) prevents it almost entirely. Figure 4.13 shows molecular level renderings of these two collapse processes for times before, during, and after jetting occurs.

Between the different structures in the hydrodynamic collapses of the two cylindrical pores, the lateral collapse effects on jetting in the two diamond shaped pores, and the various differences in mechanisms activated between pore shapes, both the orientation and shape can be expected to greatly influence the hotspot formation. The next section will focus on how these collapse

mechanisms relate to the level of energy localization in TATB hotspots, both for the thermal and latent energy contributions (total energy and excess PE) to attempt to better understand hotspot formation as a whole, as well as understand the necessary mechanisms to maximize the amount of latent PE in a hotspot.
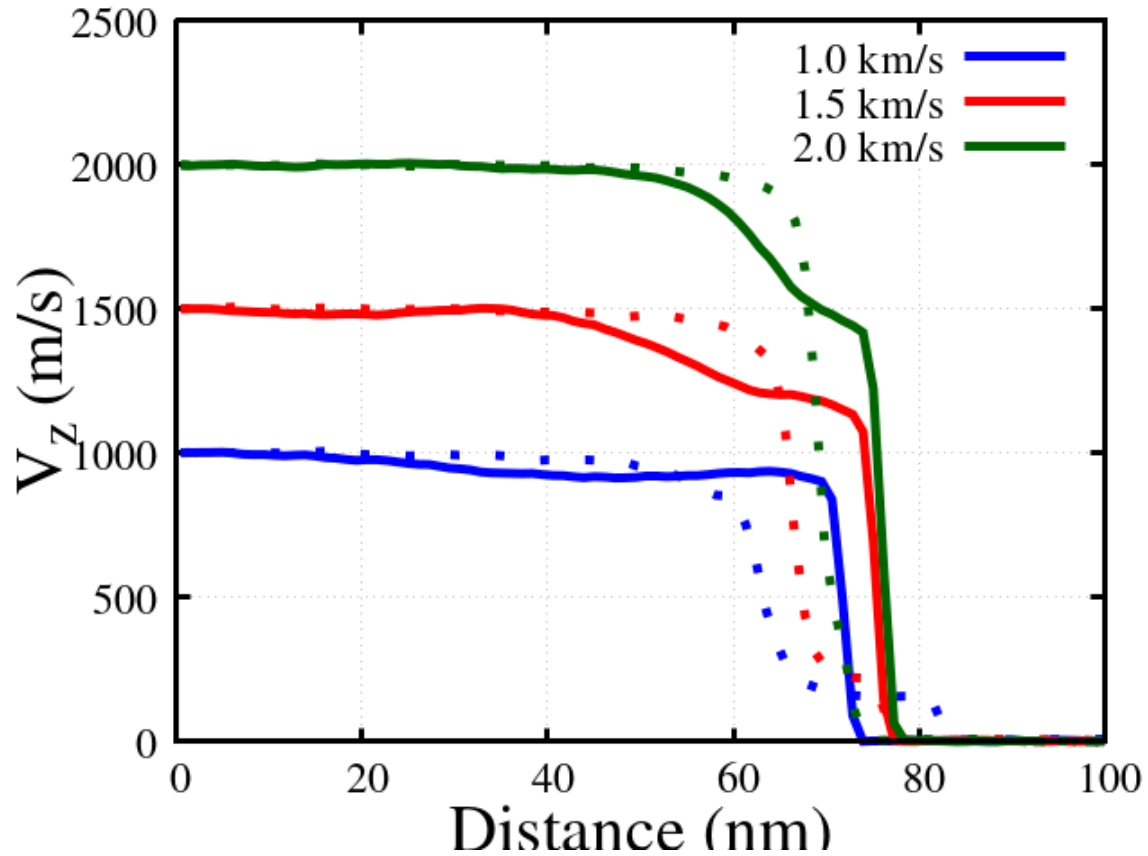
Figure 4.12: Particle velocity wave profiles for the shock waves in both TATB orientations for 1.0-2.0 km/s. Dashed lines represent (100) orientations and solid lines are (001) orientations. All profiles are taken at times before the shockwave reaches the upstream face of the pore.
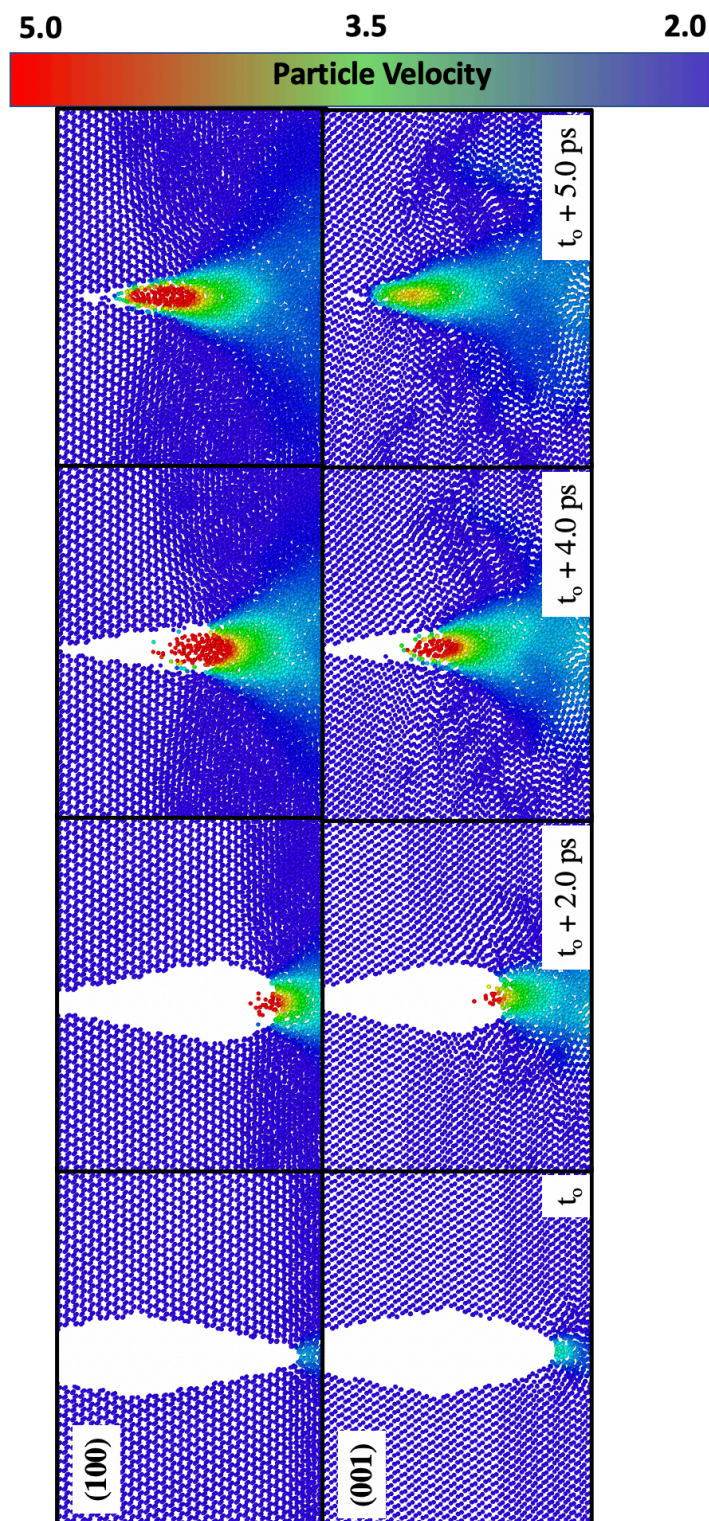
Figure 4.13: Time evolution of molecular centers of mass for the two diamond pore 2.0 km/s shocks in the (100) and (001) orientations, where color is particle velocity and t_o is the first frame in which the shockwave begins to accelerate molecules at the upstream face of the pore (initiation of ejecta).

4.4.2 Hotspot Formation

Heat maps of all hotspots generated from the pore collapses can be found in Figure 4.14, rendered with molecular level precision, and are colored either by KE (in the left columns) and PE (in the right columns right), where each set of columns represents a different particle velocity. Since they produce no latent energy for any case and produce no excess energy localization at all for the two diamond shaped pore systems, the $U_p = 0.5 \ km/s$ were omitted from the hotspot analysis. The upper bound of the color bar in Figure 4.14 is a variable and is dependent on the given U_p for each set of shocks. Hence, this upper bound is 100, 75, and 50 kcal/mol for particle velocities of 2.0, 1.5, and 1.0 km/s, respectively. Orientations and defect shapes are separated by rows.

Prior to assessing the individual hotspots, it should be noted that, outside of the hotspot, there are significantly higher shock temperatures in the bulk for (001) shocks, as compared to (100), where, for (001), $U_p = 2.0$ km/s leads to a shock velocity of 7.0 km/s and a temperature increase of 770 K. However, in the (100), there is a shock velocity and shock temperature of 6.2 km/s and 650 K, respectively. Since the (001) orientation localizes energy in shear bands, which the (100) does not, excess temperature in generated due to plasticity in the bulk, where shear bands are typically characterized as hotspots on their own. Additionally, there is significant anisotropy of the bulk PE field away from the hotspot, with much higher intramolecular PE for the (100) case, which is colder and has less localized plasticity in the bulk.
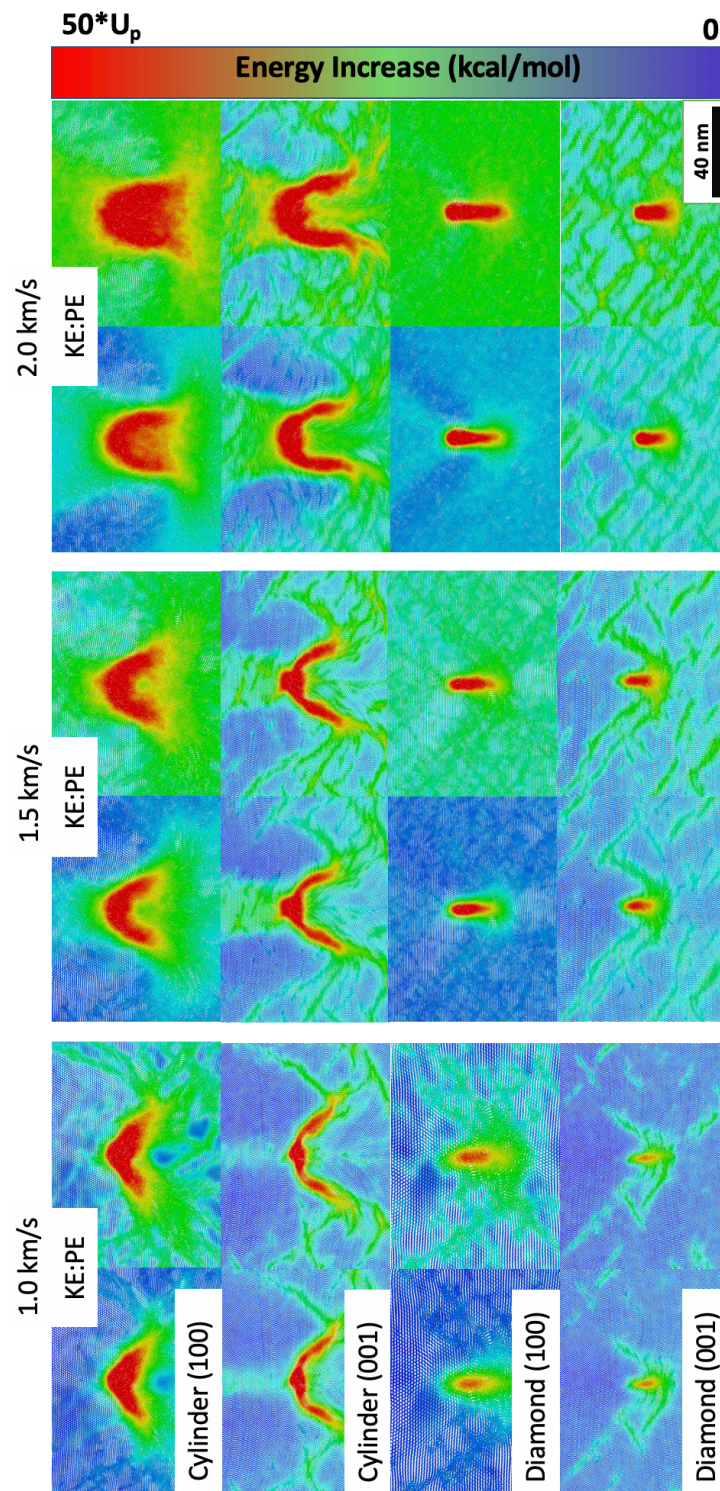
Figure 4.14: Heat maps with molecular resolutions of all hotspots at t_o + 5ps, colored in units of energy. The left columns of each set are kinetic energy, and the right column of each set is potential energy. Each set of columns represents a particle velocity. The color bar is relative with the upper bound related to the impact velocity (maximum color bar value is 50, 75, and 100 kcal/mol, for 1, 1.5, and 2 km/s respectively).

As was previously done in Figure 4.4, a distribution of the area (A) of the hotspot with temperature greater than a cutoff temperature value T (or energy 'E') is plotted in the T-A space, see Figure 4.15. The left panel of Figure 4.15 shows the T-A distributions for both orientations with cylindrical pores and the right panel shows the T-A distributions for both orientations with diamond pores, solid curves for (001) and dashed curves for (100). Since the shock temperatures in the bulk are different for the two orientations, hotspot temperatures are referenced by the associated bulk shock temperatures, which singles out the effective excess temperature, or the temperature rise due to the hotspot.

As expected in the weak shock regime, diamond pores generally result in smaller hotspots than cylindrical pores since they have a smaller initial area, and the result in lower peak temperatures due to less plastic flow occurring. However, the (100) diamond pore at $U_p = 2.0$ has a maximum temperature significantly hotter than any cylindrical pore collapse. This is most likely due to significant ejecta being able to fully expand and recompress, leading to high peak temperatures, but still a much smaller hotspot compared to pore collapse for a cylindrical pore.

To attempt to remove the hotspot size bias from the disparate initial volumes of the diamond and cylindrical pores, Figure 4.16 shows the T-A distributions for all four of the $U_p = 2.0 \ km/s$ hotspots, with a normalized area, in which the normalizing factor is the initial pore size. In the setting of this normalized area and absolute temperature (not referenced by the shock), the diamond and cylindrical shaped pore's T-A distributions mostly overlap, with the only deviation being from the high temperature jetting response. This result does not track with recent work in HMX, Ref. [6], in which the jetting in the diamond pores resulted in hotspots roughly three times hotter and with significantly larger normalized areas.
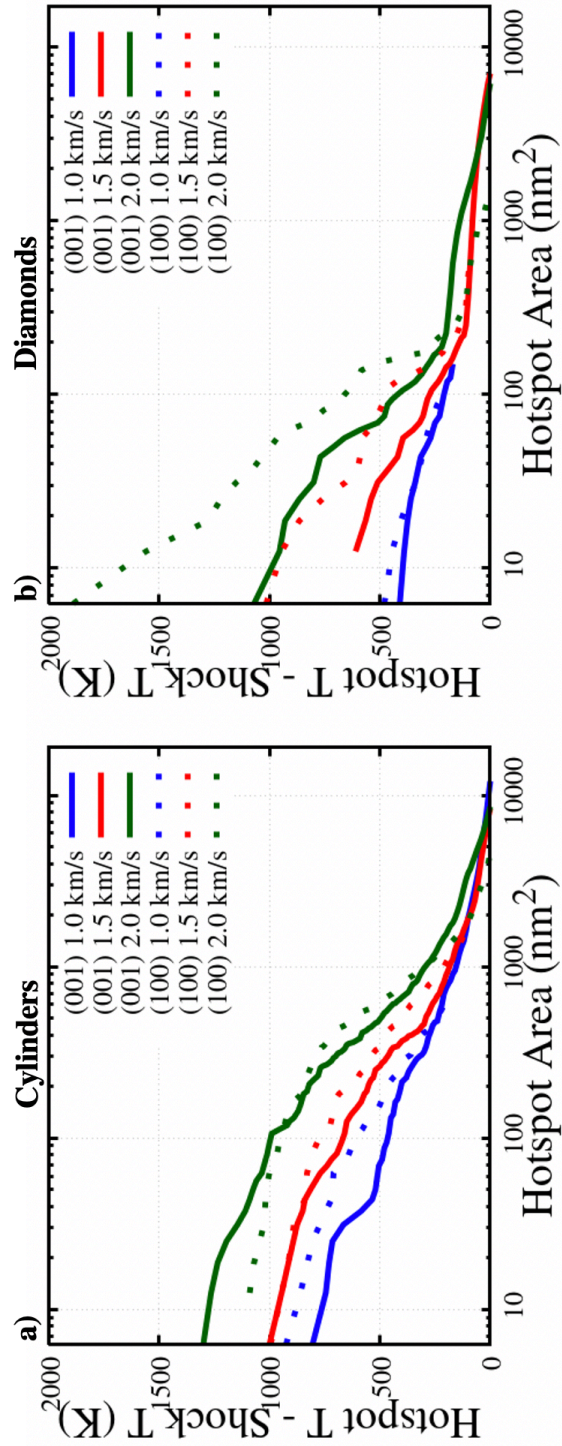
Figure 4.15: T-A cumulative distributions, referenced by the bulk shock temperature, for the cylindrical pores in panel a and the diamond pores in panel b. Dashed lines represent (100) orientations and solid lines are (001) orientations.
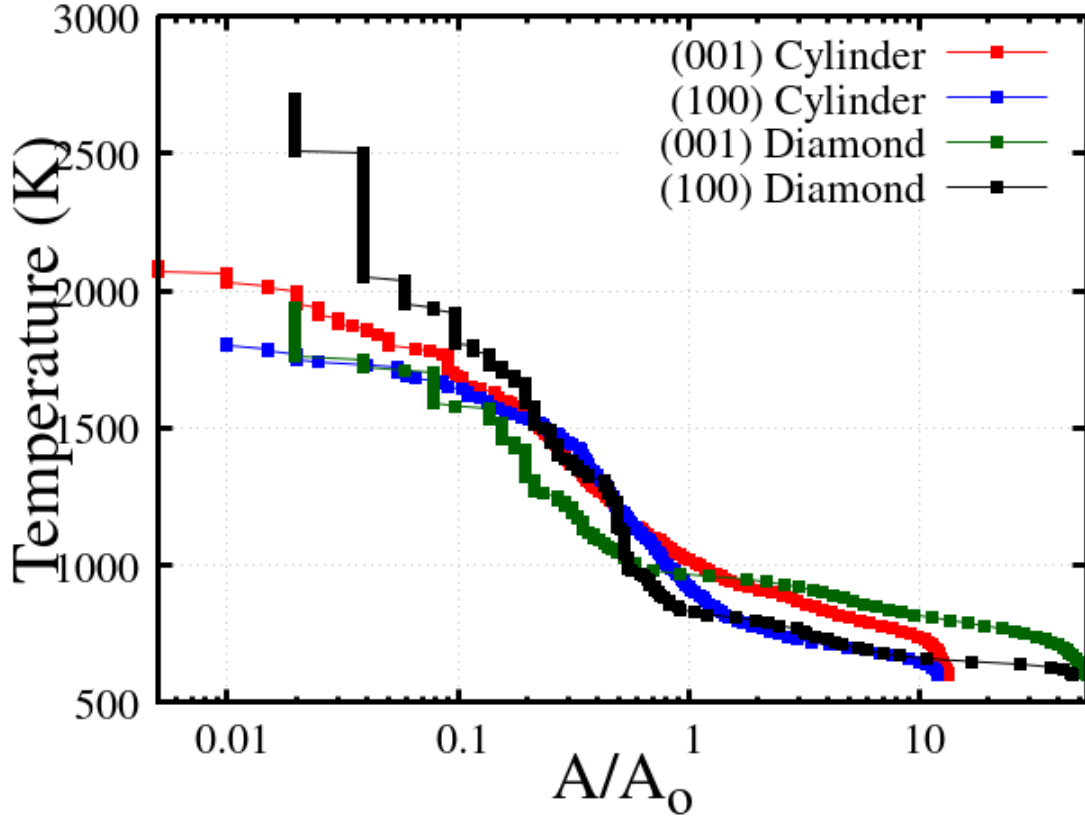
Figure 4.16: T-A distribution plot for all four 2.0 km/s shocks. Temperature is the absolute molecular vibrational temperature (not referenced by the bulk temperature) and the area is normalized by the initial area of the defect.

Since the cylindrical and diamond geometries activate significantly different collapse mechanisms under shock loading, the effects of orientation on hotspot shape and size will be studied independently for the two geometries. Under the umbrella of the cylindrical hotspots, the T-A distributions of the different orientations mostly overlap for all shock speeds. However, from inspection of the heat maps in Figure 4.14, the hotspots from shock at 2.0 km/s possess shapes that are highly unlike one another. Since the overall hotspot criticality and transition to deflagration is greatly influenced by thermal conduction [39,75], the shape of the energy localizations is of major significance to the overall ignition, growth, and coalescence of the hotspots. Within the hydrodynamic regime of the (100) orientation, the collapse results in a hotspot that is mostly ovicular in shape, indicative of its initial pore geometry. Within the hydrodynamic regime of the (001) shocks, the collapse of the pore results in a crescent-shaped region, the same hotspot described in Section 4.3. The 'core' is formed from the impact of the collapse, the 'legs' are formed

from plastic flow and shear banding along the edges of the pore. The leg-forming mechanisms are activated by shock focusing of the intact basal planes, which stay crystalline during collapse. While the core and legs of the hotspot are treated as one, singular hotspot, since they are all activated via the collapse of a single pore, the underlying mechanisms of the two discernable sections are different. These trends follow for lower shock speeds which access the viscoplastic collapse, however less discernable due to lower total energy localization.

A majority of high explosives undergo stereotypical hydrodynamic collapses for strong shocks similar to the (100) collapse process [7,8,62,63,176,192–194]. This makes the (001) collapse mechanism, which features ordered material, a unique material response that, for TATB, generates slightly hotter and larger hotspots than the pure hydrodynamic response. This tracks well with previous works that show, pound for pound, the viscoplastic response actually localizes more energy, but only occurs for weak shocks, whereas the absolute temperature of a hydrodynamic collapse hotspot is always larger, but its relative temperature is actually lower [63,195].

The diamond shaped pores, due to the limited plastic flow in the viscoplastic regime, produce no hotspot of consequence at low shock speeds, prior to ejecta formation. However, once the shock speed is high enough for shock focusing to activate jetting mechanisms, significant hotspots begin to form. The (100) orientation leads to much hotter hotspots, and slightly larger hotspots, than the hotspots formed in the (001) case. As shown in Section 4.4.1, the high-pressure elastic wave of the (001) case initiates a viscoplastic mechanism, which leads to lateral collapse of the pore, almost immediately, and prior to any ejecta formation. As the plastic wave begins to initiate jetting, the viscoplastic collapse prevents the gaseous molecules from fully expanding and recompressing upon downstream impact. The choking off of the ejecta in (001) orientation limits the amount of pressure-volume work done during collapses, causing significantly lower hotspot temperatures. Additionally, since this prevents the ejecta from spanning the total area of the pore prior to total collapse, it leads to a much smaller hotspot area than in the (100) orientation.

Changing gears to assess the localization of internal potential energy for these cases, Figure 4.17 displays E-A plots where E is the intra-molecular PE. Most of the trends with orientation, shock strength, and defect geometry from T-A distributions in Figure 4.15 hold true for the E-A distributions of intra-molecular PE as well. However, a few key disparities exist, which help to better showcase the underlying mechanisms in play for latent PE formation.

The maximum PE values for cylindrical pore collapse follow the same trend where (100) leads to higher absolute values for low particle velocities, but the (001) orientation dominates for stronger shocks. However, compared to KE where the orientation disparity was not overly large, the PE localization of the (001) greatly outperforms the (100). This outperformance is so much so that the peak PE values of the 1.5 km/s (001) are larger than that of the 2.0 km/s shock in the (100). Considerable shearing in the hotspot 'legs' of the (001) are formed by significant plastic flow that can deform the molecules. Additionally, more plastic work is needed to volumetrically fill the (001) pore due to the lack of a true hydrodynamic response where the material more readily flows.

Different collapse mechanisms leading to different levels of latent PE is indicative of a loading path dependence. Hence, two hotspots of identical size and temperature fields can have highly disparate PE fields and latent PE if the collapse mechanisms greatly differ. For the diamond shaped pores, the T-A and PE-A trends are nearly identical, showing that little to no latent PE exists in these cases. Since most of the KE is due to molecular ejecta and not plastic flow, it can be safe to assume that the latter is the more important mechanisms for PE localization. This is a critical result, as previous works have shown molecular ejecta and/or expansion and recompression to be the key mechanisms for KE localization [6,162,196].
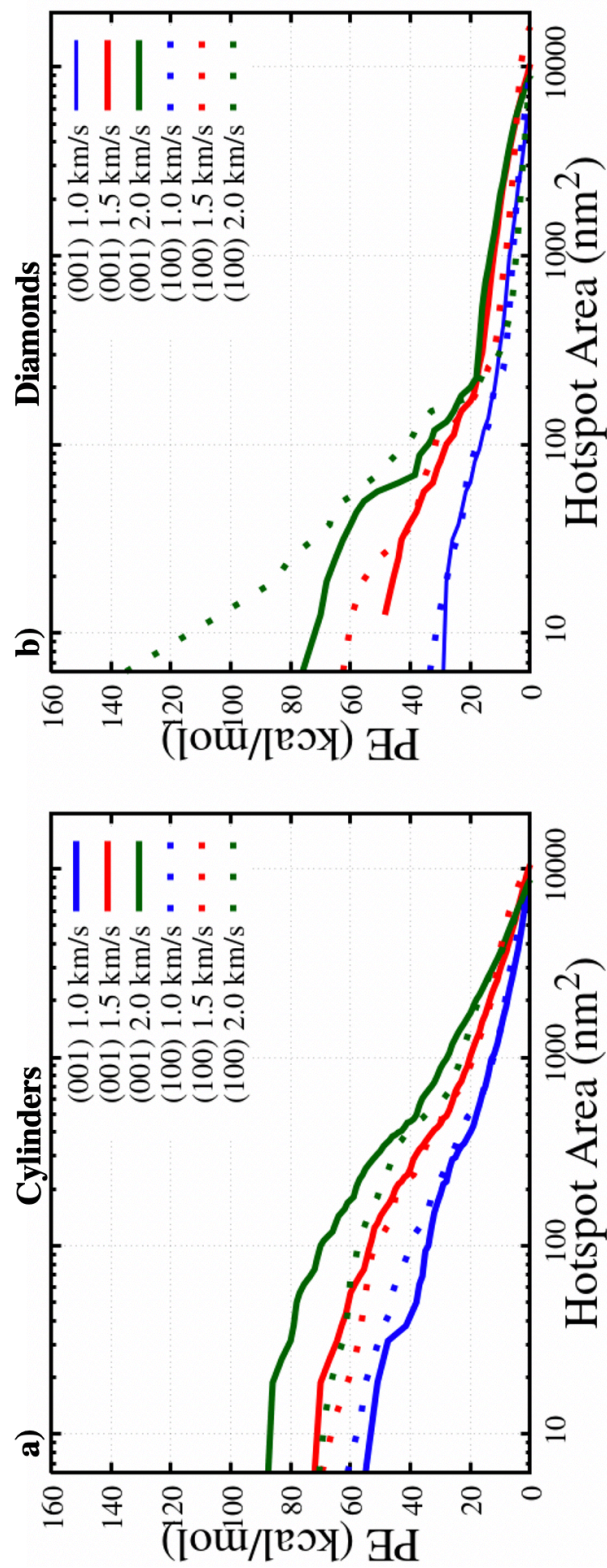
Figure 4.17: PE-A cumulative distributions, referenced by the bulk shock PE, for the cylindrical pores in panel a and the diamond pores in panel b. Dashed lines represent (100) orientations and solid lines are (001) orientations.

111

Section 4.4.3 has decisively established that the latent PE is not necessarily functional of the temperature rise of the hotspot. That is, the peaks of both KE and PE do not have a one-to-one mapping. The pore collapse simulations performed here span a variety of mechanisms for hotspot formation via pore collapse and result in hotspots of all shapes and sizes. However, much analysis has been spent on the general fields of the PE and KE, and not the underlying distributions of the latent energy state. In Figure 4.18, distributions, with molecular resolution, of the PE vs temperature are shown, where each distribution includes all molecules in the system, not just the hotspot. Each distribution is taken at $t_o + 1$ ps and are grouped into individual plots where each panel contains a single defect geometry and orientation state. The dashed line represents the expected rise in energy due to a perfect following of the classical equipartition of energy.

Equipartition appears to be well followed for all hotspots where the collapse is in the viscoplastic regime (weak shocks). That is, almost no latent PE is stored in shocks for $U_p \leq$ 1.0 km/s. The diamond shaped pores, for all shock speeds, also adhere to equipartition. It was hypothesized, in the above discussion, that the jetting mechanisms does not create much plastic flow, which is why it does not generate latent PE, which can also be seen in Figure 4.18. However, the hydrodynamic collapses, which occurs for strong shocks with cylindrical pores, leads to a distribution of PE states that, for a given temperature, is much broader than expected with significant latent PE states. This large spread of PE states is found at temperatures greater than 1000 K for $U_p \geq 1.5$ km/s. Just as with the hotspot shapes and pore collapse mechanisms, the (001) and (100) orientations lead to startlingly different PE-T distributions. The (001) system bifurcates into upper and lower bands. Figure 4.19 shows the spatial mapping of these two bands, in which the lower band is the shear band formed legs of the hotspot, as well as part of the core. The upper band, which has more latent PE for a given temperature, is localized in the region behind the core. In this region, significant plastic flow is needed to move the material into the void to fill its area. For the (100) system, the is no upper band, but a centralized upper lobe, which reaches the same high PE levels, but for a much smaller range of temperatures. Like the (001) case, the (100) localizes its latent PE to the upstream part of the hotspot, which is not where impact is, but the most plastic flow. While impact and recompression lead to high KE, it is the plasticity mechanisms that generate the latent PE. Hence, while both pore collapses undergo different mechanisms and the hotspots form differently, the governing dynamics of latent PE formation are

the same. In general, maximizing work leads to high KE, maximizing plastic material flow leads to high PE.
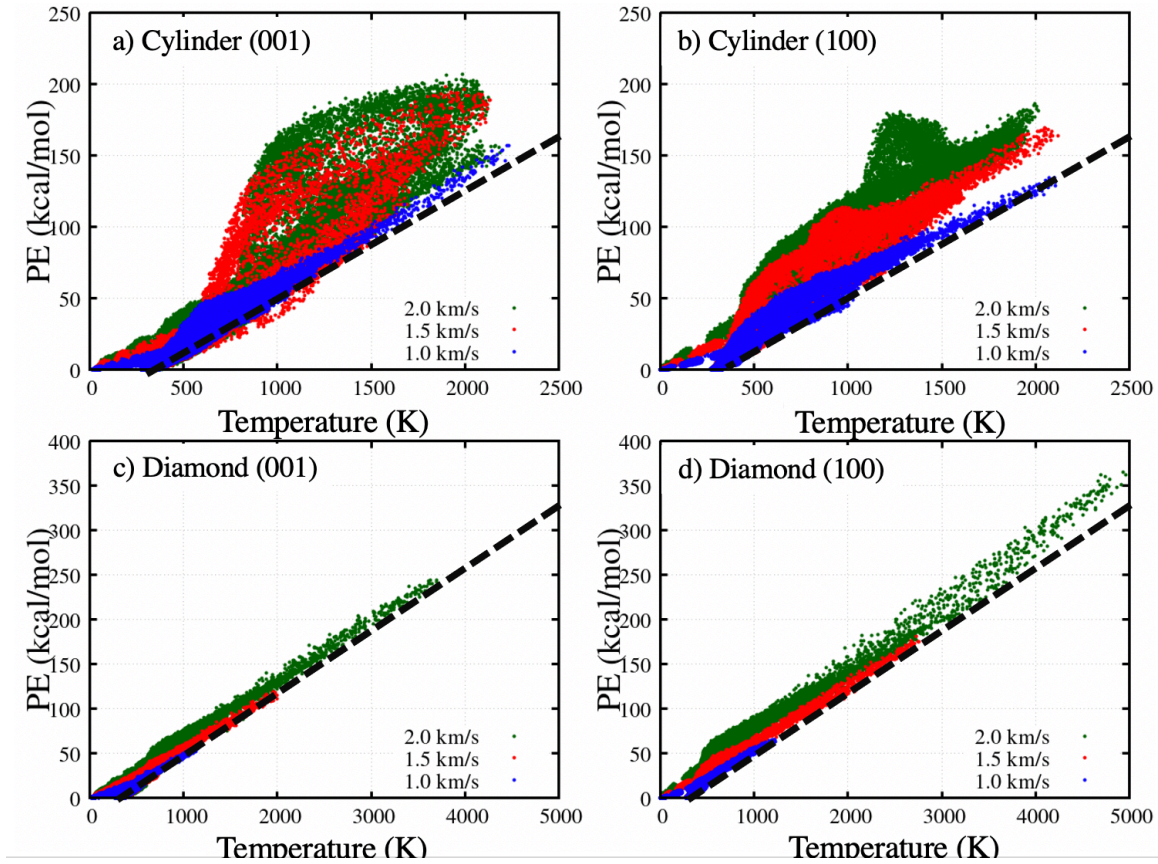
Figure 4.18: All molecule PE-T distributions for all shocks for $U_p \geq 1.0 \; km/s$. Dashed lines represent equipartition of energy. Each panel is an orientation and defect shape combination, color of points is shock speed. Distributions contain all molecules at t_o + 1.0 ps, including all bulk shocked and unshocked molecules, in addition to the hotspot.
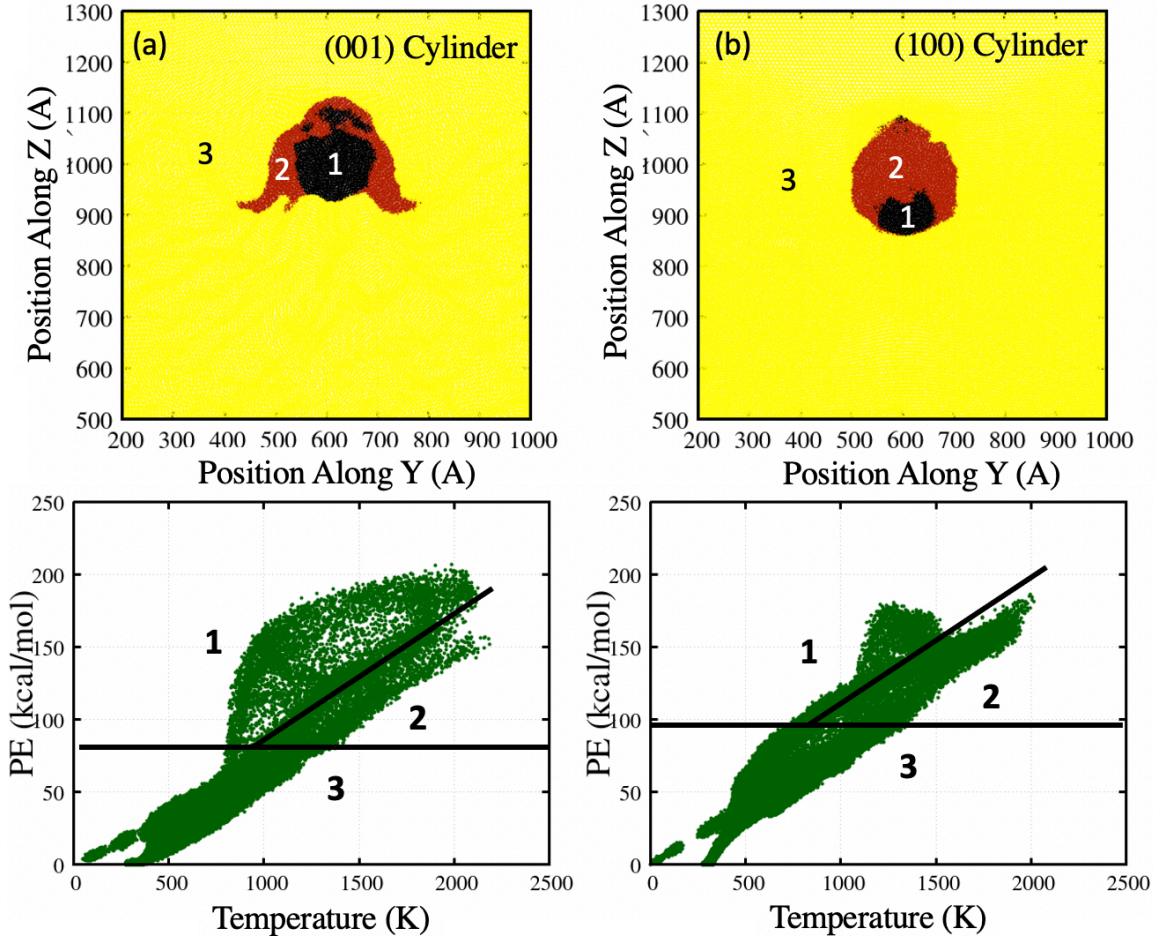
Figure 4.19: Spatial mapping of points from the PE-T distributions for 2.0 km/s cylindrical pores where coloring is based on the sections of the distributions in the lower panels.

4.4.3   Efficiency of TATB Hotspots

Figure 4.20 displays a T-A plot that is referenced and scaled for both axes. The included distributions are all four 2.0 km/s shocks from this work, and equivalent cylindrical and diamond pores at 2.0 km/s for HMX from Ref. [6]. For all cases, as was done with Figure 4.16, the area is scaled by the size of the initial defect, which is much larger for the cylinders. For the temperature, the absolute temperature is referenced by the shock temperature, which is different for each TATB orientation and HMX. The referenced temperatures are also scaled by a scaling value that corresponds to the theoretical maximum hotspot temperature proposed in Ref [162]: $k_b \Delta T = \frac{m}{3} U_s U_p$. For the cylindrical pores, TATB and HMX result in T-A distributions that have similar

maximum temperatures at small areas with TATB localizing more energy for larger areas, possibly due to shear banding effects. Hence, these two materials, for cylindrical pore collapses, have very similar efficiencies at localizing energy in hotspots. However, when comparing the HMX shock with a diamond pore to the equivalent TATB hotspot, the HMX system results in extreme hotspot temperatures nearing the maximum value (scaled T of 1.0).

One of the other scaling laws from Holian et. al., Ref. [162], is that jetting can/should occur when the shock energy is greater than the cohesive energy of the crystal: $\frac{1}{2}mU_p^2 > e_{coh}$. Comparing from the cohesive energies for TATB and HMX, the minimum U_p needed, that is 1.14 and 1.15 km/s for TATB and HMX, respectively. However, HMX jetting appears to make much better hotspots than TATB jetting mechanisms, despite similar thresholds which should lead to similar amounts of jetting. However, this scaling law is based from 1D planar gap type pores where shock focusing is not relevant, and the plasticity mechanisms for TATB and HMX are highly disparate.

Despite similar ejecta thresholds, jetted HMX molecules have much higher velocity distributions for the jetting mechanism under equivalent shock strengths, as shown in Figure 4.21. From this, it is indicative that jetting, which vital to generating hotspots with extreme temperatures, is derivative of multiple mechanisms most likely related to shock focusing and plasticity, not just the cohesive properties of the crystal. However, in the context of the current work, jetting is only critical for high KE localization, and not latent PE.

It is from these results, comparing the KE localization of TATB to HMX, a state-of-the-art standard for HE performance, that TATB's lack of ability to efficiently localize energy into hotspots becomes relevant. This may be another mechanism that leads to the insensitivity to shock in TATB, which is already describe by the formation of carbon clusters, strong hydrogen bonding in the crystal, and the formation of nitrogen rich heterocycles, which all work to slow local reaction kinetics [31,34,110,197–199].
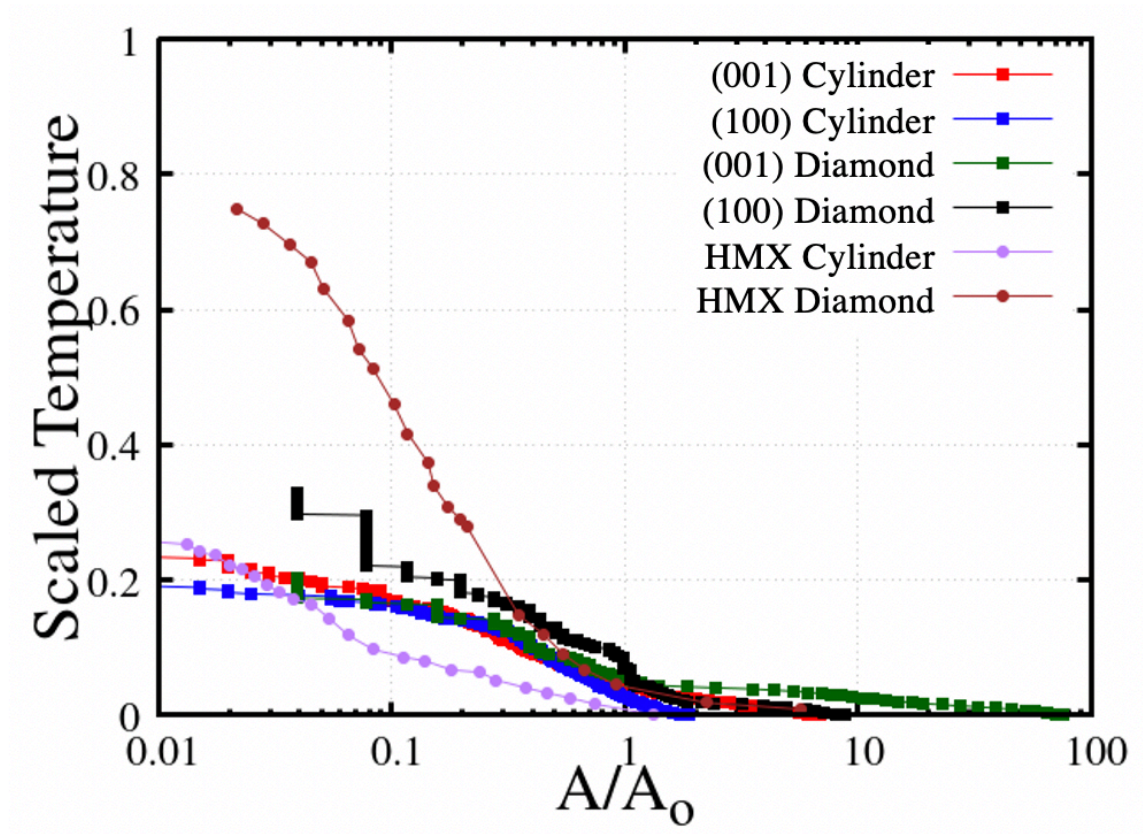
Figure 4.20: Scaled T-A distributions for $U_p = 2.0\ km/s$ where area is scaled by initial area and temperature is first referenced by the bulk shock temperature and then scaled by the theoretical maximum hotspot temperature from Holian et. al. in Ref. [162].
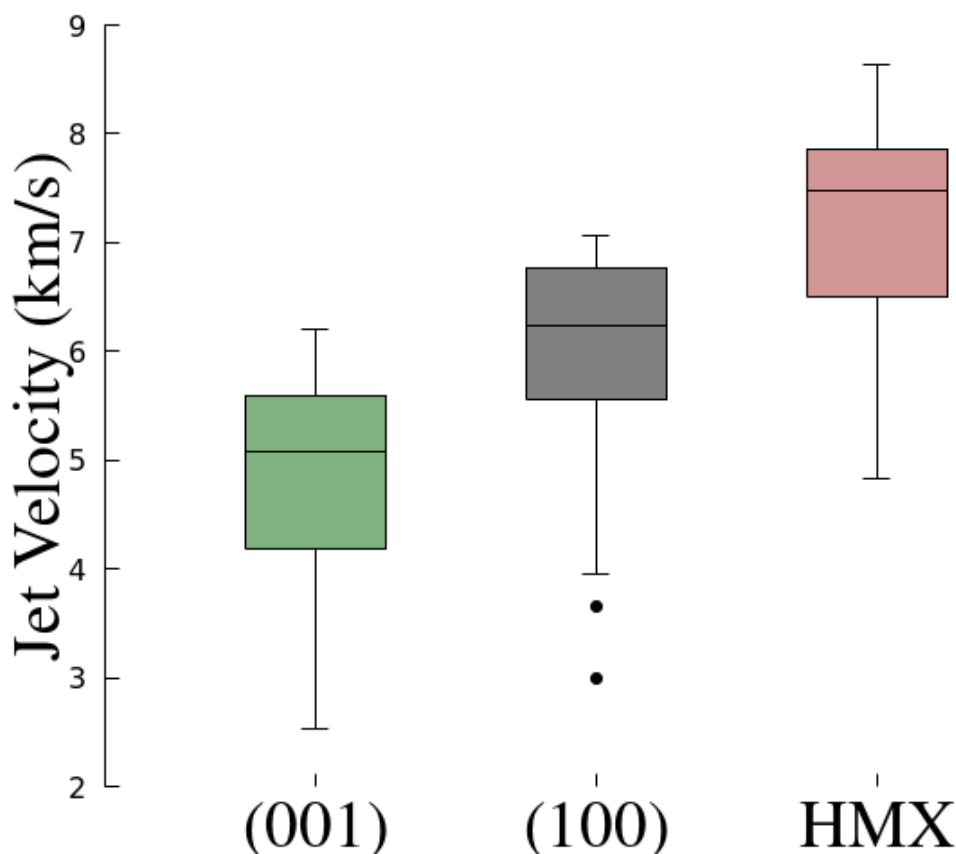
Figure 4.21: Box and whisker plots of molecular velocities in the shock direction for ejecta molecules in TATB and HMX with diamond pores for 2.0 km/s.

4.5 Conclusions

Within this chapter, which is focused on the localization of thermomechanical energy in hotspots, it is shown, through all-atom simulations of the shock induced collapse of porosity in TATB, that molecules which undergo significant plastic flow will localize potential energy from intra-molecular deformation that leads to a wider spatial extent of energy states for a given temperature that cannot be inferred from the temperature field alone. These excited PE states persist well beyond the dissipation of the temperature field as the latent PE is controlled by molecular deformations that do not relax on MD timescales. These deformations are likely to, in a reactive system, lead to mechanochemical acceleration of kinetics, generating a plausible and testable hypothesis to explain why dynamically formed hotspots react significantly faster than hotspots formed under purely thermal conditions. More generally, these works bring light on a

neglected phenomenon within hotspot formation and evolution and offers a systematic metric, the intramolecular PE, to implement mechanochemical effects into multi-physics models of shock initiation and detonation.

The PE hotspot analysis is extended to a variety of pore collapse events that vary the shock strength, the shape of the pore, and the crystallographic orientation of the TATB single crystal.

Separately, within each of the two orientations studied, the trends in the hotspot size and potency in the temperature description are roughly followed by the PE hotspots as well, with the amount of latent PE defined by the amount of local plastic flow experienced during collapse. Comparing the cylindrical and diamond shaped pores, the expected trends reverse. Molecular ejecta is known to provided excess localized thermal energy due to expansion and recompression leading to massive levels of pressure-volume work. However, molecular ejecta does not lead to significant latent potential energy in the hotspot, with most of the energy falling very close to equipartition of energy. However, for the cylindrical pore collapses, which have much less expansion and recompression, but significantly more plastic flow due to larger initial porosity, the amount of latent PE is much greater. Lastly, it is shown that TATB, compared to HMX, has a lower efficiency at localizing shock energy into the microstructure as hotspots, potentially attributing to TATB's insensitivity to shock initiation, which is typically rationalized by covalent clustering reactions and the crystal's hydrogen bonding network.

Overall, these works have shown that the latent PE stored in molecular strain energy in hotspots is significant and should be accounted for is continuum physics descriptions of reactive ignition in energetic materials. This mechanical strain energy has also been explored as a valid descriptor for plastic deformation is crystals, and potential descriptor for up-scaling many thermo-mechanical and mechanochemical events in molecular solids.

5. EXTEMPORANEOUS MECHANOCHEMISTRY IN HOTSPOTS

5.1   Introduction

In Chapter 4, the focus was on using nonreactive MD to assess intra-molecular deformations within hotspots, especially the latent internal energy from these deformations. However, the primary drawback of the nonreactive framework is the inability to determine how the latent PE affects the reactivity of the deformed molecules. In this chapter, the role of intra-molecular strain in the chemical reactivity of TATB will be assessed, specifically the mechanochemical acceleration of reaction kinetics and alteration of 1st step reaction pathways.

The 'umbrella' of mechanochemistry encompasses branches of physics and chemistry that span from ball milling aluminum powders to increase reactivity [201], to straining/rupturing individual covalent bonds in an atomic force microscope (AFM) [202], to shockwave attenuation in metal organic frameworks [203,204], to mechanically accelerated oxidation-reduction reactions in disulfides [175]. This work here will focus on the branch known as covalent mechanochemistry, which includes all acceleration and alteration of reactions due to explicit strains and deformations placed upon covalent bonds.

Covalent mechanochemistry has been specifically utilized to access otherwise forbidden reactions based upon the Woodward-Hoffman pericyclic selection rules [174,205], to strengthen polymer hydrogels without significantly restricting their yield strain and elongation abilities [206], and to trigger isomeric reactions with chromic, catalytic, and fluorescent responses in mechanophore polymer systems [207–210]. Covalent mechanochemistry can also be a significant contributor within solid-state reactions that are triggered when materials are subjected to dynamic compressions on the scales of 10s GPa of pressure and strain rates on the order of 10^8 such as astrodynamical collisions initiating the formation of prebiotic and large polypeptide molecules [52,211–214], shock induced phase transformations in carbon [50,215–217], and shock initiation of explosives in hotspots and detonation fronts [51,54,61,105,218–220]. Under rapid strain paths, additional mechanochemical influences become relevant. The quantum mechanochemical variation of the Franck−Condon Theory presents the idea that if the applied external forces to a covalent system are rapid (on the order of chemical reactions or faster), then the passage from states along the undeformed potential energy surface to states along the force-modified potential energy surface produces a nonequilibrium ensemble of vibrationally excited phonon states [221].

As a result of recent advances in both the experimental methods to reproduce mechanochemistry and computational capabilities to perform reactive calculations with quantum mechanical accuracy, direct studies of strain induced reactions in organic and molecular solids have provided substantial insight into the underlying physics of mechanochemistry [64,173]. Increases in experimental resolution and *in situ* diagnostics at the nanoscale have allowed for the direct study of applied forces on individual bonds within covalent systems such as macromolecules and proteins. AFM experiments with atomic bond scale cantilevers were able to ascertain the force-extension curve of a single covalent bond, which paved the way for a numerous experimental and computational studies of covalent mechanochemistry for isolated molecules [174,222] and individual bonds on surfaces [175,209,223]. MD calculations, typically through electronic structure and DFT based methods, have studied a menagerie of mechanochemical effects with similar resolution and experimental design to AFM studies. Topics including mechanophore elongations to induce isomerization [174,205,207,208,224], straining knotted/entangled polymers to assess reductions in strength [222,225–227], analyzing the distribution of mechanical stresses incurred during induced protein folding [228], and calculating the necessary force for bond rupture

for extensions of metal-organic junctions [229–231] have all been studied with computational methods, with many of the studies performed in tandem with experiments on nearly identical systems. To perform simulations of mechanochemical extensions, a variety of special purpose methodologies are necessary to accurately characterize and model external force response and chemical activation, with respect to the experiments. These typically include, but are not limited to, steered molecular dynamics (SMD) [232–236], constrained geometries simulate external force (CoGEF) [237], and explicit force methods such as FMPES (force-modified potential energy surface) [205], EFEI (external force explicitly included) [171], and EGO (enforced geometry optimization) [238].

A significant majority of the computational studies that aim to analyze mechanochemical effects have been limited to assessing the role of elongation (two-body forces) in which the applied force extends along a specific, single vector. However, most mechanochemistry in condensed matter molecular systems, such as polymer extrusion and shock loading, will result in significant shear and plastic flow the requires a full tensorial description of the stress to accurately describe. Many of these cases can be classified as extemporaneous mechanochemistry, in which the mechanochemical event occurs without explicit preparation or design, but as a result of the material's natural structure or environment. For most cases of extemporaneous mechanochemistry, a simple linear force cannot mimic the mechanochemical loading that a molecule experiences. Previous efforts to study extemporaneous and many-bodied influences in mechanochemistry have calculated system average reaction kinetics and pathways for organic systems under uniform shear loads [52,76,132,239]. These works embody the current state of the art and demonstrate that dynamic, mechanical loads such as shocks (which have a resolved shear) and ensemble shears will result in a reduction in activation barriers and accelerate reaction kinetics. However, there is a lack in specificity in which mechanochemical contributions cannot be assigned to individual molecules within the distribution of deformations observed. This leads to a lacking in the understanding of how explicit physics and chemistry of organic molecules are altered by intra-molecular deformations.

One of the simplest models for assessing the change in chemical kinetics due to mechanochemical effects is from Bell and was initially derived for cell adhesion [77]. The concept is centered on the idea of adding a work term to the Arrhenius exponential that lowers the

activation energy. In the Bell model, this work is described as $F * x$, as shown below, where F is the applied force and x is the reaction coordinate along which it is applied.

$$k(T) = A * \exp\left(-\frac{E_a - F * x}{k_b T}\right)$$

This model has well described simple systems [64,173,175,240] by assuming the applied force directly lowers the activation barrier for reaction. This also assumes that the deformation or applied force is not changing the reaction path or available chemical transition states, only accelerating reactions by increasing available energy for reaction initiation.

For energetic materials, the formation of hotspots, or spatial localizations of energy, has been a key concept of study for both basic sciences and engineering purposes. The previous chapter showed that during a shock induced collapse of porosity in which significant plastic flow occurs, there is a significant latent potential energy in the hotspot that is driven by intra-molecular strain. In general, the existing body of work characterizes the thermodynamic state of the hotspots almost exclusively through its temperature field. Yet, the Chapter 4 results on the PE hotspot indicates a deviation from this traditional picture that will lead to mechanochemical effects within the hotspot.

Work from Wood et. al, Ref [61], showed that the dynamical collapse of a pore in RDX leads to a hotspot that is significantly more reactive than a hotspot constructed thermally, under equilibrium conditions, the are at the same size, pressure, and temperature field. In the case of the dynamical hotspot, initial reactions occur almost immediately upon total collapse of the pore and the hotspot reaches a steady deflagration in ~40ps post collapse. The authors tentatively attributed these effects to mechanochemical acceleration of kinetics and non-equilibrium reactions. However, explicit proof of either of these was not found. It is believed the latent hotspot energy discovered in Chapter 4 potentially resolves this issue by attributing it to mechanochemistry, but additional studies to confirm this, using reactive potentials, are presented in this chapter.

Additional work on shocks in TATB using all-atom MD with a non-reactive forcefield, the same used in this work here, utilized detonation level shockwaves to initiate the shear banding mechanism in perfect crystal TATB [51]. Representative volume elements were then constructed from both material in the shear bands and in the surrounding crystalline material. Isothermal decomposition simulations using DFTB on both the shear band and bulk cells showed the reaction kinetics of the shear bands are a least an order of magnitude faster at both initiation level and detonation level conditions. Lastly, shear band material was shown to generate more NO_2 as an

intermediate than the bulk material, showing a potential change in reaction mechanism. Previous work that deformed gas phase TATB molecules using DFT showed that shear forces that bend NO_2 groups out of plane will close the HOMO-LUMO gap at improper angles of 50° or greater, which metalizes the system and delocalizes electrons, potentially altering the transition states and reaction paths of TATB under shock loading in which intra-molecular deformations take place.

Reactive molecular dynamics simulations looked at 1D hotspots in RDX in which the pore is a planar gap. For each impact velocity studied, a variety of transverse velocities were applied ballistically to all material on the downstream side of the pore [132]. This results in a controlled level of shearing during pore collapse. Hence, the particle velocity controls the level of P-V work, and the transverse velocity controls the level of plastic flow. The result was that for increasing levels of shear velocity, the necessary particle velocity to create a critical hotspot lowers significantly.

These three works discussed above have shown irrefutable evidence that some sort of mechanochemical acceleration takes place during hotspot formation and can have a significant impact on initiation, and potentially more macroscopic responses such as run to detonation and impact sensitivity. However, there is still lacking a systematic route to generate path dependent, mechanochemical models for HEs that can be implemented in coarse grained and continuum models that access significantly larger and longer length and time scales. This chapter will present a reactive pore collapse simulation that is analyzed in the context of the deformations found in the potential energy hotspot work (Chapter 4) and a new methodology, Many-Bodied Steered Molecular Dynamics (MB-SMD), that can systematically assess the alterations to kinetics and reaction pathways due to the intra-molecular deformations found in pore collapse and shear band simulations.

5.2   Methods

As was used in Chapter 3, all ReaxFF simulations conducted are with ReaxFF-2018 [7], as implemented in LAMMPS [85]. Shock simulations are conducted with a 0.1 fs timestep, and high temperature decomposition simulations are conducted with a 0.025 fs timestep. All atomic charges are updated on the fly using the QEq (charge equilibration) scheme [99] at each time step with an accuracy threshold set to 1×10^{-6}.

The pore collapse simulation is conducted in the same format as for the nonreactive pore collapses in Chapter 5, with a reverse ballistic setup [16] (see Section 2.4.1) using a particle velocity of 2.0 km/s. The supercell (without the void) is generated starting from an initial unit cell in the experimental setting of Cady and Larson [67] with new lattice parameters determined via a full triaxial relaxation with ReaxFF-2018 at ambient temperature and pressure, which results in a nearly identical density. This relaxed unit cell is extended and rotated using the generalized crystal-cutting method (GCCM) [144] such that the resulting supercell is nearly orthorhombic and the $N_{(001)}$ (normal to the basal planes) vector is aligned with resulting supercell axis Z, which is the shock direction. The resulting lattice vectors are

$$\mathbf{A} = -5\mathbf{a} - 3\mathbf{b} + 0\mathbf{c}$$
$$\mathbf{B} = \mathbf{a} - 7\mathbf{b} + 0\mathbf{c}$$
$$\mathbf{C} = \mathbf{a} + 2\mathbf{b} + 6\mathbf{c}$$

where a, b, and c are the original unit cell lattice vectors. The resulting supercell is replicated such that the shock direction Z (along $\mathbf{C}$) is ~250 nm and the X direction, lattice vector $\mathbf{A}$, is extended to be ~120 nm. The $\mathbf{B}$ direction kept as one vector length of the supercell, roughly 7 nm. A circular cross-section, cylindrical pore, with a 40 nm diameter, that extends the thickness of the cell, is cut parallel to $\mathbf{B}$ (in the X-Z) at (X, Z) fractional coordinate (1/2, 1/3). Figure 5.1 shows this initial set up as well as heat maps of temperature before, during, and after the collapse. The resulting plane of the pore, $\mathbf{A} \times \mathbf{C}$, is the plane that maximizes anisotropy from the basal plane structure. Periodic boundaries are used in the non-shock directions $\mathbf{A}$ and $\mathbf{B}$ with an open boundary used in $\mathbf{C}$, the shock direction. The final system was thermalized at 300 K in the canonical ensemble. The shock compression simulation was conducted using the micro-canonical ensemble.
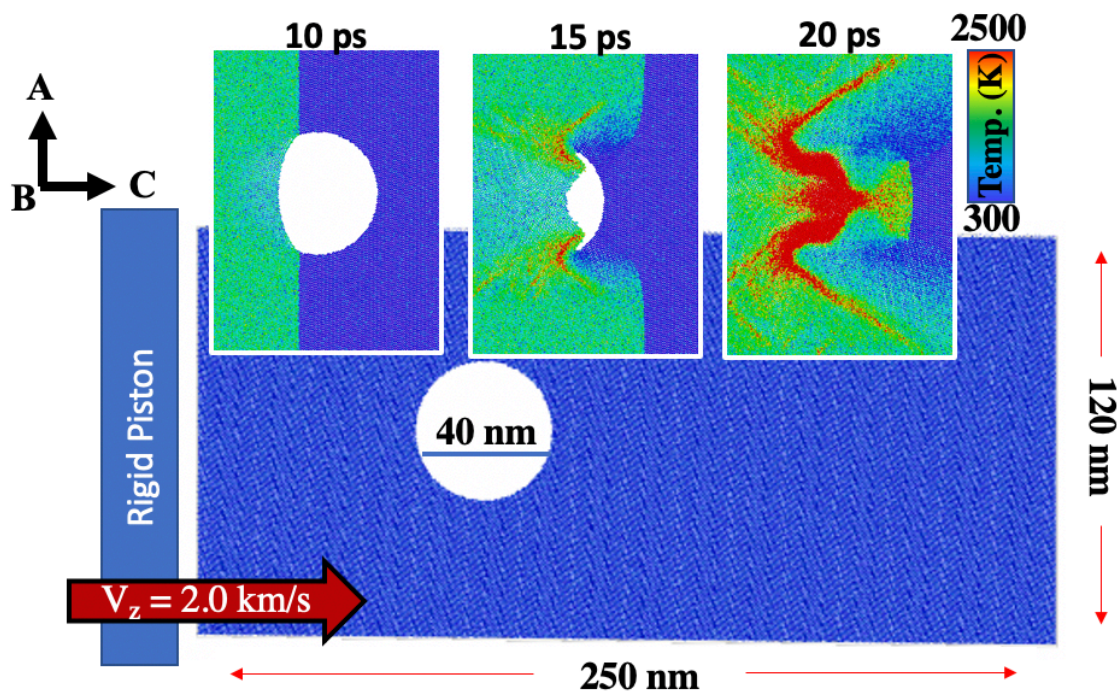
Figure 5.1: Schematic of the reactive pore collapse simulation. Inset figures to the top are colored as temperature.

In an effort to better compare the results of the hotspot to a bulk (defect free) shock with similar temperatures, the Hugoniostat method [114] (see Section 2.4.3) is employed. A 5x5x5 replication of the orthorhombic supercell is used. This cell has roughly 16,000 molecules, nearly the size of the hotspot analyzed. Shock pressures ranging from 45-70 GPa are used to reach hotspot temperatures in the perfect crystal system.

Similar to Chapter 4, a molecule by molecule averaging system is used to better assess the local thermodynamics of the hotspot and surrounding material. Position is taken as the center of mass (COM) and the COM velocity vector is used. Two molecular metrics are calculated: the thermodynamic property roto-vibrational kinetic energy and the molecular mechanical property introduced in Chapter 4, I_2/I_1, which is the ratio of the two smallest principal moments of the inertia tensor. For simplicity, the first (thermodynamic) term will be referred to as the molecule's temperature and have units of kelvin. This is calculated using a classical specific heat of $\frac{69}{2}k_b$ for the roto-vibrational modes (3N-3 modes). I_2/I_1 is unity for an equilibrium TATB molecule, which

is planar, where $I_1 \approx I_2 < I_3$. Thermal fluctuations will result in values near 1.1 and high distortions will be values above 1.5.

Since these are reactive MD calculations, additional molecular metrics for chemical reactions will need to be devised. Each molecule can be in one of three chemical states, labeled 0, 1, and 2. State 0 corresponds to an unreacted molecule. State 1 describes molecules that have undergone reactions of just the NO_2 and NH_2 groups, but not the C atoms within the ring. State 2 molecules are molecules that have broken a C-C bond in the ring. Under extreme mechanical strains, state 2 can be reached without going through state 1, however this is considered a rare event. Bond breakage is assessed using a distance cutoff criterion where the cutoff is placed at the first local minimum of the atomic distance distribution. Bonds must be broken for two consecutive frames, each frame being 0.1 ps apart, to be considered truly broken and not extreme tails of fluctuation. Each molecule will have an individual kinetic time, which is $\Delta t_{rxn} = t_2 - t_1$, where t_1 and t_2 are the times in which state 1 and state 2 are first reached, respectively. If state 2 occurs before state 1, then Δt_{rxn} is taken to be 0.1 ps. Figure 5.2 shows an example of t_1 and t_2 events in a TATB molecule. Figure 5.3 shows the time history of total t_1 and t_2 events for all molecules in a thermal decomposition, overlayed with system PE. This shows that the sum of t_1 events corresponds to the completion of the initial endothermic step and the completion of all t_2 events is the reactions full exothermicity.
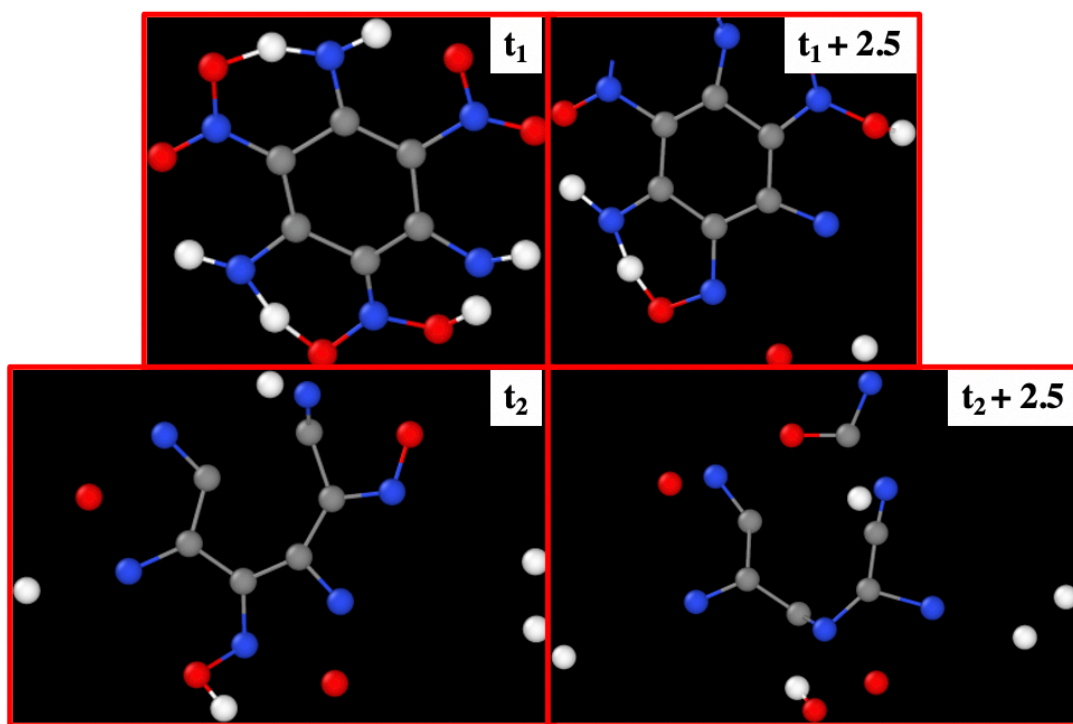
Figure 5.2: Example t_1 and t_2 events for a TATB molecule undergo decomposition.
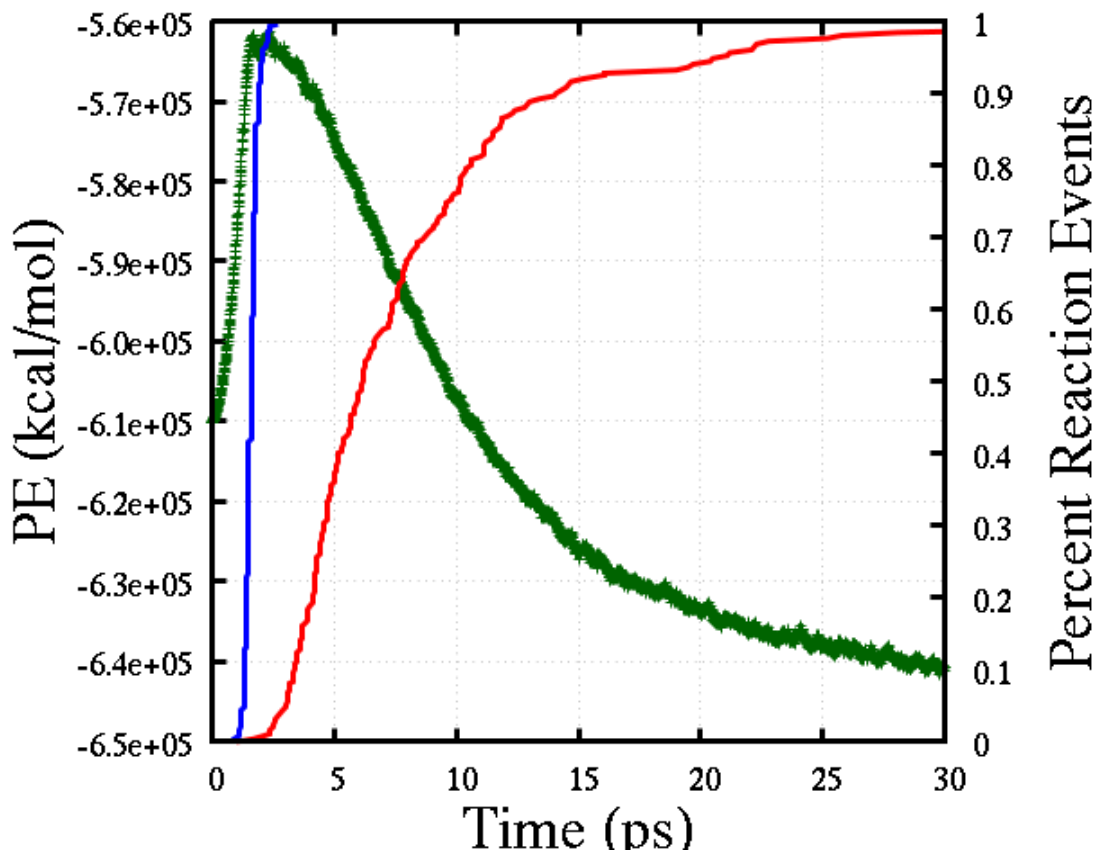
Figure 5.3: Totality of t_1 and t_2 events (blue and red) overlayed with system PE (green) for a 2500 K isothermal decomposition of a TATB perfect crystal.

In addition to the pore collapse and Hugoniostat simulations, Sections 5.5 and 5.6 will feature thermal decomposition simulations. In these simulations, an external potential will be applied to deform molecules and mimic shock induced mechanochemistry. The details of this external potential will be discussed in Section 5.4. Deformations will be applied to TATB perfect crystals, and then decomposition reactions will be initiated via linear heating. Heating rates will range from 4 K/ps to 40 K/ps. All initial temperatures will be 1000 K and heating will continue until 3000 K is reached. System kinetics will be assessed in the statistics of Kissinger,

$$\frac{\partial \ln\left(\frac{\phi}{T_p^2}\right)}{\partial\left(\frac{1}{T_p}\right)} = -\frac{E_a}{R}$$

where ϕ is the heating rate and T_p is the temperature at a critical moment that is consistently calculated for all heating rates. Here the critical time is chosen to be when the PE of the system is

128

at its maximum. Corresponding to the data in Figure 5.3, this first peak would be the point of all initial (1st step) reactions, and the corresponding energy barrier should be for that step. For all systems, the external potential that is discussed in Section 5.4 will be applied to the system at 300 K under NPT conditions to create a pre-deformed system such that all deformations are created prior to any chemical reactions occurring.

5.3   Hotspot Kinetics and Reaction Paths

To partition the molecules within the hotspot into coarsened groups for kinetic analysis, a simple k-means clustering algorithm is applied. Only molecules that reach a t_2 state are included in the clustering. Three descriptors are used in the clustering: temperature, I_2/I_1, and the slope of the temperature-time history for a 1 ps range approaching t_1. For each of these clusters, from which the molecules are not spatially correlated, the average thermodynamic and mechanic descriptors and Δt_{rxn} can be calculated.

Figure 5.4 shows both the all-atom and cluster centroids for the hotspot molecules in $T - I_2/I_1$ descriptor space. Interestingly, from the centroids, there are three clusters that have a range of temperatures while at an I_2/I_1 value near equilibrium thermal value (~1.1), and three clusters all with nearly the same temperature with increasing I_2/I_1 values. In both cases, increasing temperature and increasing I_2/I_1 leads to a decrease in Δt_{rxn} times. In this case, cluster 3, which is at an I_2/I_1 value of 1.67, reacts on the same timescale as cluster 3, which has almost no deformation but is roughly 400 K hotter than cluster 3. This shows direct proof of mechanochemical acceleration of molecules within a hotspot formed via pore collapse, in which the intra-molecular deformations shown in Chapter 4 can be held responsible.

Figure 5.5 shows cluster centroids for k-means where N is 6, 10, 17, and 25. As N increases, the coloring of the centroids, which is Δt_{rxn}, appears to form somewhat of a continuum when moving rightwards (increase temperature) or upwards (increasing deformation). These points have somewhat angled equi-color 'bands' where different T-I_2/I_1 states result in the same reaction time. This supports the idea that a simple continuous function could fully describe the mechanochemical kinetics of the system. However, efforts to do this with the below data did not prove fruitful due to the high level of degeneracy in I_2/I_1.
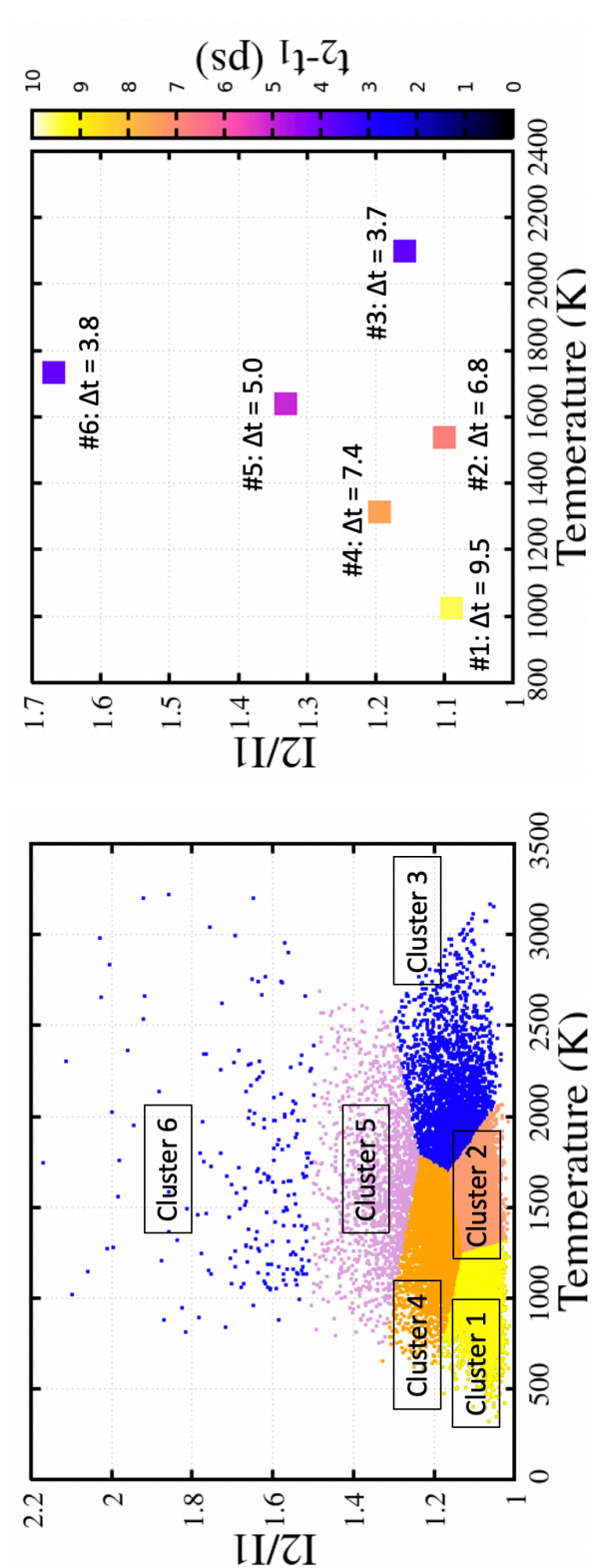
Figure 5.4: a) All molecule T – I_2/I_1 distribution colored by cluster b) cluster centroids colored by Δt_{rxn} time. Inset text is the time used for the color bar.
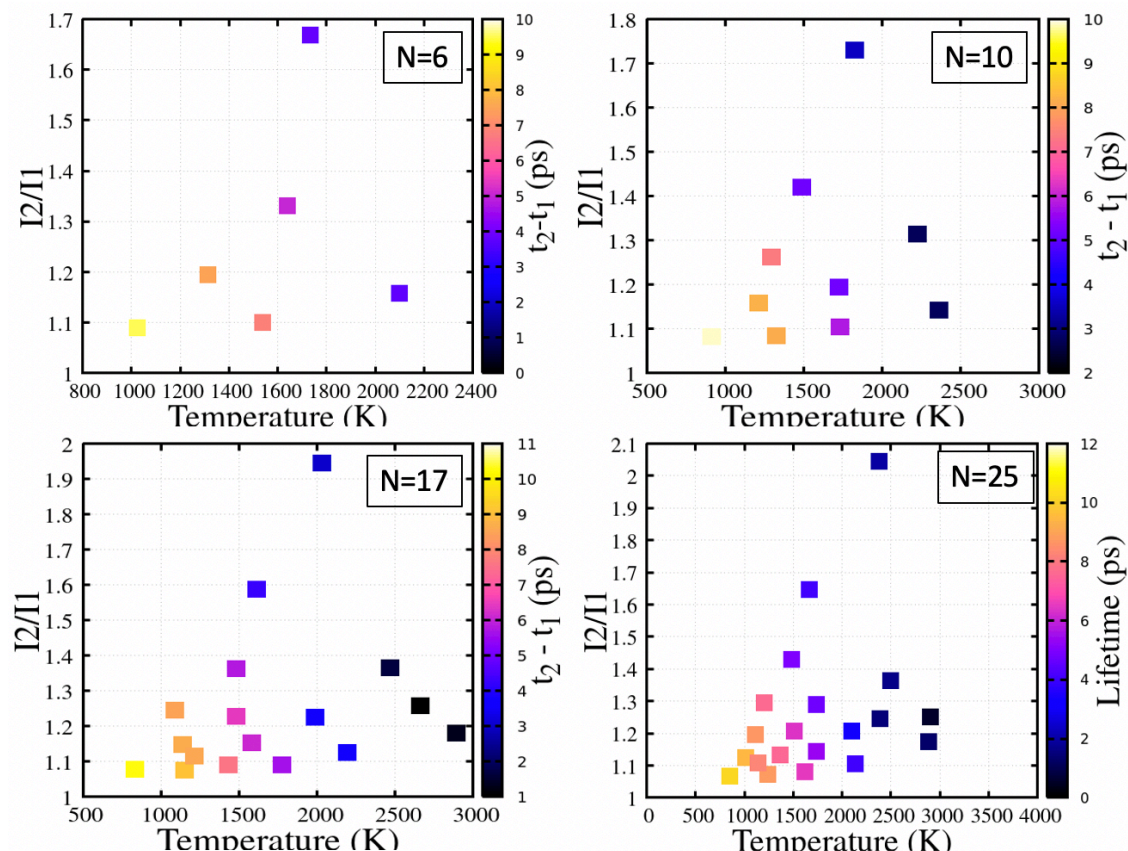
Figure 5.5: Cluster centroids for k-means clustering of the same data set used in Figure 5.4 where N = {6, 10, 17, 25}. Color of each centroid is Δt_{rxn} time.

While the cluster centroids provide important understanding in the mechanochemistry of hotspots, one of the most neglected aspects of extemporaneous mechanochemistry is the distributions of mechanochemical states found. Figure 5.6 shows the distributions of temperature and Δt_{rxn} for clusters 2, 3, 5, and 6 of the N=6 clustering, as labelled in Figure 5.4. These four clusters were chosen due to the similar temperatures of 2, 5, and 6 with increasing deformations, and the high temperature of cluster 3 that leads to similar Δt_{rxn} as cluster 6. The temperature distributions validate the assumptions about the clusters than can be made from Figure 5.4a), in which cluster 3 is mostly a high temperature tail of the low deformation molecules, and the higher deformations states have slightly higher average temperatures compared to cluster 2 because they contain high temperature tails, albeit a small number of molecules in them.

For the reaction timescale distributions, cluster 2 follows a Poisson distribution, which is the same as the Hugoniostat simulation, which should mimic a bulk shock without a hotspot. Hence,

the undeformed molecules of the hotspot are not overly different than the molecules that react without a hotspot due to strong shocks, which should be similar to high pressure, thermal chemistry. As expected from the average values being lower than that of cluster 2, the distributions of clusters 3, 5, and 6 and shift leftwards and narrow. However, rather unexpectedly, they begin to change shape, with the highest deformation cluster, cluster 6, being an exponential distribution, indicating a significant infant mortality.

The Poisson and exponential distributions, as well as their intermediate states, can be continuously described by the engineering Weibull distribution, which has two free parameters, one for the average (λ) and one for the shape (k):

$$f(x, \lambda, k) = \frac{k}{\lambda} \left(\frac{x}{\lambda}\right)^{k-1} e^{-\left(\frac{x}{\lambda}\right)^k}$$

In engineering studies and manufacturing, the Weibull distribution is often utilized as a mathematical model for part/material failure lifetimes. High k values lead to the Poisson distributions and low k values lead to exponential distributions. Processes that are well modeled by the Poisson distribution are characterized by materials failing through aging/fatigue. This is a standard end of life description. The exponential distribution, as previously noted, describes infant mortality, or unexpected early lifetime failure. Therefore, as an analogy, the undeformed molecules of cluster 2 are similar to fatigue-based end of life failure, whereas the highly deformed molecules of cluster 6 are similar to materials/parts that fail early on due to processing defects, which in this case are intra-molecular deformations brought on by plastic flow.
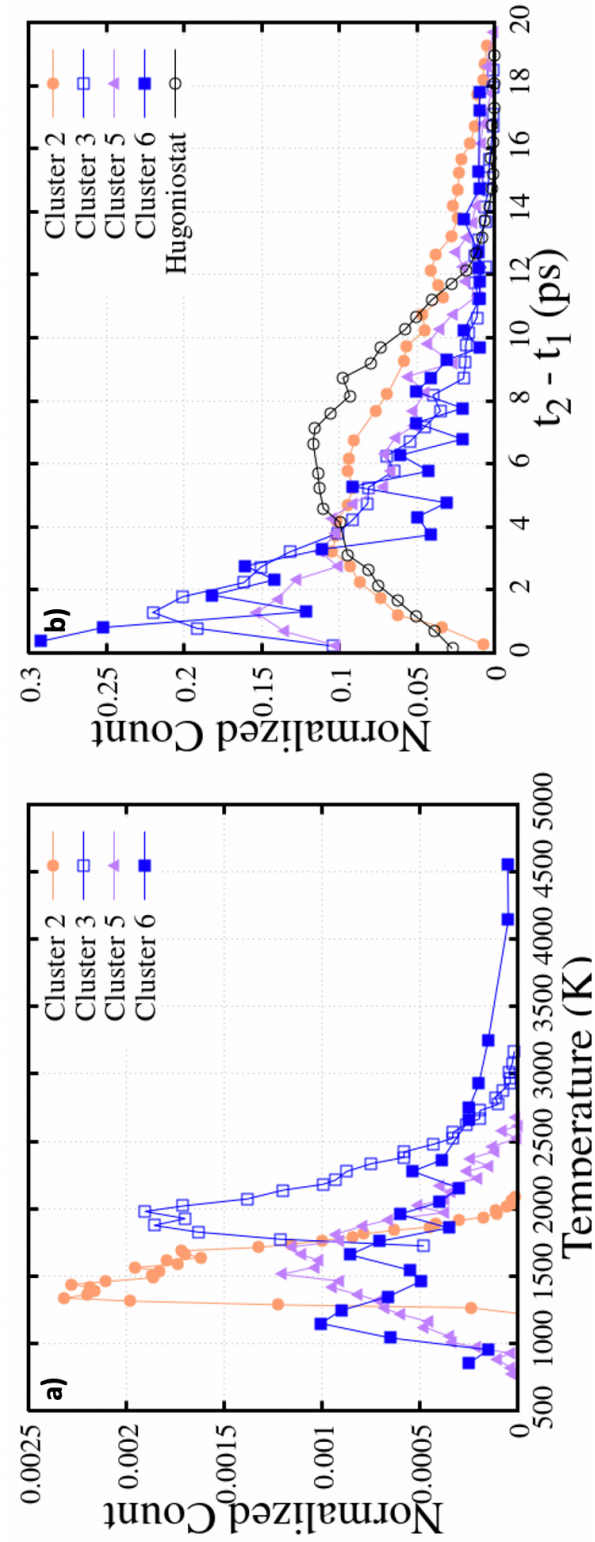
Figure 5.6: Temperature and $t_2 - t_1$ distributions for clusters 2, 3, 5, and 6. The Hugoniostat cluster comes from a shock along [001] in a perfect crystal to 50 GPa (~2200 K).

Between each cluster there are markedly different kinetics due to intra-molecular deformations. The remaining question is are these kinetic accelerations due to deformations lowering the activation barriers or altering reaction paths in a way that accelerates chemistry. For each of the six clusters, the first reaction step of each molecule can be determined, with counting done for the three most common reactions: intra-molecular hydrogen transfer, inter-molecular hydrogen transfer, and NO_2 scission. Figure 5.7 shows the percentage of each of these three reaction paths for all six clusters, with schematics of each reaction provided.

For the NO_2 scission reactions, the amount of reactions seems to been invariant to the cluster, which is an interesting contribution to previous works that showed shear banding increases NO_2 production in TATB [51]. The trends for the intra- and inter-molecular hydrogen transfer effectively mirror each other, with the amount of inter-molecular hydrogen transfer reactions, the secondary reaction with higher activation barrier, increasing with both increasing temperature (cluster 3) and increasing deformation (cluster 5 and cluster 6) as compared to the hotspot baseline (cluster 2).

While the results from using the clustering technique over a single hotspot provide significant insight into the mechanochemical events that go on, the data is not robust enough to generate a model of hotspot chemistry and reactive pore collapse simulations are computationally costly. The remainder of this chapter will be dedicated to developing and implementing a simple model for replicating deformations and mimicking extemporaneous chemistry events under equilibrium.
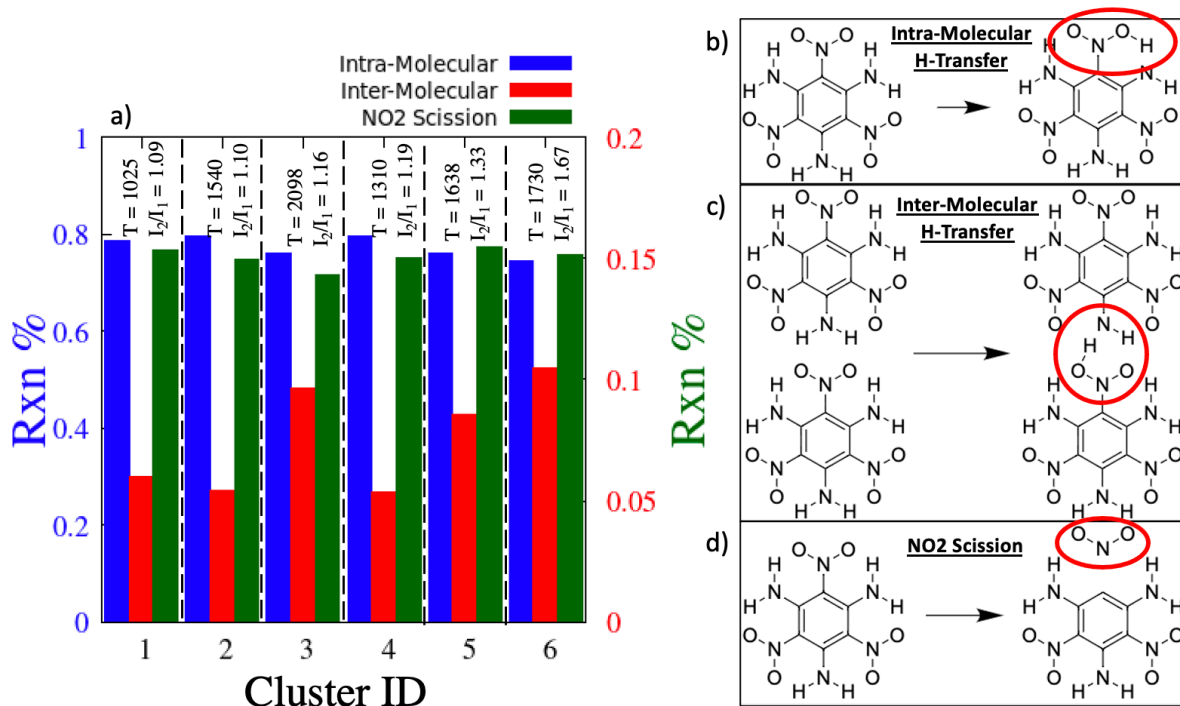
Figure 5.7: a) bar chart of the available reactions for each cluster, inter-molecular (red) and nitro group scission (green) follow the secondary y-axis on the right. b-d) Schematic representations of each of the three reactions.

5.4 Many Bodied Steered MD

The states of deformed molecules (that lead to high PE) that are discussed in Chapter 4 are most analogous to springs trapped in a box. A compressed spring (or deformed molecule) will want to naturally expand back to an equilibrium configuration. However, if a confining box, analogous to the surrounding molecules compressed to shock pressure in Chapter 4, restricts the spatial configurations of the spring, in must stay in the compressed state, unable to relax until the box relaxes.

As was shown in Section 5.3 and previous works such as Refs [51,52,61,132], extracting molecular level mechanochemical responses from large systems that undergo extemporaneous mechanochemistry can be incredibly challenging due to the noise, extreme conditions, and relatively small sample sizes of MD. Therefore, the methodology developed and described here aims to apply an external field that mimics the box that compresses the spring. However, each

simulation will have the external field applying the same deformation (with stochastic fluctuations) to every molecule in the system such that the chemical response can be parametrically mapped. This methodology has been dubbed Many-Bodied Steered Molecular Dynamics or MB-SMD.

MB-SMD is applied through using an explicit forcefield and bonding topology. In non-reactive forcefields, such as the Bedrov potential [68] described in Section 2.2, bonds, bond angles, and dihedrals are precisely listed with each atom. I.e., a list of bonds has two atom IDs per bond listed and a list of angles has 3 atoms IDs listed where 2 of the sets of two atoms are also bonded. The potentials are then defined as functions that control the bond length, angle between bonds, and angles of 4 bodied terms known as proper and improper dihedrals. A proper dihedral is a chain of 4 atoms in which the angle is the angle between the planes made by each of the outer two atoms with the center bonds (for dihedral ijkl, planes ijk and jkl). An improper dihedral is a central atom with 3 atoms bonded to it, and the angle is the out of plane bending (also defined as the angle between ijk and jkl where i is the central atom). These four-bodied systems are controlled using simple functions like a harmonic potential where

$$E = K(\phi - \phi_o)^2$$

where ϕ is the current dihedral angle, ϕ_o is the equilibrium angle, and K is a spring constant. If an additional potential is applied to fictitious four-bodied terms on top of the normal forcefield, then the molecule would deform according to the external potential. Hence, it follows that one or a series of external potentials can be used to mimic the complex deformation states found in the PE hotspots of Chapter 4 and the reactive hotspot of Section 5.3. Appendix B shows the LAMMPS implementation of MB-SMD.

Figure 5.8 shows the distributions of the deformations found in the 2.0 kms (001) cylindrical pore collapse from Chapter 4. The two primary deformations experienced by the outer nitro and amino groups are out of plane bends and in plane rotations. Compared to the normal fluctuations of a 300 K crystal, these deformations have significantly longer tails. The out of plane bend deformation is controlled by an improper dihedral that a ring carbon as the central atom and the neighboring carbons and the nitrogen of the NO_2 group, as shown in Figure 5.9. By altering the angle of the improper dihedral, the NO_2 group will bend out of plane such that the C-C-C and C-C-N planes make an angle that is normally 0° in TATB. The in-plane rotation of the NO_2 group is controlled by the proper dihedral of C-C-N-O, as shown in Figure 5.9, where the NO_2 group will rotate around the C-N bond, keeping the C-N bond nominally in the plane of the carbon ring.
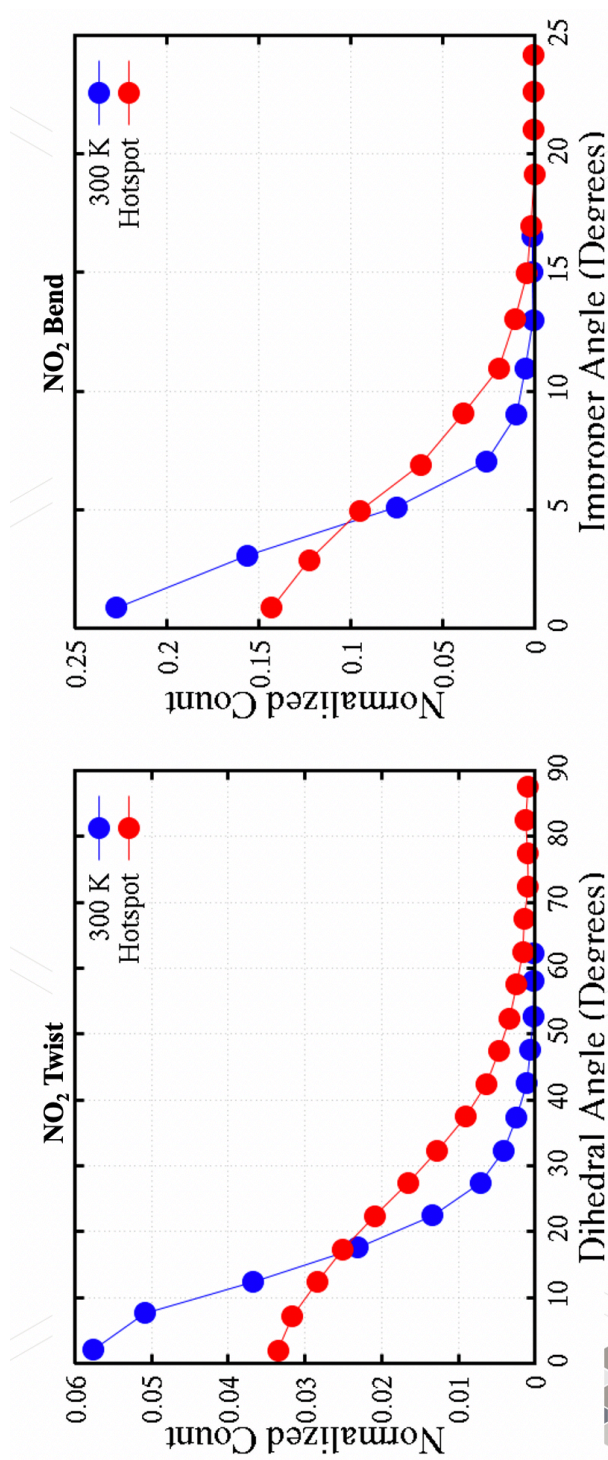
Figure 5.8: Distributions of out of plane bend (bend) and in plane rotations (twist) of NO_2 groups from nonreactive 2.0 km/s cylindrical pore collapse simulations from Chapter 4. Blue distributions are from an isothermal isochoric simulation of a perfect crystal.
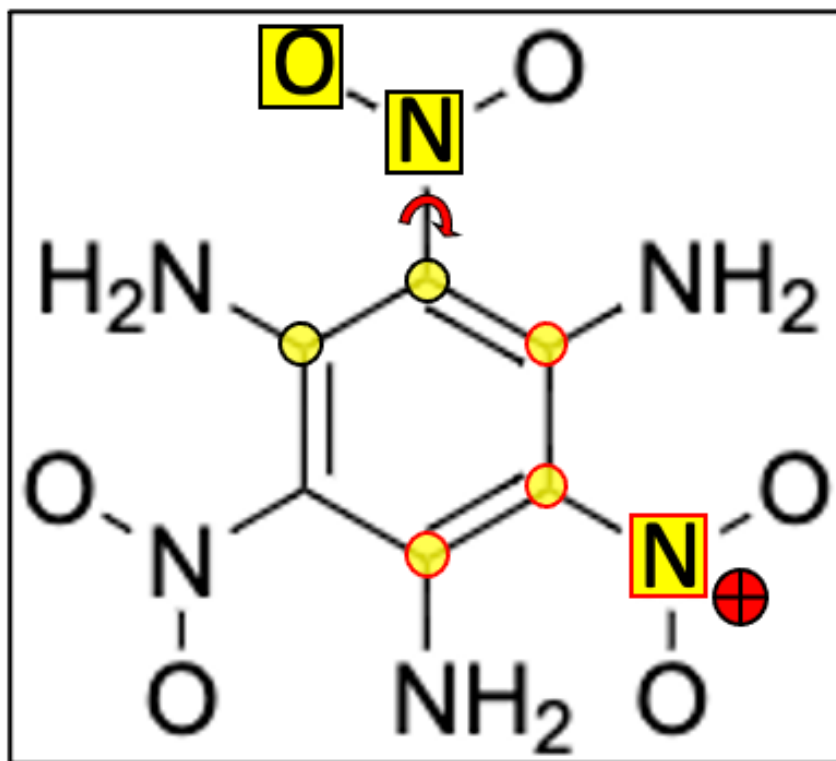
Figure 5.9: Out of plane bend and in plane rotation deformations of NO_2 groups. Red and black arrow represents rotation around C-N bond. Red and black '+' represents out of page motions. Yellow atoms with red border are included in the out of plane bend improper dihedral and yellow atoms with a black border are in plane rotation proper dihedral atoms.

Simulations of TATB perfect crystals in which one of these two deformations is placed on all NO_2 groups of all molecules are conducted under isothermal isobaric conditions at 300 K and ambient pressure. By continually updating (and increasing) the set angle of the external potential, ϕ_o, it can be shown how the molecules responds to these fields. Since all atomic dynamics are primarily controlled via the ReaxFF potential, applying an external field will fight against ReaxFF's desire for the molecule to be undeformed, leaving the actual state of the molecule to be $0 < \phi < \phi_o$. Figure 5.10 shows a scatter of set angle (ϕ_o) and measured angle (ϕ) with an $f(x) = x$ parity line. As expected, the points all fall below the parity line for angles greater than thermal fluctuations of an undeformed molecule. Interestingly, there is a bilinear response of the angle, which changes slope at (30°, 21°). This corresponds to a conformational change in the TATB

138

structure, where the central carbon ring buckles to a herringbone state and the NO_2 and NH_2 groups can more freely rotate with respect to the ring. This conformation is not stable under ambient conditions but has potentially been seen experimentally for high pressures [241].
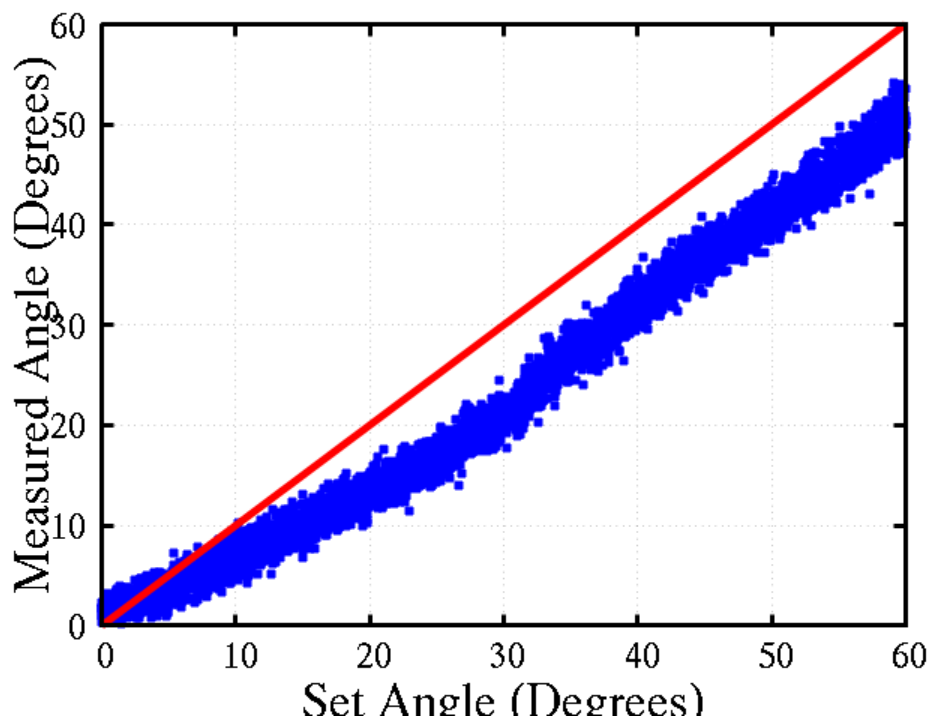
Figure 5.10: Parity plot of the actual measure NO_2 improper angle against the external potential set angle. Red line is a y=x parity line.

To inspect the state of all molecules within a TATB crystal, 250 molecules total, at a given time and a given level of deformation, Figure 5.11 shows the measured angle distribution for 300 K and ambient density with the MB-SMD parameters set to $K = 200\ kcal/mol$ and $\phi_o = 30°$. Half of the NO_2 groups point upwards, and half downwards, which is related to the crystal layering and the handedness of the molecules with respect to how the improper angle is defined. Additionally, the normal distribution of points represents the width of the fluctuations of the improper, where the standard deviation of this distribution can be slightly controlled with the spring constant parameter.

Figure 5.12 shows the resulting spread of average measured angles for a range of set angles and spring constant values, which shows that a larger spring constant, as expected, allows the external potential to "fight" against ReaxFF better and results with points closer to the parity line.

The plot should approach parity as the spring constant approaches infinity, however, an overly larger spring constant will result in unphysical vibrational dynamics for the controlled degree of freedom.

The following section will apply MB-SMD constraints to high temperature simulations that incur thermal decomposition of the TATB molecules. This will allow a parametric mapping of how these deformations effect reaction kinetics and 1st step reaction pathways.
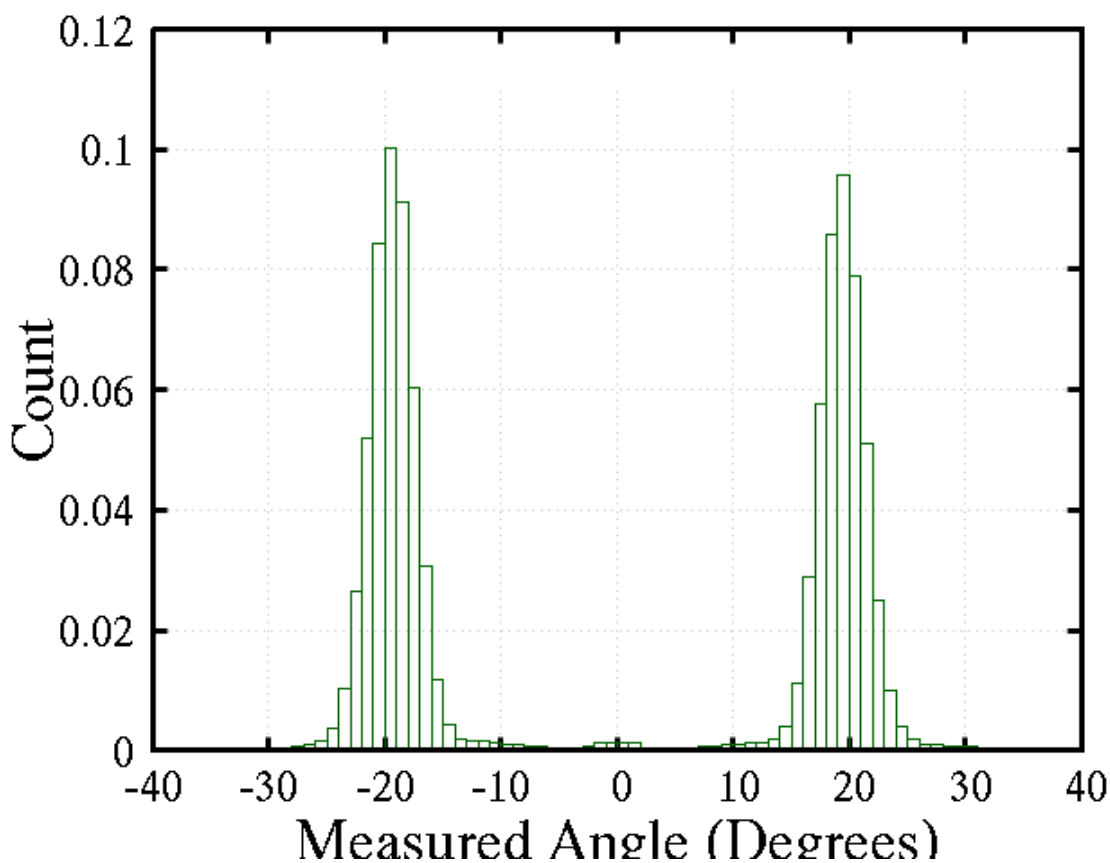
Figure 5.11: Distribution of measures improper angle states for 250 molecules in a crystal with the spring constant and set angle at 200 kcal/mol and 30°, respectively.
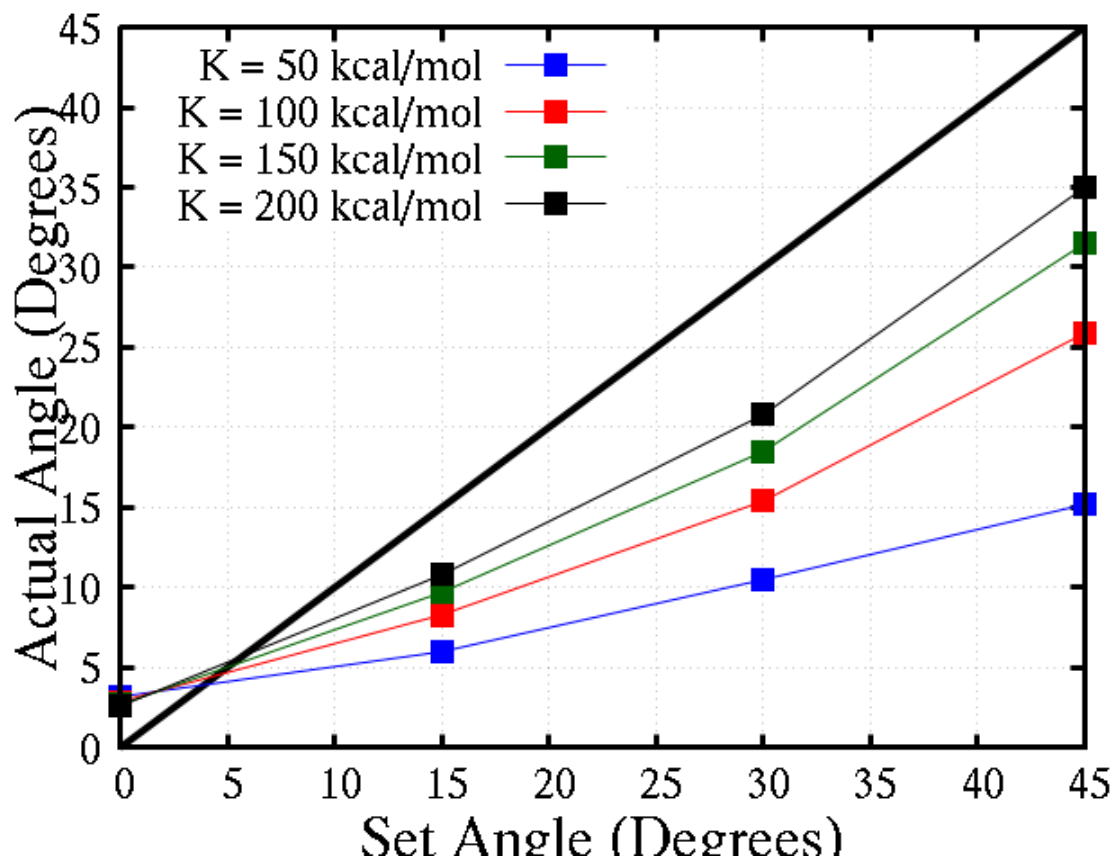
Figure 5.12: Parity plot of measured vs. set angle of the out of plane bend for a variety of spring constant and set angle choices.

5.5 Mechanochemical Kinetics Modeling and Alteration of Reaction Paths

Thermal decomposition simulations are performed in the setting of Kissinger, where kinetics can be obtained from heating samples through the onset of chemical reaction at different heating rates [242]. Here, TATB samples are heated from 1000 K to 3000 K and the external potential is turned on prior to heating to pre-deform the molecules. Figure 5.13 shows an example of this for a single spring constant for four of the utilized set angles. In this plot, the slopes of the lines are $-E_a/R$ where E_a is the activation barrier and T_d (the x-axis) is taken to be the temperature in which the ReaxFF internal potential energy is maximized.
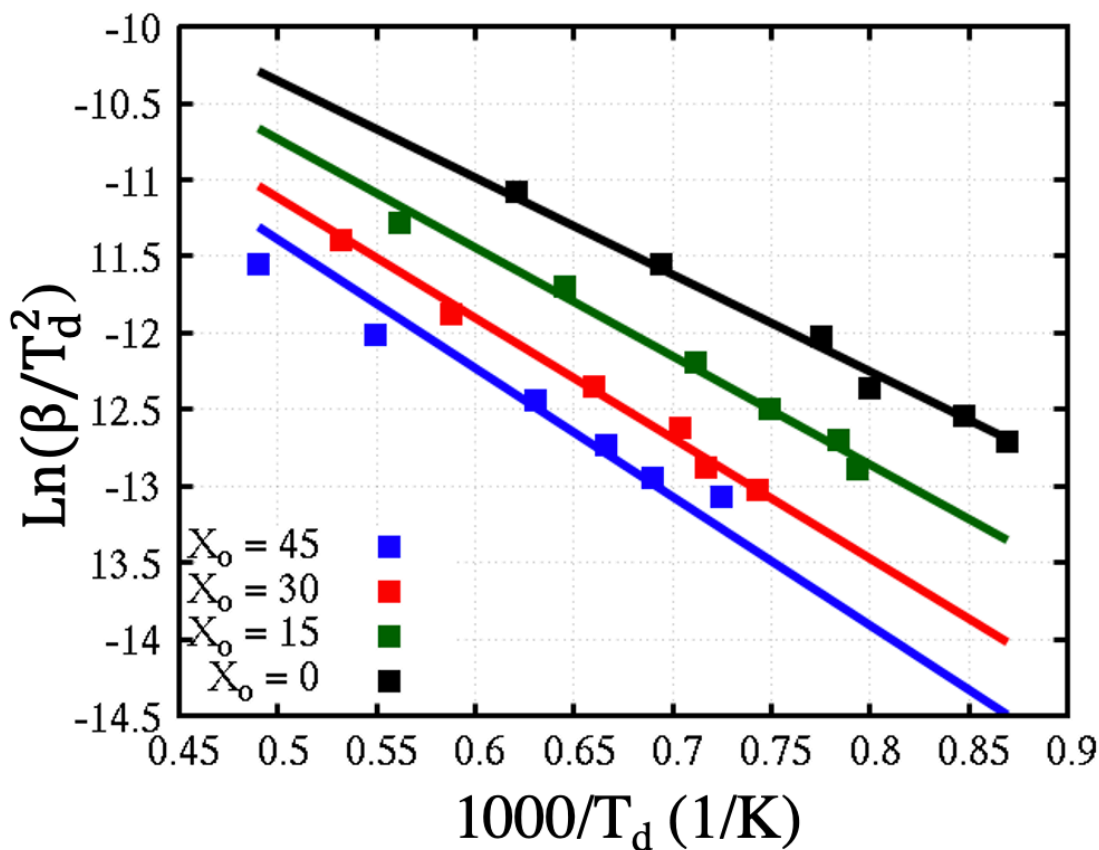
Figure 5.13: Kissinger kinetics summary plot for a variety of set angle values and heating rates for a spring constant of 100 kcal/mol. Color represents set angle, Td is taken to be the temperature when internal PE from ReaxFF is at a maximum. β is the heating rate.

From the activation barriers in Figure 5.13, as well as for a wide range of set angles and spring constants for both the out of plane (improper) deformation and the torsional (in plane rotation) deformation. Figure 5.14 shows a summary of all of the activation barriers, with the green star representing the activation energy for a system with no MB-SMD potential applied. The points with higher barriers than that of the undeformed system are points with the set angle chosen to be zero with a non-zero spring constant, which leads to a limiting of the DoF vibrations, which slows chemistry.

For both deformations, the activation energy response with the measured deformation level is linear, with the out of plane deformation showing a slight change in slope at ~20°, which is where the conformational change takes place. The linear response is somewhat expected based on the Bell model, described in Section 5.1, where the barrier decreases linearly with the applied force

for a constant reaction coordinate. Taking a derivative of the MB-SMD energy equation with respect to angle, which does not explicitly result in force, gives a linear equation with respect to set angle. Hence, if we assume the applied force is roughly linear with angle, then it tracks that the decrease in activation energy should be linear. Additionally, each set of points (different deformations) has four different spring constant choices in the data, showing that the activation barrier response is mostly invariant to the choice in spring constant. Figure 5.15 shows the data for the out of plane deformation, re-plotted where the y-axis is a decrease in E_a such that the reference is the green star point from Figure 5.14. The points are colored by spring constant, which shows that the highest spring constant (200 kcal/mol) leads to a slightly higher decrease, but outside of this, there is no trend with spring constant. Potentially, the value of 200 kcal/mol is nearing the point at which the external potential is artificially altering the molecular vibrations unphysically.
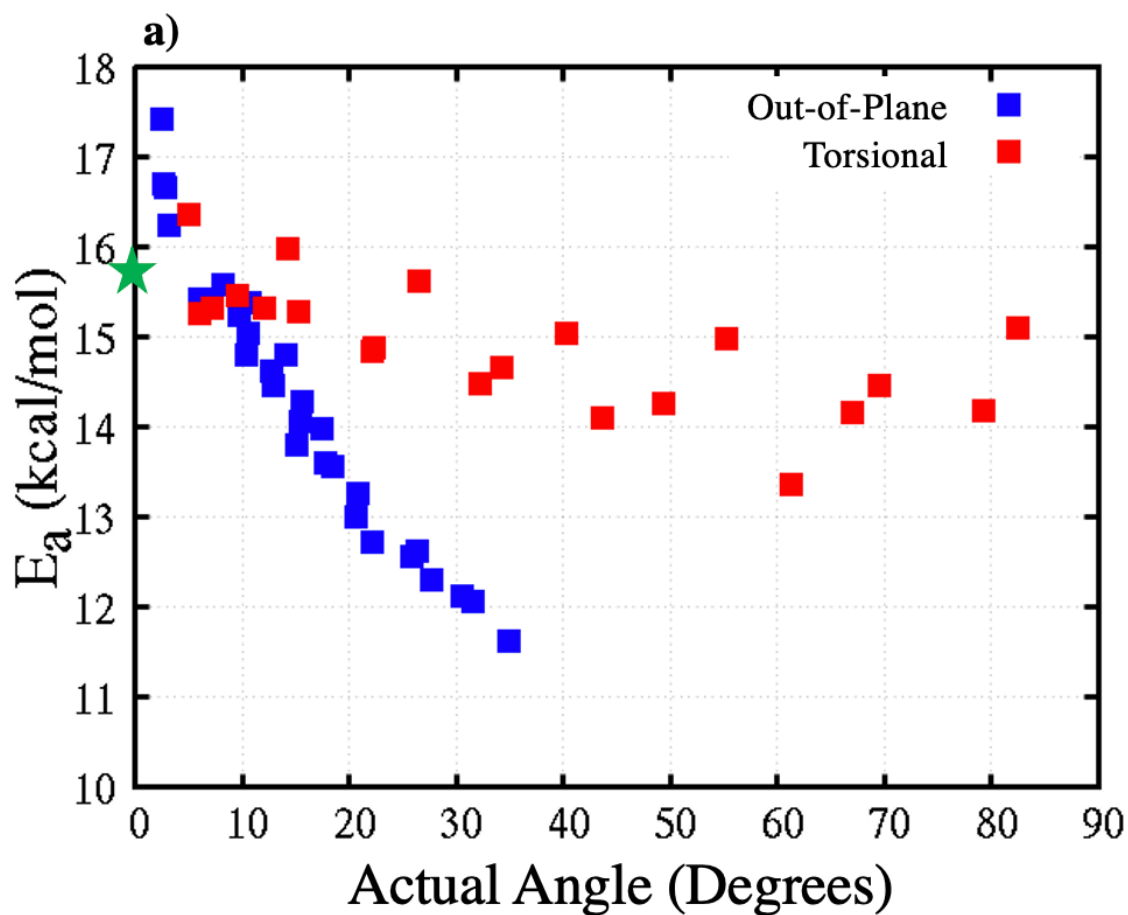
Figure 5.14: Activation energy for both the in-plane torsional rotation (red) and out of plane improper bend (blue) deformations at a variety of external potential parameters. Green star represents the activation energy of the undeformed system.
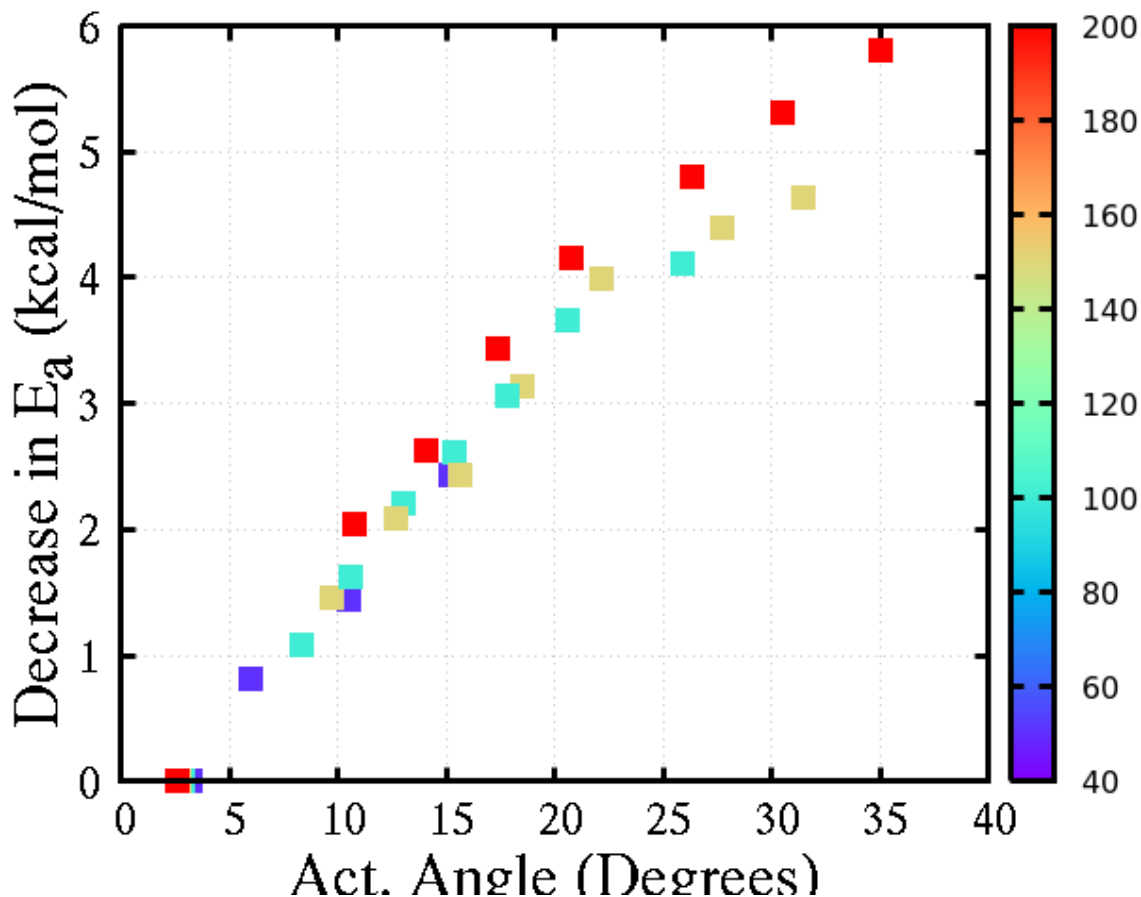
Figure 5.15: Decrease in E_a for out of plane deformations, colored by spring constant.

The interesting response is the significant difference in slope for the two different DoF. However, the resulted energy change in the system is not inherently the same for different deformations, despite the external potential function being the same harmonic function. In Figure 5.16, the results of Figure 5.14 are replotted where the y-axis is set to the decrease in activation barrier like in Figure 5.15, and the x-axis is set to be the rise in ReaxFF potential energy (no external potential energy contributions) due to the deformation at 300 K (no chemical reactions). This shows the same linear increase and bilinear slope change for the out of plane improper dihedral deformation. This also better validates the conclusion from the previous two figures that deformation of different degrees of freedom (different reaction coordinates) leads to highly different alterations in the activation barrier, even though the applied external potential energy is of a similar value. These DoFs correspond to different reaction coordinate values in the Bell model described in Section 5.1.
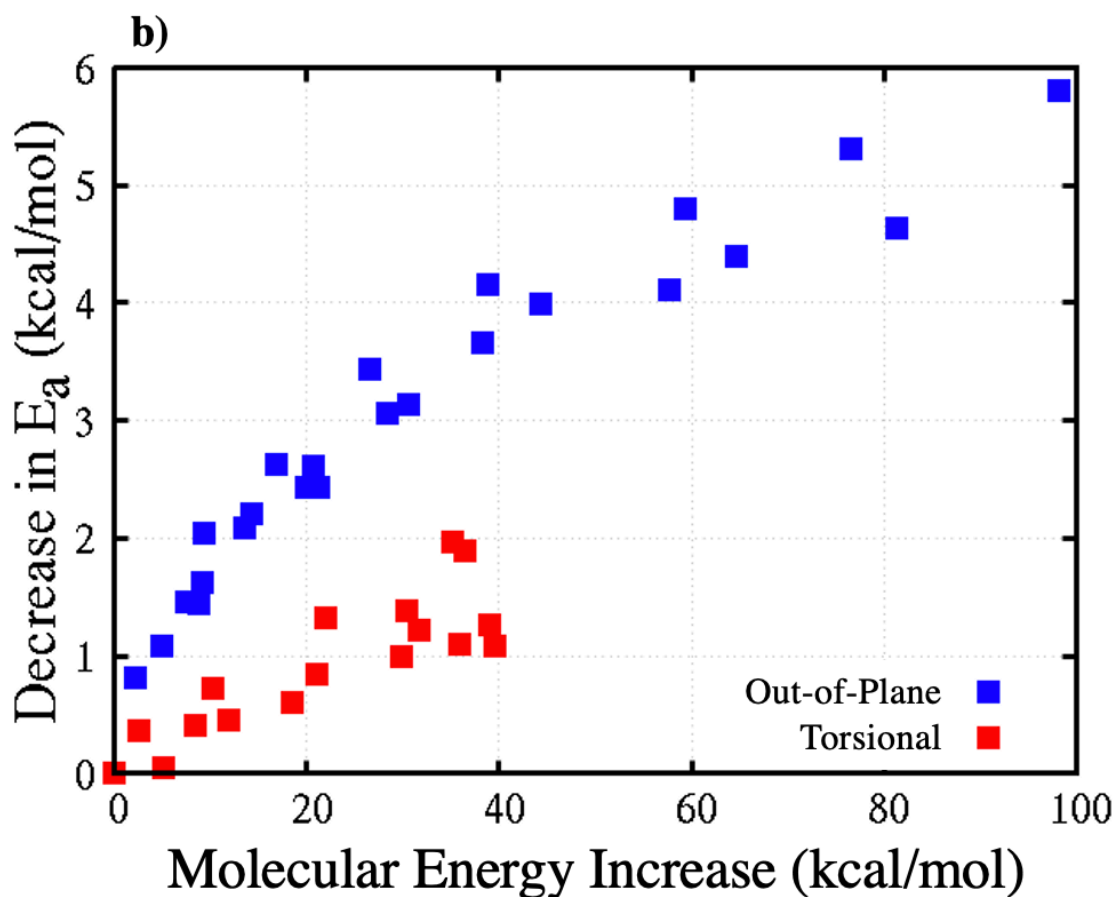
Figure 5.16: Decrease of the activation barrier for a given deformation state plotted for the rise in ReaxFF potential energy at the 300 K deformed state, which is before any chemical reactions occur.

Lastly, for kinetics, it is essential to acquire simply models that describe the kinetics for any given deformation. Using the Bell model, one can fit the function $E_a = E_{a_o} - F * x$, where the $F * x$ term is replaced by the deformation angle multiplied by a free parameter for fitting. Different fits are done for below and above the conformational change for the out of plane deformation and excluding the high deformation points of the torsional deformation, which appear to level off, using the form $\Delta E_a = F * x = m * \phi - b$. Figure 5.17 shows these best fits and Table 5.1 shows the fit parameters. The change in slope for the out of plane deformation tracks almost perfectly to the occurrence of the conformational change in the molecule. The level off in the torsional deformation can be explained in a similar argument for the molecular state.

146

The deformations are applied only to the NO_2 groups, which are hydrogen bonded to the NH_2 groups of first nearest neighbor molecules. Tracking the dihedral angles of the NH_2 groups, shown in Figure 5.18, they reach a maximum at the same angle in which the activation energy decrease begins to level off. This shows that, up to a point, the NH_2 groups deform with the NO_2 groups, until it becomes more energetically favorable to break the hydrogen bonding between them and structurally relax. These conformational changes leading to different kinetics alludes to a possible change in 1st step reaction pathways as opposed to the kinetics changing merely due to a slightly different reaction coordinate along the same degree of freedom and 1st step reaction.

Table 5.1: Best fit parameters for the out of plane and torsional deformations using a Bell type model.

Deformation	Slope (kcal/mol per degree)	Intercept (kcal/mol)
Out of Plane Lower (red)	0.21	-0.56
Out of Plane Higher (black)	0.14	0.81
Torsional Lower (red)	0.03	-0.26
Torsional Higher (black)	0.00	1.43
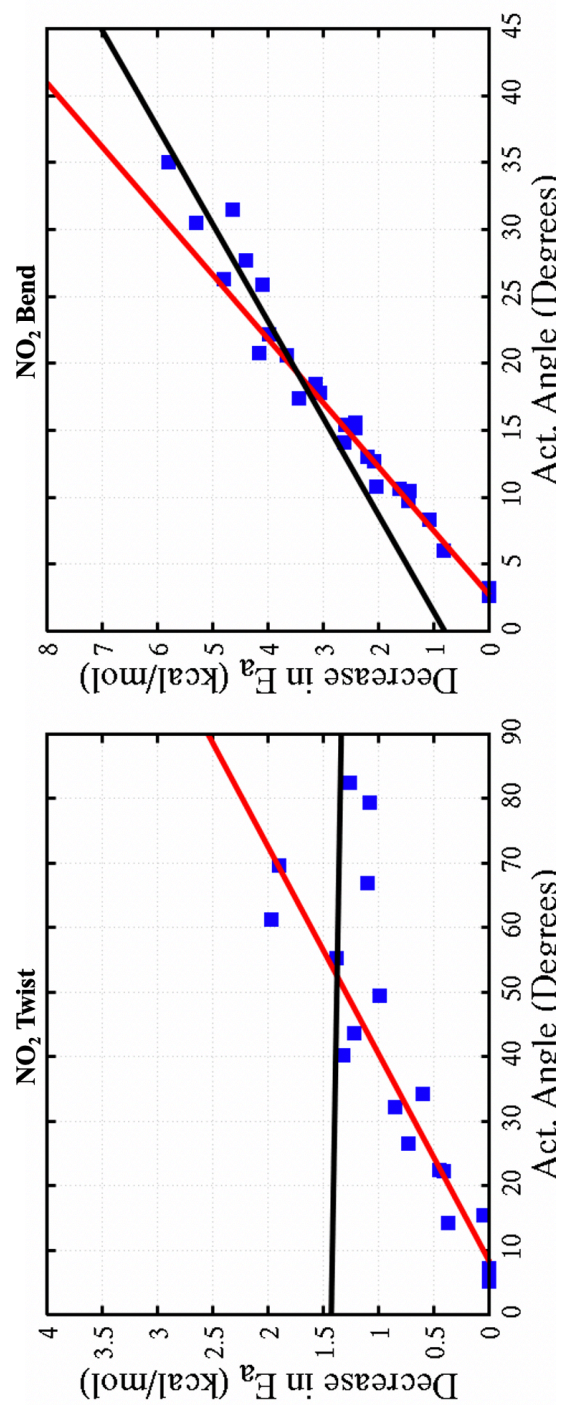
Figure 5.17: Decrease in activation energy plots with overlayed best fit functions for Bell type models of activation energy.
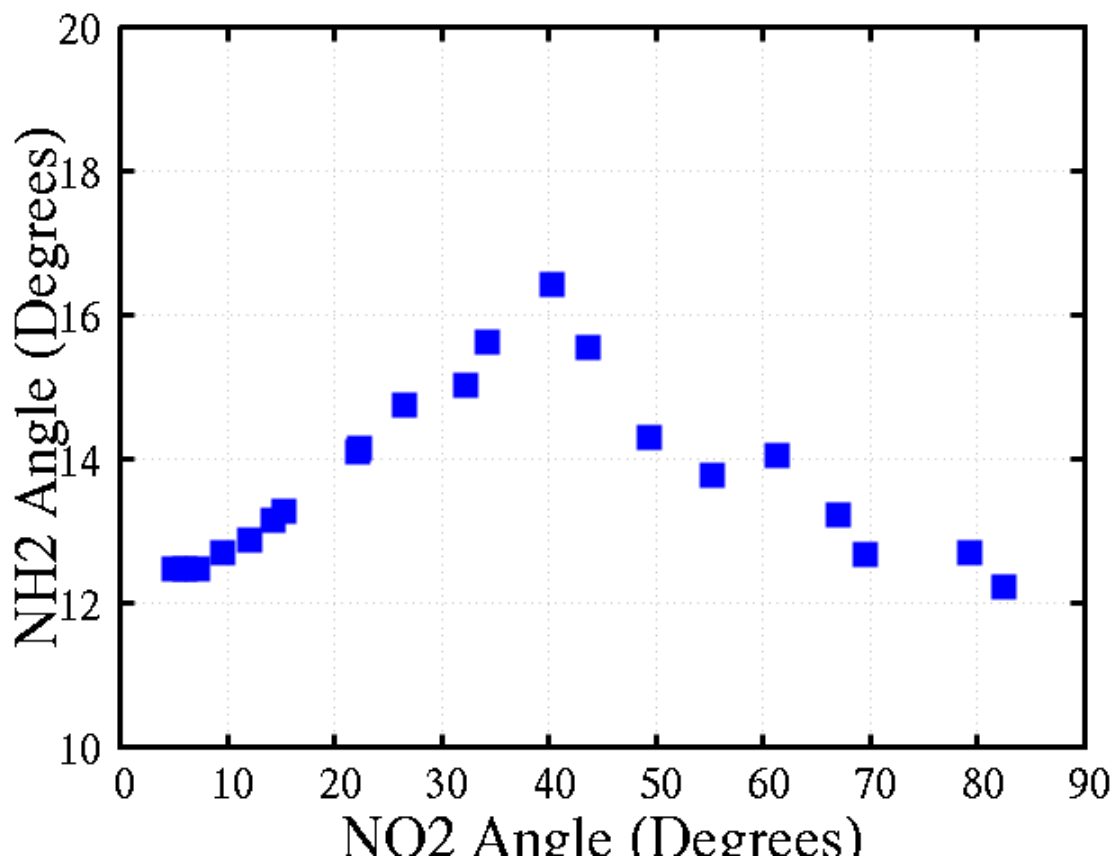
Figure 5.18: NH$_2$ group proper dihedral angle evolution during NO$_2$ proper dihedral angle deformation.

Using the inherent bond order calculations in ReaxFF, the first step reaction pathway of each molecule under each deformation can be calculated. As expected for thermal TATB chemistry, undeformed molecules undergo intra-molecular hydrogen transfer almost 100% of the time. The two primary alternatives are inter-molecular hydrogen transfer and nitro group scission, with the hydrogen transfer being the lower activation barrier, which is still roughly 10 kcal/mol higher than the intra-molecular reaction [34]. For the torsional deformations, the low deformation states all react as intra-molecular hydrogen transfers, with the inter-molecular transfer mechanism becoming active at roughly 40°, which is where the NH$_2$ groups begin to relax. The deformation forces the inter-molecular transfer to become the dominant deformation at around 60°. This alteration of path is potentially due to the NO$_2$ groups increasing in distance from the NH$_2$ groups within the same molecule, without much increasing in distance from neighboring molecule groups.

For the out of plane deformation, there is also an alteration in reaction path, however this is almost entirely NO_2 scission reaction beginning to occur at ~20°, which is where the conformational change occurs. This deformation puts strain directly on the C-N bond and drives the NO_2 group away from any NH_2 groups, on the same and neighboring molecules. These results track well for the results from the pore collapse in Section 5.3, where more intra-molecular deformation led to increased inter-molecular hydrogen transfer reactions, and in Ref. [51], where shear bands increased the amount of NO_2 formation that occurred.
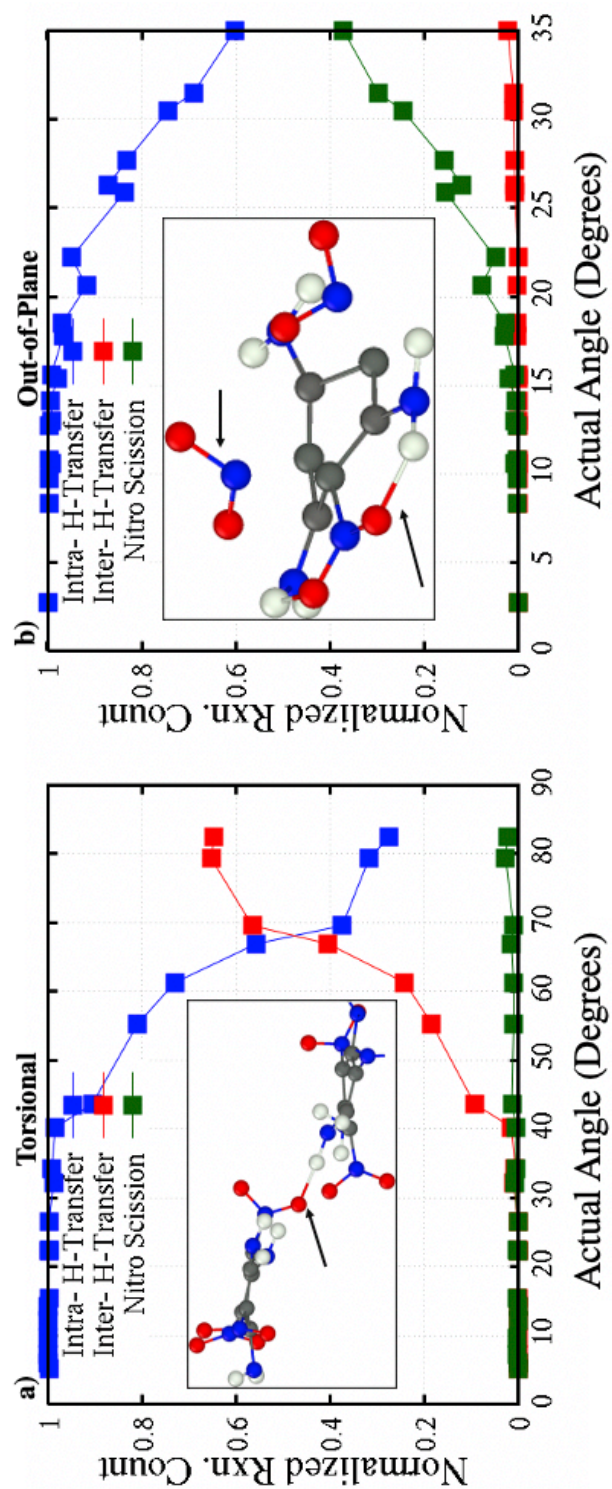
Figure 5.19: Normalized counts of 1st step reaction pathways for each level of deformation for the two applied deformations, torsional and out of plane. Inset figures shown an inter-molecular hydrogen transfer (left) and both NO2 scission and intra-molecular hydrogen transfer (right).

5.6 Conclusions

In this chapter, the mechanochemical effects of hotspots and intra-molecular deformations were explored. Mechanochemistry is an increasingly well-studied topic that has mainly focused on simple applied forces that extend covalent molecules in a linear or 1-dimensional fashion. Here, the ideas are extended to many bodied deformations that molecules are know the undergo (see Chapter 4) during the formation of a hotspot, especially shock induced pore collapse. Using a ReaxFF reactive MD calculation of shock induced pore collapse in TATB, molecules in the hotspot were clustered based on their temperature and level of intra-molecule deformation. This showed that, not only do more deformed molecules react quicker than undeformed ones at the same temperature, but they also follow somewhat different reaction statistics that is characterized by infant mortality. Additionally, these deformed molecules are more likely to undergo alternate 1st step reaction pathways such as inter-molecular hydrogen transfer.

Due to the considerable noise in the thermodynamics and kinetics of the hotspot calculation, a new methodology, known as Many-Bodied Steered Molecular Dynamics, was developed and applied to TATB molecules to mimic the deformations seen in hotspots, but under controlled conditions. MB-SMD applies an external field to specific four-bodied terms within the molecule, leading to complex intra-molecular deformations.

Mimicking the deformations shown in Chapter 4, MB-SMD shows that out of plane bending of NO_2 groups is significantly more efficient at accelerating reactions that in plane torsional rotations. Additionally, the in plane torsional rotations lead to an increase in inter-molecular hydrogen transfers, as was seen in the pore collapse calculation, yet the out of plane bending leads to NO_2 scission reactions, which is known to occur in shear banding.

The MB-SMD results are applied to simple, continuum kinetics models for mechanochemistry, which can predict the kinetics for different deformations, but must be parametrized for each. This method presents a simple route forward for parametrically studying extemporaneous mechanochemistry and mechanochemistry at extreme conditions with a low computational cost compared to simulating the actual extemporaneous event. It can also be readily applied to other topical challenges such as polymer mechanochemistry and the shock induced formation of prebiotic compounds.

6. SUMMARY AND OUTLOOK

Overall, the primary aim of this collection of works is to increase the community's overall depth of understanding into how energy localizes in molecular crystals, such as HEs, and how that localization can affect chemical reactivity and initiation. Specifically, the first set of results focused on how using the classical vs quantum description of energy, within the vibrational energy of the molecule and crystal, can influence shock and thermal initiation. This unraveled the importance of zero-point energy effects in the thresholds and timescales of chemistry and characterized interesting TATB specific effects in how low frequency modes are vital to first step reaction pathways.

The following results chapter, Chapter 4, began to explore energy localizations above that of the molecular scale, targeting hotspots. Hotpots, excess energy localizations in the crystal due to interactions between the shockwave and microstructure, are one of the dominant phenomena that influences run to detonation and detonation failure, as well as shock sensitivity. Through inspection of simulations of the shock induced collapse of porosity in TATB, it was discovered that, in hotspots, there is a significant excess of intra-molecular potential energy. This potential energy, which is latent in nature, provides a hypothesis as to why dynamically formed hotspots are more reactive than ones formed under purely thermal conditions: mechanochemistry. As the source of this latent PE is intra-molecular strain, it follows that these deformations could alter the reactivity of the local system. The latent PE is further characterized to understand the role of various pore collapse independent variables such as shock strength, pore geometry, and crystallographic orientation. The trends in PE that follow surmise one overarching conclusion: while local P-V work may be the dominant factor in maximizing hotspot temperature, local plastic flow is the dominant factor in localization of latent PE. Furthermore, the two factors do not necessarily coincide with one another.

To assess the claims that a hotspot's latent PE can lead to local, mechanochemical acceleration of reaction kinetics, Chapter 5 turns to reactive molecular dynamics simulations of pore collapse using the same general set up as the main pore collapse simulation in Chapter 4. By clustering molecules in the hotspot using temperature and intra-molecular strain as descriptors, direct trends with increase temperature or strain can be determined. Not only do molecules with high strain undergo faster decomposition, but their decomposition statistics are also altered. Undeformed

molecules follow a Poisson like distribution, whereas deformed molecules undergo decomposition timescales following an exponential decay. Lastly, inspecting first step reaction amounts from each cluster shows that deformed molecules are more likely to undergo non-primary reaction pathways. However, in trying to create simple mechanochemistry models from this hotspot, there is too much noise and the temperature and molecule strain descriptor I_2/I_1 (which is highly degenerate) do not provide enough information to produce accurate models or scaling laws.

To better model these deformed molecules, the method of Many-Bodied Steered Molecular Dynamics is developed. In MB-SMD, an external field is applied to all molecules of a system under equilibrium causing them to deform in such a way that in mimics the intra-molecular strains found in pore collapse simulations. Isothermal decomposition simulations of molecules with different levels of deformation are conducted in which the kinetics are shown to follow Bell's law. Additionally, deformations of the same energy level but on different degrees of freedom results in markedly different kinetics. Lastly, deformations to different degrees of freedom are also shown to activate different, alternative 1st step reaction pathways. The statistics and implementation of MB-SMD are discussed.

As a whole, the energetic materials community has yet to solve the grand challenge of why hotspots are so reactive and how to properly model them in a bottom-up fashion. Current ignition and growth models rely on phenomenological modeling, fit to experiments. There is yet to be a valid and consistent route for predicting sensitivity and detonation events from first principles and microstructural information alone. Simulations that target the fundamental physics of hotspots, like MB-SMD, will be crucial tools in the coming years in developing better predictive models for how energetic materials behave under extreme conditions.

As experimental diagnostics improve, such as recent in situ IR spectroscopy measurements of shocked explosives [33,35,43], better one-to-one matching with molecular simulations will be available, potentially validating the predictive results shown here. Additionally, as computational powers improve with the inclusion of graphical processing units and as the community begins to reach exoscale computing capabilities, molecular simulations will better reach the time and length scales of experimental measurements to better probe the fundamental phenomena occurring. It is this tandem of experiments and simulation, within a multiscale framework, that the best route forward in energetic materials exists. A route to unlock the fundamental physics and chemistry

that occurs and extreme conditions, while also developing predictive capabilities with high accuracy and low computational cost.

APPENDIX A. SHOCK TRAPPING INTERNAL BOUNDARY CONDITIONS IMPLIMENTATION IN LAMMPS

```
units            metal
atom_style        atomic
boundary          p p p


read_data         Al.data


pair_style     eam/alloy
pair_coeff          * *  ../NiAl.eam.alloy Al


neighbor        2.0 bin
neigh_modify    delay 2
thermo_modify  line one flush yes


compute        spa all stress/atom NULL


timestep          .001
thermo            100
thermo_style        custom step pe ke etotal temp density press pxx pyy pzz pxy pxz pyz lx ly lz


dump              d1 all custom 100 Dump.*.dump id type xu yu zu vx vy vz fx fy fz c_spa[1]
c_spa[2] c_spa[3] c_spa[4] c_spa[5] c_spa[6]
dump_modify          d1 sort id


region            top block EDGE EDGE EDGE EDGE 1150 EDGE units box
group             Top region top
delete_atoms         group Top


region            bot block EDGE EDGE EDGE EDGE EDGE 620 units box
```

```
group           Bot region bot
delete_atoms        group Bot


region          t1 block EDGE EDGE EDGE EDGE 1125 EDGE units box
group           T1 region t1
region          t2 block EDGE EDGE EDGE EDGE EDGE 650 units box
group           T2 region t2
group           Rest subtract all T1 T2


fix             f72 T1 setforce 0.0 0.0 0.0
velocity         T1 set 0.0 0.0 0.0 sum no units box
fix             f73 T2 setforce 0.0 0.0 0.0
velocity         T2 set 0.0 0.0 0.0 sum no units box


fix             f5 Rest nve
run              5000000
```

APPENDIX B. MANY-BODY STEERED MOLECULAR DYNAMICS IMPLEMENTATION IN LAMMPS

SYSTEM INITIALIZATION

units   real

boundary   p p p

atom_style   full

box tilt large

####### DATA FILES

read_data   TATB.data

POTENTIAL INFO – REAXFF AND EXTERNAL MB-SMD

special_bonds   lj/coul 1.0 1.0 1.0 angle yes dihedral yes

improper_style harmonic

improper_coeff 1 200.0 45.0

pair_style   reax/c lmp_control lgvdw yes checkqeq yes safezone 20.0 mincap 1000

pair_coeff   * * ffield-2018 C C N N O H

fix   10 all qeq/reax 1 0.0 10.0 1.0e-6 reax/c

SIMULATION SET UP

timestep   0.025

thermo_style custom step pe ke etotal temp density vol press pxx pyy pzz pxy pxz pyz lx ly lz

thermo   100

fix rbo all reax/c/bonds 200 bonds.txt

fix   spe1 all reax/c/species 1 1 200 species.out element C C N N O H

RUN DYNAMICS

velocity   all create 1000 877158 dist gaussian rot yes

fix   f1 all nvt temp 1000 3000 100.0

run   20000000

REFERENCES

[1]   G. Chapman, J. Cleese, E. Idle, T. Jones, M. Palin, and T. Gilliam, *The Spanish Inquisition*, in (BBC1, Unoted Kingdom, 1971), p. Series 2, Epsiode 2.

[2]   B. W. Hamilton, M. N. Sakano, C. Li, and A. Strachan, *Chemistry Under Shock Conditions*, Annu. Rev. Mater. Res. **51**, 101 (2021).

[3]   D. Nna-Mvondo, B. Khare, T. Ishihara, and C. P. McKay, *Experimental Impact Shock Chemistry on Planetary Icy Satellites*, Icarus **194**, 822 (2008).

[4]   M. S. Powell, P. R. Bowlan, S. F. Son, C. A. Bolme, K. E. Brown, D. S. Moore, and S. D. McGrane, *A Benchtop Shock Physics Laboratory: Ultrafast Laser Driven Shock Spectroscopy and Interferometry Methods*, Rev. Sci. Instrum. **90**, (2019).

[5]   J. W. Forbes, *Shock Wave Compression of Condensed Matter* (Springer Science & Business Media, 2013).

[6]   C. Li, B. W. Hamilton, and A. Strachan, *Hotspot Formation Due to Shock-Induced Pore Collapse in 1,3,5,7-Tetranitro-1,3,5,7-Tetrazoctane (HMX): Role of Pore Shape and Shock Strength in Collapse Mechanism and Temperature*, J. Appl. Phys. **127**, (2020).

[7]   M. A. Wood, D. E. Kittell, C. D. Yarrington, and A. P. Thompson, *Multiscale Modeling of Shock Wave Localization in Porous Energetic Material*, Phys. Rev. B **97**, 1 (2018).

[8]   C. A. Duarte, A. Hamed, J. D. Drake, C. J. Sorensen, S. F. Son, W. W. Chen, and M. Koslowski, *Void Collapse in Shocked β -HMX Single Crystals: Simulations and Experiments*, Propellants, Explos. Pyrotech. 243 (2020).

[9]   P. Zhao, S. Lee, T. Sewell, and H. S. Udaykumar, *Tandem Molecular Dynamics and Continuum Studies of Shock-Induced Pore Collapse in TATB*, Propellants, Explos. Pyrotech. **45**, 196 (2020).

[10] R. Ravelo, T. C. Germann, O. Guerrero, Q. An, and B. L. Holian, *Shock-Induced Plasticity in Tantalum Single Crystals: Interatomic Potentials and Large-Scale Molecular-Dynamics Simulations*, Phys. Rev. B - Condens. Matter Mater. Phys. **88**, 1 (2013).

[11] V. I. Levitas and R. Ravelo, *Virtual Melting as a New Mechanism of Stress Relaxation under High Strain Rate Loading*, Proc. Natl. Acad. Sci. U. S. A. **109**, 13204 (2012).

[12] S. Zhao, T. C. Germann, and A. Strachan, *Melting and Alloying of Ni Al Nanolaminates Induced by Shock Loading: A Molecular Dynamics Simulation Study*, Phys. Rev. B - Condens. Matter Mater. Phys. **76**, 1 (2007).

[13] N. Bourne, J. Millett, Z. Rosenberg, and N. Murray, *On the Shock Induced Failure of Brittle Solids*, J. Mech. Phys. Solids **46**, 1887 (1998).

[14] L. R. Rothstein and R. Petersen, *Predicting High Explosive Detonation Velocities from Their Composition and Structure*, Propellants, Explos. Pyrotech. **4**, 56 (1979).

[15] W. J. M. Rankine, *On The Thermodynamic Theory of Waves of Finite Longitudinal Disturbance*, in *Classic Papers in Shock Compression Science*, Vol. 160 (1998), pp. 133–148.

[16] B. L. Holian and G. K. Straub, *Molecular Dynamics of Shock Waves in Three-Dimensional Solids: Transition from Nonsteady to Steady Waves in Perfect Crystals and Implications for the Rankine-Hugoniot Conditions*, Phys. Rev. Lett. **43**, 1598 (1979).

[17] M. J. Cawkwell, T. D. Sewell, L. Zheng, and D. L. Thompson, *Shock-Induced Shear Bands in an Energetic Molecular Crystal: Application of Shock-Front Absorbing Boundary Conditions to Molecular Dynamics Simulations*, Phys. Rev. B - Condens. Matter Mater. Phys. **78**, 1 (2008).

[18] K. Kadau, T. C. Germann, P. S. Lomdahl, R. C. Albers, J. S. Wark, A. Higginbotham, and B. L. Holian, *Shock Waves in Polycrystalline Iron*, Phys. Rev. Lett. **98**, 1 (2007).

[19] B. L. Holian and P. S. Lomdahl, *Plasticity Induced by Shock Waves in Nonequilibrium Molecular-Dynamics Simulations*, Science (80-.). **280**, 2085 (1998).

[20] K. Kadau, T. C. Germann, P. S. Lomdahl, and B. L. Holian, *Atomistic Simulations of Shock-Induced Transformations and Their Orientation Dependence in Bcc Fe Single Crystals*, Phys. Rev. B - Condens. Matter Mater. Phys. **72**, 1 (2005).

[21] S. Zhao, T. C. Germann, and A. Strachan, *Atomistic Simulations of Shock-Induced Alloying Reactions in NiAl Nanolaminates*, J. Chem. Phys. **125**, (2006).

[22] K. Kadau, T. C. Germann, P. S. Lomdahl, and B. L. Holian, *Microscopic View of Structural Phase Transitions Induced by Shock Waves*, Science (80-.). **296**, 1681 (2002).

[23] A. W. Campbell, W. C. Davis, and J. R. Travis, *Shock Initiation of Detonation in Liquid Explosives*, Phys. Fluids **4**, 498 (1961).

[24] J. K. Dienes, Q. H. Zuo, and J. D. Kershner, *Impact Initiation of Explosives and Propellants via Statistical Crack Mechanics*, J. Mech. Phys. Solids **54**, 1237 (2006).

[25] S. Davis Herring, T. C. Germann, and N. Grønbech-Jensen, *Effects of Void Size, Density, and Arrangement on Deflagration and Detonation Sensitivity of a Reactive Empirical Bond Order High Explosive*, Phys. Rev. B **82**, 214108 (2010).

[26] D. D. Dlott and M. D. Fayer, *Shocked Molecular Solids: Vibrational up Pumping, Defect Hot Spot Formation, and the Onset of Chemistry*, J. Chem. Phys. **92**, 3798 (1990).

[27] A. Tokmakoff, M. D. Fayer, and D. D. Dlott, *Chemical Reaction Initiation and Hot-Spot Formation in Shocked Energetic Molecular Materials*, J. Phys. Chem. **97**, 1901 (1993).

[28] S. D. Park, M. R. Armstrong, I. T. Kohl, J. M. Zaug, R. Knepper, A. S. Tappan, S. Bastea, and J. J. Kay, *Ultrafast Shock-Induced Reactions in Pentaerythritol Tetranitrate Thin Films*, J. Phys. Chem. A **122**, 8101 (2018).

[29] M. R. Manaa, L. E. Fried, C. F. Melius, M. Elstner, and T. Frauenheim, *Decomposition of HMX at Extreme Conditions: A Molecular Dynamics Simulation*, J. Phys. Chem. A **106**, 9024 (2002).

[30] M. R. Manaa, E. J. Reed, L. E. Fried, G. Galli, and F. Gygi, *Early Chemistry in Hot and Dense Nitromethane: Molecular Dynamics Simulations*, J. Chem. Phys. **120**, 10146 (2004).

[31] M. R. Manaa, E. J. Reed, L. E. Fried, and N. Goldman, *Nitrogen-Rich Heterocycles as Reactivity Retardants in Shocked Insensitive Explosives*, J. Am. Chem. Soc. **131**, 5483 (2009).

[32] M. M. Islam and A. Strachan, *Reactive Molecular Dynamics Simulations to Investigate the Shock Response of Liquid Nitromethane*, J. Phys. Chem. C **123**, 2613 (2019).

[33] M. S. Powell, M. N. Sakano, M. J. Cawkwell, P. R. Bowlan, K. E. Brown, C. A. Bolme, D. S. Moore, S. F. Son, A. Strachan, and S. D. McGrane, *Insight into the Chemistry of PETN under Shock Compression through Ultrafast Broadband Mid-Infrared Absorption Spectroscopy*, J. Phys. Chem. A **124**, 7031 (2020).

[34] C. J. Wu and L. E. Fried, *Ring Closure Mediated by Intramolecular Hydrogen Transfer in the Decomposition of a Push-Pull Nitroaromatic: TATB*, J. Phys. Chem. A **104**, 6447 (2000).

[35] K. E. Brown, S. D. McGrane, C. A. Bolme, and D. S. Moore, *Ultrafast Chemical Reactions in Shocked Nitromethane Probed with Dynamic Ellipsometry and Transient Absorption Spectroscopy*, J. Phys. Chem. A **118**, 2559 (2014).

[36] M. M. Islam and A. Strachan, *Decomposition and Reaction of Polyvinyl Nitrate under Shock and Thermal Loading: A ReaxFF Reactive Molecular Dynamics Study*, J. Phys. Chem. C **121**, 22452 (2017).

[37] R. R. McGuire and C. M. Tarver, *Chemical Decomposition Models for the Thermal Explosion of Confined Hmx, Tatb, Rdx, and Tnt Explosives.*, 56 (1982).

[38] E. L. Lee and C. M. Tarver, *Phenomenological Model of Shock Initiation in Heterogeneous Explosives*, Phys. Fluids **23**, 2362 (1980).

[39] C. M. Tarver, S. K. Chidester, and A. L. Nichols, *Critical Conditions for Impact- and Shock-Induced Hot Spots in Solid Explosives*, J. Phys. Chem. **100**, 5794 (1996).

[40] N. K. Rai, O. Sen, and H. S. Udaykumar, *Macro-Scale Sensitivity through Meso-Scale Hotspot Dynamics in Porous Energetic Materials: Comparing the Shock Response of 1,3,5-Triamino-2,4,6-Trinitrobenzene (TATB) and 1,3,5,7-Tetranitro-1,3,5,7-Tetrazoctane (HMX)*, J. Appl. Phys. **128**, 1 (2020).

[41] J. A. Wickham, S. P. Beaudoin, and S. F. Son, *The Role of Adhesion and Binder Stiffness in the Impact Sensitivity of Cast Composite Energetic Materials*, J. Appl. Phys. **128**, (2020).

[42] A. C. T. Van Duin, S. Dasgupta, F. Lorant, and W. A. Goddard, *ReaxFF: A Reactive Force Field for Hydrocarbons*, J. Phys. Chem. A **105**, 9396 (2001).

[43] D. S. Moore and S. D. McGrane, *Comparative Infrared and Raman Spectroscopy of Energetic Polymers*, J. Mol. Struct. **661**–**662**, 561 (2003).

[44] W. P. Bassett and D. D. Dlott, *Shock Initiation of Explosives: Temperature Spikes and Growth Spurts*, Appl. Phys. Lett. **109**, (2016).

[45] W. P. Bassett, B. P. Johnson, N. K. Neelakantan, K. S. Suslick, and D. D. Dlott, *Shock Initiation of Explosives: High Temperature Hot Spots Explained*, Appl. Phys. Lett. **111**, (2017).

[46] M. N. Sakano, A. Hamed, E. M. Kober, N. Grilli, B. W. Hamilton, M. M. Islam, M. Koslowski, and A. Strachan, *Unsupervised Learning-Based Multiscale Model of Thermochemistry in 1,3,5-Trinitro-1,3,5-Triazinane (RDX)*, J. Phys. Chem. A **124**, 9141 (2020).

[47] J. K. Brennan, M. Lísal, J. D. Moore, S. Izvekov, I. V. Schweigert, and J. P. Larentzos, *Coarse-Grain Model Simulations of Nonequilibrium Dynamics in Heterogeneous Materials*, J. Phys. Chem. Lett. **5**, 2144 (2014).

[48] M. A. Wood and A. Strachan, *Nonequilibrium Reaction Kinetics in Molecular Solids*, Journal of Physical Chemistry C.

[49] E. J. Reed, J. D. Joannopoulos, and L. E. Fried, *Electronic Excitations in Shocked Nitromethane*, Phys. Rev. B - Condens. Matter Mater. Phys. **62**, 16500 (2000).

[50] M. P. Kroonblawd and N. Goldman, *Mechanochemical Formation of Heterogeneous Diamond Structures during Rapid Uniaxial Compression in Graphite*, Phys. Rev. B **97**, 1 (2018).

[51] M. P. Kroonblawd and L. E. Fried, *High Explosive Ignition through Chemically Activated Nanoscale Shear Bands*, Phys. Rev. Lett. **124**, 206002 (2020).

[52] B. A. Steele, N. Goldman, I. F. W. Kuo, and M. P. Kroonblawd, *Mechanochemical Synthesis of Glycine Oligomers in a Virtual Rotational Diamond Anvil Cell*, Chem. Sci. **11**, 7760 (2020).

[53] S. A. Humphry-Baker, S. Garroni, F. Delogu, and C. A. Schuh, *Melt-Driven Mechanochemical Phase Transformations in Moderately Exothermic Powder Mixtures*, Nat. Mater. **15**, 1280 (2016).

[54] J. J. Gilman, *Chemical Reactions at Detonation Fronts in Solids*, Philos. Mag. B Phys. Condens. Matter; Stat. Mech. Electron. Opt. Magn. Prop. **71**, 1057 (1995).

[55] C. A. Handley, B. D. Lambourn, N. J. Whitworth, H. R. James, and W. J. Belfield, *Understanding the Shock and Detonation Response of High Explosives at the Continuum and Meso Scales*, Appl. Phys. Rev. **5**, 011303 (2018).

[56] A. W. Campbell and J. R. Travis, *The Shock Desensitization of Pbx-9404 and Composition B-3*, Los Alamos Natl. Lab. (1985).

[57] D. M. Dattelbaum, S. A. Sheffield, D. B. Stahl, A. M. Dattelbaum, W. Trott, and R. Engelke, *Influence of Hot Spot Features on the Initiation Characteristics of Heterogeneous Nitromethane*, Int. Detonation Symp. **LA-UR-10-0**, (2010).

[58] W. C. Davis, *High Explosives The Interaction of Chemistry and Mechanics*, Los Alamos Sci. **2**, 48 (1981).

[59] D. A. Frank-Kamenetskii, *Towards Temperature Distributions in a Reaction Vessel and the Stationary Theory of Thermal Explosion.*, Dokl. Akad. Nauk SSSR **18**, (1938).

[60] N. N. Semenov, *The Calculation of Critical Temperatures of Thermal Explosion*, Z Phys Chem **48**, 571 (1928).

163

[61] M. A. Wood, M. J. Cherukara, E. M. Kober, and A. Strachan, *Ultrafast Chemistry under Nonequilibrium Conditions and the Shock to Deflagration Transition at the Nanoscale*, J. Phys. Chem. C **119**, 22008 (2015).

[62] T. R. Shan, R. R. Wixom, and A. P. Thompson, *Extended Asymmetric Hot Region Formation Due to Shockwave Interactions Following Void Collapse in Shocked High Explosive*, Phys. Rev. B **94**, (2016).

[63] H. K. Springer, S. Bastea, A. L. Nichols, C. M. Tarver, and J. E. Reaugh, *Modeling The Effects of Shock Pressure and Pore Morphology on Hot Spot Mechanisms in HMX*, Propellants, Explos. Pyrotech. **43**, 805 (2018).

[64] J. Ribas-Arino and D. Marx, *Covalent Mechanochemistry: Theoretical Concepts and Computational Tools with Applications to Molecular Nanomechanics*, Chem. Rev. **112**, 5412 (2012).

[65] O. Sen, N. K. Rai, A. S. Diggs, D. B. Hardin, and H. S. Udaykumar, *Multi-Scale Shock-to-Detonation Simulation of Pressed Energetic Material: A Meso-Informed Ignition and Growth Model*, J. Appl. Phys. **124**, (2018).

[66] D. Guo, S. V. Zybin, Q. An, W. A. Goddard, and F. Huang, *Prediction of the Chapman-Jouguet Chemical Equilibrium State in a Detonation Wave from First Principles Based Reactive Molecular Dynamics*, Phys. Chem. Chem. Phys. **18**, 2015 (2016).

[67] H. H. Cady and A. C. Larson, *The Crystal Structure of 1,3,5-Triamino-2,4,6-Trinitrobenzene*, Acta Crystallogr. **18**, 485 (1965).

[68] D. Bedrov, O. Borodin, G. D. Smith, T. D. Sewell, D. M. Dattelbaum, and L. L. Stevens, *A Molecular Dynamics Simulation Study of Crystalline 1,3,5-Triamino-2,4,6-Trinitrobenzene as a Function of Pressure and Temperature*, J. Chem. Phys. **131**, (2009).

[69] P. Zhao, M. P. Kroonblawd, N. Mathew, and T. Sewell, *Strongly Anisotropic Thermomechanical Response to Shock Wave Loading in Oriented Samples of the Triclinic Molecular Crystal 1,3,5- Triamino-2,4,6-Trinitrobenzene*, J. Phys. Chem. C **125**, 22747 (2021).

[70] P. Lafourcade, C. Denoual, and J. B. Maillet, *Irreversible Deformation Mechanisms for 1,3,5-Triamino-2,4,6-Trinitrobenzene Single Crystal through Molecular Dynamics Simulations*, J. Phys. Chem. C **122**, 14954 (2018).

[71] B. A. Steele, S. M. Clarke, M. P. Kroonblawd, I. F. W. Kuo, P. F. Pagoria, S. N. Tkachev, J. S. Smith, S. Bastea, L. E. Fried, J. M. Zaug, E. Stavrou, and O. Tschauner, *Pressure-Induced Phase Transition in 1,3,5-Triamino-2,4,6-Trinitrobenzene (TATB)*, Appl. Phys. Lett. **114**, (2019).

[72] P. Lafourcade, C. Denoual, and J. B. Maillet, *Mesoscopic Constitutive Law with Nonlinear Elasticity and Phase Transformation for the Twinning-Buckling of TATB under Dynamic Loading*, Phys. Rev. Mater. **3**, 1 (2019).

[73] M. P. Kroonblawd and T. D. Sewell, *Theoretical Determination of Anisotropic Thermal Conductivity for Initially Defect-Free and Defective TATB Single Crystals*, J. Chem. Phys. **141**, (2014).

[74] M. P. Kroonblawd and T. D. Sewell, *Predicted Anisotropic Thermal Conductivity for Crystalline 1,3,5-Triamino-2,4,6-Trinitobenzene (TATB): Temperature and Pressure Dependence and Sensitivity to Intramolecular Force Field Terms*, Propellants, Explos. Pyrotech. **41**, 502 (2016).

[75] M. P. Kroonblawd, B. W. Hamilton, and A. Strachan, *Fourier-like Thermal Relaxation of Nanoscale Explosive Hot Spots*, J. Phys. Chem. C **125**, 20570 (2021).

[76] D. Guo, Q. An, W. A. Goddard, S. V. Zybin, and F. Huang, *Compressive Shear Reactive Molecular Dynamics Studies Indicating That Cocrystals of TNT/CL-20 Decrease Sensitivity*, J. Phys. Chem. C **118**, 30202 (2014).

[77] G. I. Bell, *Models for the Specific Adhesion of Cells to Cells*, Science (80-.). **200**, 618 (1978).

[78] B. J. Alder and T. E. Wainwright, *Phase Transition for a Hard Sphere System*, J. Chem. Phys. **27**, 1208 (1957).

[79] S. L. Mayo, B. D. Olafson, and W. A. Goddard, *DREIDING: A Generic Force Field for Molecular Simulations*, J. Phys. Chem. **94**, 8897 (1990).

[80] M. S. Daw and M. I. Baskes, *Embedded-Atom Method: Derivation and Application to Impurities, Surfaces, and Other Defects in Metals*, Phys. Rev. B **29**, 6443 (1984).

[81] L. Verlet, *Computer "Experiments" on Classical Fluids. I. Thermodynamical Properties of Lennard-Jones Molecules*, Phys. Rev. **159**, 98 (1967).

[82] W. Shinoda, M. Shiga, and M. Mikami, *Rapid Estimation of Elastic Constants by Molecular Dynamics Simulation under Constant Stress*, Phys. Rev. B - Condens. Matter Mater. Phys. **69**, 16 (2004).

[83] S. J. Plimpton, D. Perez, and A. F. Voter, *Parallel Algorithms for Hyperdynamics and Local Hyperdynamics*, J. Chem. Phys. **153**, (2020).

[84] J. Glaser, T. D. Nguyen, J. A. Anderson, P. Lui, F. Spiga, J. A. Millan, D. C. Morse, and S. C. Glotzer, *Strong Scaling of General-Purpose Molecular Dynamics Simulations on GPUs*, Comput. Phys. Commun. **192**, 97 (2015).

[85] S. Plimpton, *Fast Parallel Algorithms for Short-Range Molecular Dynamics*, J. Comput. Phys. **117**, 1 (1995).

[86] S. Nosé, *A Unified Formulation of the Constant Temperature Molecular Dynamics Methods*, J. Chem. Phys. **81**, 511 (1984).

[87] M. Parrinello and A. Rahman, *Polymorphic Transitions in Single Crystals: A New Molecular Dynamics Method*, J. Appl. Phys. **52**, 7182 (1981).

[88] M. P. Kroonblawd and T. D. Sewell, *Theoretical Determination of Anisotropic Thermal Conductivity for Crystalline 1,3,5-Triamino-2,4,6-Trinitrobenzene (TATB)*, J. Chem. Phys. **139**, (2013).

[89] N. Mathew, T. D. Sewell, and D. L. Thompson, *Anisotropy in Surface-Initiated Melting of the Triclinic Molecular Crystal 1,3,5-Triamino-2,4,6-Trinitrobenzene: A Molecular Dynamics Study*, J. Chem. Phys. **143**, (2015).

[90] H. C. Andersen, *Rattle: A "Velocity" Version of the Shake Algorithm for Molecular Dynamics Calculations*, J. Comput. Phys. **52**, 24 (1983).

[91] D. Wolf, P. Keblinski, S. R. Phillpot, and J. Eggebrecht, *Exact Method for the Simulation of Coulombic Systems by Spherically Truncated, Pairwise r-1 Summation*, J. Chem. Phys. **110**, 8254 (1999).

[92] E. L. Pollock and J. Glosli, *Comments on P3M, FMM, and the Ewald Method for Large Periodic Coulombic Systems*, Comput. Phys. Commun. **95**, 93 (1996).

[93] M. J. Cawkwell and A. M. N. Niklasson, *Energy Conserving, Linear Scaling Born-Oppenheimer Molecular Dynamics*, J. Chem. Phys. **137**, (2012).

[94] B. Aradi, B. Hourahine, and T. Frauenheim, *DFTB+, a Sparse Matrix-Based Implementation of the DFTB Method*, J. Phys. Chem. A **111**, 5678 (2007).

[95] M. F. Russo and A. C. T. Van Duin, *Atomistic-Scale Simulations of Chemical Reactions: Bridging from Quantum Chemistry to Engineering*, Nucl. Instruments Methods Phys. Res. Sect. B Beam Interact. with Mater. Atoms **269**, 1549 (2011).

[96] K. Chenoweth, A. C. T. Van Duin, and W. A. Goddard, *ReaxFF Reactive Force Field for Molecular Dynamics Simulations of Hydrocarbon Oxidation*, J. Phys. Chem. A **112**, 1040 (2008).

[97] T. P. Senftle, S. Hong, M. M. Islam, S. B. Kylasa, Y. Zheng, Y. K. Shin, C. Junkermeier, R. Engel-Herbert, M. J. Janik, H. M. Aktulga, T. Verstraelen, A. Grama, and A. C. T. Van Duin, *The ReaxFF Reactive Force-Field: Development, Applications and Future Directions*, Npj Comput. Mater. **2**, (2016).

[98] L. Liu, Y. Liu, S. V. Zybin, H. Sun, and W. A. Goddard, *ReaxFF-Lg: Correction of the ReaxFF Reactive Force Field for London Dispersion, with Applications to the Equations of State for Energetic Materials*, J. Phys. Chem. A **115**, 11016 (2011).

[99] A. K. Rappé and W. A. Goddard, *Charge Equilibration for Molecular Dynamics Simulations*, J. Phys. Chem. **95**, 3358 (1991).

[100] P. Yoo, M. Sakano, S. Desai, M. M. Islam, P. Liao, and A. Strachan, *Neural Network Reactive Force Field for C, H, N, and O Systems*, Npj Comput. Mater. **7**, 1 (2021).

[101] R. K. Lindsey, N. Goldman, L. E. Fried, and S. Bastea, *Many-Body Reactive Force Field Development for Carbon Condensation in C/O Systems under Extreme Conditions*, J. Chem. Phys. **153**, (2020).

[102] H. Chan, M. J. Cherukara, B. Narayanan, T. D. Loeffler, C. Benmore, S. K. Gray, and S. K. R. S. Sankaranarayanan, *Machine Learning Coarse Grained Models for Water*, Nat. Commun. **10**, 1 (2019).

[103] L. Vlcek, M. Ziatdinov, A. Maksov, A. Tselev, A. P. Baddorf, S. V. Kalinin, and R. K. Vasudevan, *Learning from Imperfections: Predicting Structure and Thermodynamics from Atomic Imaging of Fluctuations*, ACS Nano **13**, 718 (2019).

[104] A. Strachan, A. C. T. van Duin, D. Chakraborty, S. Dasgupta, and W. A. Goddard, *Shock Waves in High-Energy Materials: The Initial Chemical Events in Nitramine RDX*, Phys. Rev. Lett. **91**, 7 (2003).

[105] E. J. Reed, M. R. Manaa, L. E. Fried, K. R. Glaesemann, and J. D. Joannopoulos, *A Transient Semimetallic Layer in Detonating Nitromethane*, Nat. Phys. **4**, 72 (2008).

[106] A. Strachan and B. Lee Holian, *Energy Exchange between Mesoparticles and Their Internal Degrees of Freedom*, Phys. Rev. Lett. **94**, 1 (2005).

[107] S. Zhao, T. C. Germann, and A. Strachan, *Molecular Dynamics Simulation of Dynamical Response of Perfect and Porous NiAl Nanolaminates under Shock Loading*, Phys. Rev. B - Condens. Matter Mater. Phys. **76**, 1 (2007).

[108] E. J. Reed, L. E. Fried, and J. D. Joannopoulos, *A Method for Tractable Dynamical Studies of Single and Double Shock Compression*, Phys. Rev. Lett. **90**, 4 (2003).

[109] R. Ravelo, B. L. Holian, T. C. Germann, and P. S. Lomdahl, *Constant-Stress Hugoniostat Method for Following the Dynamical Evolution of Shocked Matter*, Phys. Rev. B - Condens. Matter Mater. Phys. **70**, 1 (2004).

[110] M. Riad Manaa, E. J. Reed, and L. E. Fried, *Atomistic Simulations of Chemical Reactivity of TATB under Thermal and Shock Conditions*, Proc. - 14th Int. Detonation Symp. IDS 2010 837 (2010).

[111] Y. Shen, S. B. Jester, T. Qi, and E. J. Reed, *Nanosecond Homogeneous Nucleation and Crystal Growth in Shock-Compressed SiO2*, Nat. Mater. **15**, 60 (2016).

[112] H. C. Andersen, *Molecular Dynamics Simulations at Constant Pressure and/or Temperature*, J. Chem. Phys. **72**, 2384 (1980).

[113] E. J. Reed, L. E. Fried, W. D. Henshaw, and C. M. Tarver, *Analysis of Simulation Technique for Steady Shock Waves in Materials with Analytical Equations of State*, Phys. Rev. E - Stat. Nonlinear, Soft Matter Phys. **74**, 1 (2006).

[114] J. B. Maillet, M. Mareschal, L. Soulard, R. Ravelo, P. S. Lomdahl, T. C. Germann, and B. L. Holian, *Uniaxial Hugoniostat: A Method for Atomistic Simulations of Shocked Materials*, Phys. Rev. E - Stat. Physics, Plasmas, Fluids, Relat. Interdiscip. Top. **63**, 2 (2001).

[115] B. W. Hamilton, M. P. Kroonblawd, M. M. Islam, and A. Strachan, *Sensitivity of the Shock Initiation Threshold of 1,3,5-Triamino-2,4,6-Trinitrobenzene (TATB) to Nuclear Quantum Effects*, J. Phys. Chem. C **123**, 21969 (2019).

[116] B. W. Hamilton, B. A. Steele, M. N. Sakano, M. P. Kroonblawd, I. F. W. Kuo, and A. Strachan, *Predicted Reaction Mechanisms, Product Speciation, Kinetics, and Detonation Properties of the Insensitive Explosive 2,6-Diamino-3,5-Dinitropyrazine-1-Oxide (LLM-105)*, J. Phys. Chem. A **125**, 1766 (2021).

[117] P. H. Berens, D. H. J. Mackay, G. M. White, and K. R. Wilson, *Thermodynamics and Quantum Corrections from Molecular Dynamics for Liquid Water*, J. Chem. Phys. **79**, 2375 (1983).

[118] L. E. Boltzmann, *Einige Allgemeine Sätze Über Wärmegleichgewicht*, K. Akad. Der Wissensch (1871).

[119] L. E. Boltzmann, *Über Die Natur Der Gasmolecüle*, Kk Hof-Und Staatsdruckerei (1876).

[120] J. J. Waterson, *On the Physics of Media That Are Composed of Free and Perfectly Elastic Molecules in a State of Motion*, Abstr. Pap. Commun. to R. Soc. London **5**, (1851).

[121] S. N. Bose, *Plancks Gesetz Und Lichtquantenhypothese*, 178 (1924).

[122] A. Einstein, *Quantentheorie Des Einatomigen Idealen Gases*, Albert Einstein Akad. Sitzungsberichte Der Preußischen Akad. Der Wissenschaften 245 (1932).

[123] L. Proville, D. Rodney, and M. C. Marinica, *Quantum Effect on Thermally Activated Glide of Dislocations*, Nat. Mater. **11**, 845 (2012).

[124] N. Goldman, E. J. Reed, and L. E. Fried, *Quantum Mechanical Corrections to Simulated Shock Hugoniot Temperatures*, J. Chem. Phys. **131**, (2009).

[125] M. P. Kroonblawd, T. D. Sewell, and J. B. Maillet, *Characteristics of Energy Exchange between Inter- and Intramolecular Degrees of Freedom in Crystalline 1,3,5-Triamino-2,4,6-Trinitrobenzene (TATB) with Implications for Coarse-Grained Simulations of Shock Waves in Polyatomic Molecular Crystals*, J. Chem. Phys. **144**, (2016).

[126] A. Strachan, E. M. Kober, A. C. T. Van Duin, J. Oxgaard, and W. A. Goddard, *Thermal Decomposition of RDX from Reactive Molecular Dynamics*, J. Chem. Phys. **122**, (2005).

[127] C. J. Wu and L. E. Fried, *Ab Initio Study of RDX Decomposition Mechanisms*, J. Phys. Chem. A **101**, 8675 (1997).

[128] X. Xue, Y. Wen, and C. Zhang, *Early Decay Mechanism of Shocked ϵ-CL-20: A Molecular Dynamics Simulation Study*, J. Phys. Chem. C **120**, 21169 (2016).

[129] L. Zhang, S. V Zybin, A. C. T. Van Duin, S. Dasgupta, W. A. G. Iii, and E. M. Kober, *High Explosives from ReaxFF Reactive Molecular Dynamics Simulations*, Society 10619 (2009).

[130] E. J. Reed, A. W. Rodriguez, M. R. Manaa, L. E. Fried, and C. M. Tarver, *Ultrafast Detonation of Hydrazoic Acid (HN 3)*, Phys. Rev. Lett. **109**, 1 (2012).

[131] M. Sakano, B. W. Hamilton, M. M. Islam, and A. Strachan, *Role of Molecular Disorder on the Reactivity of RDX*, J. Phys. Chem. C **122**, 27032 (2018).

[132] M. M. Islam and A. Strachan, *Role of Dynamical Compressive and Shear Loading on Hotspot Criticality in RDX via Reactive Molecular Dynamics*, J. Appl. Phys. **128**, (2020).

[133] H. Dammak, Y. Chalopin, M. Laroche, M. Hayoun, and J. J. Greffet, *Quantum Thermal Bath for Molecular Dynamics Simulation*, Phys. Rev. Lett. **103**, 1 (2009).

[134] M. Ceriotti, G. Bussi, and M. Parrinello, *Nuclear Quantum Effects in Solids Using a Colored-Noise Thermostat*, Phys. Rev. Lett. **103**, 1 (2009).

[135] B. Dunweg and W. Paul, *Brownian Dynamics Simulations without Gaussian Random Numbers*, Int. J. Mod. Phys. C **2**, 817 (1991).

[136] P. A. M. Dirac, *The Lagrangian in Quantum Mechanics*, Phys. Zeitschrift Der Sowjetunion **3**, 64 (1933).

[137] R. P. Feynman and A. R. Hibbs, *Quantum Mechanics and Path Integrals* (McGraw Hill Companies Inc, New York, 1965).

[138] D. Marx and M. Parrinello, *Ab Initio Path Integral Molecular Dynamics: Basic Ideas*, J. Chem. Phys. **104**, 4077 (1996).

[139] R. Car and M. Parrinello, *Unified Approach for Molecular Dynamics and Density-Functional Theory*, Phys. Rev. Lett. **55**, 2471 (1985).

[140] J. L. Barrat and D. Rodney, *Portable Implementation of a Quantum Thermal Bath for Molecular Dynamics Simulations*, J. Stat. Phys. **144**, 679 (2011).

[141] Y. Bronstein, P. Depondt, L. E. Bove, R. Gaal, A. M. Saitta, and F. Finocchi, *Quantum versus Classical Protons in Pure and Salty Ice under Pressure*, Phys. Rev. B **93**, 1 (2016).

[142] T. Qi, C. W. Bauschlicher, J. W. Lawson, T. G. Desai, and E. J. Reed, *Comparison of ReaxFF, DFTB, and DFT for Phenolic Pyrolysis. 1. Molecular Dynamics Simulations*, J. Phys. Chem. A **117**, 11115 (2013).

[143] T. Qi and E. J. Reed, *Simulations of Shocked Methane Including Self-Consistent Semiclassical Quantum Nuclear Effects*, J. Phys. Chem. A **116**, 10451 (2012).

[144] M. P. Kroonblawd, N. Mathew, S. Jiang, and T. D. Sewell, *A Generalized Crystal-Cutting Method for Modeling Arbitrarily Oriented Crystals in 3D Periodic Simulation Cells with Applications to Crystal–Crystal Interfaces*, Comput. Phys. Commun. **207**, 232 (2016).

[145] H. H. Cady, A. C. Larson, and D. T. Cromer, *The Crystal Structure of α-HMX and a Refinement of the Structure of β-HMX*, Acta Crystallogr. **16**, 617 (1963).

[146] H. X. Ma, J. R. Song, F. Q. Zhao, H. X. Gao, and R. Z. Hu, *Crystal Structure, Safety Performance and Density-Functional Theoretical Investigation of 2,6-Diamino-3,5-Dinitropyrazine-1-Oxide (LLM-105)*, Chinese J. Chem. **26**, 1997 (2008).

[147] J. P. Perdew, K. Burke, and M. Ernzerhof, *Generalized Gradient Approximation Made Simple*, Phys. Rev. Lett. **77**, 3865 (1996).

[148] S. Grimme, *Semiempirical GGA-Type Density Functional Constructed with a Long-Range Dispersion Correction*, J. Comput. Chem. **27**, 1787 (2006).

[149] P. E. Blöchl, *Projector Augmented-Wave Method*, Phys. Rev. B **50**, 17953 (1994).

[150] D. Joubert, *From Ultrasoft Pseudopotentials to the Projector Augmented-Wave Method*, Phys. Rev. B - Condens. Matter Mater. Phys. **59**, 1758 (1999).

[151] G. Kresse and J. Furthmuller, *Efficient Iterative Schemes for Ab Initio Total-Energy Calculations Using a Plane-Wave Basis Set*, Phys. Rev. B **54**, 11169 (1996).

[152] J. Hafner, *Ab-Initio Simulations of Materials Using VASP: Density-Functional Theory and Beyond*, J. Comput. Chem. **29**, 2044 (2008).

[153] N. D. Mermin, *Thermal Properties of the Inhomogeneous Electron Gas*, Phys. Rev. **137**, 1 (1965).

[154] H. B. Callen and T. A. Welton, *Irreversibility and Generalized Noise*, Phys. Rev. **83**, 34 (1951).

[155] N. Wiener, *Generalized Harmonic Analysis*, Acta Math. **55**, 117 (1930).

[156] F. Brieuc, Y. Bronstein, H. Dammak, P. Depondt, F. Finocchi, and M. Hayoun, *Zero-Point Energy Leakage in Quantum Thermal Bath Molecular Dynamics Simulations*, J. Chem. Theory Comput. **12**, 5688 (2016).

[157] L. Patidar and S. T. Thynell, *Quantum Mechanics Investigation of Initial Reaction Pathways and Early Ring-Opening Reactions in Thermal Decomposition of Liquid-Phase RDX*, Combust. Flame **178**, 7 (2017).

[158] S. P. Marsh, LASL Shock Hugoniot Data (Vol. 5)., 1980.

[159] C. A. Duarte, C. Li, B. W. Hamilton, A. Strachan, and M. Koslowski, *Continuum and Molecular Dynamics Simulations of Pore Collapse in Shocked β -Tetramethylene Tetranitramine (β -HMX) Single Crystals* , J. Appl. Phys. **129**, 015904 (2021).

[160] B. W. Hamilton, M. P. Kroonblawd, C. Li, and A. Strachan, *A Hotspot's Better Half: Non-Equilibrium Intra-Molecular Strain in Shock Physics*, J. Phys. Chem. Lett. **12**, 2756 (2021).

[161] B. W. Hamilton, M. P. Kroonblawd, and A. Strachan, *The Potential Energy Hotspot: Effects from Impact Velocity, Defect Geometry, and Crystallographic Orientation*, J. Phys. Chem. C (2022).

[162] B. L. Holian, T. C. Germann, J. B. Maillet, and C. T. White, *Atomistic Mechanism for Hot Spot Initiation*, Phys. Rev. Lett. **89**, 1 (2002).

[163] C. L. Mader, *Initiation of Detonation by the Interaction of Shocks with Density Discontinuities*, Phys. Fluids **8**, 1811 (1965).

[164] J. Kang, P. B. Butler, and M. R. Baer, *A Thermomechanical Analysis of Hot Spot Formation in Condensed-Phase, Energetic Materials*, Combust. Flame **89**, 117 (1992).

[165] M. M. Carroll and A. C. Holt, *Static and Dynamic Pore-Collapse Relations for Ductile Porous Materials*, J. Appl. Phys. **43**, 1626 (1972).

[166] B. Sturtevant and V. A. Kulkarny, *The Focusing of Weak Shock Waves*, J. Fluid Mech. **73**, 651 (1976).

[167] J. E. Cates and B. Sturtevant, *Shock Wave Focusing Using Geometrical Shock Dynamics*, Phys. Fluids **9**, 3058 (1997).

[168] Y. Shi and D. W. Brenner, *Jetting and Detonation Initiation in Shock Induced Collapse of Nanometer-Scale Voids*, J. Phys. Chem. C **112**, 6263 (2008).

[169] C. A. Duarte, N. Grilli, and M. Koslowski, *Effect of Initial Damage Variability on Hot-Spot Nucleation in Energetic Materials*, J. Appl. Phys. **124**, 025104 (2018).

[170] L. E. Fried, *High Explosive Shock Initiation Model Based on Hot Spot Temperature*, Proc. 16th Int. Detonation Symp. 1156 (2018).

[171] J. Ribas-Arino, M. Shiga, and D. Marx, *Understanding Covalent Mechanochemistry*, Angew. Chemie - Int. Ed. **48**, 4190 (2009).

[172] X. Zhou, Y. Miao, K. S. Suslick, and D. D. Dlott, *Mechanochemistry of Metal-Organic Frameworks under Pressure and Shock*, Acc. Chem. Res. **53**, (2020).

[173] T. Stauch and A. Dreuw, *Advances in Quantum Mechanochemistry: Electronic Structure Methods and Force Analysis*, Chem. Rev. **116**, 14137 (2016).

[174] J. Wang, T. B. Kouznetsova, Z. Niu, M. T. Ong, H. M. Klukovich, A. L. Rheingold, T. J. Martinez, and S. L. Craig, *Inducing and Quantifying Forbidden Reactivity with Single-Molecule Polymer Mechanochemistry*, Nat. Chem. **7**, 323 (2015).

[175] A. P. Wiita, S. R. K. Ainavarapu, H. H. Huang, and J. M. Fernandez, *Force-Dependent Chemical Kinetics of Disulfide Bond Reduction Observed with Single-Molecule Techniques*, Proc. Natl. Acad. Sci. U. S. A. **103**, 7222 (2006).

[176] R. M. Eason and T. D. Sewell, *Molecular Dynamics Simulations of the Collapse of a Cylindrical Pore in the Energetic Material α-RDX*, J. Dyn. Behav. Mater. **1**, 423 (2015).

[177] M. P. Kroonblawd and T. D. Sewell, *Anisotropic Relaxation of Idealized Hot Spots in Crystalline 1,3,5-Triamino-2,4,6-Trinitrobenzene (TATB)*, J. Phys. Chem. C **120**, 17214 (2016).

[178] D. L. Bunker and W. L. Hase, *On Non-RRKM Unimolecular Kinetics: Molecules in General, and CH3NC in Particular*, J. Chem. Phys. 4621 (1973).

[179] E. J. Nissen, M. Bhowmick, and D. D. Dlott, *Shock-Induced Kinetics and Cellular Structures of Liquid Nitromethane Detonation*, Combust. Flame **225**, 5 (2021).

[180] M. Lísal, J. P. Larentzos, M. S. Sellers, I. V. Schweigert, and J. K. Brennan, *Dissipative Particle Dynamics with Reactions: Application to RDX Decomposition*, J. Chem. Phys. **151**, (2019).

[181] M. A. Wood, A. C. T. Van Duin, and A. Strachan, *Coupled Thermal and Electromagnetic Induced Decomposition in the Molecular Explosive AhMX; A Reactive Molecular Dynamics Study*, J. Phys. Chem. A **118**, 885 (2014).

[182] N. Mathew, M. P. Kroonblawd, T. Sewell, and D. L. Thompson, *Predicted Melt Curve and Liquid-State Transport Properties of TATB from Molecular Dynamics Simulations*, Mol. Simul. **44**, 613 (2018).

[183] J. B. Maillet, E. Bourasseau, N. Desbiens, G. Vallverdu, and G. Stoltz, *Mesoscopic Simulations of Shock-to-Detonation Transition in Reactive Liquid High Explosive*, Epl **96**, (2011).

[184] M. S. Sellers, M. Lísal, I. Schweigert, J. P. Larentzos, and J. K. Brennan, *Shock Simulations of a Single-Site Coarse-Grain RDX Model Using the Dissipative Particle Dynamics Method with Reactivity*, AIP Conf. Proc. **1793**, 1 (2017).

[185] N. K. Rai and H. S. Udaykumar, *Three-Dimensional Simulations of Void Collapse in Energetic Materials*, Phys. Rev. Fluids **3**, 1 (2018).

[186] L. L. Stevens, N. Velisavljevic, D. E. Hooks, and D. M. Dattelbaum, *Hydrostatic Compression Curve for Triamino-Trinitrobenzene Determined to 13.0 GPa with Powder X-Ray Diffraction*, Propellants, Explos. Pyrotech. **33**, 286 (2008).

[187] A. Pal and C. R. Picu, *Non-Schmid Effect of Pressure on Plastic Deformation in Molecular Crystal HMX*, J. Appl. Phys. **125**, 1 (2019).

[188] M. P. Kroonblawd, B. A. Steele, M. D. Nelms, L. E. Fried, and R. A. Austin, *Anisotropic Strength Behavior of Single-Crystal TATB*, Model. Simul. Mater. Sci. Eng. (2021).

[189] E. Jaramillo, T. D. Sewell, and A. Strachan, *Atomic-Level View of Inelastic Deformation in a Shock Loaded Molecular Crystal*, Phys. Rev. B **76**, (2007).

[190] E. Jaramillo, N. Wilson, S. Christensen, J. Gosse, and A. Strachan, *Energy-Based Yield Criterion for PMMA from Large-Scale Molecular Dynamics Simulations*, Phys. Rev. B - Condens. Matter Mater. Phys. **85**, 1 (2012).

[191] W. P. Bassett, B. P. Johnson, and D. D. Dlott, *Dynamic Absorption in Optical Pyrometry of Hot Spots in Plastic-Bonded Triaminotrinitrobenzene*, Appl. Phys. Lett. **114**, (2019).

[192] H. K. Springer, C. M. Tarver, and S. Bastea, *Effects of High Shock Pressures and Pore Morphology on Hot Spot Mechanisms in HMX*, AIP Conf. Proc. **1793**, 1 (2017).

[193] R. A. Austin, N. R. Barton, J. E. Reaugh, and L. E. Fried, *Direct Numerical Simulation of Shear Localization and Decomposition Reactions in Shock-Loaded HMX Crystal*, J. Appl. Phys. **117**, (2015).

[194] Y. Wei, R. Ranjan, U. Roy, J. H. Shin, S. Menon, and M. Zhou, *Integrated Lagrangian and Eulerian 3D Microstructure-Explicit Simulations for Predicting Macroscopic Probabilistic SDT Thresholds of Energetic Materials*, Comput. Mech. **64**, 547 (2019).

[195] C. Li, M. N. Sakano, and A. Strachan, *Shock-Induced Hotspot Formation in Amorphous and Crystalline 1,3,5,7-Tetranitro-1,3,5,7-Tetrazoctane (HMX): A Molecular Dynamics Comparative Study*, J. Appl. Phys. **130**, (2021).

[196] J. Wang, W. P. Bassett, and D. D. Dlott, *Shock Initiation of Nano-Al/Teflon: High Dynamic Range Pyrometry Measurements*, J. Appl. Phys. **121**, (2017).

[197] M. R. Manaa, N. Goldman, and L. E. Fried, *Simulation of Cluster Formation in Overdriven and Expanding TATB by Molecular Dynamics*, Proc. 15th Int. Detonation Symp. 53 (2015).

[198] S. C. Tiwari, K. I. Nomura, R. K. Kalia, A. Nakano, and P. Vashishta, *Multiple Reaction Pathways in Shocked 2,4,6-Triamino-1,3,5-Trinitrobenzene Crystal*, J. Phys. Chem. C **121**, 16029 (2017).

[199] S. Bastea, *Nanocarbon Condensation in Detonation*, Sci. Rep. **7**, 1 (2017).

[200] B. W. Hamilton and A. Strachan, *Many-Body Mechanochemistry : Intra-Molecular Strain in Condensed Matter Chemistry*, ChemRxiv (2022).

[201] K. V. Manukyan, B. A. Mason, L. J. Groven, Y. C. Lin, M. Cherukara, S. F. Son, A. Strachan, and A. S. Mukasyan, *Tailored Reactivity of Ni+Al Nanocomposites: Microstructural Correlations*, J. Phys. Chem. C **116**, 21027 (2012).

[202] M. Grandbois, M. Beyer, M. Rief, H. Clausen-Schaumann, and H. E. Gaub, *How Strong Is a Covalent Bond?*, Science (80-.). **283**, 1727 (1999).

[203] W. L. Shaw, Y. Ren, J. S. Moore, and D. D. Dlott, *Mechanochemistry for Shock Wave Energy Dissipation*, AIP Conf. Proc. **1793**, (2017).

[204] X. Zhou, Y. R. Miao, W. L. Shaw, K. S. Suslick, and D. D. Dlott, *Shock Wave Energy Absorption in Metal-Organic Framework*, J. Am. Chem. Soc. **141**, 2220 (2019).

[205] M. T. Ong, J. Leiding, H. Tao, A. M. Virshup, and T. J. Martínez, *First Principles Dynamics and Minimum Energy Pathways for Mechanochemical Ring Opening of Cyclobutene*, J. Am. Chem. Soc. **131**, 6377 (2009).

[206] Z. Wang, X. Zheng, T. Ouchi, T. B. Kouznetsova, H. K. Beech, S. Av-Ron, T. Matsuda, B. H. Bowser, S. Wang, J. A. Johnson, J. A. Kalow, B. D. Olsen, J. P. Gong, M. Rubinstein, and S. L. Craig, *Toughening Hydrogels through Force-Triggered Chemical Reactions That Lengthen Polymer Strands*, Science (80-.). **374**, 193 (2021).

[207] N. Deneke, M. L. Rencheck, and C. S. Davis, *An Engineer's Introduction to Mechanophores*, Soft Matter **16**, 6230 (2020).

[208] D. A. Davis, A. Hamilton, J. Yang, L. D. Cremar, D. Van Gough, S. L. Potisek, M. T. Ong, P. V. Braun, T. J. Martínez, S. R. White, J. S. Moore, and N. R. Sottos, *Force-Induced Activation of Covalent Bonds in Mechanoresponsive Polymeric Materials*, Nature **459**, 68 (2009).

[209] J. Sung, M. J. Robb, S. R. White, J. S. Moore, and N. R. Sottos, *Interfacial Mechanophore Activation Using Laser-Induced Stress Waves*, J. Am. Chem. Soc. **140**, 5000 (2018).

[210] A. L. B. Ramirez, Z. S. Kean, J. A. Orlicki, M. Champhekar, S. M. Elsakr, W. E. Krause, and S. L. Craig, *Mechanochemical Strengthening of a Synthetic Polymer in Response to Typically Destructive Shear Forces*, Nat. Chem. **5**, 757 (2013).

[211] M. P. Kroonblawd, R. K. Lindsey, and N. Goldman, *Synthesis of Functionalized Nitrogen-Containing Polycyclic Aromatic Hydrocarbons and Other Prebiotic Compounds in Impacting Glycine Solutions*, Chem. Sci. **10**, 6091 (2019).

[212] N. Goldman and I. Tamblyn, *Prebiotic Chemistry within a Simple Impacting Icy Mixture*, J. Phys. Chem. A **117**, 5124 (2013).

[213] N. Goldman, E. J. Reed, L. E. Fried, I. F. William Kuo, and A. Maiti, *Synthesis of Glycine-Containing Complexes in Impacts of Comets on Early Earth*, Nat. Chem. **2**, 949 (2010).

[214] Z. Martins, M. C. Price, N. Goldman, M. A. Sephton, and M. J. Burchell, *Shock Synthesis of Amino Acids from Impacting Cometary and Icy Planet Surface Analogues*, Nat. Geosci. **6**, 1045 (2013).

[215] M. R. Armstrong, R. K. Lindsey, N. Goldman, M. H. Nielsen, E. Stavrou, L. E. Fried, J. M. Zaug, and S. Bastea, *Ultrafast Shock Synthesis of Nanocarbon from a Liquid Precursor*, Nat. Commun. **11**, 1 (2020).

[216] D. Kraus, A. Ravasio, M. Gauthier, D. O. Gericke, J. Vorberger, S. Frydrych, J. Helfrich, L. B. Fletcher, G. Schaumann, B. Nagler, B. Barbrel, B. Bachmann, E. J. Gamboa, S. Göde, E. Granados, G. Gregori, H. J. Lee, P. Neumayer, W. Schumaker, T. Döppner, R. W. Falcone, S. H. Glenzer, and M. Roth, *Nanosecond Formation of Diamond and Lonsdaleite by Shock Compression of Graphite*, Nat. Commun. **7**, 1 (2016).

[217] E. Stavrou, M. Bagge-Hansen, J. A. Hammons, M. H. Nielsen, B. A. Steele, P. Xiao, M. P. Kroonblawd, M. D. Nelms, W. L. Shaw, W. Bassett, S. Bastea, L. M. Lauderbach, R. L. Hodgin, N. A. Perez-Marty, S. Singh, P. Das, Y. Li, A. Schuman, N. Sinclair, K. Fezzaa, A. Deriy, L. D. Leininger, and T. M. Willey, *Detonation-Induced Transformation of Graphite to Hexagonal Diamond*, Phys. Rev. B **102**, 104116 (2020).

[218] J. J. Gilman, *Shear-Induced Metallization*, Philos. Mag. B Phys. Condens. Matter; Stat. Mech. Electron. Opt. Magn. Prop. **67**, 207 (1993).

[219] M. R. Manaa, *Shear-Induced Metallization of Triamino-Trinitrobenzene Crystals*, Appl. Phys. Lett. **83**, 1352 (2003).

[220] C. J. Eckhardt, *Mechanochemistry: The Last Energetic Frontier*, Mol. Cryst. Liq. Cryst. **456**, 1 (2006).

[221] V. V. Rybkin, *Franck-Condon Theory of Quantum Mechanochemistry*, J. Phys. Chem. A **121**, 5758 (2017).

[222] T. Stauch and A. Dreuw, *Knots "Choke Off" Polymers upon Stretching*, Angew. Chemie - Int. Ed. **55**, 811 (2016).

[223] M. E. Grady, B. A. Beiermann, J. S. Moore, and N. R. Sottos, *Shockwave Loading of Mechanochemically Active Polymer Coatings*, ACS Appl. Mater. Interfaces **6**, 5350 (2014).

[224] Z. Huang, Q. Z. Yang, D. Khvostichenko, T. J. Kucharski, J. Chen, and R. Boulatov, *Method to Derive Restoring Forces of Strained Molecules from Kinetic Measurements*, J. Am. Chem. Soc. **131**, 1407 (2009).

[225] A. M. Saitta, P. D. Soper, E. Wasserman, and M. L. Klein, *Influence of a Knot on the Stength of a Polymer Strand*, Nature **399**, 46 (2019).

[226] M. L. Mansfield, *Knots in Hamilton Cycles*, Macromolecules **27**, 5924 (1994).

[227] A. M. Saitta and M. L. Klein, *Evolution of Fragments Formed at the Rupture of a Knotted Alkane Molecule*, J. Am. Chem. Soc. **121**, 11827 (1999).

[228] T. Stauch, M. T. Hoffmann, and A. Dreuw, *Spectroscopic Monitoring of Mechanical Forces during Protein Folding by Using Molecular Force Probes*, ChemPhysChem **17**, 1486 (2016).

[229] M. Paulsson, C. Krag, T. Frederiksen, and M. Brandbyge, *Conductance of Alkanedithiol Single-Molecule Junctions: A Molecular Dynamics Study*, Nano Lett. **9**, 117 (2009).

[230] Y. Qi, J. Qin, G. Zhang, and T. Zhang, *Breaking Mechanism of Single Molecular Junctions Formed by Octanedithiol Molecules and Au Electrodes*, J. Am. Chem. Soc. **131**, 16418 (2009).

[231] P. Vélez, S. A. Dassie, and E. P. M. Leiva, *First Principles Calculations of Mechanical Properties of 4,4'-Bipyridine Attached to Au Nanowires*, Phys. Rev. Lett. **95**, 2 (2005).

[232] C. Jarzynski, *Equilibrium Free-Energy Differences from Nonequilibrium Measurements: A Master-Equation Approach*, Phys. Rev. E **56**, 5018 (1997).

[233] C. Jarzynski, *Nonequilibrium Equality for Free Energy Differences*, Phys. Rev. Lett. **78**, 2690 (1997).

[234] S. Park, F. Khalili-Araghi, E. Tajkhorshid, and K. Schulten, *Free Energy Calculation from Steered Molecular Dynamics Simulations Using Jarzynski's Equality*, J. Chem. Phys. **119**, 3559 (2003).

[235] S. Park and K. Schulten, *Calculating Potentials of Mean Force from Steered Molecular Dynamics Simulations*, J. Chem. Phys. **120**, 5946 (2004).

[236] B. Isralewitz, M. Gao, and K. Schulten, *Steered Molecular Dynamics and Mechanical Functions of Proteins*, Curr. Opin. Struct. Biol. **11**, 224 (2001).

[237] M. K. Beyer, *The Mechanical Strength of a Covalent Bond Calculated by Density Functional Theory*, J. Chem. Phys. **112**, 7307 (2000).

[238] K. Wolinski and J. Baker, *Theoretical Predictions of Enforced Structural Changes in Molecules*, Mol. Phys. **107**, 2403 (2009).

[239] S. V. Zybin, W. A. Goddard, P. Xu, A. C. T. Van Duin, and A. P. Thompson, *Physical Mechanism of Anisotropic Sensitivity in Pentaerythritol Tetranitrate from Compressive-Shear Reaction Dynamics Simulations*, Appl. Phys. Lett. **96**, 1 (2010).

[240] J. W. Shaevitz, S. M. Block, and M. J. Schnitzer, *Statistical Kinetics of Macromolecular Dynamics*, Biophys. J. **89**, 2277 (2005).

[241] X. Sun, X. Wang, W. Liang, C. Gao, Z. Sui, M. Liu, R. Dai, Z. Wang, X. Zheng, and Z. Zhang, *Pressure-Induced Conformer Modifications and Electronic Structural Changes in 1,3,5-Triamino-2,4,6-Trinitrobenzene (TATB) up to 20 GPa*, J. Phys. Chem. C **122**, 15861 (2018).

[242] H. E. Kissinger, *Variation of Peak Temperature with Heating Rate in Differential Thermal Analysis*, J. Res. Natl. Bur. Stand. (1934). **57**, 217 (1956).

VITA

Brenden Hamilton received his PhD in Materials Engineering from Purdue University in 2022 under the supervision of Prof. Alejandro Strachan. He holds two bachelor's degrees from Purdue University in Materials Engineering and Honors Applied Physics, both earned in 2018. He is also a graduate of the Purdue Honors College in conjunction with his bachelor's degrees.

During his PhD, Brenden focused mainly on the study of shock formation of hotspots in high explosives and how molecular strain in hotspots can influence overall reactivity. He has developed methods for simulations of shock physics and simulations of many bodied mechanochemistry effects. Throughout his time at Purdue, he has also worked on upscaling atomistic models for continuum and coarse-grained simulations, predicting chemical kinetics and reaction paths of new energetic materials, thermal transport in explosives, shock loading in glassy polymers, and molecular level processes in mechanophore activation.

Brenden spent multiple summers during his PhD collaborating with staff at Lawrence Livermore National Laboratory. He has, to date, published 10 peer reviewed journal papers and given numerous conference talks and poster presentations. In 2020, he received the Purdue Materials Engineering Briney Achievement Award for early graduate career success.

Upon leaving Purdue, Brenden will be joining the Physics and Chemistry of Materials group (T-1) within the Theoretical Division at Los Alamos National Laboratory as the Director's Postdoctoral Fellow. Brenden's research focus at LANL will be on shock induced mechanochemistry for complex microstructures of high explosives and polymer binder materials.

PUBLICATIONS

Sensitivity of the Shock Initiation Threshold of 1,3,5-Triamino-2,4,6-trinitrobenzene (TATB) to Nuclear Quantum Effects

Brenden W. Hamilton,[†] Matthew P. Kroonblawd,[‡] Md Mahbubul Islam,[†] and Alejandro Strachan*,[†]

[†]School of Materials Engineering and Birck Nanotechnology Center, Purdue University, West Lafayette, Indiana 47907, United States

[‡]Physical and Life Sciences Directorate, Lawrence Livermore National Laboratory, Livermore, California 94550, United States

Ⓢ *Supporting Information*

ABSTRACT: Approximating the dynamics of atomic nuclei with classical equations of motion in molecular dynamics (MD) simulations causes an overprediction of the specific heat and omits zero-point energy which can have a significant effect on predictions of the response of materials under dynamical loading. We use quantum and classical thermostats in reactive MD simulations to characterize the effect of energy distribution on the initiation and decomposition of the explosive 1,3,5-triamino-2,4,6-trinitrobenzene (TATB) under

shock and thermal loading. Shock simulations using the multiscale shock technique (MSST) show that nuclear quantum effects not only increase the temperature rise during dynamical loading but also lower the shock temperature corresponding to the threshold for initiation of chemical reactions. The lower specific heat and presence of zero point energy contribute approximately equally to these effects. Thermal decomposition simulations show that nuclear quantum effects lower the activation barrier associated with reaction compared to classical simulations. Quite interestingly, comparing quantum and classical simulations as a function of average kinetic energy shows that classical baths result in faster kinetics as compared with quantum ones; we explore the molecular origins of this observation.
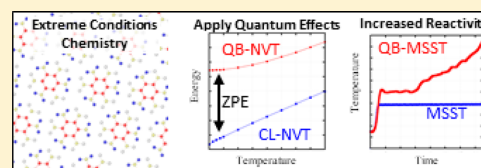
1. INTRODUCTION

The response of materials to ultrahigh strain rate mechanical loading is an area of significant scientific interest and activity. When subjected to dynamical mechanical shocks, materials respond via a combination of complex processes that can include elastic and plastic deformation,[1,2] phase transitions,[3,4] and fracture.[8] In the case of energetic materials, the increase in pressure and temperature caused by shock loading can induce chemical decomposition reactions and even lead to detonation.[5] Significant theoretical and experimental efforts have been devoted toward developing an atomistic-level understanding of the shock-induced response of a wide range of materials, including plasticity,[6,7] phase transitions,[3,4] failure,[8] and chemistry.[9,10] Computational studies using all-atom reactive and nonreactive molecular dynamics (MD) have been a critical component of larger efforts to reveal the complex processes that operate during the early stages of shock-induced initiation of explosive materials.

Early reactive MD simulations of shock impact have led to an understanding of the reaction mechanisms for initiation.[9] Advances in reactive interatomic potentials (also called force fields) have enabled the study of thermally induced chemical decomposition to better understand exothermic reactions that can eventually lead to deflagration and ignition.[11−13] Large scale simulations involving millions of atoms revealed the dynamic formation of defects during shocks as well as complex interactions between shocks and preexisting defects such as

porosity.[14−18] More recently, all-atom MD simulations of shock-induced pore collapse in α-1,3,5-trinitro-1,3,5-triazinane (α-RDX) captured the formation of a deflagration wave following the collapse of nanoscopic pores.[19,20] Complementing such nonequilibrium shock simulations, steady-state shock loading methods such as the Hugoniostat[21,22] and the Multi-Scale Shock Technique[23] (MSST) have enabled MD simulations of postshock states on substantially longer time scales through use of smaller computational cells. Mesoscale modeling[24,25] has provided additional insights into the formation of hotspots leading to initiation and deflagrations through pore collapse[26] and shock-induced shear localization.[27] Mechanisms such as shearing, friction, and multiple wave interactions are known contributors to the formation of hotspots through local heating, leading to overall initiation.[28] Direct experimental validation of MD predictions has been limited by difficulties in growing high-quality single crystals and the small time and length scales on which initiation occurs, which have prevented direct experimental characterization. Modern ultrafast spectroscopic techniques[29,30] that probe material response on the molecular level are enabling direct comparisons between experiments and predictions from MD

shock simulations to study initiation on similar time and length scales.[31−33]

Many of the response mechanisms discussed above, including plasticity and chemical reactions, are thermally activated. Thus, the ability to accurately capture the local rise in temperature following the shock front is critically important. Despite its importance, shock-induced temperature rise is often described poorly in atomistic simulations due to the standard MD approach of approximating the dynamics of atomic nuclei with classical equations of motion. Classical mechanics (CM) and quantum mechanics (QM) lead to significantly different energy distribution among the various roto-vibrational modes of an N-atom system resulting in different energy-temperature relationships. For example, within the harmonic approximation, the internal energy-temperature relationships are given by well-known relationships,

$$E_{CM}(T) = (3N - 6)k_B T \tag{1}$$

$$E_{QM}(T) = \sum_i k_B \left[\frac{\theta_i}{2} + \frac{\theta_i}{\exp\left(\frac{\theta_i}{T}\right) - 1} \right] \text{ where } \theta_i = \hbar\omega_i/k_B \tag{2}$$

which results in vast differences in constant-volume specific heat $C_V(T) = (\partial E/\partial T)_V$. Classical mechanics results in equipartition of energy among all degrees of freedom that appear squared in the Hamiltonian having an average energy of $k_B T/2$. In contrast, the uncertainty principle in QM precludes one from removing all the energy in a vibrational mode and as temperature approaches zero the energy in each vibrational model approaches its zero point energy (ZPE) $\hbar\omega/2$. Thus, CM results in a temperature-independent specific heat that is a significant overestimation of the QM result for temperatures below or similar to Debye's. For organic molecular explosives, the specific heat at room temperature is typically overestimated by a factor of 2 to 3. This difference can lead to large underpredictions in the shock-induced temperature rise, with errors on the order of hundreds of Kelvin.[34,35]

Postprocessing methods exist to correct thermodynamic properties for systems in equilibrium[36] that can be applied to gauge the temperature rise in shock simulations, were they to follow a quantum specific heat.[37] While postprocessing corrections provide insight into some nuclear quantum effects, the simulation itself, and any thermally activated processes, follow classical statistics. Quantum thermostats have been proposed as one way to correct the energy distribution in MD simulations such that vibrational energy is partitioned according to the quantum-mechanically correct Bose−Einstein distribution.[38,39] This so-called quantum thermal bath (QTB) provides the system with a zero-point energy (ZPE) and corrects for the equipartition of energy utilizing a Langevin-style thermostat. The QTB was recently coupled to the MSST (QB-MSST) to add QM corrections to shock heating,[40] which was shown to lower the initiation threshold for chemistry in methane by roughly 40%. Here we apply QB-MSST to explore the effects of quantum energy distributions in the shock-induced chemical initiation of the high-energy density material 1,3,5-triamino-2,4,6-trinitrobenzene (TATB).

TATB is a high explosive with exceptional insensitivity to accidental detonation by mechanical, thermal, and electrical insults.[41−43] There have been relatively few MD studies on the shock response of TATB owing to the practical difficulties in performing shock simulations of triclinic crystalline materials, which have only recently been solved.[44,60] Reactive MD simulations of overdriven shockwaves in TATB have shown the formation of large carbon clusters rich in nitrogen[45] and oxygen[46] that may retard reactivity due to high stability.[47] Early agglomeration of TATB molecules will trap oxygen and nitrogen atoms, preventing rapid formation of exothermic products. It is also known that higher critical temperatures are required to form a critical hotspot in TATB compared to the more sensitive explosive octahydro-1,3,5,7-tetranitro-1,3,5,7-tetrazocine (HMX).[48] TATB-based explosive formulations have much larger reaction zones than HMX formulations,[49] yet they have comparable detonation velocity and Chapman−Jouguet pressure.[50] Atomistic computational studies offer a practical route to better understand the initial steps of TATB initiation behavior, especially considering the lack of single crystal experiments.

In this article, we apply standard MSST and QB-MSST simulations to study shock-induced initiation in TATB single crystals. Through direct comparison, we isolate the influence of nuclear quantum effects that determine two key properties governing shock-initiation of chemistry, namely the specific heat and ZPE. We find that applying dynamical quantum corrections lowers both the minimum initiation shock velocity and the minimum initiation temperature, resulting in a significantly lower threshold for chemistry than would be obtained through standard quantum postcorrections of purely classical simulations.

2. SIMULATION DETAILS

2A. Atomistic Models and Force Fields. All MD simulations of TATB were performed using the LAMMPS software package[51] with the reactive force field ReaxFF to describe atomic interactions.[52,53] Details concerning trajectory integration are introduced in connection with particular simulation types described below, but in all cases the time step was set to 0.1 fs. Partial atomic charges were calculated using the charge equilibration scheme QEq[54] at each time step with an accuracy threshold set to 1×10^{-6}. In order to verify that the primary conclusions of our study are insensitive to the force field parametrization, we performed simulations using two versions of ReaxFF, namely ReaxFF-2018[55] and ReaxFF-LG.[56] ReaxFF-2018 was recently developed to study shock-to-deflagration in hexanitrostilbene (HNS) and adds the so-called low-gradient correction to improve nonbonded interactions in the ReaxFF-2014 force field developed by Wood et al.[57] Addition of low-gradient corrections for long-range London dispersion interactions in ReaxFF-2018 yields significantly improved initial density and stress states compared to the ReaxFF-2014 parametrization. We find good comparison in terms of ambient density and shock response for our present TATB shock results to both experiments and the previous ReaxFF parametrizations that include the low-gradient correction. These two ReaxFF parametrizations were chosen since, despite good comparison for unreacted shock states of TATB, they return significantly different reaction rates and final chemical species, with ReaxFF-LG reacting less rapidly than ReaxFF-2018.[58]

Due to the anisotropic nature of the TATB crystal structure, the shock direction can be expected to influence reactivity. However, since our focus is on the effect of classical vs quantum energy distribution on decomposition and reaction, we study shock loading along a single direction. All shocks

182

were performed normal to the TATB basal planes along direction $N_{(001)} = \mathbf{a} \times \mathbf{b}$ in the triclinic setting of Cady and Larson[59] with lattice vectors $\mathbf{a}$, $\mathbf{b}$, and $\mathbf{c}$. Note that due to the triclinic crystal structure, the directions $N_{(001)}$ and $\mathbf{c} = [001]$ are not parallel. Thus, we created a supercell with cell vectors $\mathbf{A}$, $\mathbf{B}$, and $\mathbf{C}$ such that $\mathbf{C}$ is nearly parallel to $\mathbf{a} \times \mathbf{b}$ and a minimal strain would result in the desired shock direction. Starting from this unit cell, the generalized crystal-cutting method (GCCM)[60] framework was used to create a near-

Figure 1. Oriented TATB cell used in all simulations. The cell Z axis of the nearly orthorhombic cell was aligned with the $N_{(001)}$ direction in the crystal. The top image is a sliced cell to only show a single crystal layer. Renderings were created with the OVITO software package.[62] Red atoms represent carbon, blue is oxygen, white is hydrogen, and yellow is nitrogen.

orthorhombic TATB cell (shown in Figure 1) with cell vectors of the super cell $\mathbf{A}$, $\mathbf{B}$, and $\mathbf{C}$ defined as

$$\mathbf{A} = -5\mathbf{a} - 3\mathbf{b} + 0\mathbf{c} \tag{3}$$

$$\mathbf{B} = \mathbf{a} - 7\mathbf{b} + 0\mathbf{c} \tag{4}$$

$$\mathbf{C} = \mathbf{a} + 2\mathbf{b} + 6\mathbf{c} \tag{5}$$

For consistency, we start all simulations for both force fields with identical unit cell (and, consequently, supercell) lattice parameters. We chose lattice parameters such that both force fields predict a hydrostatic state of nearly zero stress and match the experimental density. These lattice parameters are obtained by scaling the room temperature, zero stress, ReaxFF-2018 cell (obtained from an isothermal, isobaric MD simulation for 50 ps) to match the experimental density. The resulting lattice parameters are $a = 9.2344$ Å, $b = 9.22$ Å, $c = 6.608$ Å, $\alpha = 111.11°$, $\beta = 90.27°$, and $\gamma = 119.92°$, which yielded a nominal hydrostatic state for both force fields and stresses lower than 200 MPa. These parameters differ from the experimental values of $a = 9.010$ Å, $b = 9.028$ Å, $c = 6.812$ Å, $\alpha = 108.59°$, $\beta = 91.82°$, and $\gamma = 119.97°$.[59] We note that using the experimental lattice parameters results in the formation of defects with ReaxFF-2018, due to the low stress initiation points for twin boundaries and basal plane gliding in TATB.[61]

The cell described above was the starting point for the GCCM procedure, resulting in a supercell with 10,944 atoms (456 molecules). Since the current LAMMPS implementations of MSST and QB-MSST require orthorhombic cells, we applied very small strains ($\leq 0.05\%$) to the GCCM solution to satisfy this constraint. Cells for both force fields were fixed at the experimental crystal density 1.93 g/cm³.

2B. Shock Loading Simulations and Quantum Bath. To quantify the role of nuclear quantum effects on initiation, we investigated the response of TATB under shock loading for particle velocities (U_p) between 0.5 km/s and 3.0 km/s. Both classical MSST and QB-MSST simulations were used to model shock loading and compare effects of a quantum heat bath against a purely classical baseline. Prior to shock, all cells were equilibrated for 50 ps using canonical ensemble (NVT) simulations at 300 K. The initial NVT equilibration for classical MSST simulations was performed using a standard Langevin thermostat[63] and for QB-MSST simulations using a Langevin-style QTB thermostat.[38] Parameters for these thermostats are described in Section 2C.

The MSST method allows for smaller simulation cells compared to direct shock simulations and thus affords a drastic reduction in computational cost. This is particularly important in the present study on initiation in TATB, as it is often necessary to simulate hundreds of picoseconds to observe

Figure 2. System temperature during MSST and QB-MSST simulations with shock velocities of (a) 6 km/s and (b) 8 km/s obtained using ReaxFF-2018. Comparison of postshock temperatures will be used to assess initiation thresholds.

Figure 3. Average molecular energy using the classical and quantum heat baths for the (a) ReaxFF-2018 and (b) ReaxFF-LG force fields. The ZPE line calculated from the DOS at 1 K is shown for comparison.

significant chemical reactivity. Additionally, the MSST method is the only shock method currently coupled with the QTB in LAMMPS.

Nuclear quantum effects are expected to yield a larger temperature rise from shocks due to the lower specific heat. We define the postshock temperature as the steady system temperature directly following the shock, prior to any chemical reactivity, as shown in Figure 2. The cases shown highlight slow- and fast-reacting cases in panels (a) and (b), respectively. We see an expected difference in the postshock temperature on the order of a few hundreds of Kelvin and a resulting difference in initiation threshold. Trajectories were interpreted up to the onset of significant exothermic chemistry for the MSST simulations below the detonation velocity of TATB; this is necessary since no steady state reacted solution exists under these conditions.[64] This lack of a steady state solution will be taken advantage of later to bound predictions of detonation velocity for both MSST and QB-MSST.

2C. Isothermal Simulations with Quantum Bath and Quantum Corrections. To characterize the effects of a quantum heat bath on unreacted systems in equilibrium, we also performed *NVT* simulations with classical and quantum heat baths over a range of temperatures. This allows for direct comparisons to isolate the effects of ZPE and specific heat without the added complication of work due to shock compression or chemistry. Dynamical nuclear quantum corrections were applied using the QTB thermostat in both *NVT* and QB-MSST simulations. The frequency cutoff value used in all QTB simulations was set to 0.5 fs^{-1} with a damping parameter of 200 fs, which was found to converge predictions for the kinetic energy and ZPE following the convergence tests for QB-MSST parameters discussed in ref 40. A coupling parameter of 1.0 was used in QB-MSST. Because the QTB uses Langevin-style dynamics, all classical *NVT* simulations were performed with a standard Langevin thermostat[63] with the same 200 fs damping parameter for comparison. Figure 3 compares internal energy vs temperature relationships with quantum and classical baths for both force fields. In all cases we find the expected behavior, with the QTB simulations approaching a constant energy value as temperature tends to zero.

In order to quantitatively validate the results of the QTB, we utilize an alternative avenue to assess nuclear quantum effects: through postprocessing of classical trajectories based on the

vibrational density of states (DOS) and Bose−Einstein statistics. Vibrational DOS for postprocessing corrections were calculated from 10 ps classical *NVT* simulations. The ZPE and specific heat can then be calculated as integral relations to the DOS calculated from the atomistic velocity power spectrum.[36]

$$ZPE = k_B T \int_0^\infty d\omega * DOS(\omega)\left(\frac{x}{2} + \frac{x}{e^x - 1} - 1\right) \quad (6)$$

$$C_v = k_B \int_0^\infty d\omega * DOS(\omega)\frac{x^2 e^x}{(1 - e^x)^2} \quad (7)$$

where $x = \hbar\omega/k_B T$. The horizontal lines in Figure 3 represent the ZPE obtained from the DOS, to which we find good agreement with the QTB predictions. Furthermore, a numerical derivative of the energy-temperature response (Figure 3) was used to calculate the specific heat at constant volume, C_v, from QTB *NVT* simulations for comparison to DOS-based results. We find the QTB accurately describes C_v at temperatures of interest as shown in Figure 4. Our C_v calculations were limited to temperatures below 800 K due to the onset of initial chemical decomposition. In addition to comparing QTB and DOS-derived specific heats, Figure 4
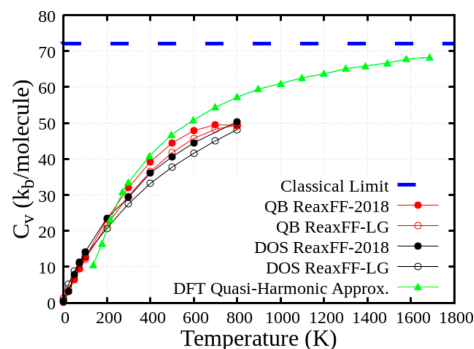
Figure 4. Specific heat of TATB crystal predicted by QTB simulations and DOS integration compared to the classical limit and gas-phase quasi-harmonic DFT[65] calculations.
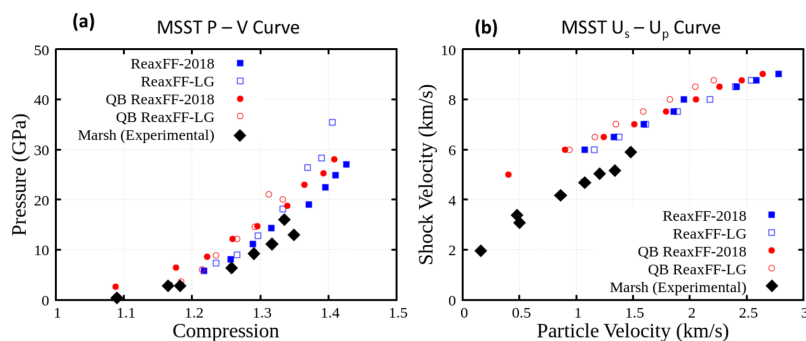
Figure 5. Unreacted (a) $P-V_0/V$ and (b) U_s-U_p shock response predicted by MSST and QB-MSST. Data from shock experiments[66] on TATB pressed powders is shown for comparison.
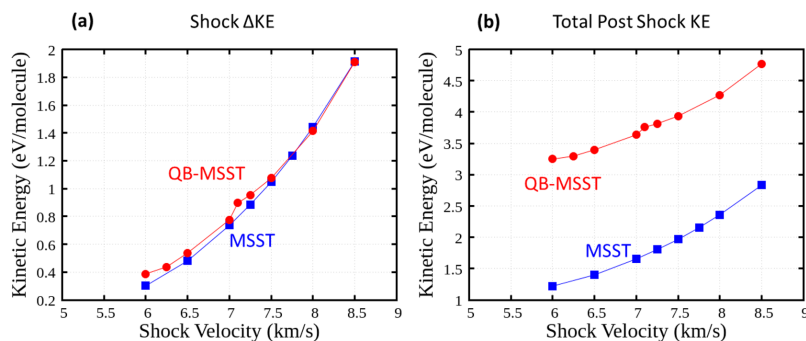
Figure 6. Kinetic energy responses for MSST and QB-MSST simulations predicted by ReaxFF-2018 showing (a) the change in kinetic energy and (b) the postshock kinetic as a function of shock velocity U_s.

compared our results with those in ref 65. The total specific heat for a TATB molecule was separated into contributions from the translational, rotational, and vibrational degrees of freedom. The translations and rotations are well-described by CM and contribute a combined $6k_B$ to the specific heat. The vibrational contributions were modeled using the temperature-dependent internal specific heat, $C_V^{int}(T)$, calculated[65] for a gas-phase TATB molecule via DFT within the quasi-harmonic approximation. This provides further validation of the accuracy with which the combination of ReaxFF and QTB describes the thermal properties of TATB.

Classical shock simulations can be postprocessed to determine the equivalent temperature rise given a quantum specific heat using the relationship between energy input and change in temperature. Given the total change in energy during shock in a classical simulation, we approximate the corresponding quantum temperature as the integration limit of the total specific heat over a temperature range that yields the same amount of energy as the classical simulation. Setting the lower integration limit to the initial temperature (300 K), we solve for the upper integration limit

$$\Delta E = \int_{300K}^{T} (6k_B + C_V^{int}(T'))dT' \tag{8}$$

where ΔE is the change in energy due to shock, $C_V^{int}(T')$ is the specific heat from the internal degrees of freedom, and $6k_B$ approximates the specific heat associated with the translational and rotational degrees of freedom per molecule. For these calculations, the change in the total change in energy is approximated as twice the change in kinetic energy, assuming equipartition.

3. SHOCK HUGONIOT AND INITIATION THRESHOLD

3A. Shock States. We performed a series of shock simulations on perfect TATB single crystals with the ultimate goal of assessing the effects of nuclear quantum effects on sensitivity and reactivity. Figure 5 shows unreacted pressure–compression (P vs V_0/V) and shock velocity vs particle velocity (U_s-U_p) curves for the different methods (obtained following shock loading but prior to reactions) along with experimental data for shocked TATB pressed powders.[66] Including quantum effects yields relatively minor differences in these particular projections of the Hugoniot (the locus of states accessible via shocks); this indicates that the shock imparts roughly the same amount of energy into the material regardless of the use of classical (CL) or QM energy distributions. The weak difference derives from the fact that the $P-V$ and U_s-U_p responses are dominated by the cold curve. The QB-MSST results have slightly higher pressures
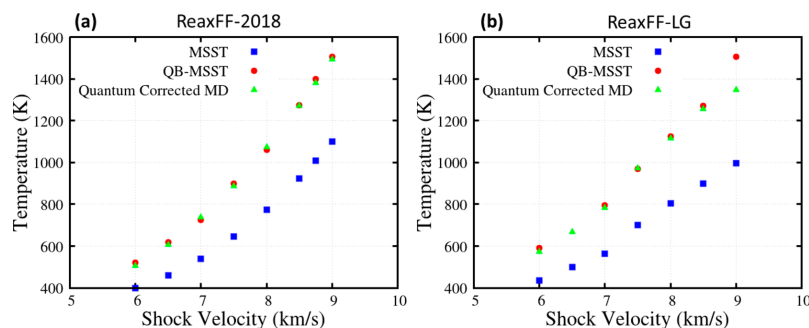
Figure 7. Comparison of postshock temperatures for MSST, QB-MSST, and a postprocessing quantum correction to MSST using a quantum specific heat[65] with (a) ReaxFF-2018 and (b) ReaxFF-LG.
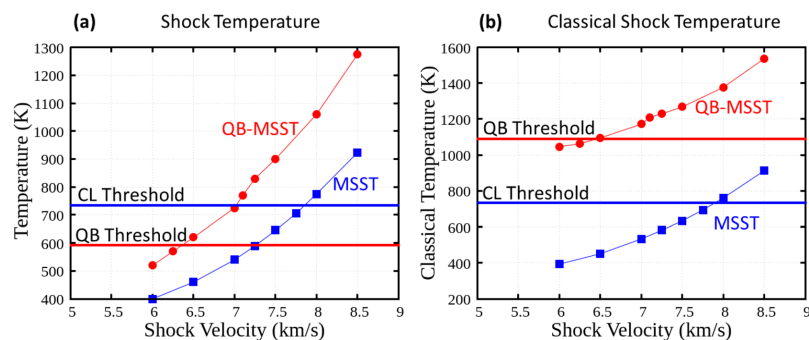
Figure 8. Comparison of postshock temperatures predicted by MSST and QB-MSST using ReaxFF-2018 in terms of (a) the temperature and (b) the classical temperature. Solid lines represent thresholds for initiation of chemistry. Note: The Classical temperature starting point for QB-MSST (300 K equivalent) is 930 K.

than their classical MSST counterparts for a given compression, which is due to the larger temperature rise generated with a quantum specific heat. Our simulations closely match the experimental pressure−compression data and overestimate the shock speeds, especially for weak shocks. One origin of this discrepancy is that the experiments and simulations had different initial densities (Marsh: 1.876 g/cm³, this work: 1.935 g/cm³). For better comparison to experiments, the negative trace of the stress tensor (i.e., the pressure) is reported here, despite a hydrostatic state not being reached prior to chemical initiation.

As discussed above, Figure 5 shows that both the $P−V_0/V$ and $U_s−U_p$ responses are roughly equivalent for both heat baths and, from the Hugoniot−Rankine jump conditions,[67] it follows that the energy imparted on the system by the shock is similar in both systems. Furthermore, Figure 6(a) shows that the change in kinetic energy is nominally the same for both systems. Despite different initial kinetic energies (due to inclusion or neglect of ZPE), the change in kinetic energy from a shock is nearly independent of the nature of heat bath, showing the partition of total shock energy between kinetic and potential is similar in both cases. While the change in kinetic energy upon shock loading is the same, the total postshock kinetic energies, Figure 6(b), are significantly different due to the presence of ZPE in the initial conditions

of the QB-MSST simulations. Thus, we could expect that even when both systems undergo similar compression during shocks, the difference in specific heat and initial kinetic energy could alter the initiation threshold governed by the onset of chemical reactions.

Figure 7 compares the shock temperature predicted by MSST and QB-MSST simulations for both force fields, as well as the quantum postcorrection of the classical MSST results. As expected, the actual temperature of the QB simulations is higher than the classical one. Postshock temperatures were obtained by averaging the instantaneous values over the first 10 ps after the system reached a steady state. This time interval is short compared with the reaction time, so the reported temperatures correspond to a shocked yet unreacted state. Postcorrections to the temperature increase are on the order of hundreds of Kelvin for the shock speeds considered here, with the magnitude of the correction generally increasing with shock strength. The excellent agreement between the postcorrection and the quantum bath simulations, as well as the previous results comparing MSST and QB-MSST, confirms that the QB-MSST simulations yield the correct shock response in pressure, temperature, volume, and energy, and thus can reliably characterize the threshold shock strength required for initiation.

3B. Thresholds for Initiation of Chemistry. One of our main objectives is to establish the effect of using a quantum bath on the threshold shock velocity needed to initiate exothermic chemistry in TATB. Here we identify the threshold as the lowest shock U_s that induces a rapid temperature increase to above 2000 K within 500 ps following compression. In practice, the threshold is bracketed with finite precision in U_s space. Figure 8 (a) shows the predicted thresholds and shock temperatures obtained using MSST and QB-MSST with ReaxFF-2018 (blue and red horizontal lines, respectively). Significant differences between the two thresholds are immediately apparent despite the fact that the changes in kinetic energy are nearly identical in the two cases (revisit Figure 6a). The threshold for QB-MSST simulations corresponds to a shock velocity of ~6.25 km/s (corresponding to U_p = 1.2 km/s and stress along the shock direction of 14 GPa) with a temperature of approximately 600 K, while classically, a much higher shock velocity is required to initiate chemistry, U_s = 8 km/s, (corresponding to U_p = 2.1 km/s and stress along the shock direction of 34 GPa) and a temperature of approximately 750 K.

One could, perhaps naively, expect a single threshold in kinetic energy for decomposition for both thermal baths, with the QB-MSST simulations reaching this value for lower U_s than classical MSST ones due to ZPE. To test this hypothesis, and, since the relationship between kinetic energy and temperature is different in the classical and quantum bath simulations, Figure 8(b) compares the kinetic energy for both cases, in terms of a kinetic temperature (T_{CL} = $2KE/3Nk_B$) that we refer to as the *classical temperature* (or simply temperature for purely classical simulations). Quite surprisingly, we find that while the actual temperature of the QB simulation corresponding to initiation is lower than the classical one, the kinetic energy content is significantly higher. Note that the classical temperature for the quantum bath system at 300 K is 930 K, making the change in classical temperature needed to reach the initiation threshold smaller for the quantum bath, despite the absolute threshold being considerably larger. Thus, as compared with the classical case, the threshold for the QB-MSST simulations corresponds to lower compression and temperature but higher overall kinetic energy (and therefore classical temperature). The remainder of the article focuses on explaining the origin of the differences in the critical values of temperature and classical temperature found in the simulations. ReaxFF-LG results show identical trends; detailed results and corresponding figures are included in Supporting Information Figure S1. Consistent with prior results for nitromethane[31] and polyvinyl nitrate,[58] the threshold for initiation for ReaxFF-LG is higher; using the QB-MSST we observe reactions for U_s = 7 km/s (corresponding to U_p= 1.6 km/s and P = 20 GPa) and higher, whereas, in classical MSST, we observe reactions for U_s = 8 km/s (corresponding to U_p = 2.1 km/s and P = 31 GPa) and higher.

We now explore whether postprocessing quantum corrections are sufficient to predict the same threshold for chemistry as obtained with QB-MSST. The idea behind this approach is to quantum correct the shock temperatures and obtain the shock strength required for the quantum temperature to match the classical temperature corresponding to initiation in the classical simulation. Of course, this ignores the role of compression and different energy distributions between classical and quantum baths. As shown in Figure 7, postprocessing MSST results using eq 8 return the same

temperature rise as QB-MSST. Using the quantum-corrected temperatures and the temperature threshold found in the MSST simulations, the threshold shock velocity is placed at around 7 km/s (intersection of blue line and red data points in Figure 8a). However, simulations including a quantum heat bath predict a threshold shock velocity of 6.25 km/s (intersection of red line and red data points in Figure 8a). This lower shock velocity threshold cannot be obtained through postprocessing of classical simulations. Overall, QB-MSST lowers the shock strength needed to initiate chemistry *in part* by producing a larger temperature rise. However, the quantum heat bath also lowers the apparent temperature needed for initiation, leading to a lower threshold shock strength than would be predicted based on temperature rise considerations alone.

Table 1 collects different state variables at the threshold for initiation of chemistry found using three approaches, namely

Table 1. Reaction Thresholds for MSST and QB-MSST, as well as Estimates Using the Quantum Postcorrected States and Classical Threshold Temperature

Shock Initiation Thresholds (ReaxFF-2018)			
		Post-Quantum-Corrected	
	MSST	MSST	QB-MSST
Pressure (GPa)	34	26	14
Shock Velocity (km/s)	8.0	7.25	6.25
Particle Velocity (km/s)	2.1	1.6	1.2
Temperature (K)	725	725	600
Classical Temperature (K)	725	725	1085
ΔClassical Temperature (K)	425	425	155

MSST, postcorrected MSST, and QB-MSST. While the QB-MSST thresholds will have effects from the quantum specific heat and ZPE, the postcorrected MSST isolates the quantum specific heat. When placed in terms of pressure, we find that the threshold predicted from MSST and QB-MSST differs by over a factor of 2. Additionally, the resulting threshold change from postcorrected MSST to QB-MSST is roughly half of the difference from MSST to QB-MSST. One interpretation of these ratios is that having the correct quantum-mechanical specific heat and ZPE are roughly equal in importance for predicting initiation of TATB.

3C. Reaction Time Scales. Figure 9 compares the reactivity for MSST and QB-MSST shocks corresponding to the same increase in temperature. To isolate temperature as the independent variable, we performed simulations with shock speeds chosen such that the initial change in temperature is equivalent while allowing differences in compression and kinetic energy (classical temperature). Temperature time histories for slow- and fast-reacting cases are shown in panels (a) and (b) of Figure 9, respectively. Stronger shocks that result in the same temperature increase exhibit similar time scales for reactivity (Figure 9b). In contrast, the QB-MSST system exhibits faster reactivity for temperatures closer to the initiation threshold (Figure 9a). While these shock simulations provide insight into the effect of nuclear quantum effects on reactivity, the differences in initial kinetic energy and work due to compression complicate making one-to-one comparisons.

3D. Comparison to Experiments: Detonation Velocity and Reaction Kinetics. We conclude the section on shock decomposition comparing our simulation results with experi-
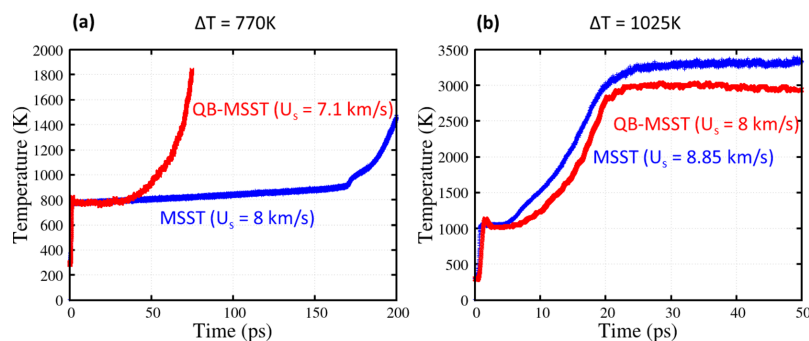
Figure 9. Temperature time evolution for ReaxFF-2018 MSST and QB-MSST shocks with the same postshock temperature: (a) 800 K and (b) 1025 K.

ments, both in terms of detonation velocity and reaction kinetics. As discussed above, a direct validation of the kinetics in the simulations is challenging due to fast temporal scales and extreme conditions, but it is worthwhile to compare our results with macroscopic detonation experiments of a 95 vol % TATB plastically bonded explosive (PBX 9502). These experiments provide information about the time scales involved in exothermic reactions and transition to detonation.[68,69] The time to detonation at room temperature was found to decrease abruptly with shock pressure, from approximately 1.7 μs at 11.62 GPa to approximately 0.6 μs at 16.22 GPa.[69] These are the time scales required to form a steady detonation wave, and exothermic processes are observed at shorter times. As discussed above, in order to observe reaction in the 0.5 ns time scale of our simulations, QB-MSST required a shock threshold of 14 GPa for ReaxFF-2018 and 33 GPa for the less reactive ReaxFF-LG. This indicates that the kinetics predicted by ReaxFF-2018 are fast compared with experiments and a direct comparison with ReaxFF-LG is not possible since the experiments did not reach the pressures required to observe reactions in MD time scales. Limitations of the force field description are likely contributors to the discrepancy with experiments. However, we note that these are not direct comparisons and care should be exercised in drawing firm conclusions. The experiments involve a composite material where hotspots are likely contributors to initiation and, more importantly, in order for the velocity gauges to detect exothermic chemistry the volume expanding chemical reactions need to propagate, couple with the leading shock, and accelerate it. In contrast, we model a homogeneous system and do not capture the coupling between the reactions and the propagating shock. Beyond experiments, we can also compare our results with prior work using a quantum-mechanics based description of atomic interactions via density functional tight binding (DFTB). Using DFTB and classical MSST to model homogeneous shocks in TATB, Manaa et al. observed significant exothermic chemistry within 100 ps for shocks with U_s = 9 km/s and no chemistry within a 400 ps run for 8 km/s.[45] Using a classical thermal bath, ReaxFF-2018 reacts in 15 ps for 9 km/s and 150 ps for 8 km/s while ReaxFF-LG reacts in 100 ps for 9 km/s and 250 ps for 8 km/s. Thus, both force fields predict chemical reactions on time scales similar to DFTB in magnitude, with ReaxFF-LG being somewhat closer than ReaxFF-2018. While density functional theory (DFT)

based simulations would provide a more reasonable point for cross-validation of ReaxFF predictions for TATB shock chemistry, direct comparisons are complicated by the fact that those simulations reported in the literature are of strongly overdriven shocks ($U_s \sim$ 10 km/s) in systems containing only a few molecules.[44]

A second validation of the force fields is to compare the detonation velocity predicted to an experimental value of 7.9 km/s.[50] Unlike the kinetics above, detonation velocity depends of the equation of the state of the products enabling a more direct comparison. MSST simulations that incite reaction but have shock speeds below the detonation velocity will not have a steady state reacted solution, leading to rapid volume divergence.[64] Reacted systems above the detonation velocity will have a steady state compressed density on the reacted Hugoniot. We predict the detonation velocity to be between the maximum U_s, in which no reacted steady state solution exists, and the minimum U_s, for which a solution does exist. For MSST, the ReaxFF-2018 force field predicts a detonation velocity bracketed between 8.1 km/s and 8.2 km/s. QB-MSST predicts a detonation velocity between 8.05 km/s and 8.075 km/s. Due to higher temperatures at a given compression, the pressure of the QB-MSST Hugoniot points should be slightly higher than their classical counterparts, leading to an increased detonation velocity. See Supporting Information Figure S2 for plots related to detonation velocity calculations.

4. THERMAL DECOMPOSITION—ROLE OF QUANTUM BATH ON CHEMISTRY

4A. Activation Energies and Overall Kinetics. Comparing thresholds for chemistry and associated kinetics for classical and quantum baths in shock simulations is complicated by the different states of compression achieved. Isothermal-isochoric decomposition simulations remove compressive work from consideration, and maintaining constant temperature simple kinetics analysis allows for a cleaner isolation of effects due to ZPE. Isothermal simulations have previously been used to extract reaction kinetics;[70,71,58,72] however, the inherent thermostatting prevents heat evolution and temperature change as in a shock ignition. We performed NVT simulations at a density of 1.93 g/cm^3 with the same super cell as for MSST simulations, using classical and QTB thermostats following the methods outlined in Section 2, for temperatures between 1500 and 3000 K using the ReaxFF-2018 force field to
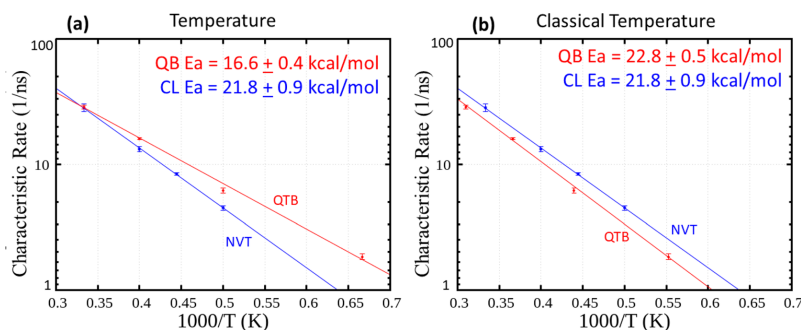
Figure 10. Arrhenius kinetics plots are shown in terms of (a) temperature and (b) classical temperature. Errors correspond to a 95% confidence interval calculated from an ensemble of five separate simulations.
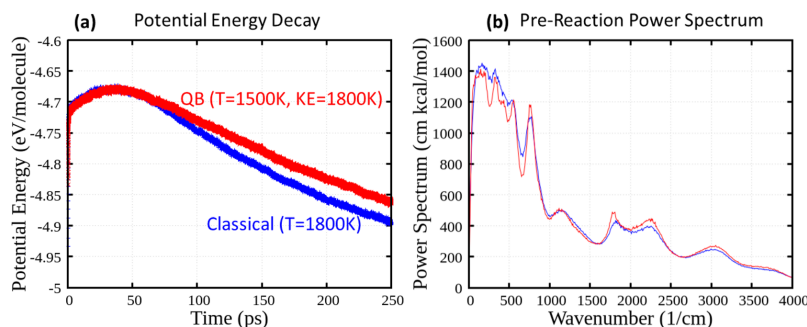
Figure 11. (a) Time history of potential energy in isothermal-isochoric decomposition at the same kinetic energy. (b) Vibrational power spectra of each system before onset of chemical reactions.

compare more directly with shock simulations conducted with this force field.

We assessed the chemical kinetics by defining a characteristic reaction time as the required time to release half of the total energy change of the reaction, or "half exothermicity". Five independent simulations were performed per state point (V,T) to gather ensemble statistics for the characteristic time. Twice the ensemble standard deviation of the ensemble mean characteristic time was taken to be the fundamental uncertainty (a 95% confidence interval), which we propagated through all subsequent analyses. Figure 10(a) shows the characteristic reaction time as a function of inverse temperature from which we extract an overall Arrhenius activation energy for TATB decomposition through weighted linear least-squares regression.[73] A similar analysis is shown in panel (b), except that it is performed in terms of the classical temperature (kinetic energy). For the classical simulations, the activation energy was determined to be 21.8 ± 0.9 kcal/mol with a prefactor of 10.9 ± 1.2 ps^{-1} and the quantum bath was found to lower both values to 16.6 ± 0.4 kcal/mol and 4.6 ± 1.1 ps^{-1}. For completeness, we reassessed the kinetics analysis in terms of classical temperature; perhaps surprisingly, the QTB data appears linear in this Arrhenius plot as well. The quantum bath with the (incorrect) classical temperature yielded a higher activation of 22.8 ± 0.5 kcal/mol, closer to the classical value, and a prefactor of 10.4 ± 1.1 p^{-1} s. More importantly and quite

surprisingly, under isokinetic conditions, the classical simulation exhibits faster kinetics and reacts in shorter time scales. While the decomposition rates for the ReaxFF-LG force field are lower than for ReaxFF-2018, the activation energies are very similar and the trends regarding classical and quantum baths and analysis are identical; details are included in Supporting Information Figure S3.

We find that the activation energy for TATB decomposition is around 21% lower in the QTB simulations as compared to those performed with a classical heat bath. The lower value for activation energy in the QTB decomposition simulations is consistent with the increased reactivity previously discussed in our shock simulations. These differences in activation energy are at least qualitatively consistent with the lower threshold for shock-induced chemistry shown in Figure 8, showing the same general trend for sensitivity to both mechanical and thermal insult. For completeness, activation energies were also obtained using the classical temperatures of the quantum bath isothermal decompositions. This second analysis shows greater similarities in reactivity for classical and quantum systems at the same kinetic energy, with the activation energies being within uncertainty of each other.

To assess how the energy distribution between modes affects kinetics, we consider that classical and quantum systems at equivalent kinetic energies will differ in terms of energy partitioning. The QTB partitions energy between modes to
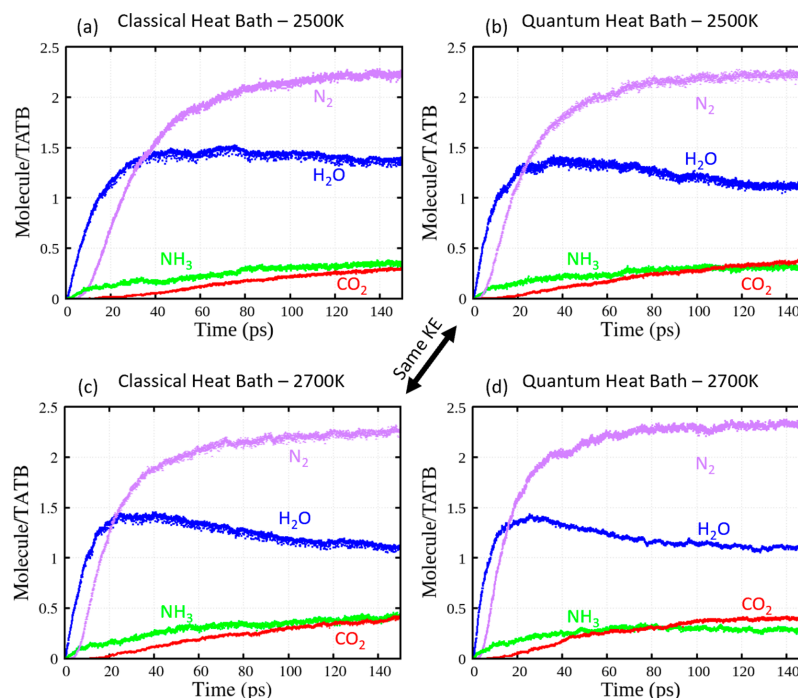
Figure 12. TATB decomposition products predicted by ReaxFF-LG using (a and c) a classical Langevin heat bath and (b and d) the QTB at selected temperatures. Panels b and c both have a classical temperature of 2700 K and are thus at the same kinetic energy.

approximately follow the Bose−Einstein distribution with a zero-point contribution whereas the energy distribution in a classical system will follow (approximately due to anharmonicities) equipartition independent of mode frequency. Modes with Debye temperature higher than the system temperature (as is the case here for high-frequency modes) will have more energy in the QTB simulations than in a classical simulation due to ZPE (that originates from the uncertainty principle). Thus, compared to a classical simulation and at the same kinetic energy, a QTB simulation will have more energy in higher frequency modes and less energy in low frequency modes. The remaining question is why the classical distribution is more effective at initiating and reacting TATB.

Figure 11 compares a classical and a QTB simulation with the same average kinetic energy (and different temperatures) corresponding to a classical temperature of 1800 K with ReaxFF-LG. See Supporting Information Figure S4 for a similar plot of ReaxFF-2018. The power spectrum obtained from atomistic velocities,[36] Figure 11(b), shows the expected energy distribution described above. Figure 11(a) shows the time history for potential energy for the two simulations. The faster reactivity rate for the classical system under identical kinetic energy conditions is potentially due to the higher energy of the low frequency modes. The initial decomposition kinetics for TATB is dominated by inter- and intramolecular hydrogen transfer.[74,75] Thus, these initial steps are associated with low frequency modes such as nitro/amine scissoring and intermolecular vibrations with increased energy in the classical

simulation. We note that this is a null point when comparing quantum and classical simulations at the same temperature (as opposed to kinetic energy) as the QTB system contains considerably more kinetic energy in every mode (via the ZPE).

4B. Decomposition and Reaction Paths. Altering the energy distribution among the various vibrational modes may change the kinetics of particular reaction paths and distort the final distribution of products. We analyzed time histories for the concentration of final product species H_2O, CO_2, NH_3, and N_2 to quantify the effects of quantum heat bath. Figure 12 shows the time evolution of these product species for cases of 2500 and 2700 K with both classical dynamics and the quantum thermal bath. Note that the 2500 K QTB simulation and the 2700 K classical simulation have the same kinetic energy. We find that reactions at the same classical temperature (panels b and c) yield very similar concentration histories at high temperatures. For reactions at the same temperature (compare panels a to b and c to d), species concentrations differ by roughly 5−10%, which is most likely caused by the roughly 5−10% difference in system kinetic energy. Our final product distribution compares well against previous MD results[76] and is in good agreement with experimental data for H_2O and N_2 production. However, we vastly underpredict the formation of CO_2 molecules.[77] The small differences in predicted reaction product time histories lead us to conclude that classical simulations might yield the same results as QTB simulations once their kinetic energies are

made consistent with quantum-mechanical expectations for ZPE.

5. SUMMARY

We presented an all-atom MD study to understand the role of nuclear quantum effects on the initiation and reactivity of TATB following shock compression and under thermal loading. Dynamical quantum corrections were applied using the quantum bath multiscale shock technique (QB-MSST). Shock simulations at various strengths were performed using both standard (classical) MSST and QB-MSST. A standard approach for applying quantum postcorrections to classical simulations was also considered. QB-MSST and postcorrected MSST simulations predict similar shock-induced temperature rises for all shock strengths considered, indicating that both approaches can correct for the quantum-mechanical nature of the specific heat that is missing in classical simulations. However, we find that nuclear quantum effects not only increase the change in temperature but also lower shock temperature at the threshold for initiation of chemical reactions. The predicted initiation threshold pressures were found to be 34, 26, and 14 GPa for MSST, postcorrected MSST, and QB-MSST approaches, respectively. We attribute these differences to the zero-point energy (ZPE) provided by the quantum bath and find that two nuclear quantum effects, namely the temperature-dependent specific heat and ZPE, are roughly equivalent in predicting the shock initiation threshold for TATB.

Standard approaches for applying quantum postcorrections to classical shock simulations neglect contributions to sensitivity from ZPE. Isothermal-isochoric (NVT) decomposition simulations were used to better isolate ZPE effects without the complication of compressive work. Comparison of classical NVT and quantum thermal bath (QTB) simulations reveals a lower activation energy for quantum bath reactions. An Arrhenius kinetics study predicts a reduction in the reaction barrier of approximately 20% due to nuclear quantum effects. The QTB incorporates ZPE as a kinetic energy contribution; thus, the classical and quantum bath simulations have different kinetic energies for a given thermostat temperature. Re-evaluating the Arrhenius kinetics results in terms of the classical temperature (scaled kinetic energy) reveals that the classical simulations exhibit a slightly higher activation energy than the QTB simulations. A vibrational power spectrum analysis shows that the increased reactivity in classical simulations is correlated with a greater amount of energy in low frequency modes, which may relate to an increase in early hydrogen transfer reactions. We show that product distributions at a given classical temperature are largely unaffected by choice of heat bath for temperatures near the classical limit. For both ReaxFF-2018 and ReaxFF-LG, in cases of shock and isothermal decomposition, we see the same trends in which the quantum effects speed up the kinetics and lower the necessary barriers to reaction.

■ ASSOCIATED CONTENT

ⓢ Supporting Information

The Supporting Information is available free of charge on the ACS Publications website at DOI: 10.1021/acs.jpcc.9b05409.

Information regarding the detonation velocity calculations for MSST and QB-MSST, as well as versions of figures from the main paper using the force field not used for the main paper version (ReaxFF-2018 and ReaxFF-LG) as we only show 1 FF result for many of the main result figures. Each Supporting Information figure's relationship to a manuscript figure is listed in the individual Supporting Information figure's caption. Figure S1: Mirror of Figure 8 in main document for thresholds but using ReaxFF-LG instead of ReaxFF-2018. Figure S2: Detonation velocity calculations using ReaxFF-2018 for both MSST and QB-MSST methods. Figure S3: Mirror of Figure 10 in main document showing kinetics for ReaxFF-LG. Figure S4: Mirror of Figure 11 using ReaxFF-2018 instead of ReaxFF-LG to show the effects of frequency dependence on energy. (PDF)

■ AUTHOR INFORMATION

Corresponding Author
*E-mail: strachan@purdue.edu.

ORCID ⓞ
Brenden W. Hamilton: 0000-0002-4524-2201
Matthew P. Kroonblawd: 0000-0002-5009-5998
Md Mahbubul Islam: 0000-0003-4584-2204

Notes
The authors declare no competing financial interest.

■ REFERENCES

(1) Zaug, J. M.; Austin, R. A.; Armstrong, M. R.; Crowhurst, J. C.; Goldman, N.; Ferranti, L.; Fried, L. E. Ultrafast dynamic response of single-crystal β-HMX (octahydro-1, 3, 5, 7-tetranitro-1, 3, 5, 7-tetrazocine). *J. Appl. Phys.* **2018**, *123*, 205902.

(2) Zhakhovsky, V. V.; Budzevich, M. M.; Inogamov, N. A.; Oleynik, I. I.; White, C. T. Two-zone elastic-plastic single shock waves in solids. *Phys. Rev. Lett.* **2011**, *107*, 135502.

(3) De Carli, P. S.; Milton, D. J. Stishovite: Synthesis by shock wave. *Science* **1965**, *147*, 144−145.

(4) Kroonblawd, M. P.; Goldman, N. Mechanochemical formation of heterogeneous diamond structures during rapid uniaxial compression in graphite. *Phys. Rev. B: Condens. Matter Mater. Phys.* **2018**, *97*, 184106.

(5) Handley, C. A.; Lambourn, B. D.; Whitworth, N. J.; James, H. R.; Belfield, W. J. Understanding the shock and detonation response of high explosives at the continuum and meso scales. *Appl. Phys. Rev.* **2018**, *5*, 011303.

(6) Holian, B. L.; Lomdahl, P. S. Plasticity induced by shock waves in nonequilibrium molecular-dynamics simulations. *Science* **1998**, *280*, 2085−2088.

(7) Bourne, N. K.; Millett, J. C. F.; Gray, G. T. On the shock compression of polycrystalline metals. *J. Mater. Sci.* **2009**, *44*, 3319−3343.

(8) Bourne, N.; Millett, J.; Rosenberg, Z.; Murray, N. On the shock induced failure of brittle solids. *J. Mech. Phys. Solids* **1998**, *46*, 1887−1908.

(9) Strachan, A.; van Duin, A. C.; Chakraborty, D.; Dasgupta, S.; Goddard, W. A., III Shock waves in high-energy materials: The initial chemical events in nitramine RDX. *Phys. Rev. Lett.* **2003**, *91*, 098301.

(10) Reed, E. J.; Manaa, M. R.; Fried, L. E.; Glaesemann, K. R.; Joannopoulos, J. D. A transient semimetallic layer in detonating nitromethane. *Nat. Phys.* **2008**, *4*, 72.

(11) Strachan, A.; Kober, E. M.; van Duin, A. C.; Oxgaard, J.; Goddard, W. A., III Thermal decomposition of RDX from reactive molecular dynamics. *J. Chem. Phys.* **2005**, *122*, 054502.

(12) Zhou, T.; Song, H.; Liu, Y.; Huang, F. Shock initiated thermal and chemical responses of HMX crystal from ReaxFF molecular dynamics simulation. *Phys. Chem. Chem. Phys.* **2014**, *16*, 13914−13931.

(13) Joshi, K.; Chaudhuri, S. Observation of deflagration wave in energetic materials using reactive molecular dynamics. *Combust. Flame* **2017**, *184*, 20−29.

(14) Cawkwell, M. J.; Sewell, T. D.; Zheng, L.; Thompson, D. L. Shock-induced shear bands in an energetic molecular crystal: Application of shock-front absorbing boundary conditions to molecular dynamics simulations. *Phys. Rev. B: Condens. Matter Mater. Phys.* **2008**, *78*, 014107.

(15) Zhao, S.; Germann, T. C.; Strachan, A. Molecular dynamics simulation of dynamical response of perfect and porous Ni/ Al nanolaminates under shock loading. *Phys. Rev. B: Condens. Matter Mater. Phys.* **2007**, *76*, 014103.

(16) Eason, R. M.; Sewell, T. D. Shock-induced inelastic deformation in oriented crystalline pentaerythritol tetranitrate. *J. Phys. Chem. C* **2012**, *116*, 2226−2239.

(17) Long, Y.; Chen, J. A molecular dynamics study of the early-time mechanical heating in shock-loaded octahydro-1, 3, 5, 7-tetranitro-1, 3, 5, 7-tetrazocine-based explosives. *J. Appl. Phys.* **2014**, *116*, 033516.

(18) Jaramillo, E.; Sewell, T. D.; Strachan, A. Atomic-level view of inelastic deformation in a shock loaded molecular crystal. *Phys. Rev. B: Condens. Matter Mater. Phys.* **2007**, *76*, 064112.

(19) Wood, M. A.; Cherukara, M. J.; Kober, E. M.; Strachan, A. Ultrafast chemistry under nonequilibrium conditions and the shock to deflagration transition at the nanoscale. *J. Phys. Chem. C* **2015**, *119*, 22008−22015.

(20) Eason, R. M.; Sewell, T. D. Molecular dynamics simulations of the collapse of a cylindrical pore in the energetic material α-RDX. *J. C. Proc. Soc. Exp. Mech.* **2015**, *1*, 423−438.

(21) Ravelo, R.; Holian, B. L.; Germann, T. C.; Lomdahl, P. S. Constant-stress Hugoniostat method for following the dynamical evolution of shocked matter. *Phys. Rev. B: Condens. Matter Mater. Phys.* **2004**, *70*, 014103.

(22) Maillet, J. B.; Mareschal, M.; Soulard, L.; Ravelo, R.; Lomdahl, P. S.; Germann, T. C.; Holian, B. L. Uniaxial Hugoniostat: A method for atomistic simulations of shocked materials. *Phys. Rev. E: Stat. Phys., Plasmas, Fluids, Relat. Interdiscip. Top.* **2000**, *63*, 016121.

(23) Reed, E. J.; Fried, L. E.; Joannopoulos, J. D. A method for tractable dynamical studies of single and double shock compression. *Phys. Rev. Lett.* **2003**, *90*, 235503.

(24) Rai, N. K.; Udaykumar, H. S. Void collapse generated meso-scale energy localization in shocked energetic materials: Non-dimensional parameters, regimes, and criticality of hotspots. *Phys. Fluids* **2019**, *31*, 016103.

(25) Handley, C. A.; Lambourn, B. D.; Whitworth, N. J.; James, H. R.; Belfield, W. J. Understanding the shock and detonation response of high explosives at the continuum and meso scales. *Appl. Phys. Rev.* **2018**, *5*, 011303.

(26) Springer, H. K.; Bastea, S.; Nichols, A. L., III; Tarver, C. M.; Reaugh, J. E. Modeling the effects of shock pressure and pore morphology on hot spot mechanisms in HMX. *Propellants, Explos., Pyrotech.* **2018**, *43*, 805−817.

(27) Austin, R. A.; Barton, N. R.; Reaugh, J. E.; Fried, L. E. Direct numerical simulation of shear localization and decomposition reactions in shock-loaded HMX crystal. *J. Appl. Phys.* **2015**, *117*, 185902.

(28) Davis, W. C. High explosives: The interaction of chemistry and mechanics. *Los Alamos Science* **1981**, *2*, 48−75.

(29) McGrane, S. D.; Moore, D. S.; Funk, D. J. Shock induced reaction observed via ultrafast infrared absorption in poly (vinyl nitrate) films. *J. Phys. Chem. A* **2004**, *108*, 9342−9347.

(30) Yang, Y.; Sun, Z.; Wang, S.; Dlott, D. D. Fast spectroscopy of laser-initiated nanoenergetic materials. *J. Phys. Chem. B* **2003**, *107*, 4485−4493.

(31) Islam, M. M.; Strachan, A. Reactive Molecular Dynamics Simulations to Investigate the Shock Response of Liquid Nitro-methane. *J. Phys. Chem. C* **2019**, *123*, 2613−2626.

(32) Brown, K. E.; McGrane, S. D.; Bolme, C. A.; Moore, D. S. Ultrafast chemical reactions in shocked nitromethane probed with dynamic ellipsometry and transient absorption spectroscopy. *J. Phys. Chem. A* **2014**, *118*, 2559−2567.

(33) Park, S. D.; Armstrong, M. R.; Kohl, I. T.; Zaug, J. M.; Knepper, R.; Tappan, A. S.; Kay, J. J. Ultrafast Shock-Induced Reactions in Pentaerythritol Tetranitrate Thin Films. *J. Phys. Chem. A* **2018**, *122*, 8101−8106.

(34) Goldman, N.; Reed, E. J.; Kuo, I. F. W.; Fried, L. E.; Mundy, C. J.; Curioni, A. Ab initio simulation of the equation of state and kinetics of shocked water. *J. Chem. Phys.* **2009**, *130*, 124517.

(35) Strachan, A.; Holian, B. L. Energy exchange between mesoparticles and their internal degrees of freedom. *Phys. Rev. Lett.* **2005**, *94*, 014301.

(36) Berens, P. H.; Mackay, D. H.; White, G. M.; Wilson, K. R. Thermodynamics and quantum corrections from molecular dynamics for liquid water. *J. Chem. Phys.* **1983**, *79*, 2375−2389.

(37) Goldman, N.; Reed, E. J.; Fried, L. E. Quantum mechanical corrections to simulated shock Hugoniot temperatures. *J. Chem. Phys.* **2009**, *131*, 204103.

(38) Dammak, H.; Chalopin, Y.; Laroche, M.; Hayoun, M.; Greffet, J. J. Quantum thermal bath for molecular dynamics simulation. *Phys. Rev. Lett.* **2009**, *103*, 190601.

(39) Barrat, J. L.; Rodney, D. Portable implementation of a quantum thermal bath for molecular dynamics simulations. *J. Stat. Phys.* **2011**, *144*, 679−689.

(40) Qi, T.; Reed, E. J. Simulations of Shocked Methane Including Self-Consistent Semiclassical Quantum Nuclear Effects. *J. Phys. Chem. A* **2012**, *116*, 10451−10459.

(41) Gibbs, T. R.; Popolato, A. *LASL Explosive Property Data*; University of California Press: Berkeley, CA, USA, 1980.

(42) Rice, S. F.; Simpson, R. L. *The Unusual Stability of TATB: A Review of the Scientific Literature, Report UCRL-LR-103683*; Lawrence Livermore National Laboratory: Livermore, CA, USA, 1990.

(43) Dobratz, B. M. *The Insensitive High Explosive Triaminotrinitro-benzene (TATB): Development and Characterization − 1888 to 1994, Report LA-13014-H*; Los Alamos National Laboratory: Los Alamos, NM, USA, 1995.

(44) Shimamura, K.; Misawa, M.; Ohmura, S.; Shimojo, F.; Kalia, R. K.; Nakano, A.; Vashishta, P. Crystalline anisotropy of shock-induced phenomena: Omni-directional multiscale shock technique. *Appl. Phys. Lett.* **2016**, *108*, 071901.

(45) Manaa, M. R.; Reed, E. J.; Fried, L. E.; Goldman, N. Nitrogen-rich heterocycles as reactivity retardants in shocked insensitive explosives. *J. Am. Chem. Soc.* **2009**, *131*, 5483−5487.

(46) Tiwari, S. C.; Nomura, K. I.; Kalia, R. K.; Nakano, A.; Vashishta, P. Multiple reaction pathways in shocked 2, 4, 6-Triamino-1, 3, 5-trinitrobenzene crystal. *J. Phys. Chem. C* **2017**, *121*, 16029−16034.

(47) He, Z. H.; Chen, J.; Wu, Q. Initial decomposition of condensed-phase 1, 3, 5-triamino-2, 4, 6-trinitrobenzene under shock loading. *J. Phys. Chem. C* **2017**, *121*, 8227−8235.

192

(48) Tarver, C. M.; Chidester, S. K.; Nichols, A. L. Critical conditions for impact-and shock-induced hot spots in solid explosives. *J. Phys. Chem.* **1996**, *100*, 5794−5799.

(49) Tarver, C. M. Multiple roles of highly vibrationally excited molecules in the reaction zones of detonation waves. *J. Phys. Chem. A* **1997**, *101*, 4845−4851.

(50) Rothstein, L. R.; Petersen, R. Predicting high explosive detonation velocities from their composition and structure. *Propellants, Explos., Pyrotech.* **1979**, *4*, 56−60.

(51) Plimpton, S. Fast parallel algorithms for short-range molecular dynamics. *J. Comput. Phys.* **1995**, *117*, 1−19.

(52) van Duin, A. C. T.; Dasgupta, S.; Lorant, F.; Goddard, W. A. ReaxFF: A Reactive Force Field for Hydrocarbons. *J. Phys. Chem. A* **2001**, *105*, 9396−9409.

(53) Chenoweth, K.; Van Duin, A. C.; Goddard, W. A. ReaxFF reactive force field for molecular dynamics simulations of hydrocarbon oxidation. *J. Phys. Chem. A* **2008**, *112*, 1040−1053.

(54) Rappe, A. K.; Goddard, W. A., III Charge equilibration for molecular dynamics simulations. *J. Phys. Chem.* **1991**, *95*, 3358−3363.

(55) Wood, M. A.; Kittell, D. E.; Yarrington, C. D.; Thompson, A. P. Multiscale modeling of shock wave localization in porous energetic material. *Phys. Rev. B: Condens. Matter Mater. Phys.* **2018**, *97*, 014109.

(56) Liu, L.; Liu, Y.; Zybin, S. V.; Sun, H.; Goddard, W. A., III ReaxFF-lg: Correction of the ReaxFF reactive force field for London dispersion, with applications to the equations of state for energetic materials. *J. Phys. Chem. A* **2011**, *115*, 11016−11022.

(57) Wood, M. A.; Van Duin, A. C.; Strachan, A. Coupled thermal and electromagnetic induced decomposition in the molecular explosive αHMX; a reactive molecular dynamics study. *J. Phys. Chem. A* **2014**, *118*, 885−895.

(58) Islam, M. M.; Strachan, A. Decomposition and Reaction of Polyvinyl Nitrate under Shock and Thermal Loading: A ReaxFF Reactive Molecular Dynamics Study. *J. Phys. Chem. C* **2017**, *121*, 22452−22464.

(59) Cady, H. H.; Larson, A. C. The crystal structure of 1, 3, 5-triamino-2, 4, 6-trinitrobenzene. *Acta Crystallogr.* **1965**, *18*, 485−496.

(60) Kroonblawd, M. P.; Mathew, N.; Jiang, S.; Sewell, T. D. A generalized crystal-cutting method for modeling arbitrarily oriented crystals in 3D periodic simulation cells with applications to crystal−crystal interfaces. *Comput. Phys. Commun.* **2016**, *207*, 232−242.

(61) Lafourcade, P.; Denoual, C.; Maillet, J. B. Irreversible Deformation Mechanisms for 1, 3, 5-Triamino-2, 4, 6-Trinitrobenzene Single Crystal Through Molecular Dynamics Simulations. *J. Phys. Chem. C* **2018**, *122*, 14954−14964.

(62) Stukowski, A. Visualization and analysis of atomistic simulation data with OVITO−the Open Visualization Tool. *Modell. Simul. Mater. Sci. Eng.* **2010**, *18*, 015012.

(63) Dünweg, B.; Paul, W. Brownian dynamics simulations without Gaussian random numbers. *Int. J. Mod. Phys. C* **1991**, *2*, 817−827.

(64) Reed, E. J.; Rodriguez, A. W.; Manaa, M. R.; Fried, L. E.; Tarver, C. M. Ultrafast detonation of hydrazoic acid (HN 3). *Phys. Rev. Lett.* **2012**, *109*, 038301.

(65) Kroonblawd, M. P.; Sewell, T. D.; Maillet, J. B. Characteristics of energy exchange between inter-and intramolecular degrees of freedom in crystalline 1, 3, 5-triamino-2, 4, 6-trinitrobenzene (TATB) with implications for coarse-grained simulations of shock waves in polyatomic molecular crystals. *J. Chem. Phys.* **2016**, *144*, 064501.

(66) Marsh, S. P. *LASL shock Hugoniot data* (Vol. *5*). Univ of California Press, 1980.

(67) Zeldovich, Y. B.; Raizer, Y. P. *Physics of shock waves and high-temperature hydrodynamic phenomena (No. FTD-MT-64−514)*. FOREIGN TECHNOLOGY DIV WRIGHT-PATTERSON AFB OH, 1965.

(68) Gustavsen, R. L.; Gehr, R. J.; Bucholtz, S. M.; Alcon, R. R.; Bartram, B. D. Shock initiation of the tri-amino-tri-nitro-benzene based explosive PBX 9502 cooled to− 55 C. *J. Appl. Phys.* **2012**, *112*, 074909.

(69) Gustavsen, R. L.; Sheffield, S. A.; Alcon, R. R. Measurements of shock initiation in the tri-amino-tri-nitro-benzene based explosive

PBX 9502: Wave forms from embedded gauges and comparison of four different material lots. *J. Appl. Phys.* **2006**, *99*, 114907.

(70) Rom, N.; Zybin, S. V.; Van Duin, A. C.; Goddard, W. A., III; Zeiri, Y.; Katz, G.; Kosloff, R. Density-dependent liquid nitromethane decomposition: molecular dynamics simulations based on ReaxFF. *J. Phys. Chem. A* **2011**, *115*, 10181−10202.

(71) Furman, D.; Kosloff, R.; Dubnikova, F.; Zybin, S. V.; Goddard, W. A., III; Rom, N.; Zeiri, Y. Decomposition of condensed phase energetic materials: Interplay between uni-and bimolecular mechanisms. *J. Am. Chem. Soc.* **2014**, *136*, 4192−4200.

(72) Sakano, M.; Hamilton, B.; Islam, M. M.; Strachan, A. Role of Molecular Disorder on the Reactivity of RDX. *J. Phys. Chem. C* **2018**, *122*, 27032−27043.

(73) Press, W. H.; Teukolsky, S. A.; Vetterling, W. T.; Flannery, B. P. *Numerical Recipes*; Cambridge University Press: New York, NY, 2007.

(74) Wu, C. J.; Fried, L. E. Ring closure mediated by intramolecular hydrogen transfer in the decomposition of a push− pull nitroaromatic: TATB. *J. Phys. Chem. A* **2000**, *104*, 6447−6452.

(75) Davis, L. L.; Brower, K. R. Shock-initiation chemistry of nitroarenes. *AIP Conf. Proc.* **1997**, *429*, 699−702.

(76) Zhang, L.; Zybin, S. V.; van Duin, A. C.; Dasgupta, S.; Goddard, W. A., III; Kober, E. M. Carbon cluster formation during thermal decomposition of octahydro-1, 3, 5, 7-tetranitro-1, 3, 5, 7-tetrazocine and 1, 3, 5-triamino-2, 4, 6-trinitrobenzene high explosives from ReaxFF reactive molecular dynamics simulations. *J. Phys. Chem. A* **2009**, *113*, 10619−10640.

(77) Ornellas, D. L. *Calorimetric determinations of the heat and products of detonation for explosives: October 1961 to April 1982 (No. UCRL-52821)*; CALIFORNIA UNIV BERKELEY LAWRENCE LIVERMORE LAB, 1982.

193

Predicted Reaction Mechanisms, Product Speciation, Kinetics, and Detonation Properties of the Insensitive Explosive 2,6-Diamino-3,5-dinitropyrazine-1-oxide (LLM-105)

Brenden W. Hamilton, Brad A. Steele, Michael N. Sakano, Matthew P. Kroonblawd, I-Feng W. Kuo, and Alejandro Strachan*

ABSTRACT: 2,6-Diamino-3,5-dinitropyrazine-1-oxide (LLM-105) is a relatively new and promising insensitive high-explosive (IHE) material that remains only partially characterized. IHEs are of interest for a range of applications and from a fundamental science standpoint, as the root causes behind insensitivity are poorly understood. We adopt a multitheory approach based on reactive molecular dynamic simulations performed with density functional theory, density functional tight-binding, and reactive force fields to characterize the reaction pathways, product speciation, reaction kinetics, and detonation performance of LLM-105. We compare and contrast these predictions to 1,3,5-triamino-2,4,6-trinitrobenzene (TATB), a prototypical IHE, and 1,3,5,7-tetranitro-1,3,5,7-tetrazoctane (HMX), a more sensitive and higher performance material. The combination of different predictive models allows access to processes operative on progressively longer timescales while providing benchmarks for assessing uncertainties in the predictions. We find that the early reaction pathways of LLM-105 decomposition are extremely similar to TATB; they involve intra- and intermolecular hydrogen transfer. Additionally, the detonation performance of LLM-105 falls between that of TATB and HMX. We find agreement between predictive models for first-step reaction pathways but significant differences in final product formations. Predictions of detonation performance result in a wide range of values, and one-step kinetic parameters show the similar reaction rates at high temperatures for three out of four models considered.
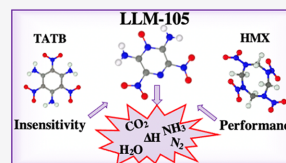
1. INTRODUCTION

2,6-Diamino-3,5-dinitropyrazine-1-oxide (LLM-105) is a relatively new high-explosive (HE) material that combines insensitivity (similar to 1,3,5-triamino-2,4,6-trinitrobenzene, TATB) with high detonation performance, approaching that of 1,3,5,7-tetranitro-1,3,5,7-tetrazoctane (HMX).[1] TATB represents the standard for insensitivity and HMX a common benchmark for performance. The development of an HE that combines these two properties is a grand challenge in the synthesis of energetic materials. Despite significant interest, little is known about how LLM-105 reacts under detonation conditions, with uncertainties in its decomposition reaction pathways, kinetics, and equations of state for the reactants and products. Filling these gaps through experiments is time consuming and costly. Furthermore, the determination of detailed chemical reaction pathways in condensed phases at extreme conditions is practically impossible with current diagnostics. Atomic-level simulations provide a means to determine this information and better understand fundamental drivers for explosive sensitivity and performance. Applying these tools to relatively uncharacterized materials, such as LLM-105, is also useful to assess the predictive power of current state-of-the-art atomistic models and can help guide and interpret future experiments. Rapid predictions of performance metrics, such as detonation velocity and Chap-

man−Jouguet (CJ) pressure, and sensitivity metrics, such as energy barriers for decomposition reactions, are important to facilitate the design of new explosives with reduced reliance on experimental testing. In particular, the ability to predict sensitivity to detonation initiation is highly desirable and remains a grand challenge due to the wide range of coupled phenomena involved.[2]

Recent progress has been made in applying theory to predict the properties of new materials and even discover new ones.[3] For example, new shape memory materials[4−6] and other high-strength metals[7] have been proposed based on theoretical calculations. These successful examples deal with structure−property relationships that can be accurately calculated with small computational domains through electronic structure calculations, typically using density functional theory (DFT), or else involve areas such as metallurgy, where there is over a century of experimental data and predictive models from which

1766

194
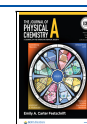
to extrapolate.[8] The problem at hand for HEs is significantly more complicated in several respects. Predicting detonation properties requires accurate models for Hugoniot curves of reactants and products, that is, the set of states accessible to shocked chemically reactive materials. This, in turn, requires determining the distribution of products at extreme pressures and temperatures. Predicting properties that depend on reaction kinetics is even more challenging. In principle, these quantities could be computed from first principles using ab initio molecular dynamics (MD) with forces obtained from electronic structure calculations using DFT. Unfortunately, the length and timescales necessary remain beyond the practical reach of DFT, even with recent advances in state-of-the-art high-performance computing. This has driven substantial interest in semiempirical quantum-based models, such as density functional tight-binding (DFTB), and empirical reactive force fields.

Over the last few decades, significant efforts have been devoted to developing accurate and computationally efficient methods to describe complex chemistry with atomic resolution.[9,10] Atomistic simulations provide a description of detailed chemistry and the prediction of multiple potential pathways for detonation chemistry.[11] Gas-phase calculations provide important information about possible decomposition paths[12−15] but neglect multimolecular processes and the environmental effects important at high pressures. Large-scale MD simulations can capture many body effects and condensed phase effects explicitly. Beyond equilibrium properties, large-scale atomistic simulations contribute to our understanding of the shock-to-detonation transition under highly nonequilibrium conditions at the grain scale. Reactive MD simulations of shock-induced pore collapse in RDX[16] and pentaerythritol tetranitrate (PETN),[17] and solid-state deflagration in RDX,[18] have helped to better understand the shock-to-deflagration transition at the molecular scale. These simulations can directly inform engineering-scale models with constitutive laws and enable predictions of the behavior of detonating HEs with complex microstructures.[19,20] Recent studies have allowed for the direct input of atomistic results to continuum scale codes for one-to-one comparison of the shock-induced mechanical response of porous HEs.[21−23] Additionally, simplified chemical reaction models have allowed for atomistically informed chemistry models in grain and mesoscale simulations.[24−27] Beyond atomistic simulations, detonation properties can be efficiently predicted via empirical thermochemical codes such as CHEETAH,[28] as well as via machine learning models;[29] however, these models cannot predict many of the properties of interest in the field.

Despite decades of work,[9] validation of atomistic simulations of chemical reactions at extreme conditions remains challenging. The combination of the increased accuracy of interatomic potentials and the increased computational capabilities, as well as modern experimental capabilities, has recently enabled direct comparisons of chemistry at extreme conditions. Recent spectroscopic work on nitromethane, polyvinyl nitrate (PVN), and pentaerythritol tetranitrate (PETN) have been reproduced utilizing reactive MD simulations.[30−34] Bassett and Dlott performed optical pyrometry experiments to measure hotspot temperatures with a high temporal resolution for a variety of HE materials.[35−37] These measurements compare well to previously predicted temperatures from both atomistic and continuum studies.[38−40] Coupling ultrafast dynamic compression experiments and machine-learned reactive force fields also

holds promise to elucidate the initial steps of soot formation during detonation.[10]

Within HE materials, insensitive high explosives (IHEs) are an important class that remains poorly understood from a basic-science perspective. IHEs such as TATB are attractive due to their capability to withstand stimuli that may otherwise lead to accidental initiation and detonation[41−43] in other materials. This insensitivity is theorized to be derivative of the formation of highly stable covalent clusters during reaction,[44,45] as well as the strong intermolecular hydrogen bonding network.[42,46] Coupling between mechanics and chemistry can drastically lower reaction barriers in plastically deformed TATB, which may indicate that sensitivity is connected to the crystal packing structure.[19] Despite much conjecture, the properties responsible for these safety characteristics are not clear.

We focus on LLM-105, a new IHE candidate molecular crystal for which limited work has been performed about the fundamental mechanics and chemistry. LLM-105 crystallizes in the monoclinic $P2_1/n$ space group,[56] with four molecules per unit cell, and exhibits a herringbone packing structure (see Figure 1). Most experimental efforts have focused on the
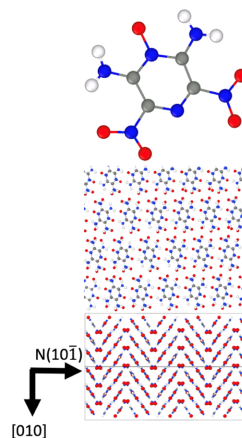
Figure 1. LLM-105 molecule (top), LLM-105 sheetlike structure with hydrogen bonding to neighbors and pseudohexagonal structure (center), and LLM-105 herringbone structure that runs normal to the [010] direction (bottom). Gray atoms represent C, blue to N, red to O, and white to H.

synthesis[47,48] and characterizing properties of formulations of LLM-105 with polymer binders.[49,50] Various studies have focused on the sensitivity of different LLM-105 composite formulations,[51−53] but little data exists for neat LLM-105. Manaa et al. employed first-principles calculations to explore the high-pressure equation of state (EoS) and formation energies,[54] which has been coupled with an experimental equation of state data.[55] Additionally, DFT calculations coupled with thermodynamic theory have allowed for predictions of detonation conditions, as well as initial thermal decomposition pathways predicted from bond dissociation energies.[56] Recent Fourier-transform infrared (FT-IR) work has shown initial reaction pathways of intramolecular H transfer and NO_2 scission reactions.[57] Additionally, in situ IR

experiments of gas-releasing reactions showed early products of H_2O and NH_3, followed by nitrogen gas products such as NO_2, NO, and HN, with a final step releasing CO_2.[58] Differential scanning calorimetry (DSC) experiments have been utilized to calculate average activation energies for a two-step reaction, where the first reaction step was 222.2 ± 0.5 kJ/mol and the second reaction step was 244.5 ± 0.5 kJ/mol.[59] The gas-phase activation energies have also been calculated at the DFT level for several proposed decomposition mechanisms for LLM-105.[60,61] However, shock-induced chemical reactions of LLM-105 are not well understood, and it is not clear whether the apparent insensitivity of LLM-105 results from it having similar chemistry and/or structure to TATB.

In this work, we use molecular dynamics with DFT, density functional tight-binding (DFTB), and the reactive force-field ReaxFF to take an expansive look at the performance, chemical kinetics, and decomposition reaction pathways of LLM-105. We parametrize an equation of state for the shock reaction products and provide a one-step reaction kinetics model. Through comparisons between LLM-105, the IHE TATB, and the comparatively sensitive HE HMX, we assess the capabilities of LLM-105 as well as identify correlations between fundamental properties that may govern insensitivity.

2. METHODS

2.1. Atomistic Models. Reactive MD simulations were performed at three different levels of theory for the description of the potential energy surface: DFT, DFTB, and ReaxFF, in increasing the level of empiricism and decreasing computation cost. In traditional DFT methods, the solution of the Kohn–Sham equations scales with the cube of the number of electrons.[66] This generally limits the practical application of DFT-MD simulations to systems with a few hundred atoms. DFTB also scales as $O(N^3)$, but with a smaller prefactor accompanied with lower accuracy. Given its short-range nature, ReaxFF scales as $O(N)$ and much larger system sizes and longer timescales are achievable, with a tradeoff in the form of accuracy and/or transferability.[30,31,34]

DFT-MD simulations were conducted using the Perdew–Burke–Ernzerhof (PBE)[62] generalized gradient approximation functional with the Grimme D2 empirical correction (PBE+D2)[63] with PAW pseudopotentials,[64,65] implemented in VASP.[66] Classical trajectories over the Born–Oppenheimer surface were solved numerically with a 0.5 fs time step. The unit cell for LLM-105 was replicated 2 × 1 × 1 times, resulting in a supercell with eight molecules (152 atoms). MD simulations were performed in the NVT ensemble. To balance computational cost and accuracy, the electronic structure was calculated with a 400 eV plane-wave energy cutoff without spin polarization, at the Γ-point only. The self-consistent field accuracy threshold was set to 1×10^{-4} eV. Partial occupancies above the fermi level were calculated with a Gaussian thermal smearing with a 0.05 eV width. A Nosé–Hoover thermostat was used with a relaxation time of 55 fs.[67]

DFTB-MD simulations were conducted using the DFTB+ code[68] at the self-consistent charge (DFTB-2) level with the integration of the equations of motion using LAMMPS.[69] We used a standard DFTB parameter set for organic molecules (mio-1-1, available at http://www.dftb.org)[70] that has previously been applied to other molecular HEs under shock conditions.[19,44] An empirical dispersion correction was applied using universal force-field terms.[71] Trajectories were integrated using extended Lagrangian Born–Oppenheimer equations of

motion with a 0.2 fs time step.[72−75] The electronic band structure was evaluated without spin polarization, at the Γ-point only, with four self-consistent field cycles per step, and with Fermi–Dirac thermal smearing in which the electron temperature set equal to the instantaneous ionic temperature.[76] DFTB simulations used the same initial cell as was used for the DFT-MD simulations. We note that the DFTB model used was not parameterized for work in HEs (especially under reactive conditions) and could potentially be improved via force matching for LLM-105.[77−79]

ReaxFF-MD simulations were conducted via LAMMPS, using two parameterizations of the ReaxFF reactive force field, which we will denote as ReaxFF-2018[80] and ReaxFF-LG.[81] Trajectories were integrated using a 0.1 fs time step. Partial atomic charges were calculated using the charge equilibration scheme[82] at each time step with an accuracy threshold set to 1×10^{-6}. Simulation cells contained 5700 atoms (5 × 5 × 3 unit cells). Both potentials have been shown to reliably predict the unreacted Hugoniot for the IHE TATB,[83] which has a relatively similar molecular and crystal structure.

2.2. Molecular Dynamics Simulation of Shock Loading. We simulate the response of LLM-105 to shock compression using the Hugoniostat method,[84,85] an equilibrium shock approximation technique. By applying a uniaxial barostat coupled with an energy bath designed to satisfy the Hugoniot jump conditions, a relatively small, periodic system can be driven to shock conditions without the need to simulate an impact. This allows for the efficient mapping of a material's Hugoniot at a modest computation cost. By sequentially applying a Hugoniostat first from the unshocked system to a state that initiates chemistry, followed by a second Hugoniostat on the fully reacted products, the reacted Hugoniot can be mapped. For the simplest model of a one-dimensional (1D) planar detonation, the leading detonation wave drives the unreacted material along a Rayleigh line to a high-pressure state on the unreacted Hugoniot. This state on the unreacted Hugoniot is known as the von Neumann spike. From the von Neuman spike, the material begins to react and release back down the Rayleigh line to a point on the product Hugoniot. For the steady-state solution to this model, the Rayleigh line is tangent to the product Hugoniot.[86] The detonation velocity is related to the slope of the line, and the Chapman–Jouguet (CJ) point (or sonic point) and its corresponding pressure obtained as the state indicated by the tangent point of the Rayleigh line and the product Hugoniot.[87]

2.3. Decomposition Kinetics and Detailed Chemical Analysis. Isothermal decomposition simulations were used to obtain reaction kinetics rates through multiple simulations performed at different temperatures. This approach has been widely used in prior studies[88−90] as constant temperature conditions enable straightforward extraction of kinetic rates through the analysis of Arrhenius plots. A Nosé–Hoover thermostat was used for the isothermal simulations with a relaxation time of 100 fs.[67] We assessed the chemical kinetics by defining the characteristic reaction lifetime as the time required for all initial LLM-105 molecules to undergo reaction. A single simulation was used to obtain the lifetime at a given temperature for ReaxFF- and DFT-based trajectories, whereas DFTB lifetimes were obtained as averages over 10 independent simulations. The large simulation cell used in the ReaxFF simulations reduces the statistical noise in extracted lifetimes, while ensemble sampling enables a more reliable determination of the lifetimes for the small cells used with DFTB. Ensemble
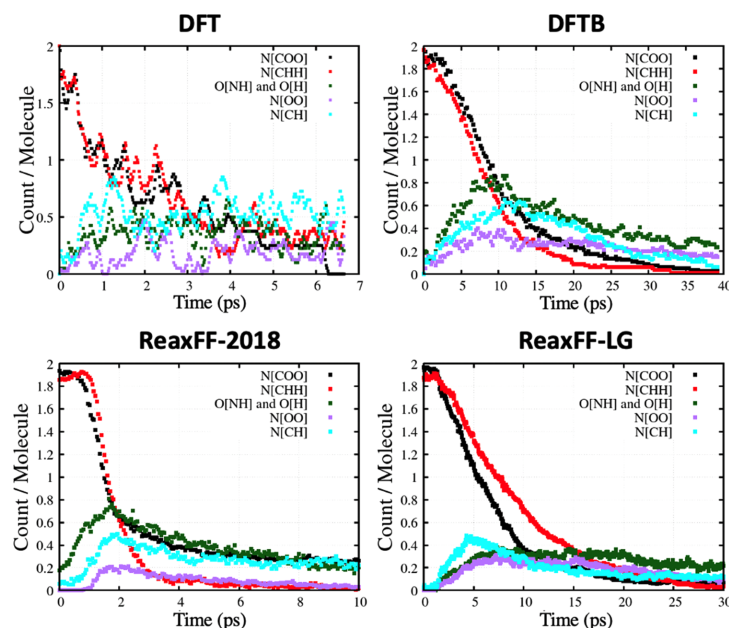
Figure 2. Bond environment histories related to NO_2 and NH_2 groups in LLM-105, as well as those associated with hydrogen transfer from NH_2 to NO_2 (inter- and intramolecular) and NO_2 scission. Time histories averaged over 10 isothermal decomposition reactions at 2250 K for DFTB and 1 simulation for DFT and ReaxFF. DFT data is smoothed with a running average scheme.

sampling was not performed for DFT-based simulations, owing to their significant computational cost. Initial starting configurations for the DFTB simulations were obtained by extracting configurations every 2 ps from an NVT simulation at 300 K. Reaction rate constants and activation energies were calculated from the temperature-dependent lifetimes $\tau = 1/k$ through a linear regression of the data plotted as $\ln(k)$ vs $1/T$.

Chemical reaction pathways were elucidated from time histories of molecular species and local bonding environment populations.[27] For detailed chemistry populations and bonding environments, a bond table was created for ReaxFF, with a bond-order cutoff of 0.5. A distance cutoff criterion was used for DFT and DFTB, with cutoffs established as the first local minimum in each per atom type radial distribution function. A bond table was reconstructed using these cutoffs and results in similar local bonding environments, as shown in the Supporting Information, SM-1. We denote these atomic bonding environment descriptors as $X[B_1B_2B_3B_4]$, where X is a central atom type and the B_i denote the atoms bonded to X, considering up to a maximum of four bonds per central atom. For example, the descriptor for O in H_2O is denoted $O[HH]$, whereas the H is denoted $H[O]$. An environment of $H[O]$ could denote the H in H_2O or the H in OH.

3. DECOMPOSITION AND REACTION MECHANISMS

3.1. Initial Reaction Pathways. We first focus on identifying the initial reaction steps of LLM-105, via thermal decomposition, by analyzing the time evolution of the individual bonding environments for each atom using all of the models applied to this study. Simulations were conducted

under isochoric−isothermal conditions. Figure 2 shows the time evolution of key selected atomic bonding environments for isothermal, isochoric, decomposition reactions at 2250 K, at a volume corresponding to the experimental lattice parameters at room temperature and pressure. The bonding environments $N[COO]$ and $N[CHH]$ (black and red in Figure 2) correspond to the NO_2 and NH_2 groups bonded to the inner ring of the LLM-105 molecule, with an initial population of two per molecule. The decomposition of these groups correlates with the rise of $O[NH]$ and $O[H]$ bonding. This is evidence of a hydrogen transfer reaction. Interestingly, such reactions are believed to be the first step in the decomposition of TATB, another insensitive HE[91] with a similar molecular and crystal structure. The increase in $O[NH]$ corresponds to a hydrogen transfer to a NO_2 group or the O bonded to the inner-ring N (either intra- or intermolecular), and the $O[H]$ environments are hydrogen transfers followed by the OH leaving the NO_2 group or inner-ring NO. Additionally, the small increase of $N[OO]$ implies NO_2 scission reactions without a hydrogen transfer. Plots for various temperatures and models are available in Supporting Information (SM-2 and SM-3). It should be noted for higher temperatures, significant amounts of bond breakage occur prior to full temperature equilibration (which can take on the order of ~1 ps). Time histories showing this initial temperature equilibration are available in the Supporting Information SM-5 for a variety of cases and models.

The lower computational cost of ReaxFF enabled similar calculations to be performed for TATB and HMX, see Figure 3a,c. The evolution of bond environments in TATB is similar

197
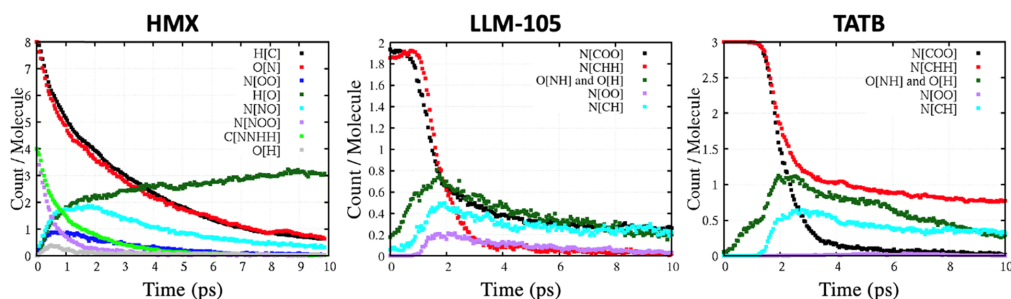
Figure 3. Bond environment time histories for the first 10 ps of decomposition for HMX, LLM-105, and TATB at 2500 K using ReaxFF-2018.
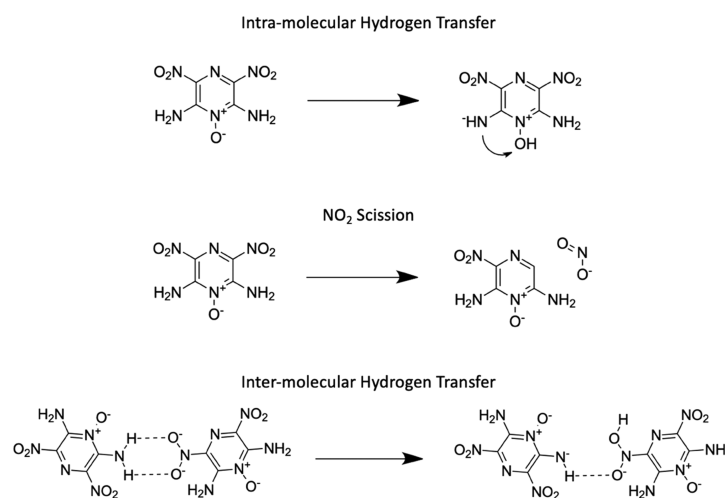
Figure 4. Potential first-step reaction pathways for LLM-105 thermal decomposition.

to those in LLM-105 and shows hydrogen transfer with almost no NO_2 formation. In contrast, the decomposition of HMX shows the significance of $N[OO]$ resulting from NO_2 scission, as well as $H[O]$, which signifies either HONO or OH formation. The low amount of $O[H]$ shows that this is mostly HONO formation; this was confirmed via molecular population analysis. These two reactions, as well as O migration to a nearby C (opening the ring), are all well-known first-step reactions for HMX decomposition.[12−14]

From direct observation of the atomic trajectories for all four models used (DFT, DFTB, and the two ReaxFF parameterizations), the three primary step reaction pathways discussed above were confirmed in all cases (intra- and intermolecular H transfer, and NO_2 scission). The only exception is that the DFT simulations did not display NO_2 scission, which was only seen in the DFTB and ReaxFF simulations. However, the timescales associated with NO_2 formation predicted by DFTB and ReaxFF are long compared to the total DFT run time. All three of the first-step reactions, shown in Figure 4, can independently lead to ring opening and the formation of various intermediates and partial ring species. These compare well to recent FT-IR results, which showed intramolecular H

transfer and NO_2 scission as first-step pathways.[57] This overall reaction pathway is similar to that of TATB,[91] which is to be expected, due to its similarity in molecular and crystal structure to LLM-105. The intermolecular hydrogen transfer reactions occur along with nearest neighbors, interacting via hydrogen bonds. Pure NO_2 scission, a common reaction in RDX and HMX,[11,12] is less common in both LLM-105 and TATB. The similarities of these initial reaction pathways for LLM-105 and TATB (e.g., a slow hydrogen transfer first step) that are dissimilar from conventional secondary explosives may have a direct correlation to insensitivity. Insensitivity has also been (speculatively) attributed to other phenomena such as the strong hydrogen bonding network of the crystal, the formation of large carbon-rich clusters, or microstructural phenomena like the collapse of porosity. Without numerous other IHEs available for comparison, all of these claims about properties governing insensitivity are conjectures but are nonetheless a place to begin the roadmap to designing new IHEs.

3.2. Intermediate and Final Reaction Products. While LLM-105 has similar initial decomposition steps to TATB, the lower relative amount of carbon and the higher relative amount of nitrogen in LLM-105 lead to moderately dissimilar
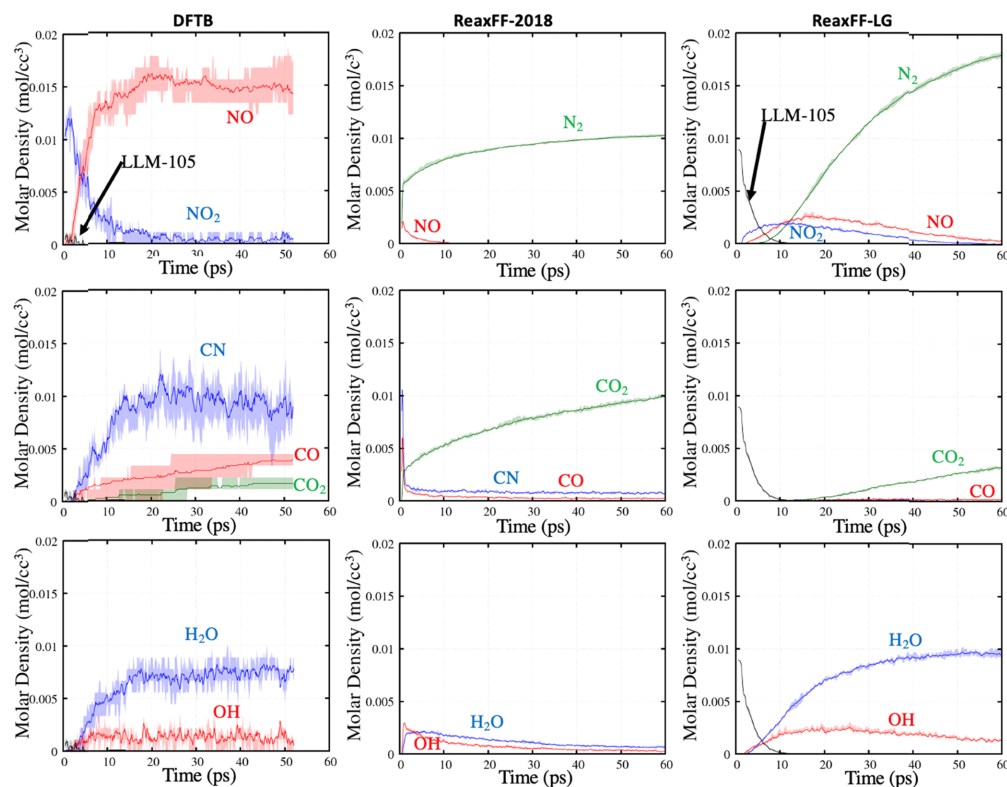
Figure 5. Time history of intermediates and products at 2500 K, averaged across 10 samples. Shaded regions represent a first and third quartile range for the sampled data. Plots are limited to the time frame of DFTB calculations.

intermediate and final products. Figure 5 shows key molecular species as predicted by DFTB, ReaxFF-2018, and ReaxFF-LG, divided into subgroups for easier comparison. Error bars on the DFTB curves correspond to the first and third quartiles over the 10 independent simulations. A few differences are immediately evident. DFTB differs from both ReaxFF models in that it does not exhibit any N_2 production, instead yielding NO as an apparent stable final product. Additionally, large amounts of CN form with DFTB in place of CO_2. Other, subtler, differences exist such as a lack of significant amounts of water in ReaxFF-2018 and slower (and overall less) CO_2 production in ReaxFF-LG. Given the discrepancies among the models, it is difficult to make definite claims about the expected final products for LLM-105. Therefore, we turn to study the formation energies of these key species in an attempt to understand the origins of these differences.

We computed formation energies for key molecular species in Figure 5 using all four models taking N_2, triplet O_2, H_2, and graphite as reference states. Potential radicals such as CN are presented here in their charge neutral state. Results are shown in Figure 6; tabulated results available in the Supporting Information SM-4. From these results, a few of the differences in product amounts can be understood; however, significant work is needed to fully understand the differences in detailed
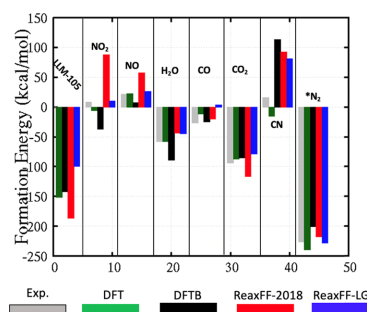
Figure 6. Formation energies of key species found in reactions. *N_2 energy is the molecular energy. Reference states used are N_2, O_2, H_2, and graphite. DFT values include zero-point-energy and using the ground-state spin and charge for each species. Values from Cheetah are not plotted due to their high similarity to experimental values.

chemistry and evolution of intermediate species from these methods. DFTB overstabilizes NO compared to the other methods and experimental values. This could partially explain the lack of N_2 formation on these early timescales, but this may

199

be a reaction timescale issue for the scope of these simulations. Additionally, DFTB stabilizes CO the most, which may explain its greater prevalence than CO_2, compared to the other models. However, the high DFTB formation energy for CN and the relative stability of H_2O in ReaxFF-2018 fail to explain their resulting trends. This indicates the importance of intermediates and reaction paths in the formation of products at the short timescales of interest in HE materials.

While the computational expense makes it difficult to study late timescale chemistry with DFT and DFTB, ReaxFF simulations can be extended to a nearly final set of products to better understand LLM-105 as compared to more well-studied HEs such as TATB and HMX. Figure 7 shows the time
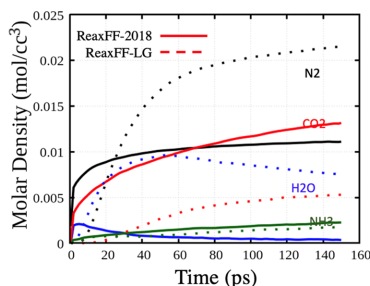
Figure 7. Time history of final products for both ReaxFF models used. ReaxFF-2018 is in solid lines and ReaxFF-LG is in dashed lines. Isothermal decomposition is at 2500 K.

history for a few final products after 150 ps for both ReaxFF potentials at 2500 K and experimental density at room temperature and pressure. ReaxFF-2018 has a rapid first step but quickly slows down. ReaxFF-LG takes longer to form products but stabilizes in concentrations on similar timescales. Table 1 compares these final product amounts to predicted and experimental values from bomb calorimeter experiments for TATB and HMX.[94] Results are also compared to the product concentrations for a constant volume explosion from the thermochemical code Cheetah.[28] Cheetah calculates chemical equilibrium states for reactants (e.g., explosives) at prescribed thermodynamic conditions, including the CJ point of steady plane detonation waves, by modeling the properties of stoichiometrically constrained product mixtures consisting of small molecules and condensed phases.[28] Due to the small time and length scales typically explored by MD simulations, they usually do not reach full chemical equilibrium, although they can provide information on kinetics, especially at early times. Comparisons between the product concentrations from Cheetah and those from MD can provide information on the likely kinetic barriers that the system needs to overcome to reach chemical equilibrium. One such barrier is the formation of condensed carbon phases,[92] which is difficult to capture at the MD scale but is well modeled by thermochemical calculations. This, along with the accuracy of the MD potentials, may explain some of the differences noted below. Cheetah calculated concentrations for HMX and TATB generally reproduce well those measured in detonation calorimeter experiments; no experimental results are available for LLM-105. Comparing the predictions from MD to Cheetah for LLM-105, ReaxFF-2018 underpredicts the amount of H_2O by a little more than an order of magnitude but predicts an approximately similar amount of N_2, CO_2, and NH_3. ReaxFF-LG has more H_2O but underpredicts the amount of CO_2. For direct comparisons with ReaxFF-LG for TATB, LLM-105, and HMX, we see that LLM-105 creates more N_2 and CO_2, but less H_2O and NH_3. For all species, ReaxFF-LG underpredicts the amount of gas production in TATB but gets the relative order correct compared to the experiment. For the order of species formation, ReaxFF-LG (early water, followed by nitrogen species, and later CO_2 production) compares well with recent spectroscopic experiments.[58] ReaxFF-2018 appears to produce all species early, with water being slightly later than nitrogen species and CO_2. LLM-105 produces overall more gaseous products than TATB, but not as much as HMX. According to the Kamlet–Jacobs (K–J) equation, the increase of gaseous product production per gram of HE leads to increased performance.[99] Additionally, if more of the original HE is forming gaseous molecules, there will be less clustering and condensates, potentially increasing the sensitivity of the HE.[44] Fewer clusters and condensates would be expected in LLM-105 relative to TATB due to the lower relative amount of carbon.

4. REACTION KINETICS

Predicting explosive sensitivity is challenging due to the multiscale nature of initiation mechanisms. Activation energies for initial decomposition reactions offer a potentially useful measure for empirical relationships between sensitivity and underlying chemical kinetics. We extracted a simple, one-step reaction kinetics model for LLM-105 from the isothermal–isochoric reactive MD simulations. Figure 8 shows the characteristic reaction rates as a function of inverse temperature for the four different models studied (DFT, DFTB, ReaxFF-2018, and ReaxFF-LG) obtained following the methods outlined in Section 2.3. This assumes that, within this temperature range, LLM-105 kinetics can be approximated with the simplest possible model, a single step governed by Arrhenius kinetics. The corresponding activation energies and kinetic prefactors are listed in Table 2. Despite dissimilar activation energies between ReaxFF-2018, DFT, and DFTB, the three show overall similar rates, especially at higher temperatures near detonation conditions. While the ReaxFF-LG has a closer activation barrier to DFTB and DFT, it

Table 1. Final Product Amounts for LLM-105 Using ReaxFF, Compared to Values for TATB and HMX[93,94]

molecule	ReaxFF-2018 (mol/cm^3)	ReaxFF-LG (mol/cm^3)	LLM-105 Cheetah (mol/cm^3)	ReaxFF-LG TATB (mol/cm^3)	TATB Cheetah (mol/cm^3)	TATB exp. (mol/cm^3)	HMX Cheetah (mol/cm^3)	HMX exp. (mol/cm^3)
N_2	1.109×10^{-2}	2.145×10^{-2}	2.604×10^{-2}	1.66×10^{-2}	2.17×10^{-2}	1.75×10^{-2}	2.47×10^{-2}	2.37×10^{-2}
CO_2	1.313×10^{-2}	5.280×10^{-3}	1.297×10^{-2}	2.80×10^{-3}	1.20×10^{-2}	1.46×10^{-2}	1.24×10^{-2}	1.24×10^{-2}
H_2O	3.335×10^{-4}	7.442×10^{-3}	1.440×10^{-2}	1.05×10^{-2}	1.89×10^{-2}	1.56×10^{-2}	1.88×10^{-2}	2.05×10^{-2}
NH_3	2.264×10^{-3}	1.783×10^{-3}	1.194×10^{-3}	3.07×10^{-3}	1.64×10^{-3}	8.23×10^{-4}	1.97×10^{-3}	2.55×10^{-3}

200
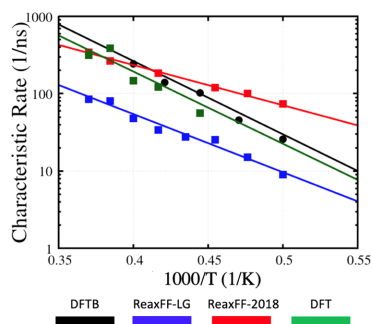
Figure 8. Arrhenius fit to time data for initial LLM-105 molecule decay (0% LLM-105 molecules remaining) as the characteristic time.

Table 2. Activation Energy and Prefactor Values Derived from Arrhenius Fits in Figure 8

model	$E_a \left(\frac{\text{kcal}}{\text{mol}} \right)$	$A \left(\frac{1}{\text{ps}} \right)$
DFT	42.8	1051.2
DFTB	43.3	1613.0
ReaxFF-LG	34.4	55.5
ReaxFF-2018	23.8	28.3

predicts slower kinetics owing to a significantly smaller prefactor. DFT compares best to recent DSC experiments in which two-step activation energies were shown to be 53.1 and 58.4 kcal/mol.[59] Comparisons to previous works on TATB and HMX kinetics[95] are shown in the Supporting Information SM-6. It should be noted that, especially at high temperatures with short reaction timescales, the anisotropy of the LLM-105 crystal structure can lead to nonhydrostatic stress states prior to gas production, melting, or amorphization through shear failure. A time history of stress components for a ReaxFF-2018 calculation at 2500 K is shown in the Supporting Information SM-7, which shows that the system is consistently at a nominally hydrostatic state.

5. DETONATION PROPERTIES

With the development of potential new IHE materials such as LLM-105, having near-TATB insensitivity is key but so is having HMX-level performance, if possible. The accuracy of detonation performance predictions is directly tied to the thermodynamic accuracy of model predictions for the product equation of state. Detonation velocity and CJ pressure are directly related to the product Hugoniot, the set of thermodynamic states available to the shock-induced reaction products.

Using the Hugoniostat shock simulation method,[84,85] we mapped the reacted and unreacted Hugoniots for LLM-105 following refs 30, 31. All shocks were conducted along the herringbones, normal to the (010) plane. The effect of shock direction on sensitivity and performance was not explored. Figure 9 shows these Hugoniot curves in P−V space obtained using DFTB and ReaxFF-2018. JWL equations of state,[96] eq 1 below, were fitted to the product Hugoniot and are listed in Table 3. A comparison figure of all JWL fits for LLM-105, as

Table 3. JWL[96] Fits for the Reacted Hugoniot Curves for MD/DFTB Methods[a]

var	DFTB	ReaxFF-2018	ReaxFF-LG	HMX[97]	TATB[98]
A (GPa)	2991.7	425666	2946.0	852.4	1361.8
B (GPa)	16927.2	147.05	2968.3	18.02	72.0
R_1	6.3	14.1	7.6	4.55	6.2
R_2	11.6	2.66	7.4	1.3	2.2
w	0.35	0.35	0.35	0.38	0.5
e_o	2.1	2.0	8.1	10.2	6.9

[a] e_o is the only nonfree variable in fitting conditions and is the heat of detonation for a product equation of state.

well as reference curves for TATB and HMX, is available in the Supporting Information SM-8.

$$P = A \left(1 - \frac{\omega}{R_1 V} \right) e^{-R_1 V} + B \left(1 - \frac{\omega}{R_2 V} \right) e^{-R_2 V} + \frac{\omega e_0}{V} \quad (1)$$

Detonation velocity and the CJ state can be determined from the Rayleigh line that passes through the initial state and is tangent to the product Hugoniot in P−V space, see Figure 9. This Rayleigh line was obtained from JWL fits to the MD data. Its slope is the detonation velocity squared and its tangent point with the product Hugoniot marks the CJ point. Table 4 presents these values, with n_{CJ} representing the volume ratio at CJ. Note that while both DFTB and LG give similar results, ReaxFF-2018 is considerably closer to K−J thermodynamic estimations and results from Cheetah (Table 4). Kamlet−
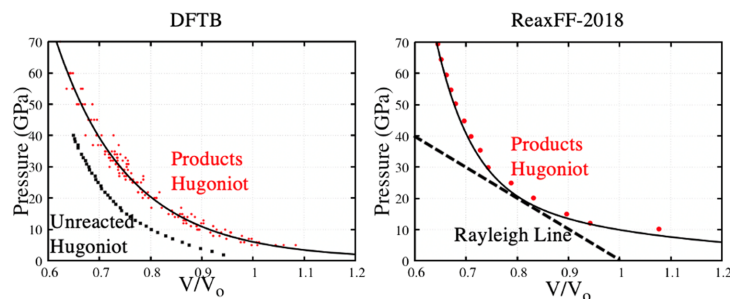
Figure 9. Predicted Hugoniot curves for DFTB and ReaxFF-2018 used to determine the performance of the system for shock along the [010]. The Rayleigh Line in the ReaxFF-2018 shows the intersection at the CJ point and has a slope related to the predicted detonation velocity.

201

Table 4. Performance Metrics for LLM-105 from Thermodynamic Calculations and MD/DFTB Simulations

	P_{CJ} (GPa)	D_v (km/s)	n_{CJ}
K−J equation	27.0	7.52	N/A
DFTB	11.7 ± 0.2	6.96 ± 0.1	0.874 ± 0.002
ReaxFF-2018	27.8 ± 0.5	8.4 ± 0.2	0.79 ± 0.05
ReaxFF-LG	10.9 ± 0.6	6.4 ± 0.2	0.863 ± 0.003
Cheetah LLM-105	33.6	8.66	N/A
K−J TATB[99]	32.6	7.93	N/A
K−J HMX[99]	38.6	9.16	N/A
TATB ReaxFF-2018[83]	32.1 ± 0.1	8.1 ± 0.1	N/A
TATB ReaxFF-LG[83]	20.0 ± 0.1	6.9 ± 0.1	N/A

Jacobs equations[99] provide a simple way to estimate detonation properties from product gas amounts (simplified product hierarchy), heat of detonation, and initial density. We use an approximate heat of detonation from DFT: 186.5 kcal/mol. However, Cheetah predicts a slightly larger CJ pressure of 33.6 GPa and detonation velocity of 8.66 km/s. This may partially be because the heat of formation in Cheetah for LLM-105 (S4) is higher than the DFT value. The error metric for the calculations (shown in Table 4) represents the numerical uncertainty in the JWL equation of state (EoS) fit and does not capture stochastic uncertainties associated with multiple runs nor model-form errors.

For ReaxFF-2018, the predicted detonation velocity of LLM-105 outperforms the prediction for TATB using the same force field (8.4−8.1 km/s, respectively).[83] The experimental value for HMX is 9.1 km/s.[41] While, based on our predictions, LLM-105 does not have HMX-level performance, it is expected to outperform TATB.

There are substantial differences in the unreacted Hugoniot curves predicted by the three models. ReaxFF-2018 shock simulations of perfect LLM-105 crystals exhibit a low threshold for the reaction. Shock pressures of only a few GPa resulted in rapid exothermic reactions, preventing us from determining the unreacted Hugoniot. In comparison, both DFTB and ReaxFF-LG must undergo shock compression of over 40 GPa before any reaction products can be observed on MD timescales, and ReaxFF-2018 predicts the shock initiation threshold of TATB to be 34 GPa. These differences in timescales and required shock pressures may be related to the differences in initial isothermal decomposition rates at low temperatures (large 1/T) captured in Figure 8. It is interesting to note that, while ReaxFF-LG consistently underpredicts performance compared to K−J Theory, ReaxFF-2018, which is nearly spot on to K−J for TATB, predicts very high performance for LLM-105 compared to all other predictions, and predicts similar detonation velocity to Cheetah. Estimating the sensitivity of an HE to compare to experimental techniques is still a grand scientific challenge.[2]

6. CONCLUSIONS

In summary, we utilized series of reactive MD simulations performed with DFT, DFTB, and two ReaxFF potentials to characterize the insensitive high-explosive LLM-105. Early chemical decomposition reaction pathways were determined to be similar to TATB, involving significant intra- and intermolecular hydrogen transfer. Notably, LLM-105 exhibits more NO_2 scission and HONO formation than TATB, which are the reactions characteristic of HMX decomposition. While the various models exhibit spread in predicted final products

and their amounts, most of these differences can be explained by the differences in formation energies of the species involved. We extracted simple one-step reaction kinetics for all four models. DFT, DFTB, and one of the ReaxFF potentials predict reaction rates on the same order of magnitude at detonation-like temperatures. Equilibrium-based shock simulations were used to characterize the detonation performance of LLM-105. We mapped the Hugoniot of the reaction products and fit it to a JWL equation of state. By solving for the Rayleigh line tangent to the product Hugoniot, detonation velocities and CJ pressures were extracted. We find that LLM-05 most likely has similar or better detonation performance to TATB, but not on the level of HMX, with Cheetah and ReaxFF-2018 predicting better performance than TATB.

Our study shows that state-of-the-art atomistic simulations can be used to gain insight into the decomposition mechanisms and detonation properties of new high-explosive materials. While high-level electronic structure calculations are expected to provide an accurate description of the processes involved, their computational cost hinders the calculation of many relevant properties of explosives. In addition, the lack of experimental results at commensurate scales precludes a rigorous assessment of how the approximations in the description of atomic interactions affect the properties of interest. Reactive force fields play a key role in reaching scales required for a direct comparison with experiments, but the associated uncertainties remain significant. Despite these limitations, we find that a combination of methods can provide bounds and semiquantitative predictions for many properties determined by the chemical reactivity of high explosives.

■ ASSOCIATED CONTENT

ⓢ Supporting Information

The Supporting Information is available free of charge at https://pubs.acs.org/doi/10.1021/acs.jpca.0c10946.

> Time history of reduced chemistry from bond environments using bond-order methods from ReaxFF and distance criteria methods for DFT and DFTB showing similar results (SM-1); variety of other temperatures and local bond environment types relevant to Figures 2 and 3 (SM-2 & SM-3); table of data corresponding to Figure 6 (SM-4); early time history of temperatures for NVT runs showing timescales of equilibration to set temperature (SM-5); kinetics plot from Figure 8 with kinetics from models for TATB and HMX overlayed (SM-6); stress tensor component time histories for an NVT run to show hydrodynamic nature despite anisotropic thermal expansions (SM-7); plot of JWL reacted EoS for LLM-105 and previous results for TATB and HMX (SM-8) (PDF)

■ AUTHOR INFORMATION

Corresponding Author

Alejandro Strachan − *School of Materials Engineering and Birck Nanotechnology Center, Purdue University, West Lafayette, Indiana 47907, United States*; Email: strachan@purdue.edu

Authors

Brenden W. Hamilton − *School of Materials Engineering and Birck Nanotechnology Center, Purdue University, West*

Lafayette, Indiana 47907, United States; ⊙ orcid.org/0000-0002-4524-2201

Brad A. Steele − *Physical and Life Sciences Directorate, Lawrence Livermore National Laboratory, Livermore, California 94550, United States;* ⊙ orcid.org/0000-0002-8703-024X

Michael N. Sakano − *School of Materials Engineering and Birck Nanotechnology Center, Purdue University, West Lafayette, Indiana 47907, United States;* ⊙ orcid.org/0000-0003-3337-4810

Matthew P. Kroonblawd − *Physical and Life Sciences Directorate, Lawrence Livermore National Laboratory, Livermore, California 94550, United States;* ⊙ orcid.org/0000-0002-5009-5998

I-Feng W. Kuo − *Physical and Life Sciences Directorate, Lawrence Livermore National Laboratory, Livermore, California 94550, United States*

Complete contact information is available at:
https://pubs.acs.org/10.1021/acs.jpca.0c10946

Notes
The authors declare no competing financial interest.

■ REFERENCES

(1) Tran, T. D.; Pagoria, P. F.; Hoffman, D. M.; Cunningham, B.; Simpson, R. L.; Lee, R. S.; Cutting, J. L. In *Small-Scale Safety and Performance Characterization of New Plastic Bonded Explosives Containing LLM-105*, Proceedings of the 12th International Detonation Symposium, 2002; pp 440−447.

(2) Bernstein, J. Ab initio study of energy transfer rates and impact sensitivities of crystalline explosives. *J. Chem. Phys.* **2018**, *148*, No. 084502.

(3) Jain, A.; Ong, S. P.; Hautier, G.; Chen, W.; Richards, W. D.; Dacek, S.; Cholia, S.; Gunter, D.; Skinner, D.; Ceder, G.; et al. Commentary: The Materials Project: A materials genome approach to accelerating materials innovation. *APL Mater.* **2013**, *1*, No. 011002.

(4) Xue, D.; Balachandran, P. V.; Hogden, J.; Theiler, J.; Xue, D.; Lookman, T. Accelerated search for materials with targeted properties by adaptive design. *Nat. Commun.* **2016**, *7*, No. 11241.

(5) Natarajan, A. R.; Van der Ven, A. First-principles investigation of phase stability in the Mg-Sc binary alloy. *Phys. Rev. B* **2017**, *95*, No. 214107.

(6) Tripathi, S.; Vishnu, K. G.; Titus, M. S.; Strachan, A. Tunability of martensitic transformation in Mg-Sc shape memory alloys: A DFT study. *Acta Mater.* **2020**, *189*, 1−9.

(7) Hao, S.; Liu, W. K.; Moran, B.; Vernerey, F.; Olson, G. B. Multi-scale constitutive model and computational framework for the design of ultra-high strength, high toughness steels. *Comput. Methods Appl. Mech. Eng.* **2004**, *193*, 1865−1908.

(8) Olson, G. B. Computational design of hierarchically structured materials. *Science* **1997**, *277*, 1237−1242.

(9) Strachan, A.; van Duin, A. C.; Chakraborty, D.; Dasgupta, S.; Goddard, W. A., III Shock waves in high-energy materials: the initial chemical events in nitramine RDX. *Phys. Rev. Lett.* **2003**, *91*, No. 098301.

(10) Armstrong, M. R.; Lindsey, R. K.; Goldman, N.; Nielsen, M. H.; Stavrou, E.; Fried, L. E.; Zaug, J. M.; Bastea, S. Ultrafast shock synthesis of nanocarbon from a liquid precursor. *Nat. Commun.* **2020**, *11*, No. 353.

(11) Strachan, A.; Kober, E. M.; van Duin, A. C.; Oxgaard, J.; Goddard, W. A., III Thermal decomposition of RDX from reactive molecular dynamics. *J. Chem. Phys.* **2005**, *122*, No. 054502.

(12) Chakraborty, D.; Muller, R. P.; Dasgupta, S.; Goddard, W. A. The mechanism for unimolecular decomposition of RDX (1, 3, 5-trinitro-1, 3, 5-triazine), an ab initio study. *J. Phys. Chem. A* **2000**, *104*, 2261−2272.

(13) Chakraborty, D.; Muller, R. P.; Dasgupta, S.; Goddard, W. A. Mechanism for unimolecular decomposition of HMX (1, 3, 5, 7-tetranitro-1, 3, 5, 7-tetrazocine), an ab initio study. *J. Phys. Chem. A* **2001**, *105*, 1302−1314.

(14) Chakraborty, D.; Muller, R. P.; Dasgupta, S.; Goddard, W. A. A Detailed Model for the Decomposition of Nitramines: RDX and HMX. *J. Comput.-Aided Mater. Des.* **2001**, *8*, 203−212.

(15) Manaa, M. R.; Fried, L. E.; Melius, C. F.; Elstner, M.; Frauenheim, T. Decomposition of HMX at extreme conditions: A molecular dynamics simulation. *J. Phys. Chem. A* **2002**, *106*, 9024−9029.

(16) Wood, M. A.; Cherukara, M. J.; Kober, E. M.; Strachan, A. Ultrafast chemistry under nonequilibrium conditions and the shock to deflagration transition at the nanoscale. *J. Phys. Chem. C* **2015**, *119*, 22008−22015.

(17) Shan, T. R.; Wixom, R. R.; Thompson, A. P. Extended asymmetric hot region formation due to shockwave interactions following void collapse in shocked high explosive. *Phys. Rev. B* **2016**, *94*, No. 054308.

(18) Joshi, K. L.; Chaudhuri, S. Reactive simulation of the chemistry behind the condensed-phase ignition of RDX from hot spots. *Phys. Chem. Chem. Phys.* **2015**, *17*, 18790−18801.

(19) Kroonblawd, M. P.; Fried, L. E. High Explosive Ignition through Chemically Activated Nanoscale Shear Bands. *Phys. Rev. Lett* **2020**, *124*, No. 206002.

(20) Fried, L. E.; Howard, W. M.; Souers, P. C. In *16th International Detonation Symposium*, Office of Naval Research, 2018.

(21) Wood, M. A.; Kittell, D. E.; Yarrington, C. D.; Thompson, A. P. Multiscale modeling of shock wave localization in porous energetic material. *Phys. Rev. B* **2018**, *97*, No. 014109.

(22) Nelms, M. D.; Kroonblawd, M. P.; Austin, R. A. *Pore Collapse in Single-Crystal TATB under Shock Compression*, No. LLNL-CONF-784800; Lawrence Livermore National Laboratory (LLNL): Livermore, CA, USA, 2019.

(23) Zhao, P.; Lee, S.; Sewell, T.; Udaykumar, H. S. Tandem Molecular Dynamics and Continuum Studies of Shock-Induced Pore Collapse in TATB. *Propellants, Explos., Pyrotech.* **2020**, *45*, 196−222.

(24) Maillet, J. B.; Soulard, L.; Stoltz, G. A reduced model for shock and detonation waves. II. The reactive case. *Europhys. Lett.* **2007**, *78*, 68001.

(25) Stewart, D. S. In *A Gibbs Formulation for Reactive Materials with Phase Change*, AIP Conference Proceedings, AIP Publishing, 2017; p 040021.

(26) Lee, K.; Joshi, K.; Chaudhuri, S.; Stewart, D. S. Mirrored continuum and molecular scale simulations of the ignition of high-pressure phases of RDX. *J. Chem. Phys.* **2016**, *144*, No. 184111.

(27) Sakano, M.; Hamed, A.; Kober, E.; Grilli, N.; Hamilton, B.; Islam, M. M.; Koslowski, M.; Strachan, A. Unsupervised learning-based multiscale model of thermochemistry in 1, 3, 5-Trinitro-1, 3, 5-triazinane (RDX). *J. Phys. Chem. A* **2020**, *124*, No. 9141.

(28) Bastea, S.; Fried, L. E. Chemical Equilibrium Detonation. In *Shock Wave Science and Technology Reference Library*; Springer, 2012; Vol. 6, pp 1−31.

(29) Elton, D. C.; Boukouvalas, Z.; Butrico, M. S.; Fuge, M. D.; Chung, P. W. Applying machine learning techniques to predict the properties of energetic materials. *Sci. Rep.* **2018**, *8*, No. 9059.

(30) Islam, M. M.; Strachan, A. Decomposition and reaction of polyvinyl nitrate under shock and thermal loading: a ReaxFF reactive molecular dynamics study. *J. Phys. Chem. C* **2017**, *121*, 22452−22464.

(31) Islam, M. M.; Strachan, A. Reactive Molecular Dynamics Simulations to Investigate the Shock Response of Liquid Nitromethane. *J. Phys. Chem. C* **2019**, *123*, 2613−2626.

(32) McGrane, S. D.; Moore, D. S.; Funk, D. J. Shock induced reaction observed via ultrafast infrared absorption in poly (vinyl nitrate) films. *J. Phys. Chem. A* **2004**, *108*, 9342−9347.

(33) Brown, K. E.; McGrane, S. D.; Bolme, C. A.; Moore, D. S. Ultrafast chemical reactions in shocked nitromethane probed with dynamic ellipsometry and transient absorption spectroscopy. *J. Phys. Chem. A* **2014**, *118*, 2559−2567.

(34) Powell, M. S.; Sakano, M. N.; Cawkwell, M. J.; Bowlan, P. R.; Brown, K. E.; Bolme, C. A.; Moore, D. S.; Son, S. F.; Strachan, A.; McGrane, S. D. Insight into the Chemistry of PETN Under Shock Compression Through Ultrafast Broadband Mid-Infrared Absorption Spectroscopy. *J. Phys. Chem. A* **2020**, *124*, 7031−7046.

(35) Bassett, W. P.; Dlott, D. D. Multichannel emission spectrometer for high dynamic range optical pyrometry of shock-driven materials. *Rev. Sci. Instrum.* **2016**, *87*, No. 103107.

(36) Bassett, W. P.; Johnson, B. P.; Salvati, L., III; Dlott, D. D. Hot-spot generation and growth in shocked plastic-bonded explosives studied by optical pyrometry. *J. Appl. Phys.* **2019**, *125*, No. 215904.

(37) Bassett, W. P.; Johnson, B. P.; Dlott, D. D. Dynamic absorption in optical pyrometry of hot spots in plastic-bonded triaminotrinitrobenzene. *Appl. Phys. Lett.* **2019**, *114*, No. 194101.

(38) Lee, E. L.; Tarver, C. M. Phenomenological model of shock initiation in heterogeneous explosives. *Phys. Fluids* **1980**, *23*, 2362−2372.

(39) Holian, B. L.; Germann, T. C.; Maillet, J. B.; White, C. T. Atomistic mechanism for hot spot initiation. *Phys. Rev. Lett.* **2002**, *89*, No. 285501.

(40) Li, C.; Hamilton, B. W.; Strachan, A. Hotspot formation due to shock-induced pore collapse in 1, 3, 5, 7-tetranitro-1, 3, 5, 7-tetrazoctane (HMX): Role of pore shape and shock strength in collapse mechanism and temperature. *J. Appl. Phys.* **2020**, *127*, No. 175902.

(41) Data, LASL Explosive Property *TR Gibbs and A. Popolato*; University of California Press: Berkeley, CA, USA, 1980.

(42) Dobratz, B. M. *The Insensitive High Explosive Triaminotrinitrobenzene (TATB): Development and Characterization—1888 to 1994*, Report LA-13014-H; Los Alamos National Laboratory: Los Alamos, NM, USA, 1995.

(43) Rice, S. F.; Simpson, R. L. *The Unusual Stability of TATB: A Review of the Scientific Literature*, Report UCRL-LR-103683; Lawrence Livermore National Laboratory: Livermore, CA, USA, 1990.

(44) Manaa, M. R.; Reed, E. J.; Fried, L. E.; Goldman, N. Nitrogenrich heterocycles as reactivity retardants in shocked insensitive explosives. *J. Am. Chem. Soc.* **2009**, *131*, 5483−5487.

(45) Tiwari, S. C.; Nomura, K. I.; Kalia, R. K.; Nakano, A.; Vashishta, P. Multiple reaction pathways in shocked 2, 4, 6-Triamino1, 3, 5-trinitrobenzene crystal. *J. Phys. Chem. C* **2017**, *121*, 16029−16034.

(46) Manaa, M. R.; Gee, R. H.; Fried, L. E. Internal rotation of amino and nitro groups in TATB: MP2 versus DFT (B3LYP). *J. Phys. Chem. A* **2002**, *106*, 8806−8810.

(47) Li, H. B.; Cheng, B. B.; Liu, S. J.; Nie, F. D.; Li, J. S. Recrystallization and Properties of LLM-105. *Chin. J. Energ. Mater.* **2008**, *6*, 294−296.

(48) Zhang, J.; Wu, P.; Yang, Z.; Gao, B.; Zhang, J.; Wang, P.; Nie, F.; Liao, L. Preparation and Properties of Submicrometer-Sized LLM-105 via Spray-Crystallization Method. *Propellants, Explos., Pyrotech.* **2014**, *39*, 653−657.

(49) Pagoria, P. F. *Synthesis, Scale-up, and Characterization of 2,6-Diamino-3,5-dinitropyrazine-1-oxide (LLM-105)*, No. UCRL-JC-130518, CONF-9806105; Lawrence Livermore National Lab: CA, USA, 1998.

(50) Tran, T. D.; Pagoria, P. F.; Hoffman, D. M.; Cunningham, B.; Simpson, R. L.; Lee, R. S.; Cutting, J. L. In *Small-Scale Safety and Performance Characterization of New Plastic Bonded Explosives Containing LLM-105*, Proceedings of the 12th International Detonation Symposium, 2002; pp 440−447.

(51) Xu, W.; An, C.; Wang, J.; Dong, J.; Geng, X. Preparation and properties of an insensitive booster explosive based on LLM-105. *Propellants, Explos., Pyrotech.* **2013**, *38*, 136−141.

(52) Li, Y. B.; Huang, H.; Li, J. S.; Li, H. B. A new HMX-based low-sensitive high energy PBX explosive containing LLM-105. *Chin. J. Explos. Propellants* **2008**, *5*, 720−726.

(53) Hoffman, D. M.; Lorenz, K. T.; Cunningham, B.; Gagliardi, F. *Formulation and Mechanical Properties of LLM-105 PBXs*, No. LLNL-CONF-402822; Lawrence Livermore National Laboratory (LLNL): Livermore, CA, USA, 2008.

(54) Manaa, M. R.; Kuo, I. F. W.; Fried, L. E. First-principles high-pressure unreacted equation of state and heat of formation of crystal 2, 6-diamino-3, 5-dinitropyrazine-1-oxide (LLM-105). *J. Chem. Phys.* **2014**, *141*, No. 064702.

(55) Stavrou, E.; Riad Manaa, M.; Zaug, J. M.; Kuo, I. F. W.; Pagoria, P. F.; Kalkan, B.; Crowhurst, J. C.; Armstrong, M. R. The high pressure structure and equation of state of 2, 6-diamino-3, 5-dinitropyrazine-1-oxide (LLM-105) up to 20 GPa: X-ray diffraction measurements and first principles molecular dynamics simulations. *J. Chem. Phys.* **2015**, *143*, No. 144506.

(56) Ma, H. X.; Song, J. R.; Zhao, F. Q.; Gao, H. X.; Hu, R. Z. Crystal Structure, Safety Performance and Density-Functional Theoretical Investigation of 2, 6-Diamino-3, 5-dinitropyrazine-1-oxide (LLM-105). *Chin. J. Chem.* **2008**, *26*, 1997−2002.

(57) Xiao, Q.; Sui, H.; Hao, X.; Chen, J.; Yin, Y.; Yu, Q.; Yang, X.; Ju, X. Application of a multi-channel in-situ infrared spectroscopy: The case of LLM-105. *Spectrochim. Acta, Part A* **2020**, No. 118577.

(58) Xiao, Q.; Sui, H.; Yu, Q.; Chen, J.; Yin, Y.; Ju, X. Gas Releasing Mechanism of LLM-105 Using Two-Dimensional Correlation Infrared Spectroscopy. *Propellants, Explos., Pyrotech.* **2019**, *44*, 1375−1383.

(59) Yu, Q.; Liu, Y.; Sui, H.; Sun, J.; Li, J. Kinetic analysis of overlapping multistep thermal decomposition of 2, 6-diamino-3, 5-dinitropyrazine-1-oxide (LLM-105). *J. Phys. Chem. C* **2018**, *122*, 25999−26006.

(60) Cheng, N.; Gan, Q.; Yu, Q.; Zhang, X.; Li, R.; Qian, S.; Feng, C. Initial mechanisms for the unimolecular thermal decomposition of 2, 6-diamino-3, 5-dinitropyrazine-1-oxide. *Molecules* **2019**, *24*, 125.

(61) Wang, J.; Xiong, Y.; Li, H.; Zhang, C. Reversible hydrogen transfer as new sensitivity mechanism for energetic materials against external stimuli: a case of the insensitive 2, 6-diamino-3, 5-dinitropyrazine-1-oxide. *J. Phys. Chem. C* **2018**, *122*, 1109−1118.

(62) Perdew, J. P.; Burke, K.; Ernzerhof, M. Generalized gradient approximation made simple. *Phys. Rev. Lett.* **1996**, *77*, 3865.

(63) Grimme, S. Semiempirical GGA-type density functional constructed with a long-range dispersion correction. *J. Comput. Chem.* **2006**, *27*, 1787−1799.

(64) Blöchl, P. E. Projector augmented-wave method. *Phys. Rev. B* **1994**, *50*, 17953.

(65) Kresse, G.; Joubert, D. From ultrasoft pseudopotentials to the projector augmented-wave method. *Phys. Rev. B* **1999**, *59*, 1758.

(66) Kresse, G.; Furthmüller, J. Efficiency of ab-initio total energy calculations for metals and semiconductors using a plane-wave basis set. *Comput. Mater. Sci.* **1996**, *6*, 15−50.

(67) Nosé, S. A unified formulation of the constant temperature molecular dynamics methods. *J. Chem. Phys.* **1984**, *81*, 511−519.

204

(68) Aradi, B.; Hourahine, B.; Frauenheim, T. DFTB+, a sparse matrix-based implementation of the DFTB method. *J. Phys. Chem. A* **2007**, *111*, 5678−5684.

(69) Plimpton, S. *Fast Parallel Algorithms for Short-Range Molecular Dynamics*, No. SAND-91-1144; Sandia National Labs: Albuquerque, NM, USA, 1993.

(70) Elstner, M.; Porezag, D.; Jungnickel, G.; Elsner, J.; Haugk, M.; Frauenheim, T.; Suhai, S.; Seifert, G. Self-consistent-charge density-functional tight-binding method for simulations of complex materials properties. *Phys. Rev. B* **1998**, *58*, 7260.

(71) Rappé, A. K.; Casewit, C. J.; Colwell, K. S.; Goddard, W. A., III; Skiff, W. M. UFF, a full periodic table force field for molecular mechanics and molecular dynamics simulations. *J. Am. Chem. Soc.* **1992**, *114*, 10024−10035.

(72) Niklasson, A. M.; Tymczak, C. J.; Challacombe, M. Time-reversible Born-Oppenheimer molecular dynamics. *Phys. Rev. Lett.* **2006**, *97*, No. 123001.

(73) Niklasson, A. M. Extended born-oppenheimer molecular dynamics. *Phys. Rev. Lett.* **2008**, *100*, No. 123004.

(74) Niklasson, A. M.; Steneteg, P.; Odell, A.; Bock, N.; Challacombe, M.; Tymczak, C. J.; Holmström, E.; Zheng, G.; Weber, V. Extended Lagrangian Born−Oppenheimer molecular dynamics with dissipation. *J. Chem. Phys.* **2009**, *130*, No. 214109.

(75) Zheng, G.; Niklasson, A. M.; Karplus, M. Lagrangian formulation with dissipation of Born-Oppenheimer molecular dynamics using the density-functional tight-binding method. *J. Chem. Phys.* **2011**, *135*, No. 044122.

(76) Mermin, N. D. Thermal properties of the inhomogeneous electron gas. *Phys. Rev.* **1965**, *137*, A1441.

(77) Goldman, N.; Fried, L. E.; Koziol, L. Using force-matched potentials to improve the accuracy of density functional tight binding for reactive conditions. *J. Chem. Theory Comput.* **2015**, *11*, 4530−4535.

(78) Kroonblawd, M. P.; Lindsey, R. K.; Goldman, N. Synthesis of functionalized nitrogen-containing polycyclic aromatic hydrocarbons and other prebiotic compounds in impacting glycine solutions. *Chem. Sci.* **2019**, *10*, 6091−6098.

(79) Kroonblawd, M. P.; Pietrucci, F.; Saitta, A. M.; Goldman, N. Generating converged accurate free energy surfaces for chemical reactions with a force-matched semiempirical Model. *J. Chem. Theory Comput.* **2018**, *14*, 2207−2218.

(80) Wood, M. A.; Kittell, D. E.; Yarrington, C. D.; Thompson, A. P. Multiscale modeling of shock wave localization in porous energetic material. *Phys. Rev. B* **2018**, *97*, No. 014109.

(81) Liu, L.; Liu, Y.; Zybin, S. V.; Sun, H.; Goddard, W. A., III ReaxFF-lg: Correction of the ReaxFF reactive force field for London dispersion, with applications to the equations of state for energetic materials. *J. Phys. Chem. A* **2011**, *115*, 11016−11022.

(82) Rappe, A. K.; Goddard, W. A., III Charge equilibration for molecular dynamics simulations. *J. Phys. Chem. A* **1991**, *95*, 3358−3363.

(83) Hamilton, B. W.; Kroonblawd, M. P.; Islam, M. M.; Strachan, A. Sensitivity of the Shock Initiation Threshold of 1, 3, 5-Triamino-2, 4, 6-trinitrobenzene (TATB) to Nuclear Quantum Effects. *J. Phys. Chem. C* **2019**, *123*, 21969−21981.

(84) Maillet, J. B.; Mareschal, M.; Soulard, L.; Ravelo, R.; Lomdahl, P. S.; Germann, T. C.; Holian, B. L. Uniaxial Hugoniostat: A method for atomistic simulations of shocked materials. *Phys. Rev. E* **2000**, *63*, No. 016121.

(85) Ravelo, R.; Holian, B. L.; Germann, T. C.; Lomdahl, P. S. Constant-stress Hugoniostat method for following the dynamical evolution of shocked matter. *Phys. Rev. B* **2004**, *70*, No. 014103.

(86) Fickett, W.; Davis, W. C. *Detonation: Theory and Experiment*; Courier Corporation, 2000.

(87) Guo, D.; Zybin, S. V.; An, Q.; Goddard, W. A., III; Huang, F. Prediction of the Chapman−Jouguet chemical equilibrium state in a detonation wave from first principles based reactive molecular dynamics. *Phys. Chem. Chem. Phys.* **2016**, *18*, 2015−2022.

(88) Rom, N.; Zybin, S. V.; Van Duin, A. C.; Goddard, W. A., III; Zeiri, Y.; Katz, G.; Kosloff, R. Density-dependent liquid nitromethane decomposition: molecular dynamics simulations based on ReaxFF. *J. Phys. Chem. A* **2011**, *115*, 10181−10202.

(89) Furman, D.; Kosloff, R.; Dubnikova, F.; Zybin, S. V.; Goddard, W. A., III; Rom, N.; Hirshberg, B.; Zeiri, Y. Decomposition of condensed phase energetic materials: Interplay between uni-and bimolecular mechanisms. *J. Am. Chem. Soc.* **2014**, *136*, 4192−4200.

(90) Sakano, M.; Hamilton, B.; Islam, M. M.; Strachan, A. Role of Molecular Disorder on the Reactivity of RDX. *J. Phys. Chem. C* **2018**, *122*, 27032−27043.

(91) Wu, C. J.; Fried, L. E. Ring closure mediated by intramolecular hydrogen transfer in the decomposition of a push−pull nitroaromatic: TATB. *J. Phys. Chem. A* **2000**, *104*, 6447−6452.

(92) Bagge-Hansen, M.; Bastea, S.; Hammons, J. A.; Nielsen, M. H.; Lauderbach, L. M.; Hodgin, R. L.; Pagoria, P.; May, C.; Aloni, S.; Jones, A.; et al. Detonation synthesis of carbon nano-onions via liquid carbon condensation. *Nat. Commun.* **2019**, *10*, No. 3819.

(93) Zhang, L.; Zybin, S. V.; van Duin, A. C.; Dasgupta, S.; Goddard, W. A., III; Kober, E. M. Carbon cluster formation during thermal decomposition of octahydro-1, 3, 5, 7-tetranitro-1, 3, 5, 7-tetrazocine and 1, 3, 5-triamino-2, 4, 6-trinitrobenzene high explosives from ReaxFF reactive molecular dynamics simulations. *J. Phys. Chem. A* **2009**, *113*, 10619−10640.

(94) Ornellas, D. L. *Calorimetric Determinations of the Heat and Products of Detonation for Explosives*, No. UCRL-52821; California Univ Berkeley Lawrence Livermore Laboratory, 1982.

(95) Tarver, C. M.; Koerner, J. G. Effects of endothermic binders on times to explosion of HMX-and TATB-based plastic bonded explosives. *J. Energ. Mater.* **2007**, *26*, 1−28.

(96) Lee, E.; Finger, M.; Collins, W. *JWL Equation of State Coefficients for High Explosives*, No. UCID-16189; Lawrence Livermore National Laboratory (LLNL): Livermore, CA, USA, 1973.

(97) Dobratz, B. M.; Crawford, P. C. *LLNL Explosives Handbook*, UCRL-52997 Rev. 2; LLNL: Livermore, CA, USA, 1985; Vol. 2.

(98) Tarver, C. M. Modeling detonation experiments on triaminotrinitrobenzene (TATB)-based explosives LX-17, PBX 9502, and ultrafine TATB. *J. Energ. Mater.* **2012**, *30*, 220−251.

(99) Kamlet, M. J.; Jacobs, S. J. Chemistry of detonations. I. A simple method for calculating detonation properties of C−H−N−O explosives. *J. Chem. Phys.* **1968**, *48*, 23−35.

205

Letter

A Hotspot's Better Half: Non-Equilibrium Intra-Molecular Strain in Shock Physics

Brenden W. Hamilton, Matthew P. Kroonblawd, Chunyu Li, and Alejandro Strachan*

Read Online

ACCESS | Metrics & More | Article Recommendations | Supporting Information

ABSTRACT: Shockwave interactions with a material's microstructure localizes energy into hotspots, which act as nucleation sites for complex processes such as phase transformations and chemical reactions. To date, hotspots have been described via their temperature fields. Nonreactive, all-atom molecular dynamics simulations of shock-induced pore collapse in a molecular crystal show that more energy is localized as potential energy (PE) than can be inferred from the temperature field and that PE localization persists beyond thermal diffusion. The origin of the PE hotspot is traced to large intramolecular strains, storing energy in modes readily available for chemical decomposition.

Potential Energy > Kinetic Energy

Larger & More Persistent | Standard Hotspot Model
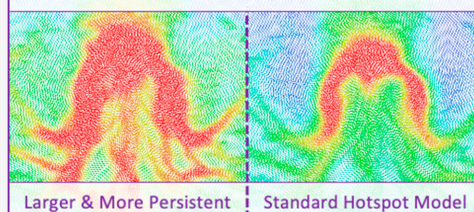
When materials are subjected to high velocity impacts, a shockwave is generated that launches a cascade of ultrafast thermal, mechanical, and chemical processes. The extreme temperature and pressure conditions typical of shock loading can lead to the formation of high-pressure phases[1,2] and synthesis of new materials,[3−6] open unexpected chemical pathways for the origins of life,[7−10] and detonate explosives.[11−13] Underpinning our physical understanding of the nucleation of these processes is the widely accepted conceptual framework in which a material's microstructure interacts with the shockwave to spatially concentrate energy.[12] In high-energy density materials, these nucleation sites, referred to as hotspots, are known to govern shock-to-detonation transition and detonation failure.[13] Hotspots are described by their temperature fields, and it is understood that a size-dependent critical temperature needs to be achieved for a hotspot to transition into a deflagration wave.[14,15] Developing a predictive understanding of hotspot formation and evolution is critical for improving continuum-level models used to assess intentional and accidental initiation and to tailor performance.

Numerous mechanisms can generate hotspots during shocks, including pore collapse, jetting, friction, crack propagation, and localized plastic deformation via dislocations or shear bands.[11,16,17] Among these, pore collapse is believed to be the dominant mode for explosive initiation. This was demonstrated through experiments where explosives were rendered nondetonable following a weak shock that collapsed porosity without inducing significant chemical reactions.[18] Gas gun experiments on gelled nitromethane with porosity controlled through either microballoons or silica beads of consistent size showed that the former produces more effective hotspots for initiation, demonstrating the potency of pore

collapse in energy localization.[19] Regardless of origin, hotspots lead to accelerated chemistry, and those above a critical size and temperature can turn into deflagration waves that may ultimately coalesce in a detonation front.[20] Continuum-level modeling has revealed the size dependence of the critical temperature needed to transition to a deflagration.[14,21] Using a model system with a simplified exothermic chemistry, atomistic simulations have described the coalescence of deflagration waves into a detonation.[22] Recent reactive molecular dynamics (MD) simulations of solid explosives have predicted the transition to deflagration following shock-induced pore collapse.[23] These dynamically formed hotspots are more reactive than counterparts of equal size, temperature, and pressure but created under equilibrium conditions.[15] Dynamic plastic failure can also chemically activate explosive materials and enhance deflagration rates.[24] While experimental observation of shock-induced hotspots remains challenging, recent optical pyrometry measurements have captured peak hotspot temperatures in heterogeneous explosives.[25−27]

Hotspots are routinely characterized and analyzed by their temperature fields, across atomistic and continuum modeling[14,23,28,29] and in experiments.[30] It is well understood that applying external forces to a molecule can accelerate and change chemical reactions through mechanochemistry.[31] This
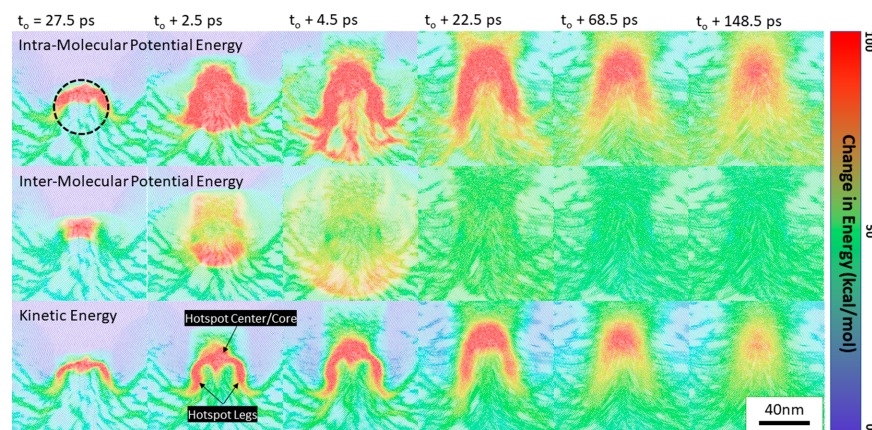
Figure 1. Trajectory snapshots rendered with the OVITO software package[46] showing the temporal evolution of the hotspot in terms of KE (temperature) and PE (separated into intra- and intermolecular terms). Time t_0 represents complete volumetric collapse of the pore. Change in energy is measured with respect to perfect crystal at 300 K and 0 GPa. The black circle in the top left frame represents the initial pore size and location.

can occur through the force altering of the potential energy surface of the molecule, lowering activation barriers.[32] Simple models and theories, such as Bell's Theory[33] and Extended Bell's Theory (EBT),[34] predict that the kinetics depend upon these applied forces. In general, mechanochemistry studies show that stretched bonds typically have shorter lifetimes and that this effect is statistical in nature.[35−38] Altering the internal conformation of molecules and intramolecular strain can also result in accelerated chemistry.[39,40]

A distinct possibility, that we consider here, is that pore collapse may lead to conditions that favor a mechanochemical acceleration of reaction kinetics in hotspots. Utilizing large-scale nonreactive MD simulations of pore collapse in 1,3,5-triamino-2,4,6-trinitrobenzene (TATB), we show that energy localization in hotspots is not well characterized by its temperature field alone. We find that the potential energy (PE) of hotspots is not only substantially greater but also persists for longer times than the kinetic energy (KE) field. This excess PE directly connects to intramolecular strains, indicating it is localized in modes relevant to chemistry. Neither the initial PE field nor its evolution can be inferred from temperature fields, yet PE may influence the energy landscape for thermally activated processes.

Energy Localization Following Pore Collapse. The pore collapse simulation resulted in a hydrodynamic collapse and significant energy localization, as is expected for strong shocks with a particle velocity of 2 km/s.[23,28,41,42] Hotspot formation from pore collapse involves the expansion of the material near the upstream surface of the pore, followed by reshock against the opposite surface until complete volumetric collapse at time t_0. Recompression and shear deformation results in substantial local heating and loss of crystalline order. Long time scale hotspot evolution past $t_0 + 27.5$ ps was predicted using shock trapping internal boundaries (STIBs, implementation details are provided in Supporting Information section SM-4). The resulting temperature field, which is directly proportional to the KE in this classical simulation, exhibits a crescent shape (see Figure 1). As expected, the increase in KE, plus local

compression and disorder, also increases PE. While the PE hotspot eventually settles into a similar shape as the KE, it is greater in magnitude, covers a larger area, and exhibits a different shape during the initial 10 ps following collapse. Interestingly, the PE is mainly stored in intramolecular terms, indicating significant strain to covalent bonds and molecular shape. Contrasting this is a largely homogeneous intermolecular PE field, which one might expect to exhibit greater localization from breaking the hydrogen-bonding network conjectured to be key to TATB's insensitivity.[43,44] The observed intramolecular localization implies that much of the excess PE is readily available in modes needed for chemical decomposition and could plausibly accelerate local kinetics within the hotspot. Importantly, excitation of these intramolecular modes is nearly instantaneous compared to the lengthy processes of energy up-pumping from lattice modes.[45]

The shape of the KE hotspot at early times ($t_0 + 2.5$ ps) reveals the mechanisms behind its origin, i.e., a rather circular central region arises from the recompression of expanding material and two legs are formed by localized shear deformation. This initial distribution quickly settles into a crescent-like shape that persists for tens of picoseconds. In marked contrast, the early shape of the PE hotspot ($t_0 + 2.5$ ps) commands a larger size and persists for longer times within heavily sheared regions ($t_0 + 4.5$ ps) before settling to a shape similar to that of the KE component. This decoupling between the KE and PE hotspots indicates a lack of local equilibrium and path-dependent states, discussed in detail below.

Reactive MD simulations of shock-induced pore collapse in RDX[23] have shown that the decomposition of a hotspot similar in size to ours requires approximately 40 ps, with early reactions seen at the impact plane within ~5 ps. Thus, the time scales in Figure 1 indicate that most of the initial reactions within the hotspot will take place in molecules trapped in excited, highly strained configurations. This excess PE localization may be the key to understanding the increased reactivity of dynamical hotspots (via mechanochemistry) as compared to those formed thermally under equivalent
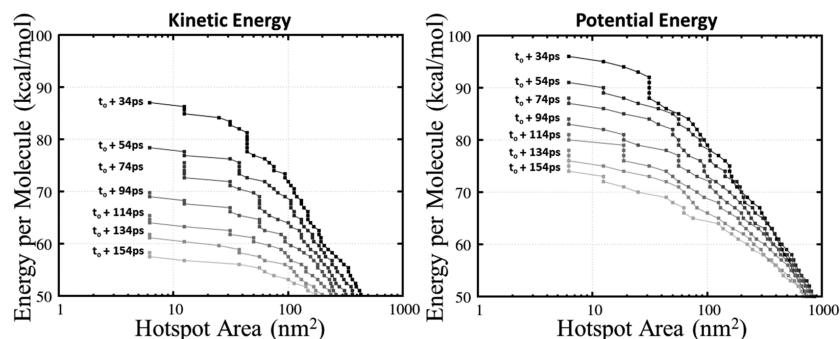
Figure 2. Hotspot energy-size distributions for KE and PE over the extended STIB time regime. Areas are discretized on a 2D Eulerian grid. Energy in both panels is measured with respect to the bulk shocked material, which quantifies the hotspot in terms of excess energy on top of that from hydrodynamic shock compression.

thermodynamic conditions observed in ref 23, as intra-molecular deformations can lead to significant altering of the chemical reactivity.[31,39,40]

Hotspot Relaxation Characteristics. To predict the time evolution of KE and PE in the dynamical hotspot, we applied STIBs to extend the simulation time well beyond the passage of the shock. We characterize the intensity and extent of KE and PE hotspots using a function, $A(E)$, that quantifies the area with energy exceeding a value E. The functions were obtained from fields computed using Eulerian binning and are shown in Figure 2 for various times. The results confirm that the PE hotspot is larger in terms of area and and has a higher specific energy than its KE counterpart and also reveal that it has a substantially longer lifetime. The peak KE value decreases ∼1.5 times faster than the peak PE value.

Since thermally activated chemical processes govern the transition to deflagration, assessing the lifetime of hotspots is key in determining the shock-induced response of explosives. While the relaxation of the hotspot KE (or temperature) can be accurately described via heat transport,[47] the mechanisms underlying the evolution of the hotspot PE are not as simple and are governed by fundamentally different physical processes (e.g., conformational changes and pressure fluctuations). The persistence of the PE allows it to affect the reaction well after the pore collapse event. To study the relaxation of the hotspot's PE, we track the time evolution of the difference in PE and KE of groups of molecules classified based on their degree of internal strain soon after the pore collapse ($t_0 + 5$ ps), see Figure 3. Internal strain is quantified by the ratio between the two smallest principal moments of inertia, I_1 and I_2, of each molecule;[48] this value is near unity for a relaxed TATB molecule as its planar shape leads to moments satisfying $I_1 \approx I_2 < I_3$ (see the Supporting Material (SM) for details). The relatively flat nature of the time histories in Figure 3 indicates negligible relaxation of the highly strained molecules beyond the thermal component that tracks the reduction in KE. That is, a significant portion of the PE rise is latent and undergoes minimal relaxation (the molecules remain highly distorted) on time scales long enough for the KE localization to be completely dissipated. Any significant structural relaxations of the highly deformed molecules would result in a large negative slope for the blue and brown curves in Figure 3. Individual
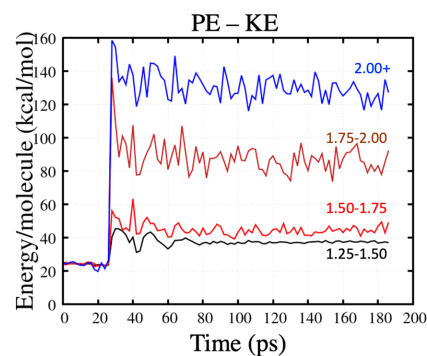
Figure 3. Time history of the difference between the change in PE and change in KE for all molecules within a 25 nm cylindrical radius of the hotspot center. Curves correspond to averages over molecules grouped by the ratio of their first and second principal moments of inertia I_2/I_1, which has a value of 1.0 for a disk. Comparatively fewer molecules have large I_2/I_1, leading to larger fluctuations in the blue and brown curves.

histories of PE and KE are available as Supporting Information (SM-7).

Spatial Localization of Potential Energy. Having established that local temperature does not fully determine the thermodynamic state of the system, we now seek a more complete characterization of PE localization. Figure 4(a) shows the local PE of each bin as a function of its temperature at $t_0 + 2.5$ ps. Curves for PE vs T in crystalline and amorphous samples at the shock pressure ($P = 22$ GPa) are included for comparison. This reveals a broad distribution of local states following pore collapse that is decidedly unlike either crystal or amorphous samples. The lack of a one-to-one PE−T relationship confirms that the hotspot state is not uniquely characterized by temperature. Furthermore, even a two-phase crystal/amorphous description of the system does not fully capture the underlying complexity found in local states at these early stages. Local states were divided into arbitrary categories (marked by the different colors) and mapped into real space in Figure 4(b). Besides the unshocked material (black), the
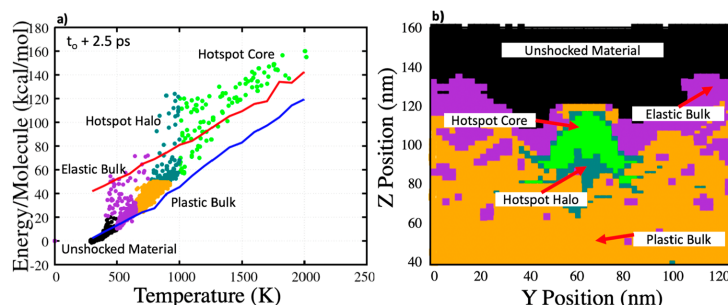
Figure 4. (a) Plot of PE as a function of temperature (points) compared to isobars for a crystal (blue line) and amorphous (red line) system. (b) System divided into zones based on PE and T showing parts that are unshocked (black, PE < −20 kcal/mol, T < 500 K), elastically compressed crystal (purple, 500 < T < 650 K), plastically deformed crystal (orange, −20 < PE < 10 kcal/mol, 650 < T < 1000 K), the hotspot halo region (forest green, PE > 10 kcal/mol, 750 < T < 1000 K), and the hotspot core (lime, T > 1000 K).

elastic precursor following the shock front (purple), and plastically shocked bulk regions (orange), we identified two distinct zones associated with the hotspot, i.e., a hotspot core (lime) surrounded by a hotspot halo (forest green). The local PE states within the hotspot core and halo regions span a wide range. The core states lie primarily above the amorphous baseline at early times due to high pressure from pore collapse reshock. The halo ranges from above the amorphous curve down to crystal-like values. Note that the maximum temperature is lower than the predicted melting point for TATB (T_m = 3400 K at 22 GPa),[49] indicating that the core and halo are highly plastically deformed solids that may explain locked-in intramolecular strain. Plots similar to Figure 4(a) at later times and as per-molecule rather than bin-averaged quantities are available in SM-5 and SM-6.

The use of a nonreactive force field enables us to separate the thermo-mechanical processes associated with hotspots from chemistry. We note that if chemistry is accelerated by the PE component of the hotspot, comparison with earlier work suggests these reaction time scales will be longer than that of hotspot formation and more similar to the time scale of PE relaxation.

State-of-the-art continuum-based models describe hotspot kinetics and chemistry in terms of temperature rise,[50,51] using chemistry models that, at most, distinguish between solid and liquid phases[14] but do not account for disordered solids or the scatter in local PE revealed by our simulations. The rise in PE adds another layer to the competition between exothermic reactions and energy dissipation that controls hotspot criticality, since the localized PE may alter the material reactivity, and its dissipation is governed by physics very different from thermal diffusion. Persistence of highly deformed molecules leads to an acceleration of local reaction kinetics in a variety of situations.[10,24,40,52−54] This latent PE persists over time scales similar to the initial exothermic chemistry predicted in reactive MD pore collapse simulations,[23,55] which could help to explain why dynamically formed hotspots are more reactive than those in pure crystalline or amorphous samples.[15]

In summary, we show through large-scale MD simulations that the PE states in hotspots resulting from shock-induced pore collapse in molecular crystals exhibit a wider spatial extent and have higher energy density with a more complex distribution than can be inferred from the temperature field.

These excited PE states arise due to significant distortions of molecular geometry that persist well beyond the dissipation of the temperature field. Our results show that persistent molecular deformations necessary for mechanochemistry arise in shocked porous molecular solids and can be measured in simulations via an easily computed metric, the intramolecular PE. This offers a plausible and testable hypothesis to explain prior puzzling MD results in which dynamically formed hotspots were found to be more reactive than thermally formed ones. The large differences between the temperature and PE fields identified here motivates a renewed analysis of hotspot dynamics, including attendant plastic work, phase transformations, and chemical kinetics, in a way that considers path-dependent mechanochemistry arising in highly strained regions. More generally, our simulations highlight a neglected physical aspect of the early stages of hotspot formation and evolution that may offer a route to improve multiphysics models of shock initiation and detonation.

COMPUTATIONAL METHODOLOGIES

All MD simulations were conducted using LAMMPS[56] and with interatomic forces described by a widely used[57−59,63,41,47] all-atom nonreactive TATB force field (TATB FF).[57−59] We note that the TATB FF's form allows for a rigorous separation of inter- and intramolecular PE terms (see SM-1). Additionally, we note that the TATB FF used here correctly reproduces TATB vibrational spectra from experiments,[47] and similar harmonic-oscillator-based force fields can reproduce experimental infrared spectral line widths in RDX and PETN,[60,61] indicating that mode relaxation characteristics are reasonably well-described by these kind of models. The classical nature of these simulations should also be considered in that it does not account for zero point energy effects or a quantum mechanical specific heat, both of which have been shown to increase reactivity in TATB.[62]

A nearly orthorhombic simulation cell was prepared using the generalized crystal-cutting method[63] starting from the triclinic $P\bar{1}$ TATB crystal structure[64] with lattice parameters determined with the TATB FF at 300 K and 1 atm.[59] The crystal was oriented such that [**100**] was aligned with $\boldsymbol{x}$, [**120**] was nearly parallel to $\boldsymbol{y}$, and the normal to the basal planes $\mathbf{N}_{(001)} = \boldsymbol{a} \times \boldsymbol{b}$ was aligned with $\boldsymbol{z}$, the shock direction. A cylindrical pore of radius of 40 nm and axis along $\boldsymbol{x}$ was created in the geometric center of a cell with (x,y,z) dimensions (3.6

nm, 122.2 nm, 273.1 nm), yielding ~12.3 million atoms. Direct shock simulations were conducted using a reverse-ballistic configuration[65] with an impact speed of 2 km/s, generating a supported shock in the target material pre-equilibrated at 300 K (see SM-2 for further details). Atomic positions, velocities, and stresses were used to compute molecular properties by local averaging within a 1.5 nm sphere about each molecule. Field properties were obtained through 2D Eulerian binning with a (y,z) bin size (2.5 nm, 2.5 nm). Additional simulation and trajectory analysis details can be found in SM-3.[66−69]

In explicit shock simulations, the cell size limits the achievable time scales due to rarefaction waves originating from free surfaces. Thus, to extend the simulation time and capture the relaxation mechanisms of the hotspot, we developed and employed shock trapping internal boundaries (STIBs), an extension of shock absorbing boundary conditions (SABCs).[70,71] In this new generalization, fixed boundaries were imposed away from the hotspot to isolate it from the multiple waves reflected from the piston, free surface, and pore collapse event. Implementation details are provided in SM-4.

■ ASSOCIATED CONTENT

Ⓢ Supporting Information

The Supporting Information is available free of charge at https://pubs.acs.org/doi/10.1021/acs.jpclett.1c00233.

> (SM-1) TATB force field description; (SM-2) classical molecular dynamics methods description; (SM-3) trajectory analysis description; (SM-4) shock trapping internal boundaries implementation; (SM-5) full distribution of molecular energies (figure of PE vs T for all molecules); (SM-6) local binned energies over time (as in Figure 4a, but at later times); and (SM-7) local decay of energy over time (showing the individual PE and KE curves used to generate Figure 3) (PDF)

■ AUTHOR INFORMATION

Corresponding Author

Alejandro Strachan − *School of Materials Engineering and Birck Nanotechnology Center, Purdue University, West Lafayette, Indiana 47907, United States*; Email: strachan@purdue.edu

Authors

Brenden W. Hamilton − *School of Materials Engineering and Birck Nanotechnology Center, Purdue University, West Lafayette, Indiana 47907, United States*; ⓘ orcid.org/0000-0002-4524-2201

Matthew P. Kroonblawd − *Physical and Life Sciences Directorate, Lawrence Livermore National Laboratory, Livermore, California 94550, United States*; ⓘ orcid.org/0000-0002-5009-5998

Chunyu Li − *School of Materials Engineering and Birck Nanotechnology Center, Purdue University, West Lafayette, Indiana 47907, United States*

Complete contact information is available at:
https://pubs.acs.org/10.1021/acs.jpclett.1c00233

Notes

The authors declare no competing financial interest.

■ REFERENCES

(1) Duvall, G. E.; Graham, R. A. Phase transitions under shock-wave loading. *Rev. Mod. Phys.* **1977**, *49*, 523.

(2) Kadau, K.; Germann, T. C.; Lomdahl, P. S.; Albers, R. C.; Wark, J. S.; Higginbotham, A.; Holian, B. L. Shock waves in polycrystalline iron. *Phys. Rev. Lett.* **2007**, *98*, 135701.

(3) Graham, R. A.; Morosin, B.; Venturini, E. L.; Carr, M. J. Materials modification and synthesis under high pressure shock compression. *Annu. Rev. Mater. Sci.* **1986**, *16*, 315.

(4) De Carli, P. S.; Milton, D. J. Stishovite: synthesis by shock wave. *Science* **1965**, *147*, 144.

(5) Mashimo, T.; Tashiro, S.; Toya, T.; Nishida, M.; Yamazaki, H.; Yamaya, S.; Oh-Ishi, K.; Syono, Y. Synthesis of the B1-type tantalum nitride by shock compression. *J. Mater. Sci.* **1993**, *28*, 3439.

(6) Armstrong, M. R.; Lindsey, R. K.; Goldman, N.; Nielsen, M. H.; Stavrou, E.; Fried, L. E.; Zaug, J. M.; Bastea, S. Ultrafast shock synthesis of nanocarbon from a liquid precursor. *Nat. Commun.* **2020**, *11*, 1.

(7) Bar-Nun, A.; Bar-Nun, N.; Bauer, S. H.; Sagan, C. Shock synthesis of amino acids in simulated primitive environments. *Science* **1970**, *168*, 470.

(8) Goldman, N.; Reed, E. J.; Fried, L. E.; William Kuo, I.-F.; Maiti, A. Synthesis of glycine-containing complexes in impacts of comets on early Earth. *Nat. Chem.* **2010**, *2*, 949.

(9) Kroonblawd, M. P.; Lindsey, R. K.; Goldman, N. Synthesis of functionalized nitrogen-containing polycyclic aromatic hydrocarbons and other prebiotic compounds in impacting glycine solutions. *Chemical Science* **2019**, *10*, 6091.

(10) Steele, B. A.; Goldman, N.; Kuo, I. F. W.; Kroonblawd, M. P. Mechanochemical synthesis of glycine oligomers in a virtual rotational diamond anvil cell. *Chemical Science* **2020**, *11*, 7760.

(11) Campbell, A. W.; Davis, W. C.; Travis, J. R. Shock initiation of detonation in liquid explosives. *Phys. Fluids* **1961**, *4*, 498.

(12) Mader, C. L. Initiation of detonation by the interaction of shocks with density discontinuities. *Phys. Fluids* **1965**, *8*, 1811.

(13) Handley, C. A.; Lambourn, B. D.; Whitworth, N. J.; James, H. R.; Belfield, W. J. Understanding the shock and detonation response of high explosives at the continuum and meso scales. *Appl. Phys. Rev.* **2018**, *5*, 011303.

(14) Tarver, C. M.; Chidester, S. K.; Nichols, A. L. Critical conditions for impact-and shock-induced hot spots in solid explosives. *J. Phys. Chem.* **1996**, *100*, 5794.

(15) Sakano, M.; Hamilton, B.; Islam, M. M.; Strachan, A. Role of Molecular Disorder on the Reactivity of RDX. *J. Phys. Chem. C* **2018**, *122*, 27032.

(16) Davis, W. C. High explosives: The interaction of chemistry and mechanics. *Los Alamos Science* **1981**, *2*, 48−75.

(17) Bowden, F. P.; Yoffe, A. D. *Initiation and growth of explosion in liquids and solids*; CUP Archive, Science: 1985.

(18) Campbell, A. W.; Travis, J. R. *Shock desensitization of PBX-9404 and composition B-3*, No. LA-UR-85-1114, CONF-850706-1; Los Alamos National Lab.: . 1985.

(19) Dattelbaum, D. M.; Sheffield, S. A.; Stahl, D. B.; Dattelbaum, A. M.; et al. Influence of hot spot features on the shock initiation of heterogeneous nitromethane. *AIP Conf. Proc.* **2009**, *1195*, 263.

(20) Campbell, A. W.; Davis, W. C.; Ramsay, J. B.; Travis, J. R. Shock initiation of solid explosives. *Phys. Fluids* **1961**, *4*, 511.

(21) Sakano, M. N.; Hamed, A.; Kober, E. M.; Grilli, N.; Hamilton, B. W.; Islam, M. M.; Koslowski, M.; Strachan, A. Unsupervised learning-based multiscale model of thermochemistry in 1, 3, 5-Trinitro-1, 3, 5-triazinane (RDX). *J. Phys. Chem. A* **2020**, *124*, 9141−9155.

(22) Herring, S. D.; Germann, T. C.; Grønbech-Jensen, N. Effects of void size, density, and arrangement on deflagration and detonation sensitivity of a reactive empirical bond order high explosive. *Phys. Rev. B: Condens. Matter Mater. Phys.* **2010**, *82*, 214108.

(23) Wood, M. A.; Cherukara, M. J.; Kober, E. M.; Strachan, A. Ultrafast chemistry under nonequilibrium conditions and the shock to deflagration transition at the nanoscale. *J. Phys. Chem. C* **2015**, *119*, 22008.

(24) Kroonblawd, M. P.; Fried, L. E. High Explosive Ignition through chemically activated nanoscale shear bands. *Phys. Rev. Lett.* **2020**, *124*, 206002.

(25) Bassett, W. P.; Johnson, B. P.; Neelakantan, N. K.; Suslick, K. S.; Dlott, D. D. Shock initiation of explosives: high temperature hot spots explained. *Appl. Phys. Lett.* **2017**, *111*, 061902.

(26) Bassett, W. P.; Johnson, B. P.; Dlott, D. D. Dynamic absorption in optical pyrometry of hot spots in plastic-bonded triaminotrinitrobenzene. *Appl. Phys. Lett.* **2019**, *114*, 194101.

(27) Bassett, W. P.; Johnson, B. P.; Salvati, III, L.; Dlott, D. D. Report No. LLNL-PROC-782256; Lawrence Livermore National Lab: Livermore, CA, 2019.

(28) Springer, H. K.; Bastea, S.; Nichols, A. L., III; Tarver, C. M.; Reaugh, J. E. Modeling the effects of shock pressure and pore morphology on hot spot mechanisms in HMX. *Propellants, Explos., Pyrotech.* **2018**, *43*, 805.

(29) Li, C.; Hamilton, B. W.; Strachan, A. Hotspot formation due to shock-induced pore collapse in 1, 3, 5, 7-tetranitro-1, 3, 5, 7-tetrazoctane (HMX): Role of pore shape and shock strength in collapse mechanism and temperature. *J. Appl. Phys.* **2020**, *127*, 175902.

(30) Bassett, W. P.; Johnson, B. P.; Salvati, L., III; Nissen, E. J.; Bhowmick, M.; Dlott, D. D. Shock initiation microscopy with high time and space resolution. *Propellants, Explos., Pyrotech.* **2020**, *45*, 223.

(31) Stauch, T.; Dreuw, A. Advances in quantum mechanochemistry: electronic structure methods and force analysis. *Chem. Rev.* **2016**, *116*, 14137−14180.

(32) Kauzmann, W.; Eyring, H. The viscous flow of large molecules. *J. Am. Chem. Soc.* **1940**, *62*, 3113−3125.

(33) Bell, G. I. Models for the specific adhesion of cells to cells. *Science* **1978**, *200*, 618−627.

(34) Konda, S. S. M.; Brantley, J. N.; Bielawski, C. W.; Makarov, D. E. Chemical reactions modulated by mechanical stress: extended Bell theory. *J. Chem. Phys.* **2011**, *135*, 164103.

(35) Beyer, M. K.; Clausen-Schaumann, H. Mechanochemistry: the mechanical activation of covalent bonds. *Chem. Rev.* **2005**, *105*, 2921−2948.

(36) Evans, E. Probing the relation between force—lifetime—and chemistry in single molecular bonds. *Annu. Rev. Biophys. Biomol. Struct.* **2001**, *30*, 105−128.

(37) Beyer, M. K. The mechanical strength of a covalent bond calculated by density functional theory. *J. Chem. Phys.* **2000**, *112*, 7307−7312.

(38) Freund, L. B. Characterizing the resistance generated by a molecular bond as it is forcibly separated. *Proc. Natl. Acad. Sci. U. S. A.* **2009**, *106*, 8818−8823.

(39) Beyer, M. K. Coupling of mechanical and chemical energy: proton affinity as a function of external force. *Angew. Chem., Int. Ed.* **2003**, *42*, 4913−4915.

(40) Ribas-Arino, J.; Marx, D. Covalent mechanochemistry: theoretical concepts and computational tools with applications to molecular nanomechanics. *Chem. Rev.* **2012**, *112*, 5412−5487.

(41) Zhao, P.; Lee, S.; Sewell, T.; Udaykumar, H. S. Tandem molecular dynamics and continuum studies of shock-induced pore collapse in TATB. *Propellants, Explos., Pyrotech.* **2020**, *45*, 196−222.

(42) Duarte, C. A.; Li, C.; Hamilton, B. W.; Strachan, A.; Koslowski, M. Continuum and molecular dynamics simulations of pore collapse in shocked *β*-tetramethylene tetranitramine (*β*-HMX) single crystals. *J. Appl. Phys.* **2021**, *129*, 015904.

(43) Dobratz, B. M. *The Insensitive High Explosive Triaminotrinitrobenzene (TATB): Development and Characterization, 1888 to 1994*, NM. Report No. LA-13014-H; Los Alamos National Lab.: 1995.

(44) Wang, Y.; Liu, Y.; Song, S.; Yang, Z.; Qi, X.; Wang, K.; Liu, Y.; Zhang, Q.; Tian, Y. Accelerating the discovery of insensitive high-energy-density materials by a materials genome approach. *Nat. Commun.* **2018**, *9*, 1.

(45) Dlott, D. D.; Fayer, M. D. Shocked molecular solids: vibrational up pumping, defect hot spot formation, and the onset of chemistry. *J. Chem. Phys.* **1990**, *92*, 3798.

(46) Stukowski, A. Visualization and analysis of atomistic simulation data with OVITO−the open visualization tool. *Modell. Simul. Mater. Sci. Eng.* **2010**, *18*, 015012.

(47) Kroonblawd, M. P.; Sewell, T. D. Anisotropic relaxation of idealized hot spots in crystalline 1, 3, 5-triamino-2, 4, 6-trinitrobenzene (TATB). *J. Phys. Chem. C* **2016**, *120*, 17214.

(48) Kopp, J. Efficient numerical diagonalization of hermitian 3× 3 matrices. *International Journal of Modern Physics C* **2008**, *19*, 523.

(49) Mathew, N.; Kroonblawd, M. P.; Sewell, T.; Thompson, D. L. Predicted melt curve and liquid-state transport properties of TATB from molecular dynamics simulations. *Mol. Simul.* **2018**, *44*, 613.

(50) Lee, K.; Joshi, K.; Chaudhuri, S.; Stewart, D. S. Mirrored continuum and molecular scale simulations of the ignition of high-pressure phases of RDX. *J. Chem. Phys.* **2016**, *144*, 184111.

(51) Long, Y.; Chen, J. Systematic study of the reaction kinetics for HMX. *J. Phys. Chem. A* **2015**, *119*, 4073.

(52) Gilman, J. J. Mechanochemistry. *Science* **1996**, *274*, 65.

(53) Riad Manaa, M. Shear-induced metallization of triaminotrinitrobenzene crystals. *Appl. Phys. Lett.* **2003**, *83*, 1352.

(54) Islam, M. M.; Strachan, A. Role of dynamical compressive and shear loading on hotspot criticality in RDX via reactive molecular dynamics. *J. Appl. Phys.* **2020**, *128*, 065101.

(55) Wood, M. A.; Kittell, D. E.; Yarrington, C. D.; Thompson, A. P. Multiscale modeling of shock wave localization in porous energetic material. *Phys. Rev. B: Condens. Matter Mater. Phys.* **2018**, *97*, 014109.

(56) Plimpton, S. Fast parallel algorithms for short-range molecular dynamics. *J. Comput. Phys.* **1995**, *117*, 1.

(57) Bedrov, D.; Borodin, O.; Smith, G. D.; Sewell, T. D.; Dattelbaum, D. M.; Stevens, L. L. A molecular dynamics simulation study of crystalline 1, 3, 5-triamino-2, 4, 6-trinitrobenzene as a function of pressure and temperature. *J. Chem. Phys.* **2009**, *131*, 224703.

(58) Kroonblawd, M. P.; Sewell, T. D. Theoretical determination of anisotropic thermal conductivity for crystalline 1, 3, 5-triamino-2, 4, 6-trinitrobenzene (TATB). *J. Chem. Phys.* **2013**, *139*, 074503.

(59) Mathew, N.; Sewell, T. D.; Thompson, D. L. Anisotropy in surface-initiated melting of the triclinic molecular crystal 1, 3, 5-triamino-2, 4, 6-trinitrobenzene: A molecular dynamics study. *J. Chem. Phys.* **2015**, *143*, 094706.

(60) Pereverzev, A.; Sewell, T. D.; Thompson, D. L. Calculation of anharmonic couplings and THz linewidths in crystalline PETN. *J. Chem. Phys.* **2014**, *140*, 104508.

(61) Pereverzev, A.; Sewell, T. D.; Thompson, D. L. Molecular dynamics study of the pressure-dependent terahertz infrared absorption spectrum of *α*-and *γ*-RDX. *J. Chem. Phys.* **2013**, *139*, 044108.

211

(62) Hamilton, B. W.; Kroonblawd, M. P.; Islam, M. M.; Strachan, A. Sensitivity of the shock initiation threshold of 1, 3, 5-triamino-2, 4, 6-trinitrobenzene (TATB) to nuclear quantum effects. *J. Phys. Chem. C* **2019**, *123*, 21969−21981.

(63) Kroonblawd, M. P.; Mathew, N.; Jiang, S.; Sewell, T. D. A generalized crystal-cutting method for modeling arbitrarily oriented crystals in 3D periodic simulation cells with applications to crystal−crystal interfaces. *Comput. Phys. Commun.* **2016**, *207*, 232.

(64) Cady, H. H.; Larson, A. C. The crystal structure of 1, 3, 5-triamino-2, 4, 6-trinitrobenzene. *Acta Crystallogr.* **1965**, *18*, 485.

(65) Holian, B. L.; Lomdahl, P. S. Plasticity induced by shock waves in nonequilibrium molecular-dynamics simulations. *Science* **1998**, *280*, 2085.

(66) Andersen, H. C. Rattle: A "velocity" version of the shake algorithm for molecular dynamics calculations. *J. Comput. Phys.* **1983**, *52*, 24.

(67) Nosé, S. A unified formulation of the constant temperature molecular dynamics methods. *J. Chem. Phys.* **1984**, *81*, 511.

(68) Hoover, W. G. Canonical dynamics: Equilibrium phase-space distributions. *Phys. Rev. A: At., Mol., Opt. Phys.* **1985**, *31*, 1695.

(69) Wolf, D.; Keblinski, P.; Phillpot, S. R.; Eggebrecht, J. Exact method for the simulation of Coulombic systems by spherically truncated, pairwise r− 1 summation. *J. Chem. Phys.* **1999**, *110*, 8254.

(70) Cawkwell, M. J.; Sewell, T. D.; Zheng, L.; Thompson, D. L. Shock-induced shear bands in an energetic molecular crystal: Application of shock-front absorbing boundary conditions to molecular dynamics simulations. *Phys. Rev. B: Condens. Matter Mater. Phys.* **2008**, *78*, 014107.

(71) Zhao, S.; Germann, T. C.; Strachan, A. Atomistic simulations of shock-induced alloying reactions in Ni/ Al nanolaminates. *J. Chem. Phys.* **2006**, *125*, 164707.

212

ANNUAL REVIEWS

Chemistry Under Shock Conditions

Brenden W. Hamilton, Michael N. Sakano, Chunyu Li, and Alejandro Strachan

School of Materials Engineering and Birck Nanotechnology Center, Purdue University, West Lafayette, Indiana 47906; email: strachan@purdue.edu

ANNUAL REVIEWS CONNECT

www.annualreviews.org

- Download figures
- Navigate cited references
- Keyword search
- Explore related articles
- Share via email or social media

Keywords

shock physics, chemistry, extreme conditions, molecular dynamics, detonation, hot spots

Abstract

Shock loading takes materials from ambient conditions to extreme conditions of temperature and nonhydrostatic stress on picosecond timescales. In molecular materials the fast loading results in temporary nonequilibrium conditions with overheated low-frequency modes and relatively cold, high-frequency, intramolecular modes; coupling the shock front with the material's microstructure and defects results in energy localization in hot spots. These processes can conspire to lead to a material response not observed under quasi-static loads. This review focuses on chemical reactions induced by dynamical loading, the understanding of which requires bringing together materials science, shock physics, and condensed matter chemistry. Recent progress in experiments and simulations holds the key to the answer of long-standing grand challenges with implications for the initiation of detonation and life on Earth.

101

213

1. INTRODUCTION AND OVERVIEW

When materials are subject to a high-velocity impact, something remarkable happens. Instead of the mechanical load spreading in space, a shock wave with a front of near-atomic thickness develops. This occurs because materials become stiffer with compression, and sound waves in the compressed material travel faster than in the unshocked region. Thus, waves pile up at the shock front. The result is that the material goes from the unloaded state to extreme conditions of stress and temperature in a very short period of time, on the order of a picosecond (10^{-12} s). **Figure 1** illustrates the truly extreme conditions associated with shock waves, ranging from the impact and shock velocities involved to the states of pressure and temperature explored, as well as associated processes. Typical impact velocities in shock experiments range from hundreds of meters per second to several kilometers per second; the shock velocities are considerably faster (a detonation wave can travel at 10 km/s). The pressures involved are in the range of a few to ~50 GPa, and temperatures can reach several thousand degrees Kelvin. Given the scales involved, it should not come as a surprise that materials subject to such insults can exhibit mechanisms not accessible through quasi-static loading. When subject to ultrafast loading at extreme conditions, materials undergo familiar processes like plastic deformation, solid–solid phase transitions, melting, and
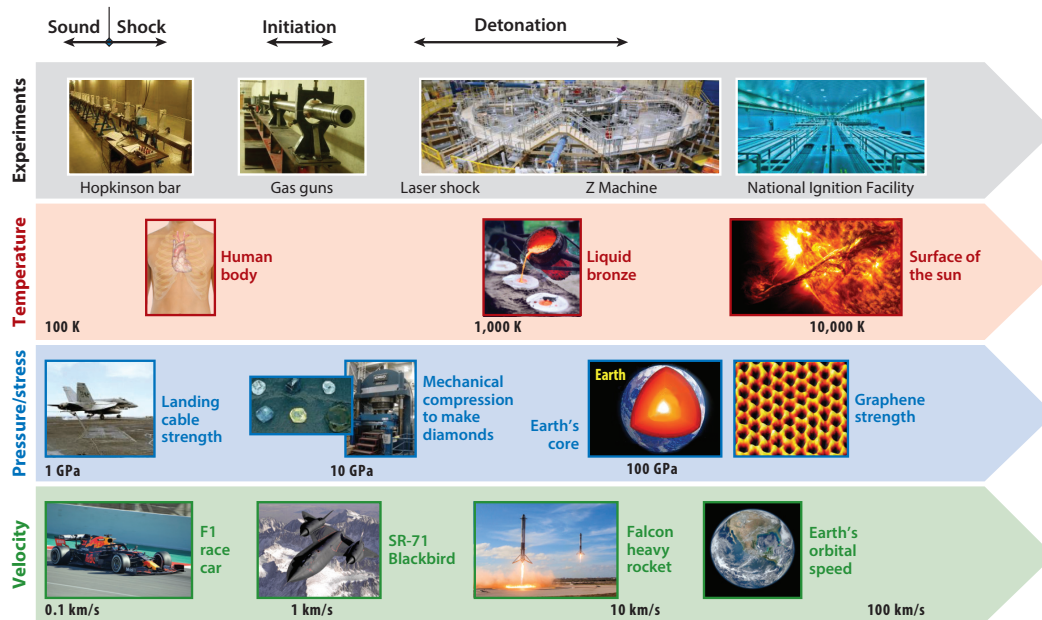
Figure 1

From low-strength acoustic waves to high-pressure impacts, the extreme conditions of shock compression lead to an extremely broad range of temperatures, pressures, and velocities. Images adapted from the following sources: Hopkinson bar and gas gun, Wayne Chen, Purdue University; Z Machine, US Department of Energy, National Nuclear Security Administration; National Ignition Facility, Christopher Michel/Flickr (CC BY 2.0); human body, Mikael Häggström/Wikipedia; liquid bronze, Takk/Wikipedia (CC BY-SA 3.0); sun, SR-71, and Earth, NASA/Wikipedia; landing cable strength, US Navy/Wikipedia; diamonds and belt press, Materialscientist/Wikipedia; Earth's core, Kelvinsong/Flickr (CC BY 2.0); graphene, US Army Materiel Command/Flickr (CC BY 2.0); F1, Alberto-g-rovi/Wikipedia (CC BY-SA 3.0); Falcon, SpaceX/Wikipedia (CC BY 1.0).

102　*Hamilton et al.*

214

chemical reactions that are driven and controlled by combinations of hydrostatic and deviatoric components of stress as well as temperature. However, these processes often exhibit interesting differences from their normal-condition counterparts. For example, shock loading can result in nonthermal melting (1), formation of phases of matter not otherwise accessible (2), and nonstatistical or path-dependent chemistry (3). Significant scientific questions regarding these processes remain open. Their experimental characterization is challenging due to the ultrafast timescales and extreme conditions involved. At the same time, modeling these phenomena puts physics-based simulations to a stress test, challenging assumptions and testing the range of applicability of constitutive models.

This article describes recent progress in our understanding of shock-induced chemistry, focusing on the exciting possibility of meaningful and direct comparisons between experiments and atomic-level simulations. We believe such efforts hold the key to providing definite answers to open science questions. Beyond basic science, understanding shock-induced chemistry has important practical applications. These range from the safe use of explosives and propellants (4, 5) to understanding the role of shock-induced formation of organic molecules in the development of life on Earth (6–8). We present our perspective on this rapidly evolving field by highlighting recent results and the state of the art; we do not aim to provide an exhaustive description of the excellent research in the field. After a brief review of shock physics and chemistry (Section 2), we discuss recent progress in experimental (Section 3) and simulation (Section 4) techniques to uncover chemistry at extreme conditions. In Section 5 we describe the state of the art and opportunities to provide definite answers to open questions. Finally, in Section 6 we provide a summary and outlook.

2. SHOCK PHYSICS AND CHEMISTRY: THE BASICS

When a projectile impacts a material at high speeds (**Figure 2**), a shock front develops, separating the unperturbed and shocked regions. This front is a few atomic or molecular distances thick and travels at supersonic speeds (below, u_s denotes shock speed) with respect to the unshocked material, and subsonic with respect to the shocked material moving at the particle speed (u_p) for a steady-state wave. The distinction between shock and acoustic waves is not sharp. A useful definition is that a shock involves significant compression and a well-defined front; the shocks of interest in this review are strong enough to cause irreversible (inelastic) processes in the target material. Shock loading explores a set of states in pressure–volume–temperature (P–V–T) space. These states, depicted in P–V space in **Figure 3a**, depend on the initial conditions and are called the Hugoniot equation of state. It should be clear that this is a collection of states accessible from the initial conditions by independent shocks, very different from, for instance, an isothermal equation of state where states are accessible from one another via reversible processes. Importantly, in the case of shocks, the material goes from the unperturbed to the shock state within a few picoseconds, and atomic simulations indicate that the path taken resembles a straight line in P–V space.

In a steady propagating shock, conservation of mass, momentum, and energy leads to the Rankine–Hugoniot jump conditions, which relate the initial conditions and final states with u_p and u_s as the only inputs:

$$\rho_s \left(u_s - u_p \right) = \rho_0 u_s, \qquad\qquad 1.$$

$$P_s - P_0 = \rho_0 u_s u_p, \qquad\qquad 2.$$

$$P_s u_p = \rho_0 u_s \left(\frac{1}{2} u_p^2 + e_s - e_0 \right). \qquad\qquad 3.$$
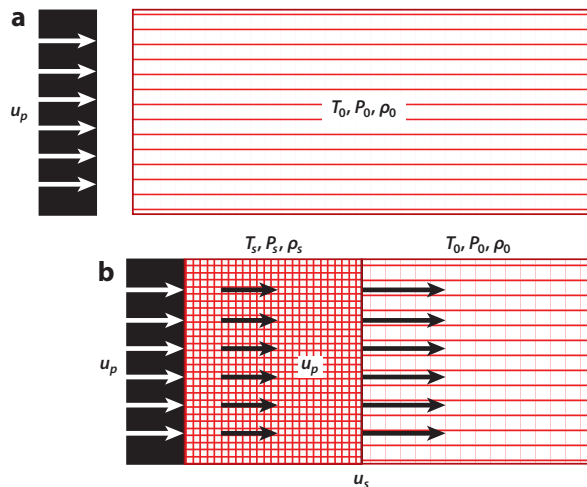
Figure 2

(*a*) Preshock (uncompressed) material in equilibrium. (*b*) Partially shocked material (left half compressed to shock state). As a shock wave propagates across a material, the pressure (P), temperature (T), density (ρ), and internal energy increase, and the material begins to propagate forward at the piston velocity (u_p). The wave itself moves at a faster shock velocity (u_s), compressing material along the way. This change of thermodynamic states is described by the Rankine–Hugoniot jump conditions.

The shock pressure (P_s), density (ρ_s), and internal energy (e_s) can be obtained from the unperturbed state (denoted with a subscript 0) and the shock and particle velocities, which are relatively easy to obtain experimentally. The line joining the initial state and the shock state in P–V space (**Figure 3**) is known as the Rayleigh line; its slope is proportional to the square of the shock velocity.

Shock temperature (T_s) is not directly obtainable from the jump conditions and is difficult to measure experimentally. Section 2.1.2 discusses recent progress in shock temperature measurements, but an estimate can be obtained from the equation of state and the energy increase from
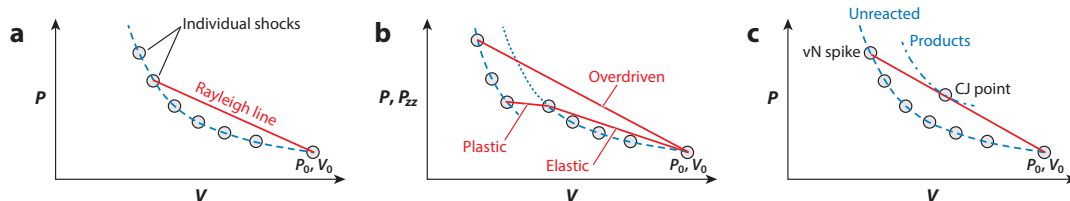
Figure 3

Example Hugoniots for (*a*) a simple elastic compression, (*b*) an elastic–plastic response of a material, and (*c*) shock-induced chemical reactions (volume expanding). The line joining the initial state and the shock state is known as the Rayleigh line; its slope is proportional to the square of the shock velocity. Abbreviations: CJ point, Chapman–Jouguet point; vN spike, von Neumann spike.

104   Hamilton et al.

the jump conditions (9):

$$e_s - e_0 = \int_{T_0}^{T_s} C_v(T')\mathrm{d}T',$$

4.

where $C_v(T)$ is the specific heat.

The increase in stress and temperature caused by the shock induces a series of materials processes through which the system attempts to minimize its free energy under new conditions. This response includes plasticity, phase transformations (including melting), and chemical reactions. Inspection of **Figure 2** shows that the initial load of a material under shock loading is uniaxial, compressive strain (lateral relaxation affects only narrow regions of the material near free surfaces, since sound waves propagate more slowly than the shock and are neglected here unless otherwise noted). Under these conditions, the stress along the loading direction (let us assign the z axis to it) will be higher than the transverse stress. Thus, near the shock front a nonhydrostatic stress condition with $|\sigma_{zz}| > |\sigma_{xx}| \sim |\sigma_{yy}|$ provides the driving force for plasticity. If this driving force surpasses the strength of the material, plastic deformation will occur (**Figure 3b**); recall that pressure and stress differ according to sign ($\sigma_{zz} = -P_{zz}$). Plastic deformation reduces the free energy of the material and brings it to a near-hydrostatic state, reducing P_{zz} and increasing the transverse pressure components (**Figure 3**). The material jumps from one Hugoniot curve (elastic compression) to a different one that includes plasticity. Under certain circumstances a two-wave structure can form, as shown by the two Rayleigh lines in **Figure 3**, with a leading elastic wave followed by a plastic wave propagating at a slower speed (10). Similar effects occur when shocks induce volume-collapsing processes via either chemical reactions, as in benzene (11, 12), or collapse of porosity (13). These processes can be used to attenuate shock waves for protection against high-velocity impacts (14, 15).

2.1. Shock-Induced Chemistry

Shock-induced chemistry is the focus of this review, and we pay special attention to cases where the ultrafast loading and extreme conditions induce processes not commonly observed otherwise. As mentioned above, dynamical loading can lead to the formation of phases that are metastable under ambient conditions, chemical decomposition under nonstatistical conditions, and chemistry that is so fast that it can interact with and affect the propagating shock.

A projectile will sustain a shock for a finite amount of time, as expansion from the projectile's free surface (opposite the impact surface) will eventually catch up and weaken the shock. Thus, an inert material's shock waves propagate unimpeded for a finite time (which depends on the material's properties and the thickness of the impactor) and then weaken and dissipate. Materials processes, including chemistry, can interfere with the propagating shock front if they change the pressure of the shock material (either reduce it or increase it) and if they are fast enough. Section 2.1.1 discusses the effect of volume-collapsing and -expanding processes on the steady propagation of shocks, followed by a discussion of the initiation of chemistry in Section 2.1.2.

2.1.1. Steady-state response.
Figure 3b,c illustrates the role of volume-changing chemistry on the propagation of the shock. In the case of volume-collapsing processes, the result is a reduction of pressure, as indicated in **Figure 3b**. The effect on the propagating shock is similar to that of plasticity. However, unlike plasticity, which is volume conserving, chemical reactions and the collapse of porosity reduce the stress along all directions. Both experiments and simulations have demonstrated that such volume-collapsing processes can attenuate the propagation of shocks. For example, benzene undergoes a transformation in which sp^2 carbon atoms in the ring react to form diamond-like structures involving sp^3 bonds, which reduces volume. Coarse-grained,

217

particle-based simulations using the ChemDID mesoscale approach (14, 16, 17) quantified the effect of endothermicity, volume reduction, and reaction timescales on the attenuation of the shock (15). Materials with fast, volume-collapsing processes are attractive for protection against ballistic impacts.

Figure 3c illustrates the opposite effect. Here, the chemical reactions are volume expanding and exothermic. This is the case for explosives. As the reaction behind the shock wave increases pressure and the reacting material expands, the resulting waves can catch up with the front and sustain it. This process is known as a detonation; the leading shock initiates chemistry, and the chemistry sustains the shock. The simplest model for detonation is described by the Zel'dovich–von Neumann–Doering (ZND) theory. Under steady state, the shock front of a one-dimensional detonation takes the material to a high pressure point on the unreacted Hugoniot known as a von Neumann spike (**Figure 3c**). At this point, the material begins to react and expand across a finite reaction zone, which ends at the Chapman–Jouguet (CJ) point. Beyond this point, also known as the sonic point, reactions cannot reach the detonation due to the decreased sound speed caused by the expansion. Reactions continue beyond the CJ point, but they do not affect the detonation. **Figure 3c** shows that the Rayleigh line that starts at the initial condition and is tangent to the products' Hugoniot represents a steady shock and the detonation velocity can be obtained from its slope. The intersection of this Rayleigh line with the Hugoniot of the reactants marks the von Neumann spike. **Figure 4** schematically represents the shock-to-detonation transition in an ideal energetic material; the steady-state diagram on the far right depicts the von Neumann spike and the CJ point. For a more detailed description of the ZND theory and detonation theory, see Reference 5.

2.1.2. Initiation of chemical reactions. With a basic understanding of steady-state shocks and detonation, we can now begin to tackle a more challenging problem: how a detonation starts and how it fails. The shock-to-detonation transition is a grand challenge at the intersection of shock physics, chemistry at extreme conditions, and materials science. At first sight, the shock initiation of a detonation may seem like an improbable feat, since kinetic energy in a macroscopic projectile needs to find its way into individual bond vibrations (with characteristic lengths of angstroms and times of tens of femtoseconds) in short enough times for the chemistry to couple to the propagating shock. Two phenomena play a central role in enabling this process: spatial localization of energy and spectral delocalization of energy.
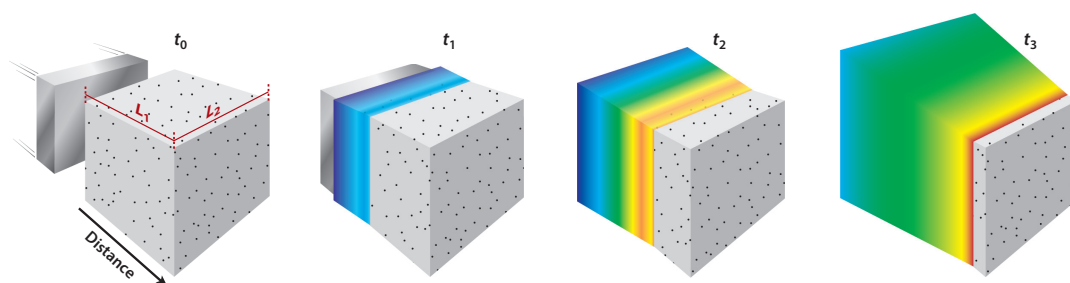

Figure 4

Schematic representation of the shock-to-detonation transition. The initial shock triggers chemical reactions that build up and result in a steady-state detonation. Color represents temperature, and the figure represents the volume expansion as reactions occur. Figure adapted from Reference 18.
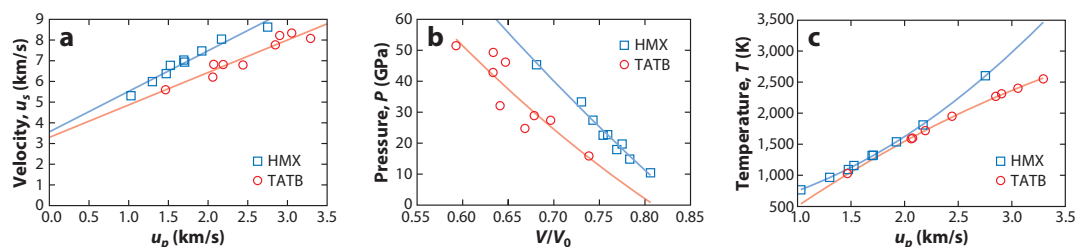
Figure 5

Example Hugoniot curves for HMX (1,3,5,7-tetranitro-1,3,5,7-tetrazoctane) (19) and TATB (1,3,5-triamino-2,4,6-trinitrobenzene) (20). (*a*) Shock velocity–particle velocity. (*b*) Pressure–volume. (*c*) Temperature–particle velocity. Temperature is calculated from Equation 4 using temperature-dependent specific heats (21, 22).

Since chemistry is a thermally activated process, knowledge of shock-induced temperature is critical. To estimate temperatures, we start with experimental Hugoniot curves for two widely used high-energy-density (HE) materials, 1,3,5,7-tetranitro-1,3,5,7-tetrazoctane (HMX) and 1,3,5-triamino-2,4,6-trinitrobenzene (TATB) (19, 20) (**Figure 5*a,b***). With specific heats from References 21 and 22, we estimate the shock temperatures using Equation 4. From this simple analysis we find that a shock with a particle velocity of 2 km/s would result in ~1,600 K for HMX and ~1,550 K for TATB. At these temperatures we would expect very slow chemical decomposition. Furthermore, these temperatures are in stark contrast with results from recent experiments that used optical pyrometry to measure values above 6,000 K for comparable shock strengths. While these measurements probably include the effect of exothermic chemical reactions, measurements in inert materials result in temperatures in the 2,500 K range (23). The sharp difference is that Equation 4 assumes a homogeneous material, neglecting the energy localization that originates from the interaction between the propagating wave and the material microstructure and defects. Energy localization into hot spots is not the exception, as most materials of interest are not homogeneous but rather microstructurally complex composites. In fact, common explosives consist of grains of the HE material (molecular crystals) bonded by a polymer. Energy localization in hot spots is discussed in Section 5.2, and a list of common HE materials and their properties is available in References 129 and 130.

Beyond spatial localization, energy needs to flow from low-frequency, long-wavelength modes that couple strongly with the propagating shock to the high-frequency, localized modes responsible for chemistry. This process of thermalization is called up-pumping (24). Interestingly, chemistry can start in timescales comparable to this equilibration, that is, while the material is away from thermal equilibrium. The degree of such nonstatistical chemistry and its importance for shock initiation are not fully understood.

3. EXPERIMENTAL TOOLS FOR ULTRAFAST CHEMISTRY AT EXTREME CONDITIONS

3.1. Shock Generation

Shock waves in the lab are typically launched via high-velocity projectile impact on the target material. The impactor can be accelerated using either a gas gun or a laser pulse. Single-stage gas guns can launch flyer plates with velocities up to ~1 km/s, resulting in shock pressures of tens of gigapascals (25). As compared with lasers, guns can launch larger projectiles, resulting in more
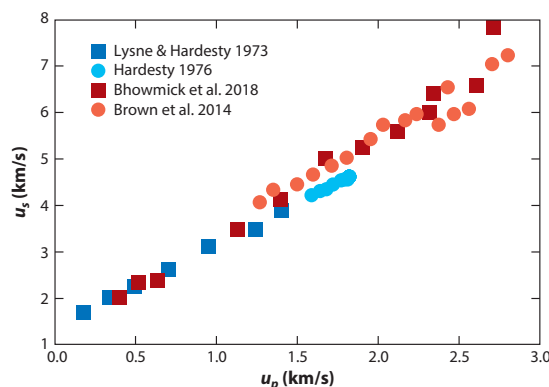
Figure 6

Hugoniot curves of nitromethane using gas gun–induced (*shades of blue*) and laser-induced shock (*shades of red*). Data were obtained from References 30–33.

planar shocks and longer (microseconds) sustained pulse widths (controlled by the width of the impactor). Two-stage gas guns can reach up to 200 GPa (25).

While direct exposure to pulsed lasers can cause shocks in absorbing materials, lasers are often used to launch projectiles into the target material (26, 27). Laser setups can have a smaller lab footprint (down to tabletop setup), can enable multiple shots in a single sample, and can reach much higher shock pressures (28). However, the relatively small sample size limits the time of sustained shocks. These challenges can be overcome, and state-of-the-art laser shocks can reproduce standard bulk shock results. **Figure 6** shows $u_s - u_p$ data from various studies using gas gun– and laser-driven shocks. Lasers can also be used to generate interesting shock configurations, including convergent shocks that result in extremely high pressures (29).

Large-scale laser facilities provide access to regimes beyond gas guns and tabletop laser experiments. Lab-scale laser shocks can reach shock pressures of up to hundreds of megabars (1 Mbar = 100 GPa) (34). These facilities, such as the Laboratory for Laser Energetics (35), the National Ignition Facility (36), and the Z Machine (37), have enabled the study of matter at extreme conditions beyond those of a detonating explosive. The conditions achievable can mimic those of supernovas (34), nuclear detonations (36), and the cores of planets and stars (38). The increased availability and access to such facilities will afford significant opportunities for rapid growth in the body of knowledge about extreme-conditions phenomena in matter.

3.2. Shock Characterization: Thermomechanics

Equally important for exquisite control over the planarity and uniform strength of the shock is characterizing the propagating shock front and the shock state. Ideally, one would like to assess the time evolution of the shock front and the state of the shocked materials, including heterogeneities.

Stress and strain gauges can provide information about impact conditions, and piezoelectric pins allow the determination of shock velocity by measuring time of passage. Methods such as streak camera spectroscopy (39), VISAR (velocity interferometer system for any reflector) (40), photon Doppler velocimetry (41, 42), and Fabry–Pérot interferometry (43) can measure a free surface or an interface's position–time history to obtain the particle and/or shock velocity. Additionally, the shock front itself can generally be measured directly in transparent materials (44).

Direct measurement of wave velocity and impact speed/pressure is most common, but it does not always provide the full state of the shocked material. This demonstrates the importance of impedance-matching techniques using shock standards (44), which can supplement direct measurements of shock speed (and/or pressure) (45).

With knowledge of the initial state and the propagation velocities of the various waves, one can use the jump conditions (Equation 3) and/or impedance matching with standard materials to obtain state variables like pressure. Temperature can only be indirectly assessed from such measurements using an equation of state, as discussed in Section 2. This approach, however, assumes that the material is homogeneous and ignores energy localization into hot spots. Thus, direct measurements of temperature are highly desirable.

Temperature can be assessed using several tools, including thermal emissivity and other radiation (46), as well as Raman spectroscopy (47). Thermal emissivity (optical pyrometry) measures temperature by relying on assumptions such as a gray-body approximation for the material. While very powerful, this technique is skewed toward the highest temperature, providing no information about the temperature distribution or the area distribution of these temperatures. Additionally, the temperature readings cannot identify the source, whether solely from mechanical heating or from chemical reactions. However, recent pyrometry experiments of shocked HMX have been able to spatially map the high-temperature regions (48). These experiments showed that the early, high-temperature regions are spatially located where there was an initial large void in the HMX crystal. This finding corroborates the modeling and theory that defects lead to the all-important hot spots, which then drive initial chemistry.

3.3. Shock Characterization: Structural Transitions and Chemistry

The techniques discussed above provide only indirect information about chemistry. Establishing an atomic- or molecular-level understanding of chemistry under extreme conditions requires tools capable of assessing atomic and molecular structures. While researchers have a range of tools to accomplish that, the challenge with shocks is the ultrafast nature of the processes. Thus, characterization needs to be done in a single shot using X-rays, infrared (IR) radiation, or electrons. For example, in situ synchrotron X-ray diffraction has enabled the characterization of shock-induced phase transformations such as that of highly oriented pyrolytic graphite to a hexagonal diamond phase (49).

Cutting-edge experimental techniques have been developed and refined for analysis of shock-induced chemistry as well. Commonly used for this purpose is ultrafast IR absorption (50, 51). Molecular vibrations with associated dipole moments emit and absorb electromagnetic radiation at their characteristic frequencies, which lie in the IR regime. Thus, IR spectroscopy provides a fingerprint of materials with information about the vibrational modes present that can be assigned to molecular moieties. With picosecond time resolution, ultrafast IR spectroscopy enables the observation of the time evolution of IR active modes during and following the shock wave. Early research showed the disappearance of peaks associated with NO_2 when poly(vinyl nitrate) (PVN) was shocked to 18 GPa. Over the last decade, experimental advances have increased the spectral range of ultrafast IR to now enable researchers to follow the evolution of multiple modes and obtain more detailed information regarding chemical reactions (33, 52).

Raman spectroscopy has been used to study time-resolved chemical changes in nitromethane (NM) (53). Raman has also been a crucial tool in understanding phase transformations in energetic crystals (54). Additionally, visible transient absorption spectroscopy and ultrafast dynamic ellipsometry have been used to measure the timescales of shock-induced reaction initiation (55) and to map the reacted Hugoniot of NM (33).

In summary, spectroscopy methods have shown chemical initiation of various HE materials on picosecond timescales, in good agreement with reactive molecular dynamics (MD) simulations (52, 56). Challenges remain in mapping detailed chemical reaction pathways and species across time in experiments. However, the ability to couple these methods with atomic-resolution simulation techniques may open the door to a definite understanding of shock-induced chemical reactions.

4. SIMULATION TOOLS FOR ULTRAFAST CHEMISTRY AT EXTREME CONDITIONS

Uncovering chemistry at extreme conditions requires not only an atomistic description but also a dynamical approach that does not assume equilibrium. This is especially important because this chemistry can be influenced by the ultrafast mechanical loading and can occur, or be initiated, away from local thermodynamic equilibrium. Such a description can only be provided by MD simulations, which follow the dynamics of individual atoms solving the classical equations of motion. While not without approximations, MD provides an optimal balance between accuracy and computational intensity. The only fundamental approximation in MD is the use of classical (as opposed to quantum) mechanics, but, in practice, atomic forces are also invariably approximated. The fast timescales of shock-induced processes enable a direct comparison between experiments and MD simulations which is not possible in other applications. As discussed in Section 5.1, below, one-to-one comparison between experiments and simulations could result in the definite understanding of chemistry under extreme conditions. In addition, MD simulations play a key role in connecting first-principles descriptions of materials via electronic structure calculations and continuum models (57).

4.1. Molecular Dynamics Simulations

MD simulations numerically solve the time evolution of each individual atom in a material using Newton's laws. This requires knowledge of the force acting on each atom which, excluding external fields, is caused by neighboring atoms. These forces can be obtained from first principles using quantum mechanical calculations of the electronic structure of the material. The energy of a system of interacting atoms can be obtained from the time-independent Schrödinger equation:

$$H(\{r_i\}; \{R_i\})\Psi(\{r_i\}; \{R_i\}) = V(\{R_i\})\Psi(\{r_i\}; \{R_i\}), \qquad 5.$$

where $\{r_i\}$ are the coordinates of the electrons and $\{R_i\}$ are the ionic coordinates (taken as classical point particles) in the system. H is the Hamiltonian operator representing the total energy of the system, and $\Psi(\{r_i\}; \{R_i\})$ is the wave function of the electrons; both depend parametrically on the positions of the ions, $\{R_i\}$, which create the external potential under which the electrons live. We note that the Schrödinger equation is an eigenvalue problem in the space of functions; the eigenvalue, $V(\{R_i\})$, represents the energy of the system and depends only on the ionic positions. Note that we are taking ions as classical point particles and we are solving for the electrons assuming that the ions are stationary. This is the Born–Oppenheimer approximation and is justified by the fact that massive ions (recall that a single proton is approximately 2,000 times more massive than an electron) have relaxation timescales much longer than those of electrons; in other words, electrons are so fast that they see ions as immobile and find their ground state for each ionic configuration.

The energy $V(\{R_i\})$ includes contributions from the kinetic energy of the electrons, as well as electron–ion, ion–ion, and electron–electron interactions. As such, $V(\{R_i\})$ represents the many-body potential energy landscape under which the ions move. By adding the kinetic energy of ions

we can construct a classical Hamiltonian to describe the motion of ions:

$$H = V(\{R_i\}) + \sum_{i=1}^{3N} P_i^2/2M_i, \qquad\qquad 6.$$

where N is the number of ions, P_i represents the momentum associated with coordinate R_i, and M_i is the atomic mass. The time evolution of the system is given by Hamilton's $3N$ coupled equations of motion:

$$\dot{R}_i = \frac{\partial H}{\partial P_i} = P_i/M_i \qquad\qquad 7.$$

and

$$\dot{P}_i = -\frac{\partial H}{\partial R_i} = -\frac{\partial V}{\partial R_i}. \qquad\qquad 8.$$

In summary, knowledge of the potential energy surface of the system allows us to solve, numerically, for the time evolution of the system of interest. Statistical mechanics is then used to extract thermodynamic quantities from the atomistic system. Note, importantly, that thermodynamic equilibrium is not assumed in an MD simulation; thermodynamic equilibrium results from the nonharmonic interaction of a large number of particles following classical dynamics. For example, one can start a simulation with a uniform distribution of velocities, and the system will naturally evolve to the Maxwell-Boltzmann distribution. Alternatively, a solid can be started at a temperature above its melting temperature, and the dynamics will result in melting, assuming that a critical liquid nucleus can be nucleated within the simulation time.

While powerful, MD is not without approximations. The two most fundamental ones have to do with the description of interatomic forces and the use of classical, not quantum, mechanics. The effect of these approximations is discussed in Sections 4.2.2, 4.2.3, and 5.1, below.

While atomic forces could be obtained directly by solving the Schrödinger equation, this is impractical for nearly all systems of interest. Thus, approximations are made to make the problem tractable. Density functional theory (DFT) provides a good balance between accuracy and computational cost and has been invaluable for understanding structures and reaction paths in several cases of interest, both in the gas phase (e.g., 58, 59) and for condensed phases (60). Unfortunately, its computational intensity restricts DFT simulations to approximately 1,000 atoms and relatively short timescales, limiting the types of processes that can be simulated. Interatomic potentials or force fields, which average out electrons and replace them with effective atomic interactions, represent an important alternative. Bond order potentials that describe model chemistry (the so-called AB system) were used in an early demonstration of the power of MD simulations to describe shock-induced chemistry (61, 62). The development of ReaxFF (63) enabled the description of realistic HE materials (64, 65). ReaxFF describes atomic interactions as the sum of various terms including covalent, van der Waals, and electrostatic interactions. Covalent interactions are based on the concept of partial bond orders, a many-body function of the atomic coordinates and types. Bond orders affect bond stretch, angle bending, torsions, and other terms. In addition, electrostatics are computed with environment-dependent charges calculated using electronegativity equalization (66). An intermediate method between DFT and force fields is total energy tight binding, which retains a quantum description of electrons but requires empirical parameterization (67, 68).

4.2. Simulating Shocks with Molecular Dynamics

Techniques used to model shock loading with MD can be grouped into two categories: nonequilibrium and equilibrium. The former is the simplest to set up and mimics experiments by explicitly

modeling a high-velocity impact. A common setup is to drive the target material into a stationary, rigid piston or momentum mirror, which generates a sustained shock. This technique is very powerful because no approximations are made regarding the shock propagation, nature of the shock front, timescales involved in loading, or shock state, beyond those implicit in MD. However, as discussed below, this approach is computationally intensive. To address this limitation, researchers have developed simulation techniques to take a sample to a desired shocked state controlling temperature and pressure, either to satisfy the Rankine–Hugoniot jump conditions (69) or to follow the Rayleigh line (70). Since there are no propagating shocks, the simulation can be run for long times and smaller simulation domains can be used (as small as 1,000 atoms). The following subsections present additional details about modeling shock waves and describe their pros and cons.

4.2.1. Nonequilibrium shock simulations. In nonequilibrium shock simulations, as in most experiments, the control variable is the particle or piston velocity. It is common to drive a target material toward a rigid wall described either with a momentum mirror or with a rigid and immobile section of the material. The simulation starts by adding the desired impact velocity to all the atoms in the target over their equilibrium thermal velocities antiparallel to the shock direction (toward the piston). The dynamics of the system is then standard, adiabatic MD. This is called a reverse-ballistic configuration (71) and is equivalent to a standard flyer plate approach (ballistic) via Galilean invariance. Such shock simulations are easy to set up, as they use adiabatic MD, with no need for special boundary conditions, thermostats to control temperature, or barostats to control system pressure. More importantly, they make no approximations regarding the shock front, how quickly each section of the material is loaded, or the loading path. This technique has provided a view into materials processes at extreme conditions with unparalleled detail, ranging from shock-induced phase transformations in polycrystalline iron (72, 73) and plasticity in tantalum (74) and nanocrystalline copper (75) to shock compaction of porous materials (76), the initial shock-induced chemical reaction in 1,3,5-trinitro-1,3,5-triazinane (RDX) (64), and the transition from shock to deflagration in high explosives (3). Massive direct shock simulations in HE materials have improved our understanding of how energy localization (hot spots) leads to the initiation of reactive materials (3, 77). These methods have also been invaluable for shock-induced phase transformations (78, 79) and compaction of granular reactive materials (76, 80).

While very powerful, this type of simulation is computationally intensive, and only relatively short times can be achieved. This is because when the shock reaches the free surface of the target, opposite to the impact plane, a rarefaction wave starts propagating back into the system, changing the thermodynamic state. Thus, doubling the simulation time requires (in addition to running longer) doubling the system size, which quadruples the simulation cost. This is important when the shock-induced response is relatively slow, as is the case with chemistry. Therefore, processes like the shock-to-detonation transition and steady detonation propagation cannot be simulated using MD for realistic systems. Model materials have been designed to enable atomic- or molecular-level descriptions of detonation initiation (81, 82).

One approach to extending simulation timescales is to prevent the rarefaction from occurring by using shock front–absorbing boundary conditions (SFABCs) (78, 83). In the past, this was achieved via two methods: either placing a second piston at the downstream surface, preventing surface expansion and locking the system at shock density (83), or using symmetric shocks with periodic boundaries, such that the two shock waves annihilate each other at the downstream surfaces (78). These methods can be useful for further investigation of how the shocked system evolves in time. The use of SFABCs does not increase computational cost but can be difficult to implement.

A more recent method that improves upon SFABCs is the shock trapping internal boundary (STIB) method (84). In traditional SFABCs, it is nearly impossible to consistently absorb nonplanar shock waves, nearly always requiring a homogeneous sample. By creating rigid-body regions in between waves and an area of interest, the reflection and rarefaction waves are trapped outside the area of interest. This is increasingly useful for simulations of hot spots via the shock collapse of a void, which creates numerous waves of differing speeds. The STIBs can trap all waves away from the hot spot, and all material beyond the STIBs can be removed, decreasing computational cost significantly.

4.2.2. Equilibrium shock simulations. Even with recent computational advances, studying phenomena on timescales longer than the shock passage time is challenging, prompting the development of equilibrium shock approximation techniques. These methods model the shock as a homogeneous compression of the entire system. Two widely known methods, the Hugoniostat (69, 85) and the multiscale shock technique (MSST) (70, 86), are able to mimic the shock compression of a sample without the need for an impact simulation or a shock front. These simulations take the simulation cell to a shock state homogeneously and are used on fully periodic systems. Thus, the simulation time is independent of system size. While the two methods work in different ways, both conserve the jump conditions and can replicate some results of direct shock simulations. The development of these techniques has allowed for closer study of shock-induced chemistry (87), plasticity, and phase transformations (88). Additionally, using either method, running numerous shocks in HE materials at varying strengths (reactive regime) enables mapping of the reactive Hugoniot, providing the capability to predict detonation velocity and the CJ state of the material. These methods can also enable the use of a quantum thermal bath (89) to control energy flow, which distributes the total energy according to the Bose–Einstein (as opposed to the classical Maxwell–Boltzmann) distribution, providing a more accurate description of specific heat and incorporating zero-point energy (90, 91).

While MSST and the Hugoniostat are not without limitations (see the next subsection), their computational expedience makes them attractive for characterizing, for example, the Hugoniot of materials. These techniques have also enabled the study of kinetically driven events, such as chemical reactions and phase transitions, on long timescales not accessible to direct shocks (88).

4.2.3. Nonequilibrium versus equilibrium simulations of shock interactions with defects. A series of papers (69, 70, 85) have shown that both the Hugoniostat and MSST can replicate the thermomechanical properties of the shock state in homogeneous materials. However, this may not hold true for heterogeneous, composite materials or materials with defects that can couple with the shock front. For the initiation of chemistry, we are interested in the shock-induced collapse of porosity and the resulting energy localization into hot spots. This subsection compares nonequilibrium MD and Hugoniostat simulations of shock-induced collapse of a cylindrical pore with a circular cross section. For relatively weak shocks ($u_p = 0.5$ km/s), pore collapse occurs following the passage of the shock, driven by the high compressive stress in the shocked material; this is the so-called viscoplastic regime. **Figure 7** shows that the shape of the pore during collapse and the associated temperature field are very similar between the two simulation techniques. However, stronger shocks result in a hydrodynamic collapse, in which the upstream side of the voids flows into the vacuum with speeds comparable to that of the shock front. Dissipation-associated plastic flow and the recompression of the expanding material lead to energy localization. In this case, the shock front is central to the process and the Hugoniostat predictions bear little resemblance to
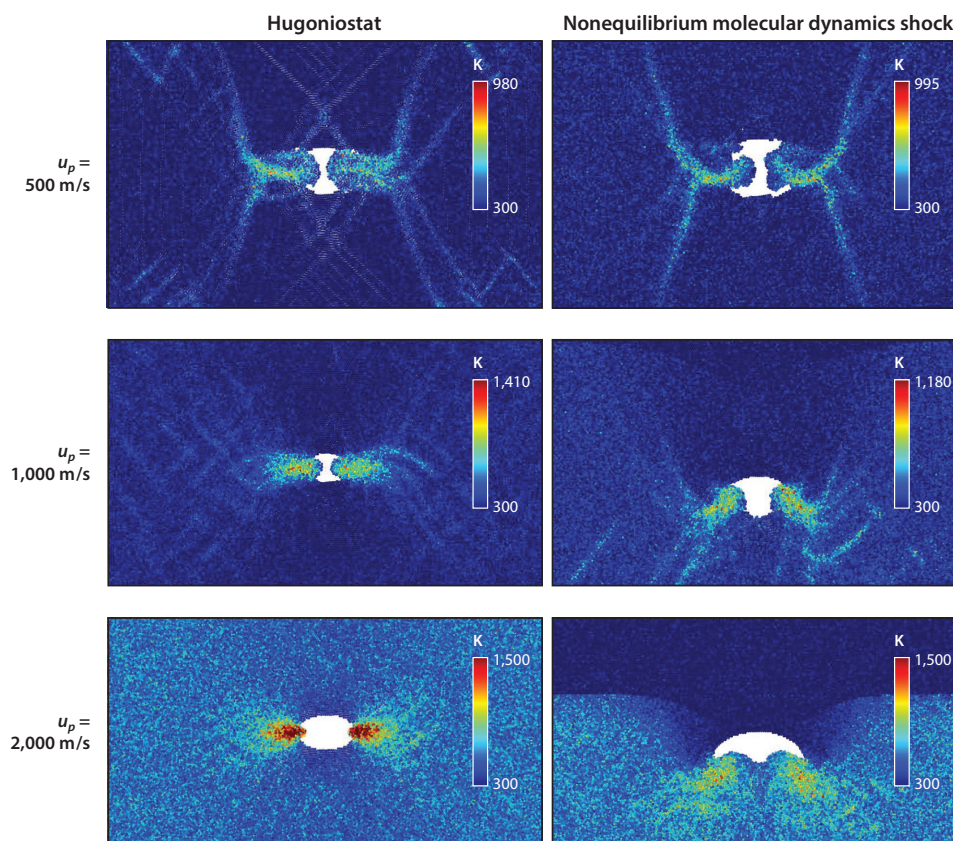
225

| | Hugoniostat | Nonequilibrium molecular dynamics shock |

Figure 7

Pore collapse response of HMX (1,3,5,7-tetranitro-1,3,5,7-tetrazoctane) under the equilibrium shock technique Hugoniostat and under shock compression (nonequilibrium molecular dynamics).

the explicit shock simulation, indicating that one should take care when using the Hugoniostat or MSST to model processes that involve strong coupling to the shock front.

5. TOWARD DETAILED CHEMISTRY AT EXTREME CONDITIONS

As discussed in Section 2.1.2, the initiation of chemistry and other thermally activated processes depends very strongly on microstructure, while other properties, like detonation velocity, are dominated by thermochemistry. This is common in materials science; for example, elastic constants are weakly dependent on microstructure, but strength and toughness are dominated by it. The quest to determine chemistry at extreme conditions can thus be divided into two classes of efforts. The first includes homogeneous, or microstructurally simple, materials overdriven to observe chemical reactions. These efforts are discussed in Section 5.1. The second class includes efforts to understand energy localization into hot spots and how these heterogeneities affect the initiation of chemical reactions. A selection of these efforts are discussed in Section 5.2.

114   Hamilton et al.

226

5.1. Chemistry in Homogeneous Systems

Shock compression of a sufficient strength can incite rapid chemical reactions. Probing chemical reaction pathways is exceedingly difficult at extreme conditions. Thus, much of the early research on characterizing detailed chemical reactions in condensed systems at extreme conditions involved MD with tight binding, DFT, and reactive force fields. Manaa and collaborators (68) at Lawrence Livermore National Laboratory used tight binding to study the decomposition of HMX at conditions near the CJ point and extracted rates for the formation of key products. Early DFT-based MD simulations on NM showed intermolecular hydrogen transfer as the initial reaction, consistent with experimentally proposed mechanisms (60). Research on the initial chemistry in TATB provided insight into its insensitivity (92). Other tight-binding studies using MSST simulations led to the interesting observation of a semimetallic layer at the NM detonation front (93), as well as the ultrafast (10-ps completion) detonation of HN_3 (94). Complementing this research, the development of the reactive force field ReaxFF, and its parameterization for CHNO systems, enabled larger spatial scales and longer simulation times. This development led to the first nonequilibrium shocks in RDX (64), which showed ultrafast chemistry near the shock front as well as thermal decomposition at a wide range of temperatures (65).

At that time, it was impossible to experimentally validate the detailed chemistry predicted by this early research. However, simulations provided reasonable results, final populations consistent with experiments, and good agreement in terms of thermomechanics like equations of state and $u_s - u_p$ curves. A definite validation of these predictions can only be done with experiments capable of characterizing detailed chemistry. A major breakthrough involved ultrafast spectroscopy coupled with laser-driven shocks, resulting in the first picture of chemical reactions at extreme conditions (51).

Moore, McGrane, and collaborators pioneered the use of ultrafast spectroscopy coupled to laser-driven shocks to assess chemistry at extreme conditions (50). They found a loss of absorption associated with the NO_2 group when PVN films were shocked to 18 GPa (51). Remarkably, the reactions were observed in timescales of tens of picoseconds (**Figure 8a**). Reactive MD simulations (87) using ReaxFF showed remarkable similarities in the threshold shock strength required for ultrafast chemistry, in the decomposition timescales, and in the chemical path involving NO_2 (**Figure 8b**).

This early experimental research involved relatively narrow spectral ranges, enough to observe single peaks, but progress over the last decade has increased the spectral range accessible via single-shot spectroscopy (95). This increase in spectral range is depicted in **Figure 8c**, which shows results for NM shocked to 18–20 GPa. The plot indicates changes in transmission, highlighting absorption in spectral regions not present in unreacted NM. The changes in transmission mark the formation of intermediate species and/or products. Reactive MD simulations (96) (**Figure 8d**) show similar features. The simulations enable a detailed analysis of the molecular processes involved during decomposition and subsequent reactions as well as their effect on the evolving spectra. However, the results for PVN and NM indicate differences between the experiments and simulations in the frequencies associated with the various molecular processes and in the overall shape of the spectra.

Most recently, experiments on shocked 2,2-bis[(nitrooxy)methyl]propane-1,3-diyl dinitrate (PETN) (**Figure 8e**) captured the entire spectral range of interest, allowing the researchers to assess possible decomposition mechanisms (52). The experiments ruled out previously proposed initial decomposition mechanisms like HNO_3 formation, HONO elimination, and NO_3 scission (52). MD Hugoniostat simulations (**Figure 8f**) show approximate agreement on the threshold for initiation of chemistry in 100-ps timescales, but the details of the spectra evolution do not

227

EXPERIMENTS
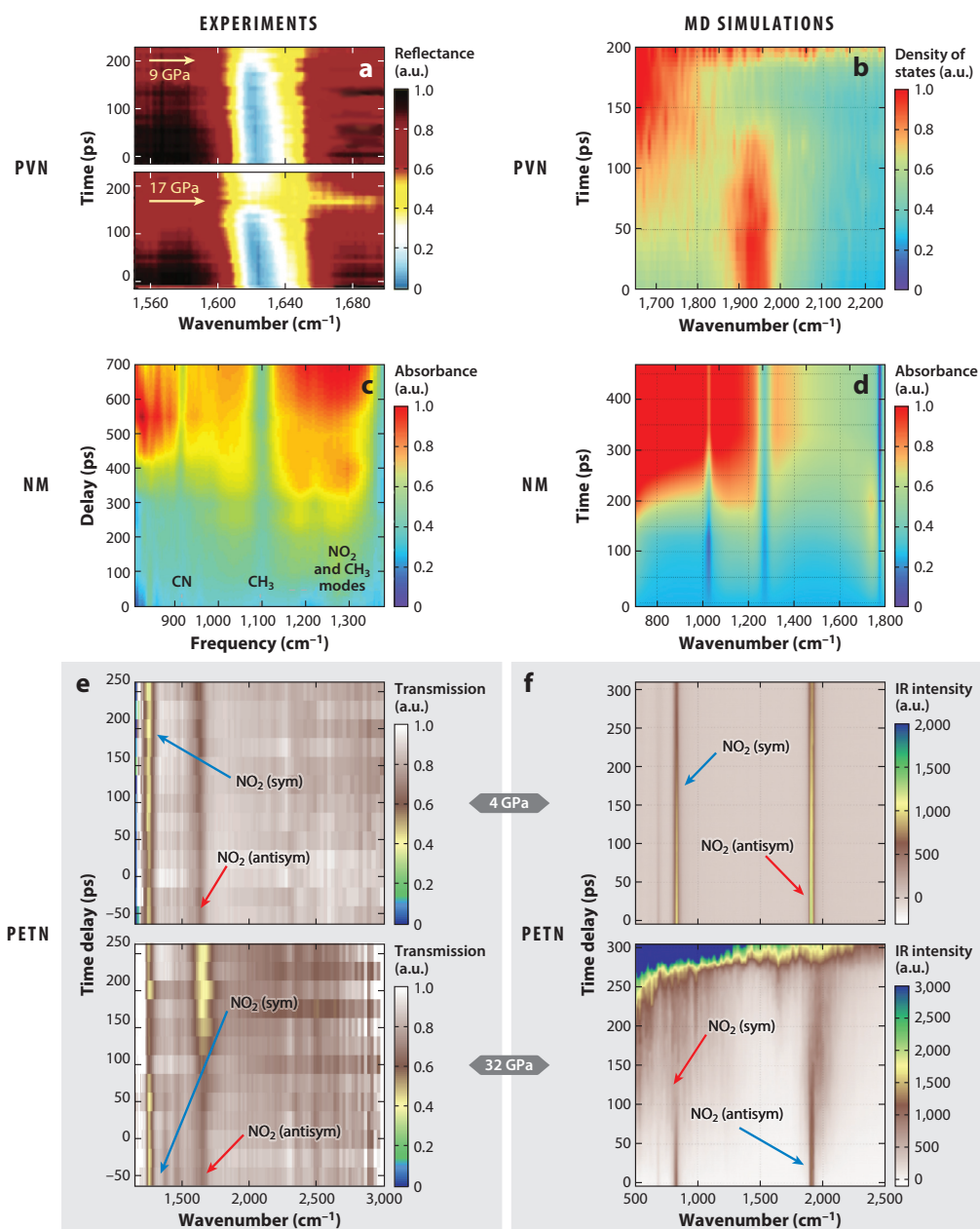
MD SIMULATIONS

(*Caption appears on following page*)

Figure 8 (*Figure appears on preceding page*)

Comparison of IR spectra evolution under shock loading for various high-energy-density materials between (*a,c,e*) experiments and (*b,d,f*) MD simulations. (*a*) PVN films shocked to 18 GPa. (*b*) Simulated PVN shocked to 18 GPa. (*c*) NM shocked to 18–20 GPa. (*d*) Simulated NM shocked to 18 GPa. (*e*) PETN shocked to 4 and 32 GPa. (*f*) Simulated PETN shocked to 4 and 32 GPa. The red areas represent absorption in spectral regions not present in unreacted NM. Abbreviations: MD, molecular dynamics; NM, nitromethane; PETN, 2,2-bis[(nitrooxy)methyl]propane-1,3-diyl dinitrate; PVN, poly(vinyl nitrate). Panel *a* adapted with permission from Reference 51, copyright 2004 American Chemical Society. Panel *b* adapted with permission from Reference 87, copyright 2017 American Chemical Society. Panel *c* adapted with permission from Reference 95; experimental image courtesy of Shawn McGrane and Michael Powell. Panel *d* adapted with permission from Reference 96, copyright 2019 American Chemical Society. Panels *e* and *f* adapted with permission from Reference 52, copyright 2020 American Chemical Society.

match what is observed in experiments. MD simulations suggest NO and NO_2 as dominant mechanisms, but NO is inconsistent with results from experiments, while the formation of NO_2 remains indeterminate.

In addition to characterizing the chemistry, shock experiments on NM have measured visible transient absorption spectra and interface particle and shock velocities by using ultrafast dynamic ellipsometry. This technique resulted in the direct measurement of the volume-expanding reaction, the reacted Hugoniot curve (33). A similar transition to the reacted Hugoniot was observed in ReaxFF with similarly predicted particle velocities (96) (**Figure 9**). Additionally, calculated sound speeds at zero piston velocity, as well as CJ pressure and detonation velocities extracted from Crussard curves, were within the uncertainty ranges of other experiments (32). These dynamic ellipsometry experiments have also been applied to shock-induced, volume-decreasing reactions and shock-induced polymerization of liquids (55).

These methodologies have also been applied to chemistry related to the formation of biological compounds such as amino acids. Theoretical studies of the shock compression and postimpact relaxation of comet ice demonstrated the synthesis of C–N oligomers that break apart and react to form glycine-containing complexes upon shock relief (97). Consistent with ab initio simulations, experimental shock studies of comet-like ice resulted in the formation of several amino acids (98). More recent research has investigated the resulting chemistry from high-pressure
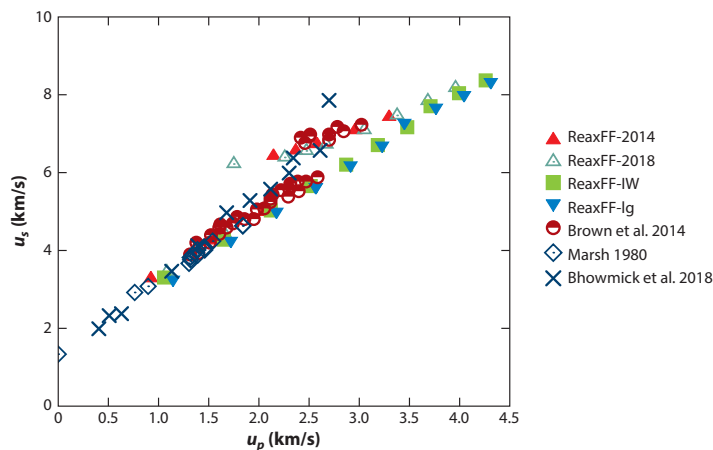

Figure 9

$u_s - u_p$ data for nitromethane experiments and simulations at various shock pressures. Figure adapted with permission from Reference 96, copyright 2019 American Chemical Society.

and high-temperature conditions on a water–glycine solution that resulted in the formation of nitrogen-containing polycyclic aromatic hydrocarbons, important prebiotic precursors (99).

In summary, research over the last two decades has, for the first time, enabled one-to-one comparison between experiments and atomistic simulations capable of shedding light on chemistry under extreme conditions. The combination of these two methods will be key to determining detailed chemistry at extreme conditions. Even after all the challenges associated with shock generation and ultrafast broadband spectroscopy are solved, mapping spectral features to molecular structures will be challenging for reacting systems at high temperatures and pressures. Thus, reactive MD simulations are needed to solve this challenge. Recent research indicates that state-of-the-art atomistic simulation methods describe thermomechanics and chemical kinetics rather accurately, but additional work is needed to capture detailed chemistry. Reactive MD simulations make two fundamental approximations that should be carefully studied. The first is the accuracy of the method used to compute forces, as force fields, tight binding, and even DFT make approximations that can affect predictions. Recent research on machine learning of reactive interatomic potentials may approach the required accuracy and enable quantitative comparisons with experiments (100). The second fundamental approximation in MD, the use of classical (rather than quantum) dynamics, has attracted far less attention. As recent publications have shown, a classical distribution of energy (which leads to a specific heat approximately three times too high for molecular materials) and the lack of zero-point energy can have a strong effect on the shock-induced chemistry (90, 91). The lack of quantum ionic dynamics effects also affects the calculation of IR spectra (see the sidebar titled Comparing Classical and IR Spectra). Research focused on incorporating quantum effects on MD simulations of chemistry at extreme conditions would be of great importance to the field.

5.2. Hot Spots

While the homogeneous rise in temperature and pressure caused by shock waves is capable of initiating chemistry, as discussed in Section 5.1, chemical reactions, and even detonations, are observed for relatively weak shocks where homogeneous heating would not result in appreciable chemistry. This is because the energy deposited by the shock is often not evenly distributed throughout the material. Energy localization results in hot spots with temperatures well above the average value which are conducive to chemical reactions. The importance of hot spots in the shock initiation of chemistry as well as of the shock-to-detonation transition and detonation failure in heterogeneous HE materials is well established (101).

COMPARING CLASSICAL AND IR SPECTRA

Molecular vibrations can exist on quantized energy levels, populated according to the Bose–Einstein distribution, and IR spectroscopy measures photon processes that result in transition between allowed states. For harmonic oscillators, the energy difference between states is associated with the characteristic frequency $\hbar\omega$. In reality, anharmonicities result in slightly different energy differences, and IR spectra at extreme conditions include multiple peaks associated with each mode. In MD simulations, which are inherently classical and therefore obey Maxwell–Boltzmann statistics, the current approach for obtaining IR spectra is to compute the Fourier transform of the charge–velocity autocorrelation function (128). This nonquantized, nondiscrete dynamics results in a broad peak enveloping all the available modes (as opposed to a series of sharp peaks). Thus, the nature of the classical and quantum spectra should be taken into consideration when comparing experimental and MD results.

A variety of processes lead to energy localization in shocked solids (102), including plastic deformation via dislocation slip or shear bands (103), crack propagation (104, 105), interfacial friction, and collapse of porosity (106). The reactivity of a hot spot, and whether it will transform into a deflagration wave or quench, depends on both its temperature and its size (107). This is because thermal transport and initial endothermic chemical reactions present in most HE materials tend to quench the hot spot before exothermic reactions can generate energy and start a self-sustaining reaction wave. Smaller hot spots cool down faster and, consequently, require higher initial temperatures to become critical. Thus, predictive models capable of capturing the shock-to-deflagration and shock-to-detonation transitions require knowledge of temperature and size (or, better, the temperature field). The significant challenges involved in the experimental determination of these quantities, given the fast timescales (subnanosecond) and small length scales (from tens of nanometers to micrometers), has hindered the development of predictive models and understanding of hot-spot formation and criticality. Only recently have experiments begun to provide quantitative information about hot-spot temperatures, and molecular simulations have now captured the phenomena of hot-spot formation and reactivity using realistic models.

Significant research has been done on shear band formation and chemistry. Shock simulations in single-crystal RDX samples showed significant shear banding (83, 103) and associated heating. These shear bands have a relatively slow rise time, requiring SFABCs to fully explore their thermodynamics. Kroonblawd & Fried (108) explored the chemical reactivity of sheared TATB at detonation conditions. They found that the molecular disorder associated with shear banding can significantly lower the activation barrier for chemistry and lead to potentially order-of-magnitude-faster local chemistry. However, it has been well established that pore collapse is the dominant mechanism in the initiation of heterogeneous HE materials; this topic is the focus of the remainder of this section.

The importance of porosity for shock initiation of chemistry has been established by the desensitization of materials observed following their compression, via either weak shocks or static means, which collapses porosity without initiating chemistry (4, 109). Additionally, pores created via microbeads and microballoons in gelled NM demonstrate that multiple smaller pores are more efficient than a few large ones, and that balloons (pores) are more efficient at localizing energy than discontinuities (beads) (110).

5.2.1. Mechanical formation of hot spots.

The mechanisms underlying shock-induced pore collapse depend on shock strength and pore size and geometry. At low shock strength, viscoplastic deformation driven by pressure is the dominant process (111). This collapse occurs following the passage of the shock front and is relatively slow. For stronger shocks, a hydrodynamic regime is observed. When the leading shock front reaches the pore, the upstream surface expands into the pore and is recompressed as it collides with the downstream surface (112). MD simulations have provided insight into these processes and resulted in simple models to assess the maximum expected heating based on these processes (77). As mentioned above, measuring hot-spot temperatures is challenging, but recent research is shedding light on this important process.

Pyrometry with nanosecond time resolution is providing information about hot spots under conditions of interest for shock initiation. In a series of studies, Bassett, Dlott, and colleagues (23, 113) used optical pyrometry on laser-driven shocks to assess how chemistry and microstructure affect hot-spot formation. They found temperatures in the 4,000–7,000 K range for a variety of HE materials. Interestingly, PETN-based materials with microporosity resulted in temperatures around 6,000 K, whereas pressed systems with only nanoscale pores resulted in lower temperatures of approximately 4,000 K (23). The inclusion of various gases as well as shock under vacuum demonstrated the importance of gas compression in achieving high temperatures well above
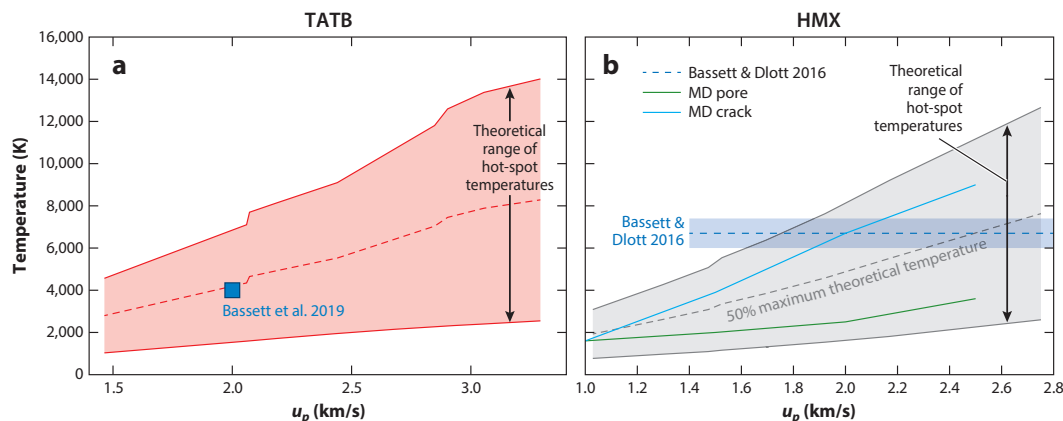
Figure 10

A version of **Figure 5** showing a band of possible hot-spot temperatures for (*a*) TATB and (*b*) HMX, overlaid with experimental and theoretical hot-spot temperature measurements from References 113, 116, 117. The cyan and green lines in panel *b* show the predictions by the MD simulations. Abbreviations: HMX, 1,3,5,7-tetranitro-1,3,5,7-tetrazoctane; MD, molecular dynamics; TATB, 1,3,5-triamino-2,4,6-trinitrobenzene.

4,000 K (23). As indicated by MD simulations, this gas can be composed of jetted HE material. The temporal resolution of these experiments does not enable separation between the thermomechanical formation of the hot spot and the possible additional heating due to chemical reactions, but experiments on inert molecular crystals of sucrose show similar temperatures to PETN. However, shocked SiO_2 showed almost no early time history hot spots (23).

As discussed above, these temperatures are significantly higher than those predicted by Equation 4 (**Figure 5**), as expected due to the role of hot spots. More surprising is that the experimental values are also higher than those in void-collapse simulations in RDX (2,000 K before chemistry and 4,000 K after) (3), PETN (2,000 K before chemistry and 4,000 K after) (114), and 1,3,5-trinitro-2-[2-(2,4,6-trinitrophenyl)ethenyl]benzene (HNS) (1,500 K before and 3,000 K after) (115).

To begin to understand this discrepancy, we can turn to the model derived by Holian et al. (77) that provides an expression for the maximum temperature expected following the jetting/vaporization and recompression of the expanding gas. The authors predicted the maximum temperature to be (77)

$$\triangle T_{max} = \frac{m}{k_B D} u_s u_p, \qquad 9.$$

where k_B is the Boltzmann constant, D is dimensionality, and m is mass. This number for most HE materials is well over 4,000 K. **Figure 10** shows the band of possible temperatures from bulk values (not hot spots) obtained using Equation 4 to the maximum possible hot-spot temperature predicted by Equation 9. Experimental and computational values for hot-spot temperatures are overlaid, showing that cylindrical pore collapse simulations do not approach the maximum value or the experimental values (113).

Motivated by the geometrical simplicity of pores simulated via MD (often cylindrical with circular cross sections), Li et al. (116) studied pore collapse with various shapes in an effort to explain the disparities in temperature between MD simulations and pyrometry experiments. Interestingly, crack-like voids (diamonds with a 5:1 aspect ratio) resulted in larger and hotter hot spots than

did cylindrical voids with the same length (cylinder volume > crack volume). The simulations revealed that the crack shape resulted in higher shock focusing, which in turn led to vaporization and jetting. The low densities achieved by the expanding material (significantly lower than in the hydrodynamic regime observed for cylindrical pores) resulted in additional P–V work and higher temperatures, above 7,000 K. These resulting temperatures from the cracks confirm both the scaling laws derived by Holian et al. (77) and the high temperature readings from experiments (113). **Figure 10b** depicts the predictions by the MD simulations in HMX. While discrepancies persist between simulations and experiments and uncertainties in both techniques are not fully understood, these more direct comparisons are providing significant insight into the formation of hot spots.

To date, hot spots have been characterized solely by their temperature fields, but recent research has challenged these assumptions. Nonreactive MD simulations on TATB showed that within the hot spot the local rise in potential energy was higher than what could be surmised from the kinetic energy (temperature) (84). Perhaps more importantly, the energy localization as potential energy was more persistent than the temperature localization. The simulations revealed that the origin of the potential energy hot spot was largely intramolecular deformations. This means that this stored energy is readily available for chemical reactions. Mounting information indicates that the reactivity of hot spots is more complex than a simple increase in temperature.

5.2.2. Hot-spot reactivity. Once a hot spot is formed, the next question to address is whether it is potent enough to turn into a deflagration wave. The constructive interaction of deflagration waves can then cause a detonation (118). The traditional view of hot-spot evolution is that as soon as it forms it starts to cool down as a result of thermal diffusion and the first, endothermic chemical steps (important for safety). In order to become critical, a hot spot needs to stay hot enough for a long enough time to allow the exothermic reactions to kick in, increase its temperature, diffuse this heat outward, and generate a self-sustaining reaction wave.

Tarver et al. (107) pioneered the modeling of hot spots by combining a reduced-order chemical kinetics model derived from experiments with thermal transport. The authors quantified how the critical temperature decreases with increasing hot-spot size for HMX and TATB. More recently, Wood et al. (3) used large-scale reactive MD simulations to model hot-spot formation, by shock-induced void collapse in RDX, and its subsequent evolution. For shocks with particle velocities of 2 km/s, the simulations revealed that 20-nm-diameter voids resulted in hot spots that subsequently quenched. In contrast, a 40-nm-diameter void resulted in a larger hot spot, which turned into self-sustaining deflagration waves (**Figure 11**). This research and that by Shan et al. (114) at Sandia National Laboratories provided the first full atomic-level picture of the shock-to-deflagration transition.

Interestingly, the collapse of the 40-nm-diameter pore resulted in ultrafast, multistep chemistry (**Figure 11c–e**) that occurs while the system is away from local equilibrium, with molecular centers of mass significantly hotter than intramolecular modes (**Figure 11a,b**). Such short timescales indicate that nonstatistical chemistry can play a role in the initiation of nanoscale hot spots. The fast formation of final, exothermic products prevents the hot spot from cooling down. Following these early events, the core of the hot spot fully reacts, reaching a temperature of ∼4,000 K (see the row labeled 32 ps in **Figure 11a,b,e**). Finally, a deflagration wave forms with a front speed of up to 250 m/s, which is comparable to the values reported for HMX in a diamond-anvil cell at similar pressures (119). To assess the possible role of the initial nonequilibrium state and the ultrafast loading, Wood et al. (3) simulated hot spots that were nominally identical but produced under quasi-equilibrium conditions. These thermal hot spots were created by use of a thermostat to match the dynamical ones in thermodynamic state (pressure and temperature field) and

233

(*a*) Molecular centers of mass temperatures (T_{com}), (*b*) molecular vibrational temperatures (T_{vib}), and population fractions for (*c*) RDX, (*d*) intermediate species, and (*e*) final product gases at different times during the development process of the hot spot. Abbreviation: RDX, 1,3,5-trinitro-1,3,5-triazinane. Figure adapted with permission from Reference 3, copyright 2015 American Chemical Society.
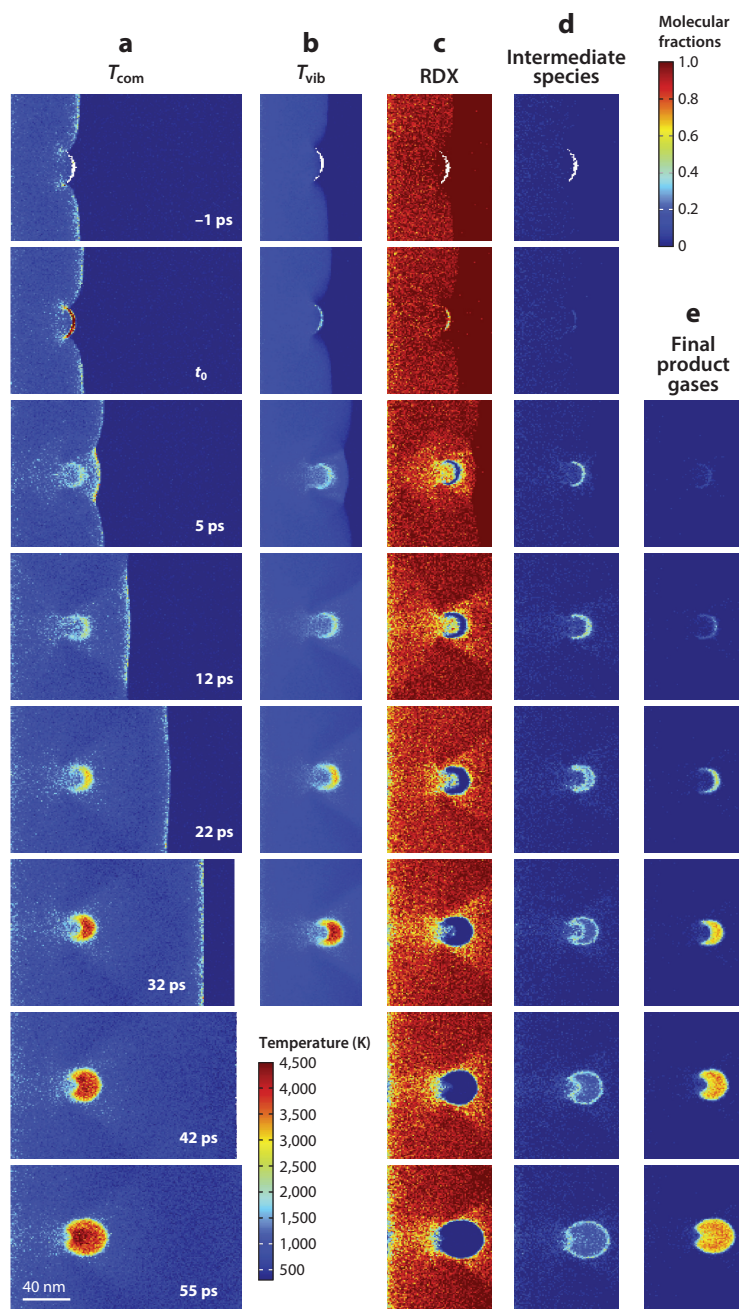
size. Interestingly, the comparison indicated that the formation of intermediates and products was much slower in the thermal hot spots than in the dynamic ones. Thus, the authors concluded that hot-spot reactivity is path dependent. Several mechanisms were put forward as possible explanations for this observation: (*a*) mechanochemistry, that is, the high-velocity impact that significantly strains molecules and lowers barriers for chemistry; (*b*) amorphization during the pore collapse, resulting in large driving forces for decomposition; and (*c*) nonstatistical chemistry near the shock front and impact surfaces, where the various degrees of freedom in the material are not in local thermal equilibrium. A state of fast collisions between relatively cold molecules could accelerate certain chemical processes. Shan et al. (114) also observed the early formation of product gases like H_2O and N_2 within 10 ps of the shock-induced void collapse of PETN in ReaxFF simulations. They concluded that the hot spot formed from the conversion of large collisional velocities into intramolecular energy (mechanochemistry), which then rapidly developed into gaseous products.

With the goal of testing one of the hypotheses put forward in Reference 3, Sakano et al. (120) studied how molecular structure affects chemical reactions kinetics in RDX, both in the case of homogeneous decomposition and for hot spots. They compared reactive MD simulations on crystalline and amorphous RDX and found that the reactivity in the amorphous systems was slightly faster than in their crystalline counterparts. A detailed analysis of their simulations indicated that the difference between amorphous and crystalline RDX response could be explained by fast initial endothermic processes associated with the loss of crystalline order. This difference also manifested in the amorphous hot spots exhibiting slightly lower critical temperatures, that is, the lowest temperature required to result in a deflagration wave. However, the difference in reactivity was not enough to account for the considerable increase in reactivity observed in the dynamic hot spot. Thus, the mechanics of pore collapse is likely to play a role in reactivity, at least for nanoscale pores that require high temperatures.

The mechanical loads during collapse are rather complex. As discussed in Section 5.2.1, pore geometry affects hot-spot temperatures, and shape also affects the types of mechanical loads experienced by the material. Flat sections of a pore exhibit rather uniaxial expansion and compression, while the side walls experience significant shear during collapse. Islam & Strachan (121) used a one-dimensional planar gap to independently control the uniaxial (compressive) and shear components of dynamical hot spots in RDX. They found that the addition of shear reduces the critical impact speed required for a hot spot to become critical. Interestingly, the addition of a shear component to the load affected the decomposition path, providing strong evidence of mechanochemistry. Further confirmation of the importance of mechanochemistry has been observed in simulations of shear-induced mechanochemical events in amorphous glycine that resulted in the formation of water, structural analogs to glycine, heterocyclic molecules, large oligomers, and polypeptides (122).

Other studies have looked into the effects of chemistry as a result of hot-spot formation in similar HE materials. Zhou et al. (123) studied the development of hot spots in HMX following an induced thermal shock wave, where the temperature in the core was kept at 3,000 K and the temperature of the bulk region was held under adiabatic conditions. Such large temperature gradients resulted in a thermal shock wave that propagated back and forth across the two regions before dying out. Systems under compression resulted in faster thermal transport and early chemistry via N–NO$_2$ dissociation. Reaction burn fronts were calculated to be around 70 m/s, very similar to the values obtained for RDX (120). Joshi et al. (124) studied the interface of RDX and product gases, which occurs at the reaction front of hot spots, and its relationship to the vibrational up-pumping theory proposed by Dlott & Fayer (24). They observed intermolecular energy transfer between the extremely hot gases and the unreacted RDX, which excited the C–H, C–N, and N–N vibrational modes. Very little change was observed in the chemical decomposition mechanism

235

when quantum nuclear effects using the quantum thermal bath were included. However, the authors noted a change in which mode was excited first among N–N, C–H, and C–N, depending on input temperature. This research implies that nonequilibrium states and temperature gradients can activate different chemical pathways, leading to slower or faster product formation. This is especially important when considering the development of hot spots under dynamic conditions.

Progress is also occurring in the experimental characterization of hot spots and heterogeneities. The optical pyrometry experiments discussed above provide information about only the maximum temperature in the system and the volume fraction of the hottest region as a function of time with no spatial information. The addition of microscopy and high-speed cameras has enabled imaging of hot spots with a spatial resolution of ∼2 μm and a temporal resolution of a few nanoseconds (48). Microscopy on shocked NM revealed a heterogeneous temperature distribution, indicating the presence of hot spots in a liquid material. The origin of this spatial localization is different from those discussed above in solids; flow instabilities, heterogeneous chemistry, and impurities can all contribute to nonhomogeneous processes. Similar research on a sample consisting of an HMX particle embedded in polymer correlated hot spots with microstructural features and defects, most notably energy localization around a large void and at interfaces. In addition to microscopy, phase-contrast imaging using synchrotron X-rays has recently enabled the observation of dynamical pore collapse and cracking induced by dynamical loading (125, 126). These experimental tools have the potential to quantify the potency of various microstructural features, defects, and processes in generating critical hot spots and will provide invaluable information for mesoscale modeling efforts (115, 126, 127).

This body of work clearly indicates that the picture of shock loading taking the material to a state given by the Rankine–Hugoniot jump conditions applies only to long-term phenomena, after the significant heterogeneities that originate from the coupling of the shock wave with microstructure and defects have been averaged out. These initial heterogeneities are critical in the initiation of chemistry and subsequent processes like detonation. The presence of hot spots, and heterogeneous shock conditions in general, could affect the shock-induced synthesis of amino acids and other important prebiotic molecules. The complex microstructure and porosity of comets, meteorites, and the planetary surfaces they impact can be expected to result in significant energy localization into hot spots that can affect both the decomposition of carbon-containing compounds and the synthesis of new molecules of biological relevance.

6. SUMMARY AND OUTLOOK

Progress in theory, simulations, and experiments over the last two decades opens the very real opportunity to develop definite answers to long-standing challenges in the field of chemistry at extreme conditions. Laser-driven shocks in small samples have been demonstrated to reproduce larger-scale gas gun experiments, and IR and visible spectroscopy, as well as microscopy, are providing a picture of shock-induced materials' response with exquisite resolution. These analyses range from measuring the temperature of hot spots and spatially visualizing them to performing IR spectroscopy with wide spectral ranges capable of capturing the majority of the processes of interest. While these experiments are not without limitations, they can be complemented by simulations that are becoming increasingly capable of modeling realistic materials.

We believe the combination of ultrafast IR spectroscopy and reactive MD simulations will provide a detailed description of chemical reactions at extreme conditions. Progress is required to improve the accuracy of atomistic simulations to best match the experimental observables and to provide a path to mapping spectral features to molecular processes. Importantly, these tools

should be capable of quantifying possible nonstatistical, path-dependent chemistry predicted by simulations. In addition, hot-spot characterization will be critical for developing the predictive understanding we seek. Experiments can now characterize the formation and temperatures associated with energy localization, and this information is being used for model validation. In turn, the models will be critical to help interpret experiments and resolve processes beyond the reach of experiments. These efforts are poised to provide answers to long-standing challenges at the intersection of shock physics, materials science, and chemistry as well as to enable predictive understanding of chemistry at extreme conditions.

DISCLOSURE STATEMENT

The authors are not aware of any affiliations, memberships, funding, or financial holdings that might be perceived as affecting the objectivity of this review.

LITERATURE CITED

1. Levitas VI, Ravelo R. 2012. Virtual melting as a new mechanism of stress relaxation under high strain rate loading. *PNAS* 109:13204–7
2. De Carli PS, Milton DJ. 1965. Stishovite: synthesis by shock wave. *Science* 147:144–45
3. Wood MA, Cherukara MJ, Kober EM, Strachan A. 2015. Ultrafast chemistry under nonequilibrium conditions and the shock to deflagration transition at the nanoscale. *J. Phys. Chem. C* 119:22008–15
4. Campbell A, Davis W, Ramsay J, Travis J. 1961. Shock initiation of solid explosives. *Phys. Fluids* 4:511–21
5. Fickett W, Davis WC. 2000. *Detonation: Theory and Experiment*. Mineola, NY: Dover
6. Miller SL. 1953. A production of amino acids under possible primitive earth conditions. *Science* 117:528–29
7. Bar-Nun A, Bar-Nun N, Bauer S, Sagan C. 1970. Shock synthesis of amino acids in simulated primitive environments. *Science* 168:470–72
8. Barak I, Bar-Nun A. 1975. The mechanisms of amino acids synthesis by high temperature shock-waves. *Orig. Life* 6:483–506
9. Berens PH, Mackay DH, White GM, Wilson KR. 1983. Thermodynamics and quantum corrections from molecular dynamics for liquid water. *J. Chem. Phys.* 79:2375–89
10. Germann TC, Holian BL, Lomdahl PS, Ravelo R. 2000. Orientation dependence in molecular dynamics simulations of shocked single crystals. *Phys. Rev. Lett.* 84:5351–54
11. Dick RD. 1970. Shock wave compression of benzene, carbon disulfide, carbon tetrachloride, and liquid nitrogen. *J. Chem. Phys.* 52:6021–32
12. Dattelbaum DM, Sheffield SA, Coe JD. 2017. Shock-driven chemistry and reactive wave dynamics in liquid benzene. *AIP Conf. Proc.* 1793:040020
13. Banlusan K, Strachan A. 2016. Shockwave energy dissipation in metal–organic framework MOF-5. *J. Phys. Chem. C* 120:12463–71
14. Antillon E, Banlusan K, Strachan A. 2014. Coarse grain model for coupled thermo-mechano-chemical processes and its application to pressure-induced endothermic chemical reactions. *Model. Simul. Mater. Sci. Eng.* 22:025027

15. Antillon E, Strachan A. 2015. Mesoscale simulations of shockwave energy dissipation via chemical reactions. *J. Chem. Phys.* 142:084108

16. Strachan A, Holian BL. 2005. Energy exchange between mesoparticles and their internal degrees of freedom. *Phys. Rev. Lett.* 94:014301

17. Lin KH, Holian BL, Germann TC, Strachan A. 2014. Mesodynamics with implicit degrees of freedom. *J. Chem. Phys.* 141:064107

18. Bdzil JB, Stewart DS. 2007. The dynamics of detonation in explosive systems. *Annu. Rev. Fluid Mech.* 39:263–92

19. Zaug JM, Austin RA, Armstrong MR, Crowhurst JC, Goldman N, et al. 2018. Ultrafast dynamic response of single-crystal β-HMX (octahydro-1,3,5,7-tetranitro-1,3,5,7-tetrazocine). *J. Appl. Phys.* 123:205902

20. Marshall M, Fernandez-Pañella A, Myers T, Eggert J, Erskine D, et al. 2020. Shock hugoniot measurements of single-crystal 1,3,5-triamino-2,4,6-trinitrobenzene (TATB) compressed to 83 GPa. *J. Appl. Phys.* 127:185901

21. Sewell TD, Menikoff R. 2004. Complete equation of state for β-HMX and implications for initiation. *AIP Conf. Proc.* 706:157–62

22. Kroonblawd MP, Sewell TD, Maillet JB. 2016. Characteristics of energy exchange between inter- and intramolecular degrees of freedom in crystalline 1,3,5-triamino-2,4,6-trinitrobenzene (TATB) with implications for coarse-grained simulations of shock waves in polyatomic molecular crystals. *J. Chem. Phys.* 144:064501

23. Bassett WP, Johnson BP, Neelakantan NK, Suslick KS, Dlott DD. 2017. Shock initiation of explosives: high temperature hot spots explained. *Appl. Phys. Lett.* 111:061902

24. Dlott DD, Fayer MD. 1990. Shocked molecular solids: vibrational up pumping, defect hot spot formation, and the onset of chemistry. *J. Chem. Phys.* 92:3798–812

25. Dlott DD. 1999. Ultrafast spectroscopy of shock waves in molecular materials. *Annu. Rev. Phys. Chem.* 50:251–78

26. Moore DS, McGrane SD, Funk DJ. 2007. Ultrashort laser shock dynamics. In *Shock Wave Science and Technology Reference Library*, Vol. 2: *Solids I*, ed. Y Horie, pp. 47–104. Berlin: Springer

27. Dlott DD. 2011. New developments in the physical chemistry of shock compression. *Annu. Rev. Phys. Chem.* 62:575–97

28. Swift DC, Niemczura JG, Paisley DL, Johnson RP, Luo SN, Tierney TE IV. 2005. Laser-launched flyer plates for shock physics experiments. *Rev. Sci. Instrum.* 76:093907

29. Veysset D, Maznev AA, Pezeril T, Kooi S, Nelson KA. 2016. Interferometric analysis of laser-driven cylindrically focusing shock waves in a thin liquid layer. *Sci. Rep.* 6:24

30. Lysne P, Hardesty D. 1973. Fundamental equation of state of liquid nitromethane to 100 kbar. *J. Chem. Phys.* 59:6512–23

31. Hardesty D. 1976. An investigation of the shock initiation of liquid nitromethane. *Combust. Flame* 27:229–51

32. Bhowmick M, Nissen EJ, Dlott DD. 2018. Detonation on a tabletop: nitromethane with high time and space resolution. *J. Appl. Phys.* 124:075901

33. Brown KE, McGrane SD, Bolme CA, Moore DS. 2014. Ultrafast chemical reactions in shocked nitromethane probed with dynamic ellipsometry and transient absorption spectroscopy. *J. Phys. Chem. A* 118:2559–67

34. Kritcher AL, Swift DC, Döppner T, Bachmann B, Benedict LX, et al. 2020. A measurement of the equation of state of carbon envelopes of white dwarfs. *Nature* 584:51–54

35. Waxer L, Maywar D, Kelly J, Kessler T, Kruschwitz B, et al. 2005. High-energy petawatt capability for the OMEGA laser. *Opt. Photonics News* 16:30–36

36. Miller GH, Moses EI, Wuest CR. 2004. The National Ignition Facility: enabling fusion ignition for the 21st century. *Nucl. Fusion* 44:S228

37. Knudson MD. 2012. Megaamps, megagauss, and megabars: Using the Sandia Z Machine to perform extreme material dynamics experiments. *AIP Conf. Proc.* 1426:35–42

38. Millot M, Dubrovinskaia N, Černok A, Blaha S, Dubrovinsky L, et al. 2015. Shock compression of stishovite and melting of silica at planetary interior conditions. *Science* 347:418–20

39. Rice M, McQueen RG, Walsh J. 1958. Compression of solids by strong shock waves. In *Solid State Physics*, Vol. 6: *Advances in Research and Applications*, ed. F Seitz, D Turnbull, pp. 1–63. Amsterdam: Elsevier

40. Barker LM. 2000. The development of the VISAR, and its use in shock compression science. *AIP Conf. Proc.* 505:11–18

41. Strand OT, Goosman D, Martinez C, Whitworth T, Kuhlow W. 2006. Compact system for high-speed velocimetry using heterodyne techniques. *Rev. Sci. Instrum.* 77:083108

42. Jensen B, Holtkamp D, Rigg P, Dolan D. 2007. Accuracy limits and window corrections for photon Doppler velocimetry. *J. Appl. Phys.* 101:013523

43. Barker L. 1972. Laser interferometry in shock-wave research. *Exp. Mech.* 12:209–15

44. Forbes JW. 2013. *Shock Wave Compression of Condensed Matter: A Primer*. New York: Springer Sci. Bus. Media

45. Walsh JM, Christian RH. 1955. Equation of state of metals from shock wave measurements. *Phys. Rev.* 97:1544–56

46. Bassett WP, Dlott DD. 2017. 32-channel pyrometer with high dynamic range for studies of shocked nanothermites. *AIP Conf. Proc.* 1793:060012

47. Pangilinan G, Gupta Y. 1997. Use of time-resolved Raman scattering to determine temperatures in shocked carbon tetrachloride. *J. Appl. Phys.* 81:6662–69

48. Bassett WP, Johnson BP, Salvati L III, Nissen EJ, Bhowmick M, Dlott DD. 2020. Shock initiation microscopy with high time and space resolution. *Propellants Explos. Pyrotech.* 45:223–35

49. Stavrou E, Bagge-Hansen M, Hammons JA, Nielsen MH, Steele BA, et al. 2020. Detonation-induced transformation of graphite to hexagonal diamond. *Phys. Rev. B* 102:104116

50. Moore DS, McGrane SD. 2003. Comparative infrared and Raman spectroscopy of energetic polymers. *J. Mol. Struct.* 661:561–66

51. McGrane S, Moore D, Funk D. 2004. Shock induced reaction observed via ultrafast infrared absorption in poly(vinyl nitrate) films. *J. Phys. Chem. A* 108:9342–47

52. Powell MS, Sakano MN, Cawkwell MJ, Bowlan PR, Brown KE, et al. 2020. Insight into the chemistry of PETN under shock compression through ultrafast broadband mid-infrared absorption spectroscopy. *J. Phys. Chem. A* 124:7031–46

53. Gupta Y, Pangilinan G, Winey J, Constantinou CP. 1995. Time-resolved molecular changes in a chemically reacting shocked energetic liquid. *Chem. Phys. Lett.* 232:341–45

54. Dreger Z, Tao Y, Gupta Y. 2013. Polymorphs of 1,1-diamino-2,2-dinitroethene (FOX-7): isothermal compression versus isobaric heating. *Chem. Phys. Lett.* 584:83–87

55. Dang N, Bolme C, Moore D, McGrane S. 2012. Shock induced chemistry in liquids studied with ultrafast dynamic ellipsometry and visible transient absorption spectroscopy. *J. Phys. Chem. A* 116:10301–309

56. McGrane SD, Dang NC, Whitley VH, Bolome CA, Moore D. 2010. *Transient absorption spectroscopy of laser shocked explosives*. Tech. Rep., Los Alamos Natl. Lab., Los Alamos, NM

57. van der Giessen E, Schultz PA, Bertin N, Bulatov VV, Cai W, et al. 2020. Roadmap on multiscale materials modeling. *Model. Simul. Mat. Sci. Eng.* 28:043001

58. Chakraborty D, Muller RP, Dasgupta S, Goddard WA. 2000. The mechanism for unimolecular decomposition of RDX (1,3,5-trinitro-1,3,5-triazine), an ab initio study. *J. Phys. Chem. A* 104:2261–72

59. Schweigert IV. 2015. Ab initio molecular dynamics of high-temperature unimolecular dissociation of gas-phase RDX and its dissociation products. *J. Phys. Chem. A* 119:2747–59

60. Manaa MR, Reed EJ, Fried LE, Galli G, Gygi F. 2004. Early chemistry in hot and dense nitromethane: molecular dynamics simulations. *J. Chem. Phys.* 120:10146–53

61. Elert ML, Deaven DM, Brenner DW, White C. 1989. One-dimensional molecular-dynamics simulation of the detonation of nitric oxide. *Phys. Rev. B* 39:1453(R)

62. Brenner DW, Robertson D, Elert M, White C. 1993. Detonations at nanometer resolution using molecular dynamics. *Phys. Rev. Lett.* 70:2174–77

63. Van Duin AC, Dasgupta S, Lorant F, Goddard WA. 2001. ReaxFF: a reactive force field for hydrocarbons. *J. Phys. Chem. A* 105:9396–409

64. Strachan A, van Duin AC, Chakraborty D, Dasgupta S, Goddard WA III. 2003. Shock waves in high-energy materials: the initial chemical events in nitramine RDX. *Phys. Rev. Lett.* 91:098301

239

65. Strachan A, Kober EM, van Duin AC, Oxgaard J, Goddard WA III. 2005. Thermal decomposition of RDX from reactive molecular dynamics. *J. Chem. Phys.* 122:054502

66. Mortier WJ, Van Genechten K, Gasteiger J. 1985. Electronegativity equalization: application and parametrization. *J. Am. Chem. Soc.* 107:829–35

67. Bock N, Cawkwell M, Coe J, Krishnapriyan A, Kroonblawd M, et al. 2008. LATTE. *Software Package*. **https://doi.org/10.5281/zenodo.1297664**

68. Manaa MR, Fried LE, Melius CF, Elstner M, Frauenheim T. 2002. Decomposition of HMX at extreme conditions: a molecular dynamics simulation. *J. Phys. Chem. A* 106:9024–29

69. Ravelo R, Holian B, Germann T, Lomdahl P. 2004. Constant-stress Hugoniostat method for following the dynamical evolution of shocked matter. *Phys. Rev. B* 70:014103

70. Reed EJ, Fried LE, Joannopoulos J. 2003. A method for tractable dynamical studies of single and double shock compression. *Phys. Rev. Lett.* 90:235503

71. Holian BL, Lomdahl PS. 1998. Plasticity induced by shock waves in nonequilibrium molecular-dynamics simulations. *Science* 280:2085–88

72. Kadau K, Germann TC, Lomdahl PS, Holian BL. 2005. Atomistic simulations of shock-induced transformations and their orientation dependence in bcc Fe single crystals. *Phys. Rev. B* 72:064120

73. Kadau K, Germann TC, Lomdahl PS, Albers RC, Wark JS, et al. 2007. Shock waves in polycrystalline iron. *Phys. Rev. Lett.* 98:135701

74. Ravelo R, Germann T, Guerrero O, An Q, Holian B. 2013. Shock-induced plasticity in tantalum single crystals: interatomic potentials and large-scale molecular-dynamics simulations. *Phys. Rev. B* 88:134101

75. Bringa EM, Caro A, Wang Y, Victoria M, McNaney JM, et al. 2005. Ultrahigh strength in nanocrystalline materials under shock loading. *Science* 309:1838–41

76. Cherukara MJ, Germann TC, Kober EM, Strachan A. 2014. Shock loading of granular Ni/Al composites. Part 1: Mechanics of loading. *J. Phys. Chem. C* 118:26377–86

77. Holian BL, Germann TC, Maillet JB, White CT. 2002. Atomistic mechanism for hot spot initiation. *Phys. Rev. Lett.* 89:285501

78. Zhao S, Germann TC, Strachan A. 2006. Atomistic simulations of shock-induced alloying reactions in Ni/Al nanolaminates. *J. Chem. Phys.* 125:164707

79. Zhao S, Germann TC, Strachan A. 2007. Molecular dynamics simulation of dynamical response of perfect and porous Ni/Al nanolaminates under shock loading. *Phys. Rev. B* 76:014103

80. Cherukara MJ, Germann TC, Kober EM, Strachan A. 2016. Shock loading of granular Ni/Al composites. Part 2: Shock-induced chemistry. *J. Phys. Chem. C* 120:6804–13

81. Heim AJ, Grønbech-Jensen N, Germann TC, Holian BL, Kober EM, Lomdahl PS. 2007. Influence of interatomic bonding potentials on detonation properties. *Phys. Rev. E* 76:026318

82. Maillet JB, Bourasseau E, Desbiens N, Vallverdu G, Stoltz G. 2011. Mesoscopic simulations of shock-to-detonation transition in reactive liquid high explosive. *Eur. Phys. Lett.* 96:68007

83. Cawkwell M, Sewell TD, Zheng L, Thompson DL. 2008. Shock-induced shear bands in an energetic molecular crystal: application of shock-front absorbing boundary conditions to molecular dynamics simulations. *Phys. Rev. B* 78:014107

84. Hamilton BW, Kroonblawd MP, Li C, Strachan A. 2021. A hotspot's better half: non-equilibrium intramolecular strain in shock physics. *J. Phys. Chem. Lett.* 12:2756–62

85. Maillet JB, Mareschal M, Soulard L, Ravelo R, Lomdahl PS, et al. 2000. Uniaxial Hugoniostat: a method for atomistic simulations of shocked materials. *Phys. Rev. E* 63:016121

86. Reed EJ, Fried LE, Manaa MR, Joannopoulos J. 2004. *A multi-scale approach to molecular dynamics simulations of shock waves*. Tech. Rep., Lawrence Livermore Natl. Lab., Livermore, CA

87. Islam MM, Strachan A. 2017. Decomposition and reaction of polyvinyl nitrate under shock and thermal loading: a ReaxFF reactive molecular dynamics study. *J. Phys. Chem. C* 121:22452–64

88. Shen Y, Jester SB, Qi T, Reed EJ. 2016. Nanosecond homogeneous nucleation and crystal growth in shock-compressed SiO_2. *Nat. Mater.* 15:60–65

89. Dammak H, Chalopin Y, Laroche M, Hayoun M, Greffet JJ. 2009. Quantum thermal bath for molecular dynamics simulation. *Phys. Rev. Lett.* 103:190601

90. Qi T, Reed EJ. 2012. Simulations of shocked methane including self-consistent semiclassical quantum nuclear effects. *J. Phys. Chem. A* 116:10451–59

91. Hamilton BW, Kroonblawd MP, Islam MM, Strachan A. 2019. Sensitivity of the shock initiation threshold of 1,3,5-triamino-2,4,6-trinitrobenzene (TATB) to nuclear quantum effects. *J. Phys. Chem. C* 123:21969–81

92. Manaa MR, Reed EJ, Fried LE, Goldman N. 2009. Nitrogen-rich heterocycles as reactivity retardants in shocked insensitive explosives. *J. Am. Chem. Soc.* 131:5483–87

93. Reed EJ, Manaa MR, Fried LE, Glaesemann KR, Joannopoulos J. 2008. A transient semimetallic layer in detonating nitromethane. *Nat. Phys.* 4:72–76

94. Reed EJ, Rodriguez AW, Manaa MR, Fried LE, Tarver CM. 2012. Ultrafast detonation of hydrazoic acid (HN_3). *Phys. Rev. Lett.* 109:038301

95. Bowlan P, Powell M, Perriot R, Martinez E, Kober EM, et al. 2019. Probing ultrafast shock-induced chemistry in liquids using broad-band mid-infrared absorption spectroscopy. *J. Chem. Phys.* 150:204503

96. Islam MM, Strachan A. 2019. Reactive molecular dynamics simulations to investigate the shock response of liquid nitromethane. *J. Phys. Chem. C* 123:2613–26

97. Goldman N, Reed EJ, Fried LE, Kuo IFW, Maiti A. 2010. Synthesis of glycine-containing complexes in impacts of comets on early Earth. *Nat. Chem.* 2:949–54

98. Martins Z, Price MC, Goldman N, Sephton MA, Burchell MJ. 2013. Shock synthesis of amino acids from impacting cometary and icy planet surface analogues. *Nat. Geosci.* 6:1045–49

99. Kroonblawd MP, Lindsey RK, Goldman N. 2019. Synthesis of functionalized nitrogen-containing polycyclic aromatic hydrocarbons and other prebiotic compounds in impacting glycine solutions. *Chem. Sci.* 10:6091–98

100. Yoo P, Sakano MN, Desai S, Islam MM, Liao P, Strachan A. 2021. Neural network reactive force field for C, H, N, and O systems. *npj Comput. Mater.* 7:9

101. Handley C, Lambourn B, Whitworth N, James H, Belfield W. 2018. Understanding the shock and detonation response of high explosives at the continuum and meso scales. *Appl. Phys. Rev.* 5:011303

102. Davis WC. 1981. High explosives: the interaction of chemistry and mechanics. *Los Alamos Sci.* 2:48–75

103. Jaramillo E, Sewell TD, Strachan A. 2007. Atomic-level view of inelastic deformation in a shock loaded molecular crystal. *Phys. Rev. B* 76:064112

104. Dienes J, Zuo Q, Kershner J. 2006. Impact initiation of explosives and propellants via statistical crack mechanics. *J. Mech. Phys. Solids* 54:1237–75

105. Grilli N, Duarte CA, Koslowski M. 2018. Dynamic fracture and hot-spot modeling in energetic composites. *J. Appl. Phys.* 123:065101

106. Campbell A, Davis W, Travis J. 1961. Shock initiation of detonation in liquid explosives. *Phys. Fluids* 4:498–510

107. Tarver CM, Chidester SK, Nichols AL. 1996. Critical conditions for impact- and shock-induced hot spots in solid explosives. *J. Phys. Chem.* 100:5794–99

108. Kroonblawd MP, Fried LE. 2020. High explosive ignition through chemically activated nanoscale shear bands. *Phys. Rev. Lett.* 124:206002

109. Campbell A, Travis J. 1985. *Shock desensitization of PBX-9404 and composition B-3.* Tech. Rep., Los Alamos Natl. Lab., Los Alamos, NM

110. Dattelbaum D, Sheffield S, Stahl D, Dattelbaum A. 2009. Influence of hot spot features on the shock initiation of heterogeneous nitromethane. *AIP Conf. Proc.* 1195:263–66

111. Carroll M, Holt A. 1972. Static and dynamic pore-collapse relations for ductile porous materials. *J. Appl. Phys.* 43:1626–36

112. Mader CL. 1965. Initiation of detonation by the interaction of shocks with density discontinuities. *Phys. Fluids* 8:1811–16

113. Bassett WP, Dlott DD. 2016. High dynamic range emission measurements of shocked energetic materials: Octahydro-1,3,5,7-tetranitro-1,3,5,7-tetrazocine (HMX). *J. Appl. Phys.* 119:225103

114. Shan TR, Wixom RR, Thompson AP. 2016. Extended asymmetric hot region formation due to shock-wave interactions following void collapse in shocked high explosive. *Phys. Rev. B* 94:054308

115. Wood MA, Kittell DE, Yarrington CD, Thompson AP. 2018. Multiscale modeling of shock wave localization in porous energetic material. *Phys. Rev. B* 97:014109

241

116. Li C, Hamilton BW, Strachan A. 2020. Hotspot formation due to shock-induced pore collapse in 1,3,5,7-tetranitro-1,3,5,7-tetrazoctane (HMX): role of pore shape and shock strength in collapse mechanism and temperature. *J. Appl. Phys.* 127:175902

117. Bassett WP, Johnson BP, Dlott DD. 2019. Dynamic absorption in optical pyrometry of hot spots in plastic-bonded triaminotrinitrobenzene. *Appl. Phys. Lett.* 114:194101

118. Herring SD, Germann TC, Grønbech-Jensen N. 2010. Effects of void size, density, and arrangement on deflagration and detonation sensitivity of a reactive empirical bond order high explosive. *Phys. Rev. B* 82:214108

119. Esposito AP, Farber DL, Reaugh JE, Zaug JM. 2003. Reaction propagation rates in HMX at high pressure. *Propellants Explos. Pyrotech.* 28:83–88

120. Sakano M, Hamilton B, Islam MM, Strachan A. 2018. Role of molecular disorder on the reactivity of RDX. *J. Phys. Chem. C* 122:27032–43

121. Islam MM, Strachan A. 2020. Role of dynamical compressive and shear loading on hotspot criticality in RDX via reactive molecular dynamics. *J. Appl. Phys.* 128:065101

122. Steele BA, Goldman N, Kuo IFW, Kroonblawd MP. 2020. Mechanochemical synthesis of glycine oligomers in a virtual rotational diamond anvil cell. *Chem. Sci.* 11:7760–71

123. Zhou T, Song H, Liu Y, Huang F. 2014. Shock initiated thermal and chemical responses of HMX crystal from ReaxFF molecular dynamics simulation. *Phys. Chem. Chem. Phys.* 16:13914–31

124. Joshi K, Losada M, Chaudhuri S. 2016. Intermolecular energy transfer dynamics at a hot-spot interface in RDX crystals. *J. Phys. Chem. A* 120:477–89

125. Kerschen NE, Sorensen CJ, Guo Z, Mares JO, Fezzaa K, et al. 2019. X-ray phase contrast imaging of the impact of a single HMX particle in a polymeric matrix. *Propellants Explos. Pyrotech.* 44:447–54

126. Duarte CA, Hamed A, Drake JD, Sorensen CJ, Son SF, et al. 2020. Void collapse in shocked-HMX single crystals: simulations and experiments. *Propellants Explos. Pyrotech.* 45:243–53

127. Austin R, Barton N, Howard W, Fried L. 2014. Modeling pore collapse and chemical reactions in shock-loaded HMX crystals. *J. Phys. Conf. Ser.* 500:052002

128. Boulard B, Kieffer J, Phifer C, Angell C. 1992. Vibrational spectra in fluoride crystals and glasses at normal and high pressures by computer simulation. *J. Non-Cryst. Solids* 140:350–58

129. Marsh SP, ed. 1980. *LASL Shock Hugoniot Data*, Vol. 5. Berkeley: Univ. Calif. Press

130. Popolato TR, Gibbs A. 1980. *LASL Explosive Property Data*. Los Angeles: Univ. Calif. Press

Contents

v

Current Interest

Indexes

Errata

An online log of corrections to *Annual Review of Materials Research* articles may be
found at http://www.annualreviews.org/errata/matsci

Article

The Potential Energy Hotspot: Effects of Impact Velocity, Defect Geometry, and Crystallographic Orientation

Brenden W. Hamilton, Matthew P. Kroonblawd, and Alejandro Strachan*

Cite This: https://doi.org/10.1021/acs.jpcc.1c10226

Read Online

ACCESS | Metrics & More | Article Recommendations | Supporting Information

ABSTRACT: In energetic materials, the localization of energy into "hotspots" is known to dictate the initiation of chemical reactions and detonation. Recent all-atom simulations have shown that more energy is localized as internal potential energy (PE) than can be inferred from the kinetic energy (KE) alone. The mechanisms associated with pore collapse and hotspot formation are known to depend on pore geometry and dynamic material response such as plasticity. Therefore, we use molecular dynamics (MD) simulations to characterize shock-induced pore collapse and the subsequent formation of hotspots in 1,3,5-triamino-2,4,6-trinitrobenzene

(TATB), a highly anisotropic molecular crystal, for various defect shapes, shock strengths, and crystallographic orientations. We find that the localization of energy as PE is consistently larger than the KE in cases with significant plastic deformation. An analysis of MD trajectories reveals the underlying molecular- and crystal-level processes that govern the effect of orientation and pore shape on PE localization. We find that the regions of highest PE relate to the areas of maximum plastic deformation, while KE is maximized at the point of impact. Comparisons against octahydro-1,3,5,7-tetranitro-1,3,5,7-tetrazocine (HMX) reveal less energy localization in TATB, which could be a contributing factor to the latter's insensitivity.
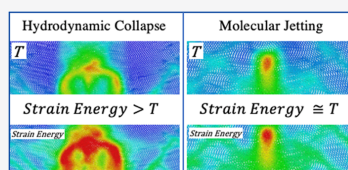
1. INTRODUCTION

Shockwave-induced chemistry can result in a myriad of processes such as detonation,[1−3] the formation of pre-biotic compounds that may have contributed to the formation of life on earth,[4−8] and the synthesis of new materials and phases.[9−11] Often, shock-induced chemistry is triggered or enhanced by energy localization into hotspots that form as the shockwave interacts with the material's microstructure.[12] In the case of energetic materials, hotspots of sufficient size and temperature can become critical and transition into deflagration waves and can eventually lead to detonation. Several mechanisms can result in the formation of hotspots, but the collapse of porosity is known to dominate the initiation of energetic materials. This was first shown through shock desensitization experiments where high explosives (HEs) were rendered non-detonable after an initial weak shock caused the collapse of porosity without igniting significant amounts of material.[13] The inclusion of inhomogeneities via silica micro-beads and cavities via micro-balloons in gelled nitromethane also demonstrated the superiority of the latter in triggering detonations, decreasing the run to detonation.[14]

Significant efforts have been devoted to understanding the formation, nature, and criticality of hotspots. Physics-based scaling laws for planar void collapse supported by atomistic simulations predicted a theoretical maximum temperature achieved during pore collapse and highlighted the importance of material expansion into the void, maximizing pressure−volume work during recompression.[15] Recent molecular dynamics (MD) simulations have shown that diamond-shaped voids, elongated along the shock direction, result in larger and

hotter hotspots than equiaxed pores.[16] This is due to the focusing of shockwave energy at the tip of the diamond, leading to molecular jetting and the formation of a low-density expanding plume. Volumetric work done to recompress the plume achieves temperature values close to the maximum predicted in ref 15. Three-dimensional calculations of the collapse of spherical and octahedron-shaped pores in octahydro-1,3,5,7-tetranitro-1,3,5,7-tetrazocine (HMX) showed only a nominal difference in temperature;[17] however, pores were limited to 8 nm in the shock direction, which would limit molecular jetting.[16] Continuum modeling techniques have been used to explore pore aspect ratio[18] and the resultant shear banding[19] in HMX pore collapse simulations, and to compare HMX and 1,3,5-triamino-2,4,6-trinitrobenzene (TATB).[20] In recent years, the computational efficiency of all-atom simulations has enabled direct scale bridging with grain-scale models, opening new routes to parameterize and validate the accuracy of those models for predicting shock-induced pore collapse.[21−23]

Atomic-level understanding of shock-induced chemistry was greatly increased by the development of reactive force fields (FF), such as ReaxFF, which allowed for explicit simulation of

shock ignition and thermal decomposition in solid HEs such as RDX.[24,25] ReaxFF simulations using a compressive shear protocol have been utilized to explore the interplays of mechanics on chemistry.[26,27] Reactive MD techniques such as density functional tight binding have been used to explore the chemical reactivity of TATB under thermal and shock loading, as well as mechanical, shear-induced metallization.[28−30] The extended timescales of these techniques have allowed for the prediction of reactive properties like detonation velocity and pressure,[31,32] IR spectra evolution,[33−35] and detailed chemical reaction pathways.[36−39] Reactive force fields have also enabled explicit simulation of nanoscale hotspots[40] and the upscaling of chemical reaction models for mesoscale and coarse-grained simulations.[41]

Quite surprisingly, reactive MD simulations have shown that nanoscale hotspots formed following the dynamical collapse of porosity are markedly more reactive than otherwise identical hotspots at the same temperature and pressure in a compressed perfect crystal.[42,43] A possible explanation for this observation is that disorder and amorphization in molecular crystals can lead to accelerated reactions compared to bulk crystalline materials,[40,44] and recent advances in continuum hotspot modeling have begun to include a "shear band activation" term to address this.[45] Recent MD simulations of shock-induced pore collapse in TATB showed that significantly more energy is localized as intramolecular potential energy (PE) than into internal temperature or kinetic energy (KE).[46] This excess PE is the result of large intramolecular deformations that do not significantly relax on timescales comparable to the onset of exothermic chemistry. Nonreactive, hotspot thermal conduction simulations in TATB showed that hotspots formed from the collapse of 40 nm pores take nearly a full nanosecond to equilibrate with the surrounding material.[47] Assessments on the decay of the PE hotspot show almost no relaxation of intramolecular deformations within ~200 ps of collapse,[46] well within the typical timescale of exothermic relaxation in similar reactive pore collapse simulations.[42,43]

Molecular deformations such as these can lead to the mechanochemical acceleration of reactions and alter reaction pathways.[48] Recent work in RDX combining planar pore collapse with an additional shear component directly linked hotspot criticality to the level of shear loading.[49] Excess localized PE provides a plausible explanation to the puzzling difference in reactivity between dynamically and thermally generated hotspots[42] and for chemical activation through forming nanoscale shear bands.[44] For numerous other covalent molecules, intramolecular deformation is known to accelerate reactions,[50,51] delocalize electrons,[1,30] and open forbidden reaction pathways.[52] The intramolecular PE is a quantitative measure of these deformations that may enable modeling their effect on chemical kinetics.[46,53] For this study, we use nonreactive simulations, where covalent bonds cannot break; this allows us to isolate the initial intramolecular deformations leading to chemical acceleration and characterize their persistence under mechanical relaxation processes. These simulations are designed to assess the generality of prior observations on the PE hotspot. In particular, we seek to understand whether localization of energy in intramolecular deformations arises and persists for a range of shock strengths, for porosities of different shapes, and whether the shock direction influences this behavior in materials with consid-

erable anisotropy in their mechanical and thermal properties.[21,47,53]

To address this gap in knowledge, we characterize how different pore collapse mechanisms operating at various shock strengths (e.g., viscoplastic, hydrodynamic, molecular jetting) impacts the relative intensity and shape of the hotspot as well as the partitioning of the localized energy into kinetic (temperature) and potential (molecular strain) terms. We focus here on hotspots in the insensitive HE TATB, as its layered structure[54] leads to perhaps the greatest mechanical and thermal anisotropy for any explosive. This enables us to explore bounding cases for the role of shock orientation on the formation of hotspots. Recent work from Lafourcade et al. showed a strong orientation dependence for deformation mechanisms in TATB under controlled strain conditions[55] that leads to analogous deformations under shock conditions.[56] For instance, compressive stresses along [100] result in an inelastic chevron-like buckling of the basal planes, whereas resolved shear stresses along (011)-type planes result in a nonbasal gliding of the planes. Under weak stresses, the TATB crystal layers will glide in-plane[55,57,58] while detonation-level shocks lead to the formation of nanoscale shear bands.[44] Analysis of dynamical axial compression simulations of TATB crystal showed that the intramolecular strain energy (PE) was a reliable metric to distinguish between various mechanisms for plastic flow that result in considerable anisotropy in the mechanisms of intramolecular strain localization.[53] These observations indicate that pore collapse could exhibit a high degree of effects as well as anisotropy and shock strength.

The role of TATB anisotropy in shock loading response of the perfect single crystal has been well characterized for a shock strength near 10 GPa. All-atom simulations were used to study the perfect crystal shock response in a variety of crystallographic orientations.[56] This showed significant effects on the wave structure (single vs two-wave response), elastic wave speeds, and deformation mechanisms, which ranged from a variety of crystal-level defect formations to plasticity and intense shear localization. Coupled MD and continuum simulations explored the mechanics of pore collapse for various orientations and shock speeds for cylindrical pores.[21] The strong disparity between the all-atom and the isotropic, elastic−plastic continuum models at low shock speeds highlighted the significance of anisotropic strength effects on the formation of hotspots.

Our previous work characterized the role of pore shape, size, and shock strength in hotspot formation in HMX.[16] We use identical geometries here to enable a direct comparison between TATB (considered an insensitive explosive) and HMX (a high-performance material). The extreme temperatures (>7000 K) found in HMX following the collapse of diamond-shaped pores elongated along the shock propagation direction corresponds well to the theoretical maximum temperature[15] and recent experimental reactive hotspot measurements from Bassett et al.[59−61] These high temperatures are possibly related to the jetting and gasification of material into the void, which is later recompressed by the shockwave. Holian et al. showed for simple one-dimensional (1D) shocks in a model system that jetting occurs when the energy embedded by the shock is greater than the crystal cohesive energy: $1/2mU_p^2 > E_{coh}$.[15] However, events such as plasticity (e.g., dislocation motion or shear banding) and shock focusing at curved surfaces can alter the local energy deposited during shock compression.
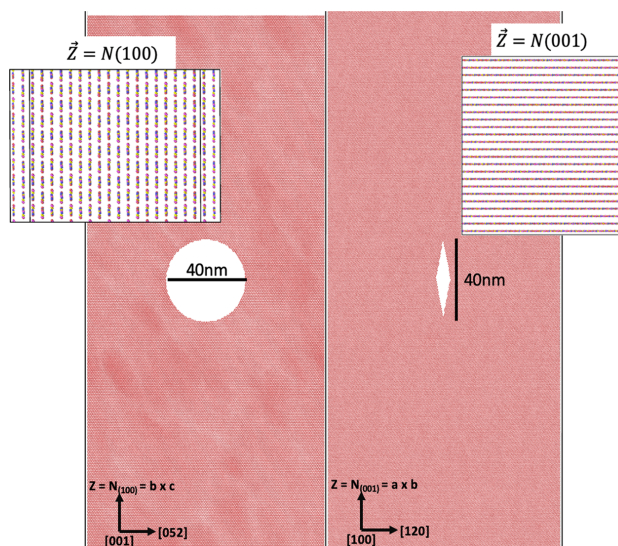
B

Figure 1. Simulation setup for shock interaction with a cylindrical pore (left) and a diamond (right) pore elongated along the shock direction; insets display the two crystallographic orientations studied for both pores. Shocks propagate from bottom to top, with periodic boundary conditions in the other two directions.

This study assesses the localization of energy, both kinetic and potential, in TATB following the shock-induced collapse of porosity. The use of two void shapes allows us to evaluate the role of molecular jetting, hydrodynamic collapse, and viscoplastic collapse, whereas the two crystallographic orientations used bound the single-crystal plastic response[53] to elucidate the role of molecular/crystal-level processes involved in hotspot formation. We find that TATB follows the general trends observed in HMX[16] in terms of shock strength and pore shape, but with an important quantitative difference in which TATB hotspots do not reach the same extreme temperatures (7000+ K). Unlike in HMX, the temperatures achieved in TATB are only a fraction of the theoretical maximum. Our atomistic simulations provide insight into the underlying molecular processes that control the collapse mechanisms and the overall hotspot shape and temperature, with the PE hotspot strength generally determined by the amount of induced plastic deformation. We find that the mechanisms in play, discussed below, may also be a contributing factor to the insensitivity of TATB. Finally, we find that in all cases with significant plastic flow, more energy in hotspots is stored as PE than as KE.

2. METHODS

MD simulations were conducted using the LAMMPS package[62] and a validated version of a nonreactive, nonpolarizable force field for TATB.[63] The force field includes tailored harmonic bond stretch and angle bend terms for flexible molecules,[64] RATTLE constraints that fix the N–H bonds to their equilibrium values,[65] and an intramolecular O–H repulsion term that was implemented as a bonded interaction.[66] The covalent bond vibrations, angle bends, and improper dihedrals were modeled using harmonic functions. Proper dihedrals were modeled using a cosine series. Van der Waals interactions were modeled using the Buckingham potential (exponential repulsion and an r^{-6} attractive term) combined with short-ranged r^{-12} potentials that compensate for the divergence in the Buckingham potential at small separation. The nonbonded terms were evaluated in real space within an 11 Å cutoff. Electrostatic interactions were calculated between constant partial charges located on the nuclei and were evaluated using the short-ranged Wolf potential with a damping parameter of 0.2 Å^{-1} and an 11 Å cutoff.[67] All intramolecular nonbonded interactions are excluded by design, which allows for rigorous separation of inter- and intramolecular potential energy terms.

Nearly orthorhombic simulation cells were prepared using the generalized crystal-cutting method[68] starting from the triclinic $P\bar{1}$ TATB crystal structure[54] with lattice parameters determined with the TATB FF at 300 K and 1 atm. For the orientation denoted as (001), the crystal was oriented such that [100] was aligned with x, [120] was nearly parallel to y, and the normal to the basal planes $\mathbf{N}_{(001)} = \mathbf{a} \times \mathbf{b}$ was aligned with z, the shock direction. For the (100) orientation, $\mathbf{N}_{(100)} = \mathbf{b} \times \mathbf{c}$ was aligned with z, and the x axis was aligned with [001] (lattice vector $\mathbf{c}$). For cylindrical pores with circular cross sections, a diameter of 40 nm was used with the axis of symmetry along x, centering the void in the geometric center of a cell. For diamond-shaped pores (also cylindrical with axis along x), the diamond was cut with the long axis aligned with the shock direction (z) and the short axis aligned with the y direction (the simulation is thin in the x direction). The length was 40 nm, and its maximum width was 8 nm. Renderings of both defect shapes and the utilized crystallographic orientations are displayed in Figure 1.

Free surfaces were generated normal to the shock direction (z) by adding a 5 nm region of vacuum that removes the periodicity in that direction to prevent self-interactions.
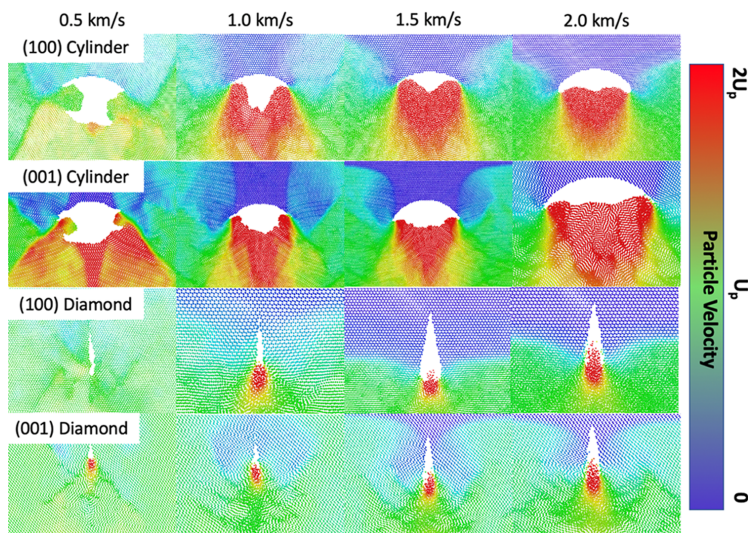
Figure 2. Molecular CM velocities in the shock direction during pore collapse. Color bar relative to initial impact velocity.

Periodic boundaries were utilized in both nonshock directions. The thermalized systems were equilibrated at 300 K using a 25 ps isothermal−isochoric (NVT ensemble) simulation with a Nosé−Hoover-style thermostat and a 0.5 fs timestep.[69] To accelerate the equilibration of the system after the free surfaces were created, during the first 2.5 ps, atomic velocities were reinitialized stochastically from the Maxwell−Boltzmann distribution every 0.5 ps and were rescaled to the target temperature every 0.05 ps to attenuate breathing modes incurred by the surface tension. These configurations were used as the starting point for reverse ballistic shock simulations using adiabatic MD (NVE ensemble) with a 0.2 fs timestep. In the reverse ballistic setup,[70] the piston velocity, U_p, was added to the thermal velocities of the atoms, leading to an impact on the rigid piston that generates a shock front traveling through the sample in the opposite direction at the shock speed, U_s. Molecules with center of mass (CM) positions with $z \leq 1.5$ nm were held fixed throughout the shock simulation to simulate the rigid and infinitely massive piston. We ran shock simulations at U_p = 0.5, 1.0, 1.5, and 2.0 km/s for each pore shape and crystal orientation case, yielding a total of 16 simulations.

Simulation trajectories were analyzed on a molecule-by-molecule basis. The molecular center of mass (CM) positions and velocities were computed as weighted sums over all 24 atoms in each molecule. The total molecular kinetic energy KE_{tot}, and the separate contributions from the molecular translational KE_{trans}, and roto-librational and vibrational KE_{ro-vib} degrees of freedom were computed as

$$K_{tot} = \sum \frac{1}{2} m_i \mathbf{v}_i \cdot \mathbf{v}_i$$

and

$$K_{trans} = \frac{1}{2} \mathbf{MV} \cdot \mathbf{V}$$

and

$$K_{ro-vib} = K_{tot} - K_{trans}$$

where lowercase variables represent mass and velocity of individual atoms and uppercase variables represent CM (molecular) values. The ro−vib kinetic energies KE_{ro-vib} were interpreted as the molecular temperature T and were scaled to kelvin units through

$$K_{ro-vib} = \frac{63}{2} k_B T$$

where k_B is the Boltzmann constant and the factor of 63 arises from the 3 roto-librational and 60 unconstrained vibrational degrees of freedom in the TATB molecule. The intramolecular PE is defined as

$$PE_{intra} = \sum PE_{bond} + \sum PE_{ang} + \sum PE_{dih} + \sum PE_{imp}$$

where each of the PE terms is summed over the total number of bonds/angles/dihedrals in the molecule and are described by the harmonic, cosine series, and tabulated terms of the force field[63] described at the beginning of Section 2. All molecular properties were locally averaged within a sphere 1.5 nm in radius about each molecule CM to smooth fluctuations.

3. CRYSTAL-LEVEL PROCESSES OF PORE COLLAPSE

3.1. Cylindrical Pores with Circular Cross Sections. We begin by assessing the collapse of porosity at molecular and crystal-level scales, looking specifically at the structure of the collapsing material, as this can heavily influence the shape, size, and strength of the hotspot.[16,23] Assessing just the cylindrical pores first (see Figure 2), the general shape of the collapsing material only shows minor dependence on the crystal orientation (row 1 vs row 2 in Figure 2) but, as expected, strong dependence on shock strength (various columns of Figure 2). For U_p = 0.5 km/s, cylindrical pores collapse laterally via a viscoplastic process driven by the compressive stresses following the passage of the shock. With increasing
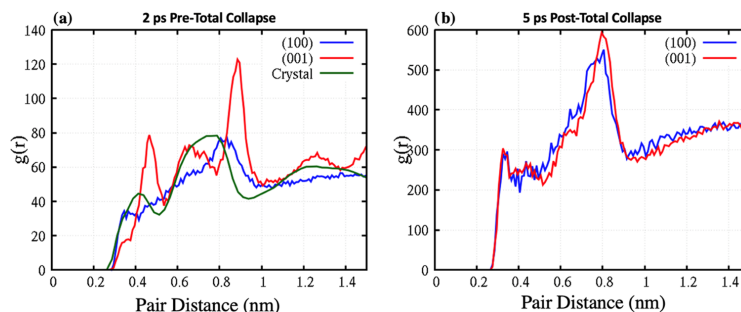
Figure 3. Radial distribution functions for the pore collapse (mid-collapse) and the hotspot, for both orientations, cylindrical void, at 2.0 km/s. Crystal $g(r)$ represents the perfect crystal at the shock pressure for (001) with U_p = 2.0 km/s.

shock strength, the collapse transitions to a hydrodynamic regime where the upstream surface expands into the void on a timescale similar to the passage of the shock. In this regime, the stresses involved are significantly higher than the material strength[53,55,71] and the deforming material behaves approximately like a fluid (hence the name hydrodynamic).

In the case of a hydrodynamic collapse, the material is often assumed to have little to no strength. From this, as could be expected, the collapsing material under (100) shocks appears to be amorphized by the fast plastic deformation, with no noticeable structure seen in Figure 2. Quite surprisingly, for (001) shocks, the collapsing material appears to retain a significant degree of crystalline order. In this case, this orientation of the crystal is significantly more compressible in the shock direction,[63] and the TATB basal planes become highly deformed via intralayer sliding and nonbasal gliding, as well as plane buckling, but remain locally structured. This retained structure in the basal planes is likely related to the small number of slip systems available for plastic deformation[55] in conjunction with dislocation motion instability under shock-like pressures[72] that leads to nanoscale shear banding[44,56] as a primary plastic response for this orientation.

To further characterize the structure of the collapsing material, Figure 3 displays the radial distribution functions obtained from the molecular centers of mass for both orientation's collapsing regions for the cylindrical pore and the shocked crystal for U_p = 2.0 km/s. The crystal baseline averages over layer sliding and nonbasal glide defects, which broadens peaks on top of thermal fluctuation. This clearly confirms the structural difference in the collapsing material for the two orientations. While both orientations result in mostly amorphous material in the hotspot after the collapse and recompression (Figure 3b), the collapsing material is structured for the (001) and amorphous for the (100) (Figure 3a). Differences with respect to the perfect crystal arise due to both plastic deformation and a complicated pressure gradient in the collapsing material. The different deformation paths and localization of plastic flow in these two different collapses for the "hydrodynamic" regime at U_p = 2.0 km/s are expected to influence the characteristics of the resulting hotspot.

3.2. Cylindrical Pores with Diamond Cross Sections. In the case of the diamond-shaped pores, weak shock collapses are dominated by lateral collapse, analogous to the lateral, viscoplastic collapse in circular cylinders. However, while the viscoplastic mechanism in the cylinder is dominated by plastic flow and material deformation, the high-aspect-ratio diamonds

simply close without much plastic work being done on the surrounding material. This results in almost no discernable hotspot.

For strong shocks, the collapse process is dominated by molecular ejecta. When a shockwave reaches a flat free surface, the material expanding into vacuum travels at $2U_p$.[73] In the case of nonplanar defects, shock focusing can lead to much higher ejecta velocities.[74,75] From the anisotropic elasticity and plasticity in TATB,[55] it is reasonable to anticipate that the two orientations may result in different amounts of ejecta. However, the two diamond pores exhibit similar amounts of ejecta at early times, which agrees well with the relationship from Holian et al., stating that jetting occurs when the shock energy is greater than the crystal's cohesive energy, $1/2mU_p^2 > E_{coh}$,[1515] setting the assumption that the onset of jetting should be mostly orientation-independent.

The main difference between the two orientations is the location of the shock front relative to the ejecta. In the (100) case, the ejecta expands out in front of the shockwave (transition from blue to green in Figure 2). For the (001) case, the reverse occurs, with the shock wave ahead of the ejecta. This occurs despite the shock speed of the (001) case being higher than in the (100) case, U_s of 7.02 vs 6.23 km/s,[21] respectively. For the (001) shock, the ejected molecules have velocities between 4 and 6 km/s, and between 5 and 7 km/s for (100), allowing the ejecta to expand quicker. See Figure S1 in the Supporting Information (SI) for full velocity distributions.

As shown in Figure 4, both orientations have a two-wave feature. In the (100) case, shown in dashed curves, the leading wave particle velocity is $U_p \cong 0.2$ km/s and causes almost no pressure increase. In the (001) case shown in solid curves, the leading wave is $U_p \cong 1.4$ km/s. For (100), the trailing wave U_p = 2.0 km/s initiates jetting, allowing the ejecta to accelerate past this wave. For the (001) case, the leading wave of $U_p \cong 1.4$ km/s does not promptly initiate ejecta but does significantly increase the pressure in the bulk. Ejecta do not form until the $U_p \cong 2.0$ km/s wave reaches the pore. Thus, the first wave initiates lateral collapse of the pore prior to ejecta formation, with the lateral collapse choking off the ejecta before it can recompress on the downstream face of the pore. For (100), the ejecta can fully expand and be fully recompressed. Renderings of the time history of both diamond collapse processes are shown in Figure S2 in the SI. These differences in material expansion history will result in different
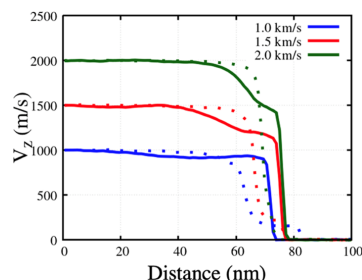
Figure 4. Wave profiles in the bulk system for each impact velocity measured with respect to unshocked material. Dashed curves represent the (100) orientation, and solid curves the (001) orientation. Both systems have a "two-wave" feature, with the (100) leading wave causing particle velocities on the order of 200 m/s, whereas the (001) leading wave leads to significant velocity (and therefore pressure) increase.

structural characteristics upon recompression that may have bearing on both kinetic and potential energy localization.

4. TEMPERATURE AND POTENTIAL ENERGY FIELDS OF HOTSPOTS

Figure 5 shows molecular renderings for the various hotspots generated after pore collapse colored by both KE (left) and PE (right) in a given column, for U_p = 1.0−2.0 km/s. The 0.5 km/s results are omitted from this post-collapse analysis as the relative energy difference in the KE and PE hotspots formed from cylindrical pores was smaller than thermal fluctuations, and the diamond pore cases produced almost no hotspot at all. Note that the color bar upper bound depends on U_p and is 100, 75, and 50 kcal/mol for the 2.0, 1.5, and 1.0 km/s cases, respectively. Each pair of columns collects a shock speed, with the left panels of each group showing temperature (in units of KE) and the right half showing intramolecular PE. Each row corresponds to an orientation and defect pair.
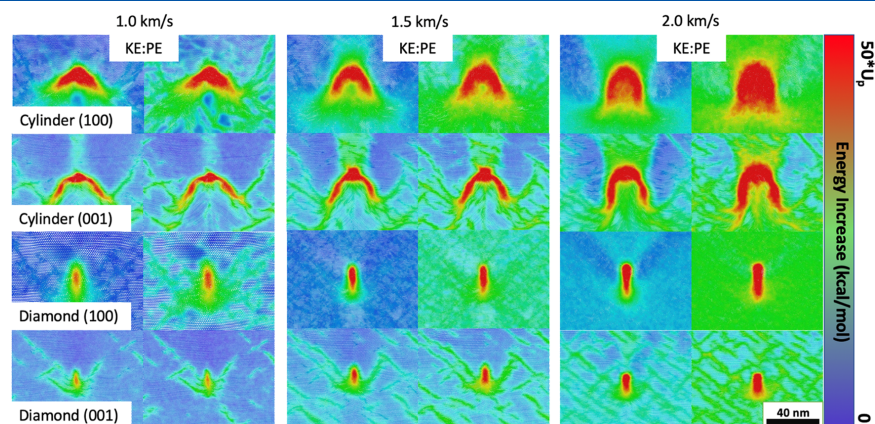
We note that the significant anisotropy of TATB is manifested in the markedly different shock-induced plasticity and the associated dissipation away from the hotspot areas. This, together with the anisotropic elasticity, results in significantly higher bulk temperatures for (001) shocks compared to (100). For example, a (001) shock with U_p = 2.0 km/s has a shock velocity of 7.0 km/s and results in a temperature increase of ∼770 K, whereas a (100) shock with the same particle velocity has a U_s of 6.2 km/s and an average temperature of ∼650 K, which is consistent with those found in ref 21. In addition, (100) shocks lead to relatively homogeneous temperature fields in the bulk, whereas the (001) orientation localizes energy in shear bands, which can account for the excess temperature. Characteristic hotspot energy magnitudes and structural sizes and shapes are discussed in detail below.

4.1. Role of Pore Shape and Shock Speed. The potency of a hotspot is related to both its size and temperature, since the critical temperature for ignition decreases with increasing size.[76] Thus, to quantify the thermal fields of hotspots, we compute the area (A) of the hotspot with temperature exceeding a value temperature (T) and plot this relationship in the T−A space. Figure 6 shows the T−A plots for cylindrical pores (a) and diamond pores (b) for various U_p and shock orientations; solid curves indicate (001) shocks while dotted curves denote (100) shocks. To single out the rise in temperature from the collapse of porosity, we reference the temperature field to the corresponding bulk shock temperature, which may include heating from shear band formation in strong shock cases.

Inspection of Figure 6 shows that the collapse of diamond pores results in smaller and colder hotspots than that of cylindrical pores, except for the strongest (100) shocks where the maximum temperature resulting from the collapse of diamond pores is over 500 K higher than in the case of cylindrical pores. In our previous work comparing pore shape for HMX,[16] the diamond pores showed temperatures 2−3 times larger than cylindrical pores from the rapid recompression of ejecta. In TATB, the same ejecta form in diamond
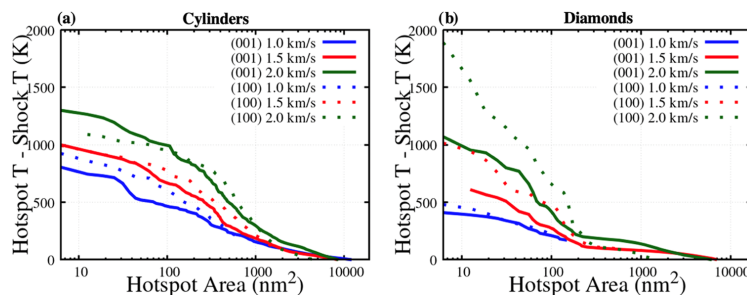

Figure 5. Molecular renderings of all hotspots at 5 ps after the total collapse of porosity, colored as both kinetic energy (which is proportional to temperature) and intramolecular potential energy. Color bar relative to impact velocity (max value: 50, 75, and 100 kcal/mol for 1, 1.5, and 2 km/s, respectively).

Figure 6. Temperature−area cumulative plots for (a) cylinder voids and (b) diamond voids. Impact speed shown by color, orientation shown by point shape.

pores; however, the resulting peak temperatures are much lower.

Hotspots from cylindrical pores are much larger than that of diamond pores. This is due to the significant difference in initial area, allowing for more mechanical work to occur in cylindrical collapses. Figure 7 shows the $T−A$ plots for the U_p
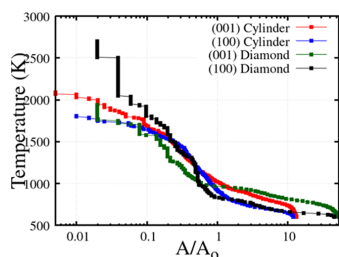

Figure 7. $T−A$ plot (absolute temperature) for both void shapes and crystal orientations at a 2.0 km/s impact speed.

= 2.0 km/s cases in which the area is normalized by the original area of the pore. This normalization shows that the diamond and cylindrical pores in TATB result in roughly the same relative hotspot temperature distributions, which is in marked contrast to HMX in which diamonds were much more efficient in localizing KE.[16]

Looking at peak temperatures, for weaker shocks, the cylindrical pores are much hotter than the diamonds. As can be

seen from the collapse mechanisms in Figure 2, the viscoplastic collapse of cylinders undergoes much more plastic deformation than for diamond pores, resulting in hotter hotspots. As shock speed increases, the trend begins to reverse due to the presence of molecular ejecta in the diamond pores and only a hydrodynamic collapse in the cylinders. There is some disparity in these results for the different orientations that will be discussed in Section 4.2. Overall, for both shapes, hotspot size and temperature increase with increasing shock speed, as expected.

4.2. Role of Shock Orientation. Due to their significant disparity in initial shape, we assess the role of crystallographic orientation on hotspot formation for the cylindrical and diamond pores separately. Starting with the two cylindrical pore crystal orientation cases, it is evident that, despite their similar temperature−area plots (Figure 6a), the temperature fields command highly dissimilar shapes (see Figure 2). The (100) shock direction cylindrical pore collapse results in a rather equiaxed hotspot, indicative of the initial void shape. However, the (001) shocks result in a crescent-shaped hotspot, with a discernable "core" (top center) and "legs" (lower flanks). While the maximum temperatures and extent of the energy localization are similar for the two shock directions (see Figure 3a), differences in the initial temperature fields and post-shock densities can result in different thermal dissipation rates[47] and may therefore exhibit different thresholds for reaction/deflagration. Thus, the criticality of the hotspots following the collapse of such pores can be expected to depend on shock direction. These observations also apply for lower
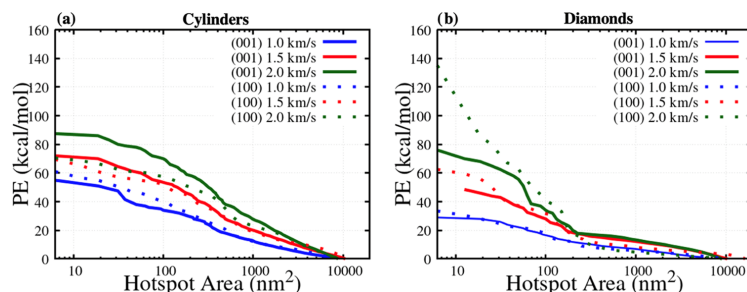

Figure 8. PE−A plot for cylinder and diamond pores. Organized the same as Figure 6, with the y axis corresponding 0−2200 K in temperature units.
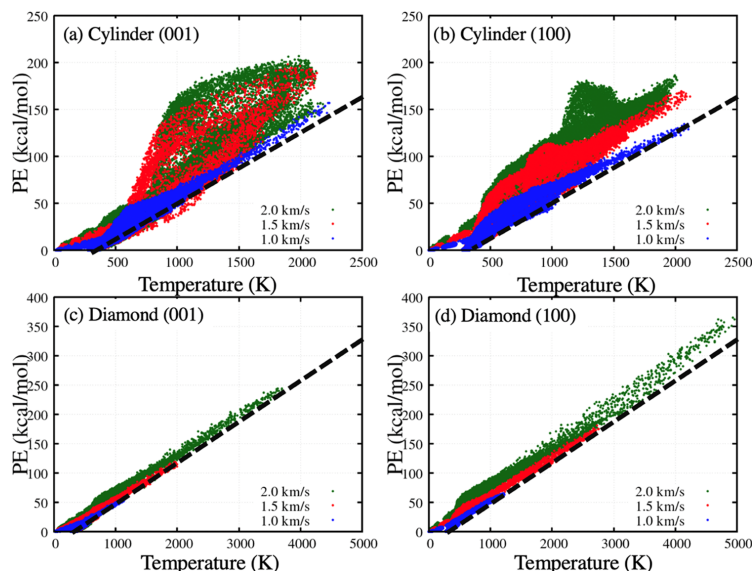
Figure 9. PE−temperature plots for all of the hotspots for all four orientation/shape cases where PE is the rise in intramolecular PE from the unshocked 300 K state. The labels on each plot designate the defect shape, shock direction. Color designates shock strength. Distributions taken at t_o + 1.0 ps. Dashed lines represent classical equipartition of energy.

shock speeds, but the difference is most evident in the hydrodynamic cases.

The crystal scale processes (e.g., intense shearing and plasticity) that create these differing shapes stem from the fully hydrodynamic collapse of the (100) case and the retained crystal structure in the (001), as shown in Figures 2 and 3. As is seen in a majority of high explosives, the hydrodynamic collapse leads to a uniform, circular hotspot.[18,23,42,43,56] The (001) collapse features the ordered material impacting on the downstream face of the pore and highly sheared material that flank the collapsing material. These sheared regions result in the long "legs" of the crescent shape as shown in Figure 6. As shown in Figure 2, the (100) cases begin to act more hydrodynamic at lower U_p, leading to the slightly higher temperatures seen in Figure 6a, whereas the shear localization along of the (001) case at higher U_p leads to a higher peak temperature, with very similar respective areas for all speeds.

For weak shocks, little discernable difference exists in the hotspots formed from diamond pores. At higher speeds, the (100) direction diamond pore hotspots reach significantly higher temperatures and areas. As discussed in Section 3.2 and shown in SM-2, the two-wave feature of the (001) direction leads to a lateral collapse of the pore prior to ejecta being able to fully expand and recompress. The choked-off ejecta of the (001) case cannot generate as much mechanical work as the (100) case, leading to lower temperatures. Additionally, since the ejecta cannot extend across the longitudinal length of the pore, the (001) hotspot itself covers less total area.

4.3. Localization of Potential Energy. We now focus on the localization of energy in PE following the collapse of porosity, assessing any differences in trends from that of the temperature description of the hotspot. Figure 8 shows PE vs cumulative area (PE−A) plots for intramolecular potential

energy that are analogous to the T−A plots in Figure 6. We find that the trends described above for the temperature fields (in terms of the role of shock strength, orientation, and pore shape) mostly apply to the localization of PE, but some important differences should be highlighted.

While the maximum temperature of the (001) cylindrical pore was greater than that of the (100) case, the difference in PE is significantly larger. The difference is so substantial that the peak PE values for the 1.5 km/s (001) shock surpass the 2 km/s (100) shock at very small areas (Figure 8a). This is most likely a result of the significant shear localization at the sides of the pore collapse in the (001) cylinder leading to highly deformed molecules, similar to the formation of shear bands.[44]

The T−A curve shown in Figure 6a for the (100) cylindrical pore with U_p = 1.5 km/s is slightly higher than that for the (001) shock at small areas and considerably higher at larger areas. However, this trend reverses in terms of PE in Figure 8a, with the (001) shock cylindrical pore collapse leading to a slightly "hotter" hotspot in PE terms for all areas. This is indicative of a loading path dependence in how hotspot energy partitions between KE and PE. In Section 5, we will more closely inspect the PE−T distributions for all cases at early times for which disparity in KE and PE is largest.

The T−A and PE−A trends are relatively closer in the case of diamonds in which significantly less plastic flow occurs. This may be attributable to the difference in the initial area or the dissimilar collapse mechanisms.

5. PE−T DISTRIBUTIONS

It was established in ref 46 that hotspots are not fully described by their KE fields; the energy localized as PE cannot be inferred from the KE and the mapping is not one-to-one. The hotspots analyzed in Section 4 show a wide range of PE and
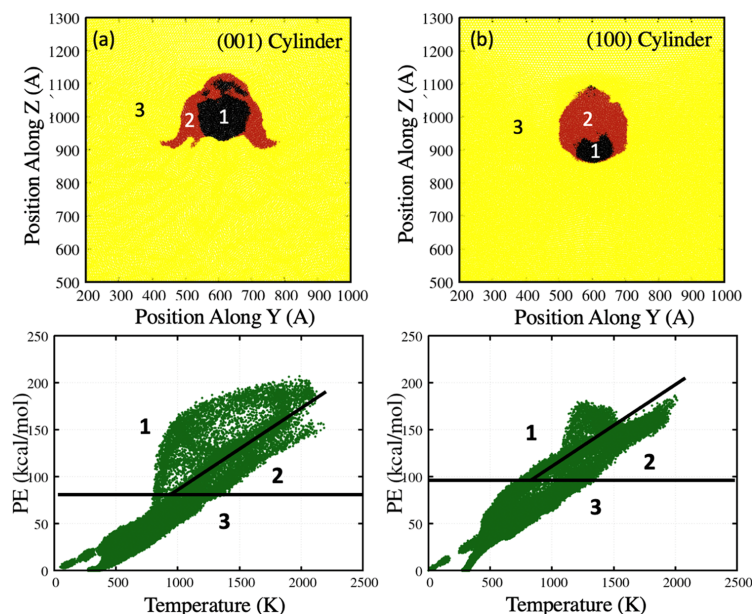
Figure 10. Spatial location of the molecules of the 2.0 km/s cylindrical pore collapses. Bottom panels show the PE(T) distributions from Figure 9, with three regions depicted that are colored appropriately in the spatial plot with region 1 in the black, region 2 in red, and region 3 in yellow.

temperature states for various pore shapes and shock strengths. In this section, we quantify the relationship between PE and temperature for all of the cases studied to assess the role of shock strength, orientation, and defect shape on the disparity between the two energies.

Figure 9 displays scatter plots of local PE vs temperature for the various hotspots right after total collapse of the void ($t_o + 1$ ps). These plots are broken into four subsets based on shock orientation and defect shape. The data represent the entire system at a single snapshot in time and thus show the unshocked state (low PE and temperature), the shocked states at a range of times behind the leading wave, and the hotspot. Dashed lines represent classical equipartition of energy.

As expected, the total PE and temperature are lower for weaker shocks, as is the spread of PE states for a given temperature. For weaker shocks, the system closely follows equipartition in which energy is equally shared between degrees of freedom that appear as quadratic terms in the Hamiltonian, which leads to approximately equal KE and thermal PE. We find a strikingly broad distribution of PE states in the case of cylindrical pores, while collapsed diamonds show a simpler relationship between PE and T, in which they mostly follow equipartition of energy. In the case of the cylindrical pores, the spread of PE states for a given temperature is most noticeable at mid temperatures (>800 K for U_p = 2.0 km/s). Quite interestingly, (001) shocks result in two distinct PE branches while the (100) shocks exhibit a high-PE hump at intermediate hotspot temperatures, with almost all points existing in excess PE compared to classical equipartition of energy (dashed black lines in Figure 9). The lack of excess in PE for the diamond pores is most likely related to the lack of plastic flow, which larger diamonds could plausibly still induce.

To understand the processes that result in high-PE states, corresponding to highly deformed molecules, we map the molecules corresponding to the high-PE branch in the 2 km/s (001) and the hump in the 2 km/s (100) into real space; see Figure 10. This shows that, in both cases, the high-PE states do not correspond spatially to the impact plane where the expanding material collides with the downstream face of the pore. Rather, they correspond to the areas directly behind this, which have the highest degree of plastic deformation. This observation explains why the diamond pores do not show high-PE states for a given KE, as little plastic flow is needed to fill the void space. The initial location plots of the various colored atoms from Figure 10 are available in Figure S3 in the SI, in which most of the black areas are in front of the pore and the red areas are in the rim of the pore.

6. ENERGY LOCALIZATION EFFICIENCY: TATB VS HMX

Figure 11 compares the temperature fields (T vs cumulative area plots) resulting from the collapse of pores in TATB and HMX for 2.0 km/s. Note that the HMX results are for 40 nm diamond and cylindrical pores from ref 16. For all cases, the area is scaled by the initial defect area for the pores and we scale the temperature rise ($T_{shock} - T_{bulk}$) by the theoretical maximum hotspot temperature from ref 15: $k_B \Delta T = m/3 U_s U_p$, where m is the mass of the molecule. As shown in Figure 7, TATB pores have similar efficiency at localizing energy, except for a (100) shock with a diamond pore, where we find higher temperatures. The collapse of cylindrical pores in HMX results in hotspots with similar temperature distributions to TATB. However, Figure 11 shows that diamond pores result in significantly higher temperatures in HMX than in TATB.
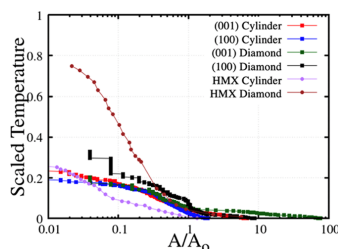
I

Figure 11. Scaled temperature−area plots for shocks, and two HMX shocks from ref 16.

Using the cohesive energy scaling law for jetting from Holian et al. in ref 15, $1/2 m U_p^2 > E_{coh}$ (see Section 3.2), we can compare E_{coh}/m (where m is taken to be the molecular weight) as an assessment of each material's propensity to jet. For TATB and HMX, respectively, this value is 6.7×10^{-3} and 6.9×10^{-3} eV/molecule, or more coherently, the necessary U_p to jet is 1.14 and 1.15 km/s for TATB and HMX, respectively. However, the energy localized from diamond pores is greater for HMX than for either orientation in TATB. Another key difference is that the velocities of jetted HMX molecules are significantly higher than either of the TATB orientations. SM-1 shows the distributions of molecular center of mass velocities for jetted molecules in both 2.0 km/s diamond cases and an HMX 40 nm diamond from ref 16. Despite similar E_{coh}/MW values, jetted HMX molecules possess much higher KE for equivalent shock and defect conditions. This indicates that jetting, which may be key to high-temperature hotspots seen experimentally,[59−61] is the result of not just the cohesive properties of the crystal but complex microstructural phenomena related to crystal defects and stress relaxation mechanisms. The present results indicate that jetting by itself serves mostly to increase the KE of a hotspot and does not lead to significant differences in the localization of PE on the length scales studied here.

These results widen a few questions regarding TATB: Do TATB crystalline defects and shear bands alleviate more energy in the bulk than HMX, causing less violent pore collapse and weaker hotspots? Here, we show a lower efficiency in generating hotspots in TATB relative to HMX, which may help to account for insensitivity to shock initiation that is typically rationalized by molecular and chemical traits such as covalent clustering reactions[77,78] and the crystal's strong 2D hydrogen-bonding network.[30,79] The overall mechanisms behind molecular jetting and massive hotspot temperatures are still not fully understood, but obviously play a significant role in the criticality of hotspots and the overall thermomechanical response of a material under shock loading.

7. CONCLUSIONS

In summary, we have shown that the greater localization of intramolecular potential energy (PE) than kinetic energy (KE) occurs in TATB for a variety of impact velocities, defect shapes, and crystallographic orientations. This shows that the results of ref 46 are a more general finding for a variety of shock states. Within each orientation, the trends seen in PE are nearly the same as those seen in temperature, with excess PE in cases with significant plastic flow. Between orientations, the difference in hotspot shape and size can be broadly explained

by the molecular and crystal-level processes occurring during the collapse, such as shear localization and lateral relaxations of the shocked crystal. For cylindrical pores, both hotspots reach similar temperatures and total areas. However, for diamond pores, while both orientations lead to significant molecular spall, an orientation-dependent temperature is evident. We show that this results from the shockwave progressing past the far end of the diamond pore prior to spallation in some cases, which causes lateral compression of the diamond pore that chokes off the jetted material and limits the maximum hotspot temperature. For all strong shock cases in cylindrical pores ($U_p \geq 1.5$ km/s), there is no direct mapping between the KE and PE of the hotspot, implying that the thermodynamic state of the hotspot cannot be characterized by temperature alone. Finally, we compare scaled hotspot temperatures in TATB to previous results for HMX, showing a potential inefficiency of TATB to create high-temperature hotspots from mechanisms such as molecular ejecta. This result opens new questions about the general role of crystal-level defect formation in forming hotspots and how microstructure and crystallography affect shock focusing at defects, especially in cases of molecular ejecta.

■ ASSOCIATED CONTENT

Ⓢⓘ Supporting Information

The Supporting Information is available free of charge at https://pubs.acs.org/doi/10.1021/acs.jpcc.1c10226.

> Diamond pore ejecta velocity distribution (SM-1); diamond pore ejecta time evolution (SM-2); and spatial localization of PE (SM-3) (PDF)

■ AUTHOR INFORMATION

Corresponding Author

Alejandro Strachan − School of Materials Engineering and Birck Nanotechnology Center, Purdue University, West Lafayette, Indiana 47907, United States; Email: strachan@purdue.edu

Authors

Brenden W. Hamilton − School of Materials Engineering and Birck Nanotechnology Center, Purdue University, West Lafayette, Indiana 47907, United States; ⓞ orcid.org/0000-0002-4524-2201

Matthew P. Kroonblawd − Physical and Life Sciences Directorate, Lawrence Livermore National Laboratory, Livermore, California 94550, United States; ⓞ orcid.org/0000-0002-5009-5998

Complete contact information is available at:
https://pubs.acs.org/10.1021/acs.jpcc.1c10226

Notes

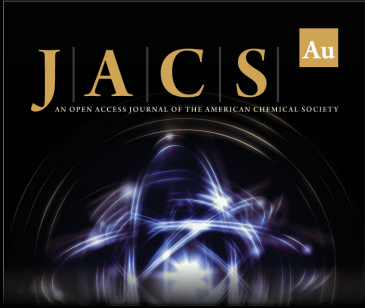The authors declare no competing financial interest.

■ REFERENCES

(1) Reed, E. J.; Manaa, M. R.; Fried, L. E.; Glaesemann, K. R.; Joannopoulos, J. D. A Transient Semimetallic Layer in Detonating Nitromethane. *Nat. Phys.* **2008**, *4*, 72−76.

(2) Bastea, S. Nanocarbon Condensation in Detonation. *Sci. Rep.* **2017**, *7*, No. 42151.

(3) Reed, E. J.; Rodriguez, A. W.; Manaa, M. R.; Fried, L. E.; Tarver, C. M. Ultrafast Detonation of Hydrazoic Acid (HN 3). *Phys. Rev. Lett.* **2012**, *109*, No. 038301.

(4) Goldman, N.; Tamblyn, I. Prebiotic Chemistry within a Simple Impacting Icy Mixture. *J. Phys. Chem. A* **2013**, *117*, 5124−5131.

(5) Goldman, N.; Reed, E. J.; Fried, L. E.; William Kuo, I. F.; Maiti, A. Synthesis of Glycine-Containing Complexes in Impacts of Comets on Early Earth. *Nat. Chem.* **2010**, *2*, 949−954.

(6) Martins, Z.; Price, M. C.; Goldman, N.; Sephton, M. A.; Burchell, M. J. Shock Synthesis of Amino Acids from Impacting Cometary and Icy Planet Surface Analogues. *Nat. Geosci.* **2013**, *6*, 1045−1049.

(7) Kroonblawd, M. P.; Lindsey, R. K.; Goldman, N. Synthesis of Functionalized Nitrogen-Containing Polycyclic Aromatic Hydrocarbons and Other Prebiotic Compounds in Impacting Glycine Solutions. *Chem. Sci.* **2019**, *10*, 6091−6098.

(8) Steele, B. A.; Goldman, N.; Kuo, I. F. W.; Kroonblawd, M. P. Mechanochemical Synthesis of Glycine Oligomers in a Virtual Rotational Diamond Anvil Cell. *Chem. Sci.* **2020**, *11*, 7760−7771.

(9) Shen, Y.; Reed, E. J. Quantum Nuclear Effects in Stishovite Crystallization in Shock-Compressed Fused Silica. *J. Phys. Chem. C* **2016**, *120*, 17759−17766.

(10) Shen, Y.; Jester, S. B.; Qi, T.; Reed, E. J. Nanosecond Homogeneous Nucleation and Crystal Growth in Shock-Compressed SiO₂. *Nat. Mater.* **2016**, *15*, 60−65.

(11) Armstrong, M. R.; Lindsey, R. K.; Goldman, N.; Nielsen, M. H.; Stavrou, E.; Fried, L. E.; Zaug, J. M.; Bastea, S. Ultrafast Shock Synthesis of Nanocarbon from a Liquid Precursor. *Nat. Commun.* **2020**, *11*, No. 353.

(12) Hamilton, B. W.; Sakano, M. N.; Li, C.; Strachan, A. Chemistry Under Shock Conditions. *Annu. Rev. Mater. Res.* **2021**, *51*, 101−130.

(13) Campbell, A. W.; Travis, J. R. *Shock Desensitization of PBX-9404 and Composition B-3*, LA-UR-85-1114; Los Alamos National Lab. (LANL), 1985.

(14) Dattelbaum, D. M.; Sheffield, S. A.; Stahl, D. B.; Dattelbaum, A. M.; Trott, W.; Engelke, R. *Influence of Hot Spot Features on the Initiation Characteristics of Heterogeneous Nitromethane*, LA-UR-10-01472; Los Alamos National Lab. (LANL), 2010.

(15) Holian, B. L.; Germann, T. C.; Maillet, J. B.; White, C. T. Atomistic Mechanism for Hot Spot Initiation. *Phys. Rev. Lett.* **2002**, *89*, No. 285501.

(16) Li, C.; Hamilton, B. W.; Strachan, A. Hotspot Formation Due to Shock-Induced Pore Collapse in 1,3,5,7-Tetranitro-1,3,5,7-Tetrazoctane (HMX): Role of Pore Shape and Shock Strength in Collapse Mechanism and Temperature. *J. Appl. Phys.* **2020**, *127*, No. 175902.

(17) Long, Y.; Chen, J. Theoretical Study of the Defect Evolution for Molecular Crystal under Shock Loading. *J. Appl. Phys.* **2019**, *125*, No. 065107.

(18) Springer, H. K.; Bastea, S.; Nichols, A. L.; Tarver, C. M.; Reaugh, J. E. Modeling The Effects of Shock Pressure and Pore Morphology on Hot Spot Mechanisms in HMX. *Propellants, Explos., Pyrotech.* **2018**, *43*, 805−817.

(19) Austin, R. A.; Barton, N. R.; Reaugh, J. E.; Fried, L. E. Direct Numerical Simulation of Shear Localization and Decomposition

Reactions in Shock-Loaded HMX Crystal. *J. Appl. Phys.* **2015**, *117*, No. 185902.

(20) Rai, N. K.; Sen, O.; Udaykumar, H. S. Macro-Scale Sensitivity through Meso-Scale Hotspot Dynamics in Porous Energetic Materials: Comparing the Shock Response of 1,3,5-Triamino-2,4,6-Trinitrobenzene (TATB) and 1,3,5,7-Tetranitro-1,3,5,7-Tetrazoctane (HMX). *J. Appl. Phys.* **2020**, *128*, No. 085903.

(21) Zhao, P.; Lee, S.; Sewell, T.; Udaykumar, H. S. Tandem Molecular Dynamics and Continuum Studies of Shock-Induced Pore Collapse in TATB. *Propellants, Explos., Pyrotech.* **2020**, *45*, 196−222.

(22) Duarte, C. A.; Li, C.; Hamilton, B. W.; Strachan, A.; Koslowski, M. Continuum and Molecular Dynamics Simulations of Pore Collapse in Shocked β-Tetramethylene Tetranitramine (β -HMX) Single Crystals. *J. Appl. Phys.* **2021**, *129*, No. 015904.

(23) Wood, M. A.; Kittell, D. E.; Yarrington, C. D.; Thompson, A. P. Multiscale Modeling of Shock Wave Localization in Porous Energetic Material. *Phys. Rev. B* **2018**, *97*, No. 014109.

(24) Strachan, A.; van Duin, A. C. T.; Chakraborty, D.; Dasgupta, S.; Goddard, W. A. Shock Waves in High-Energy Materials: The Initial Chemical Events in Nitramine RDX. *Phys. Rev. Lett.* **2003**, *91*, No. 098301.

(25) Strachan, A.; Kober, E. M.; Van Duin, A. C. T.; Oxgaard, J.; Goddard, W. A. Thermal Decomposition of RDX from Reactive Molecular Dynamics. *J. Chem. Phys.* **2005**, *122*, No. 054502.

(26) Zybin, S. V.; Goddard, W. A.; Xu, P.; Van Duin, A. C. T.; Thompson, A. P. Physical Mechanism of Anisotropic Sensitivity in Pentaerythritol Tetranitrate from Compressive-Shear Reaction Dynamics Simulations. *Appl. Phys. Lett.* **2010**, *96*, No. 081918.

(27) Guo, D.; An, Q.; Goddard, W. A.; Zybin, S. V.; Huang, F. Compressive Shear Reactive Molecular Dynamics Studies Indicating That Cocrystals of TNT/CL-20 Decrease Sensitivity. *J. Phys. Chem. C* **2014**, *118*, 30202−30208.

(28) Riad Manaa, M.; Reed, E. J.; Fried, L. E. In *Atomistic Simulations of Chemical Reactivity of TATB under Thermal and Shock Conditions*, Proceedings of the 14th International Detonation Symposium, IDS, 2010; pp 837−843.

(29) Manaa, M. R.; Goldman, N.; Fried, L. E. In *Simulation of Cluster Formation in Overdriven and Expanding TATB by Molecular Dynamics*, Proceedings of the 15th International Detonation Symposium, 2015; pp 53−59.

(30) Manaa, M. R. Shear-Induced Metallization of Triamino-Trinitrobenzene Crystals. *Appl. Phys. Lett.* **2003**, *83*, 1352−1354.

(31) Hamilton, B. W.; Kroonblawd, M. P.; Islam, M. M.; Strachan, A. Sensitivity of the Shock Initiation Threshold of 1,3,5-Triamino-2,4,6-Trinitrobenzene (TATB) to Nuclear Quantum Effects. *J. Phys. Chem. C* **2019**, *123*, 21969−21981.

(32) Guo, D.; Zybin, S. V.; An, Q.; Goddard, W. A.; Huang, F. Prediction of the Chapman-Jouguet Chemical Equilibrium State in a Detonation Wave from First Principles Based Reactive Molecular Dynamics. *Phys. Chem. Chem. Phys.* **2016**, *18*, 2015−2022.

(33) Islam, M. M.; Strachan, A. Decomposition and Reaction of Polyvinyl Nitrate under Shock and Thermal Loading: A ReaxFF Reactive Molecular Dynamics Study. *J. Phys. Chem. C* **2017**, *121*, 22452−22464.

(34) Islam, M. M.; Strachan, A. Reactive Molecular Dynamics Simulations to Investigate the Shock Response of Liquid Nitromethane. *J. Phys. Chem. C* **2019**, *123*, 2613−2626.

(35) Powell, M. S.; Sakano, M. N.; Cawkwell, M. J.; Bowlan, P. R.; Brown, K. E.; Bolme, C. A.; Moore, D. S.; Son, S. F.; Strachan, A.; McGrane, S. D. Insight into the Chemistry of PETN under Shock Compression through Ultrafast Broadband Mid-Infrared Absorption Spectroscopy. *J. Phys. Chem. A* **2020**, *124*, 7031−7046.

(36) Zhang, L.; Zybin, S. V.; van Duin, A. C. T.; Dasgupta, S.; Goddard, A. G., III; Kober, E. M. Carbon Cluster Formation during Thermal Decomposition of Octahydro-1,3,5,7-tetranitro-1,3,5,7-tetrazocine and 1,3,5-Triamino-2,4,6-trinitrobenzene High Explosives from ReaxFF Reactive Molecular Dynamics Simulations. *J. Phys. Chem. A* **2009**, 10619−10640.

(37) Hamilton, B. W.; Steele, B. A.; Sakano, M. N.; Kroonblawd, M. P.; Kuo, I. F. W.; Strachan, A. Predicted Reaction Mechanisms, Product Speciation, Kinetics, and Detonation Properties of the Insensitive Explosive 2,6-Diamino-3,5-Dinitropyrazine-1-Oxide (LLM-105). *J. Phys. Chem. A* **2021**, *125*, 1766−1777.

(38) Wu, C. J.; Fried, L. E. Ab Initio Study of RDX Decomposition Mechanisms. *J. Phys. Chem. A* **1997**, *101*, 8675−8679.

(39) Wu, C. J.; Fried, L. E. Ring Closure Mediated by Intramolecular Hydrogen Transfer in the Decomposition of a Push-Pull Nitro-aromatic: TATB. *J. Phys. Chem. A* **2000**, *104*, 6447−6452.

(40) Sakano, M.; Hamilton, B. W.; Islam, M. M.; Strachan, A. Role of Molecular Disorder on the Reactivity of RDX. *J. Phys. Chem. C* **2018**, *122*, 27032−27043.

(41) Sakano, M. N.; Hamed, A.; Kober, E. M.; Grilli, N.; Hamilton, B. W.; Islam, M. M.; Koslowski, M.; Strachan, A. Unsupervised Learning-Based Multiscale Model of Thermochemistry in 1,3,5-Trinitro-1,3,5-Triazinane (RDX). *J. Phys. Chem. A* **2020**, *124*, 9141−9155.

(42) Wood, M. A.; Cherukara, M. J.; Kober, E. M.; Strachan, A. Ultrafast Chemistry under Nonequilibrium Conditions and the Shock to Deflagration Transition at the Nanoscale. *J. Phys. Chem. C* **2015**, *119*, 22008−22015.

(43) Shan, T. R.; Wixom, R. R.; Thompson, A. P. Extended Asymmetric Hot Region Formation Due to Shockwave Interactions Following Void Collapse in Shocked High Explosive. *Phys. Rev. B* **2016**, *94*, No. 054308.

(44) Kroonblawd, M. P.; Fried, L. E. High Explosive Ignition through Chemically Activated Nanoscale Shear Bands. *Phys. Rev. Lett.* **2020**, *124*, No. 206002.

(45) Fried, L. E. In *High Explosive Shock Initiation Model Based on Hot Spot Temperature*, Proceedings of the 16th International Detonation Symposium, 2018; pp 1156−1163.

(46) Hamilton, B. W.; Kroonblawd, M. P.; Li, C.; Strachan, A. A Hotspot's Better Half: Non-Equilibrium Intra-Molecular Strain in Shock Physics. *J. Phys. Chem. Lett.* **2021**, *12*, 2756−2762.

(47) Kroonblawd, M. P.; Hamilton, B. W.; Strachan, A. Fourier-like Thermal Relaxation of Nanoscale Explosive Hot Spots. *J. Phys. Chem. C* **2021**, *125*, 20570−20582.

(48) Ribas-Arino, J.; Marx, D. Covalent Mechanochemistry: Theoretical Concepts and Computational Tools with Applications to Molecular Nanomechanics. *Chem. Rev.* **2012**, *112*, 5412−5487.

(49) Islam, M. M.; Strachan, A. Role of Dynamical Compressive and Shear Loading on Hotspot Criticality in RDX via Reactive Molecular Dynamics. *J. Appl. Phys.* **2020**, *128*, No. 065101.

(50) Wiita, A. P.; Ainavarapu, S. R. K.; Huang, H. H.; Fernandez, J. M. Force-Dependent Chemical Kinetics of Disulfide Bond Reduction Observed with Single-Molecule Techniques. *Proc. Natl. Acad. Sci. U.S.A.* **2006**, *103*, 7222−7227.

(51) Stauch, T.; Dreuw, A. Advances in Quantum Mechanochemistry: Electronic Structure Methods and Force Analysis. *Chem. Rev.* **2016**, *116*, 14137−14180.

(52) Ong, M. T.; Leiding, J.; Tao, H.; Virshup, A. M.; Martínez, T. J. First Principles Dynamics and Minimum Energy Pathways for Mechanochemical Ring Opening of Cyclobutene. *J. Am. Chem. Soc.* **2009**, *131*, 6377−6379.

(53) Kroonblawd, M. P.; Steele, B. A.; Nelms, M. D.; Fried, L. E.; Austin, R. A. Anisotropic Strength Behavior of Single-Crystal TATB. *Modell. Simul. Mater. Sci. Eng.* **2021**, *30*, No. 014004.

(54) Cady, H. H.; Larson, A. C. The Crystal Structure of 1,3,5-Triamino-2,4,6-Trinitrobenzene. *Acta Crystallogr.* **1965**, *18*, 485−496.

(55) Lafourcade, P.; Denoual, C.; Maillet, J. B. Irreversible Deformation Mechanisms for 1,3,5-Triamino-2,4,6-Trinitrobenzene Single Crystal through Molecular Dynamics Simulations. *J. Phys. Chem. C* **2018**, *122*, 14954−14964.

(56) Zhao, P.; Kroonblawd, M. P.; Mathew, N.; Sewell, T. Strongly Anisotropic Thermomechanical Response to Shock Wave Loading in Oriented Samples of the Triclinic Molecular Crystal 1,3,5- Triamino-2,4,6-Trinitrobenzene. *J. Phys. Chem. C* **2021**, *125*, 22747−22765.

(57) Kroonblawd, M. P.; Sewell, T. D. Theoretical Determination of Anisotropic Thermal Conductivity for Initially Defect-Free and Defective TATB Single Crystals. *J. Chem. Phys.* **2014**, *141*, No. 184501.

(58) Steele, B. A.; Clarke, S. M.; Kroonblawd, M. P.; Kuo, I. F. W.; Pagoria, P. F.; Tkachev, S. N.; Smith, J. S.; Bastea, S.; Fried, L. E.; Zaug, J. M.; et al. Pressure-Induced Phase Transition in 1,3,5-Triamino-2,4,6-Trinitrobenzene (TATB). *Appl. Phys. Lett.* **2019**, *114*, No. 191901.

(59) Bassett, W. P.; Johnson, B. P.; Neelakantan, N. K.; Suslick, K. S.; Dlott, D. D. Shock Initiation of Explosives: High Temperature Hot Spots Explained. *Appl. Phys. Lett.* **2017**, *111*, No. 061902.

(60) Bassett, W. P.; Johnson, B. P.; Dlott, D. D. Dynamic Absorption in Optical Pyrometry of Hot Spots in Plastic-Bonded Triaminotrini-trobenzene. *Appl. Phys. Lett.* **2019**, *114*, No. 194101.

(61) Bassett, W. P.; Johnson, B. P.; Salvati, L.; Nissen, E. J.; Bhowmick, M.; Dlott, D. D. Shock Initiation Microscopy with High Time and Space Resolution. *Propellants, Explos., Pyrotech.* **2020**, *45*, 223−235.

(62) Plimpton, S. Fast Parallel Algorithms for Short-Range Molecular Dynamics. *J. Comput. Phys.* **1995**, *117*, 1−19.

(63) Bedrov, D.; Borodin, O.; Smith, G. D.; Sewell, T. D.; Dattelbaum, D. M.; Stevens, L. L. A Molecular Dynamics Simulation Study of Crystalline 1,3,5-Triamino-2,4,6- Trinitrobenzene as a Function of Pressure and Temperature. *J. Chem. Phys.* **2009**, *131*, No. 224703.

(64) Kroonblawd, M. P.; Sewell, T. D. Theoretical Determination of Anisotropic Thermal Conductivity for Crystalline 1,3,5-Triamino-2,4,6-Trinitrobenzene (TATB). *J. Chem. Phys.* **2013**, *139*, No. 074503.

(65) Andersen, H. C. Rattle: A "Velocity" Version of the Shake Algorithm for Molecular Dynamics Calculations. *J. Comput. Phys.* **1983**, *52*, 24−34.

(66) Mathew, N.; Sewell, T. D.; Thompson, D. L. Anisotropy in Surface-Initiated Melting of the Triclinic Molecular Crystal 1,3,5-Triamino-2,4,6-Trinitrobenzene: A Molecular Dynamics Study. *J. Chem. Phys.* **2015**, *143*, No. 094706.

(67) Wolf, D.; Keblinski, P.; Phillpot, S. R.; Eggebrecht, J. Exact Method for the Simulation of Coulombic Systems by Spherically Truncated, Pairwise r-1 Summation. *J. Chem. Phys.* **1999**, *110*, 8254−8282.

(68) Kroonblawd, M. P.; Mathew, N.; Jiang, S.; Sewell, T. D. A Generalized Crystal-Cutting Method for Modeling Arbitrarily Oriented Crystals in 3D Periodic Simulation Cells with Applications to Crystal−Crystal Interfaces. *Comput. Phys. Commun.* **2016**, *207*, 232−242.

(69) Nosé, S. A Unified Formulation of the Constant Temperature Molecular Dynamics Methods. *J. Chem. Phys.* **1984**, *81*, 511−519.

(70) Holian, B. L.; Lomdahl, P. S. Plasticity Induced by Shock Waves in Nonequilibrium Molecular-Dynamics Simulations. *Science* **1998**, *280*, 2085−2088.

(71) Taw, M. R.; Yeager, J. D.; Hooks, D. E.; Carvajal, T. M.; Bahr, D. F. The Mechanical Properties of As-Grown Noncubic Organic Molecular Crystals Assessed by Nanoindentation. *J. Mater. Res.* **2017**, *32*, 2728−2737.

(72) Pal, A.; Picu, C. R. Non-Schmid Effect of Pressure on Plastic Deformation in Molecular Crystal HMX. *J. Appl. Phys.* **2019**, *125*, No. 215111.

(73) Forbes, J. W. *Shock Wave Compression of Condensed Matter*; Springer Science & Business Media, 2013.

(74) Sturtevant, B.; Kulkarny, V. A. The Focusing of Weak Shock Waves. *J. Fluid Mech.* **1976**, *73*, 651−671.

(75) Cates, J. E.; Sturtevant, B. Shock Wave Focusing Using Geometrical Shock Dynamics. *Phys. Fluids* **1997**, *9*, 3058−3068.

(76) Tarver, C. M.; Chidester, S. K.; Nichols, A. L. Critical Conditions for Impact- and Shock-Induced Hot Spots in Solid Explosives. *J. Phys. Chem. A* **1996**, *100*, 5794−5799.

L

(77) Manaa, M. R.; Reed, E. J.; Fried, L. E.; Goldman, N. Nitrogen-Rich Heterocycles as Reactivity Retardants in Shocked Insensitive Explosives. *J. Am. Chem. Soc.* **2009**, *131*, 5483−5487.

(78) Tiwari, S. C.; Nomura, K. I.; Kalia, R. K.; Nakano, A.; Vashishta, P. Multiple Reaction Pathways in Shocked 2,4,6-Triamino-1,3,5-Trinitrobenzene Crystal. *J. Phys. Chem. C* **2017**, *121*, 16029−16034.

(79) Manaa, M. R.; Gee, R. H.; Fried, L. E. Internal Rotation of Amino and Nitro Groups in TATB: MP2 versus DFT (B3LYP). *J. Phys. Chem. A* **2002**, *106*, 8806−8810.

M

List of Contributing Author Publications:

- Sakano, M., Hamilton, B., Islam, M. M., & Strachan, A. (2018). Role of Molecular Disorder on the Reactivity of RDX. *The Journal of Physical Chemistry C*, *122*(47), 27032-27043.

- Li, C., Hamilton, B. W., & Strachan, A. (2020). Hotspot formation due to shock-induced pore collapse in 1, 3, 5, 7-tetranitro-1, 3, 5, 7-tetrazoctane (HMX): Role of pore shape and shock strength in collapse mechanism and temperature. *Journal of Applied Physics*, *127*(17), 175902.

- Sakano, Michael N., Ahmed Hamed, Edward M. Kober, Nicolo Grilli, Brenden W. Hamilton, Md Mahbubul Islam, Marisol Koslowski, and Alejandro Strachan. "Unsupervised learning-based multiscale model of thermochemistry in 1, 3, 5-Trinitro-1, 3, 5-triazinane (RDX)." *The Journal of Physical Chemistry A* 124, no. 44 (2020): 9141-9155.

- Duarte, C. A., Li, C., Hamilton, B. W., Strachan, A., & Koslowski, M. (2021). Continuum and molecular dynamics simulations of pore collapse in shocked β-tetramethylene tetranitramine (β-HMX) single crystals. *Journal of Applied Physics*, *129*(1), 015904.

- Kroonblawd, M. P., Hamilton, B. W., & Strachan, A. (2021). Fourier-like Thermal Relaxation of Nanoscale Explosive Hot Spots. *The Journal of Physical Chemistry C*, *125*(37), 20570-20582.